COSMOLOGICAL SIMULATIONS WITH AGN FEEDBACK

By

Philip Taylor

A THESIS SUBMITTED TO THE UNIVERSITY OF HERTFORDSHIRE
IN PARTIAL FULFILMENT OF THE REQUIREMENTS OF
DOCTOR OF PHILOSOPHY
CENTRE FOR ASTROPHYSICS RESEARCH
APRIL 2015

Abstract

We implement a model for, and study the effects of, AGN feedback in cosmological hydrodynamical simulations. In our model, black holes form high-density, primordial gas, to imitate the likely channels of black hole formation in the early Universe. We find that a black hole seed mass of $10^{2-3}h^{-1}M_{\odot}$ is required to produce simulations that match the cosmic star formation rate density, and present-day black hole mass – velocity dispersion and galaxy size – velocity dispersion relations. We therefore suggest that Population III stars can be the progenitors of the super-massive black holes seen today.

Using our fiducial model, we run two large simulations ($(25h^{-1}$ Mpc$)^3$), one with and one without AGN feedback. With these, we follow the population of galaxies that forms across cosmic time, and find that the inclusion of AGN feedback improves the agreement of simulated and observed galaxy properties, such as the mass and luminosity functions. This agreement is best at $z = 0$, and fairly good out to $z = 2 - 3$. Evidence for downsizing in the evolution of galaxies is found, both in the present-day colour–magnitude and $[\alpha/\mathrm{Fe}]$–velocity dispersion relations, and by the fact that high-mass galaxies attain their present-day metallicity earlier and faster than do low-mass ones.

With our hydrodynamical simulations, we can also investigate the internal structure of galaxies, and look at the effects of galaxy mergers and AGN feedback on the stellar and gas-phase metallicity gradients of galaxies. Stellar metallicity gradients are found to be sensitive to galaxy mergers, while gas-phase metallicity gradients are more affected by AGN activity. This suggests that simultaneous measurements of these two quantities can help disentangle the actions of mergers and AGN feedback on a galaxy's history.

Finally, we develop a new method to identify massive AGN-driven outflows from the most massive simulated galaxy. These events cause the intra-cluster medium to be hotter and more chemically enriched compared to the simulation without AGN feedback, and therefore AGN feedback may be required in order to attain the metallicities observed in clusters.

Contents

List of Figures

List of Tables

1
Introduction

1.1 Galaxy Formation & Evolution

It is widely believed that the Universe began some $13 - 14$ billion years ago. This event, the Big Bang, created all the matter present in the Universe today. However, models of Big Bang nucleosynthesis, backed up by observations of near-pristine environments, indicate that the only elements created at this time were hydrogen, helium, and lithium (Schramm & Turner, 1998; Burles et al., 2001; Steigman, 2004). In addition, it is believed that a period of super-luminal expansion of space, known as inflation, occurred extremely early in its life, smoothing inhomogeneities on vast scales. It is therefore a fundamental question to understand how the Universe changed from its smooth, chemically-simple initial state to the one we see today.

1.1.1 Large Scale Structure

The early Universe was sufficiently hot, and its energy budget dominated by photons, that all baryonic matter was ionised. However, it cooled as it expanded, and after $\sim 380,000$ years, electrons and nuclei were able to combine and form neutral atoms, an event known as recombination. Photons could then travel unimpeded through space; today we observe these as the Cosmic Microwave Background (CMB) radiation, first identified by Penzias & Wilson (1965).

Measurements of the CMB are crucial to our understanding of the subsequent evolution of the Universe, and surveys by the Cosmic Background Explorer (COBE; Mather, 1982), Wilkinson Microwave Anisotropy Probe (WMAP; Bennett et al., 2003), and Planck (Planck Collaboration et al., 2014) satellites, amongst others, have provided a wealth of data on its properties. The CMB spectrum is very well fit by a black body spectrum with characteristic temperature $T = 2.7255 \pm 0.0006$ K (Fixsen, 2009), and spatial anisotropies are seen with amplitudes of order the uncertainty in this value. These deviations from isotropy have two sources: variations in the distribution of matter at the surface of last scattering (primary anisotropies); or due to interactions between the CMB and intervening matter (secondary anisotropies). The primary anisotropies are born from quantum fluctuations writ large by inflation, and are the seeds of the largest scale structure in the Universe. Regions of higher-than-average temperature are indicative of over densities, with the opposite true for regions of lower-than-average temperature. Over time, high-density regions collapsed under gravity, forming Mpc-scale filaments and sheets of dark matter (DM, see Section 1.1.2), while under-dense regions became more rarefied, leading to vast voids (Fabian, 1992). This arrangement of DM is commonly referred to as the cosmic web; it is illustrated in Fig. 1.1, which shows the projected distribution of mass in DM at $z = 0$ in a simulation $25h^{-1}$ Mpc on a side (see Section 3.2 for details).

DM dominates the mass budget of the Universe (e.g., Planck Collaboration et al., 2015), and so baryonic matter and galaxies trace this DM structure on large scales. It is to the properties of galaxies and their formation that we know turn our attention.

1.1.2 Galaxies

Galaxies are gravitationally bound collections of DM, gas, stars, and dust. Most are believed to host super-massive black holes (BHs, $M_{\rm BH} > 10^6 M_\odot$).

Based on their appearance alone, Hubble (1926) divided galaxies (extragalactic nebulae) into two broad categories, forming his now eponymous sequence. Structureless ellipticals formed one category, further sub-divided by ellipticity, while spirals formed the other, with distinctions being made between those with and without bars, and the tightness of the winding of the spiral arms. However, this was a purely taxonomic exercise, and did not provide an explanation as to how galaxies formed or evolved.

Today, there exist two competing theories to explain the formation of galaxies: a ‘top-down’ scenario; and a ‘bottom-up’ one. In the top-down model (Eggen et al., 1962), galaxies are formed from the monolithic collapse of a massive gas cloud. Clouds with high angular momentum would naturally form a rotationally supported disk, but still collapse in the direction perpendicular to its plane, producing thin disks as observed. On the other hand, clouds with low net angular momentum would not settle into a disk, and instead be pressure-supported, forming elliptical galaxies. The bottom-up model (Searle & Zinn, 1978) posits a hierarchical formation process in which proto-galaxies, formed mostly of gas and DM, coalesce. Since the DM interacts only through gravity and is non-dissipative, it forms a halo around the growing galaxy. The gas collapses towards the centre, and rotates more rapidly to conserve angular momentum, creating a disk of star-forming gas.

In the most successful model of structure formation, Cold Dark Matter (CDM), all structure forms hierarchically; small haloes collapse first, and merge over time to form ever larger ones. This has been challenged observationally, however, by

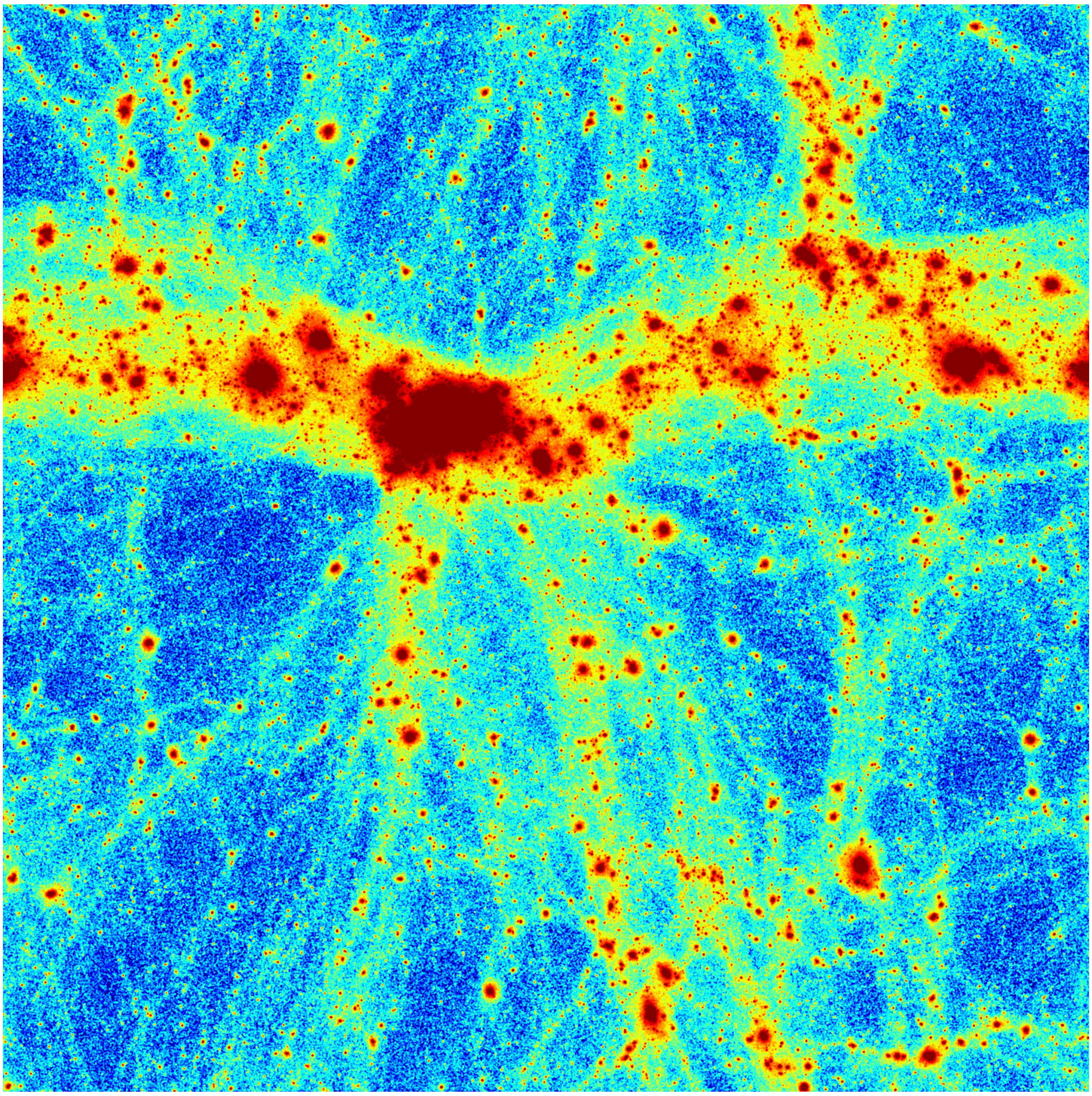

FIGURE 1.1: Projected DM mass distribution of a cosmological simulation in $(25h^{-1}$ Mpc$)^3$ box. The colour is saturated in high-density (red) regions to allow the lower density cosmic web to be seen more clearly.

the downsizing phenomenon (e.g., Cowie et al., 1996; Juneau et al., 2005; Bundy et al., 2006; Stringer et al., 2009), whereby the mass of the most rapidly star-forming galaxies decreases with time. Similar phenomena have also been observed as the evolution in mass-to-light ratios (Treu et al., 2005), and the enhancement of α elements (Thomas et al., 2003) in early-type galaxies.

Early-Type Galaxies

Early-type galaxies (ETGs) have elliptical shapes, featureless distributions of stars (although their kinematics may not be so smooth; see e.g. Krajnović et al. 2008), and are dispersion-supported. They are preferentially found in denser environments (the so-called morphology–density relation; Dressler 1980; Cappellari et al. 2011), which hints at their possible formation via mergers (see Section 1.1.3). Usually devoid of significant quantities of cold, star-forming gas, and hosting old, relatively high-metallicity stars, ETGs tend to have red integrated colours.

Late-Type Galaxies

Late-type galaxies (LTGs) display a more diverse range of morphological types than do ETGs, with a thin, rotationally-supported stellar disk, spiral arms, and sometimes a central bar and bulge. Star formation is often ongoing in the spiral arms of these systems, where there exists a large mass of cold, molecular gas. This means that the stellar population tends to be younger than in ETGs, and so they typically appear, on average, bluer.

1.1.3 Galaxy Mergers

Mergers between galaxies are believed to play an extremely important role in their evolution. Perhaps their most striking effect is to alter the morphology and internal structure of galaxies, with major mergers transforming spirals into ellipticals (Toomre & Toomre, 1972; Hopkins et al., 2008). There is no consensus for what constitutes a major merger, but having a mass ratio greater than $\sim 1/4$ is a common definition (e.g., McIntosh et al., 2008; Kaviraj et al., 2009). Major mergers in which one or both of the galaxies is gas-rich ('damp' and 'wet' respectively) can trigger both star formation and AGN activity (see Section 1.2; Hopkins et al. 2008). Star formation is enhanced when the galaxies pass near to one-another, as well as when they initially coalesce, but this also efficiently funnels gas to the centre of the galaxy causing its BH to grow rapidly, which heats the ISM and may remove gas from the galaxy, quenching star formation. The rearrangement of stellar orbits also causes stellar metallicity gradients to become shallower in ETGs (see Section 5.4; Kobayashi 2004). A corollary to this, therefore, is that it may be possible to deduce the merging history of a galaxy from its present day structure, kinematics, and metallicity profile. Such events are more common in denser environments such as groups and clusters, and the ETG formed may continue to grow through dissipationless ('dry') mergers with other ETGs (McIntosh et al., 2008). Mergers therefore play a key role in determining the present-day properties of galaxies.

1.2 Feedback Processes

The merging scenario outlined in the previous section affects the progenitor galaxies on all scales. As well as the gross structure, baryonic processes that influence the subsequent evolution of the galaxy are also triggered. In this section, I discuss the feedback from stars and AGN, in all stages of a galaxy's life, not just during mergers.

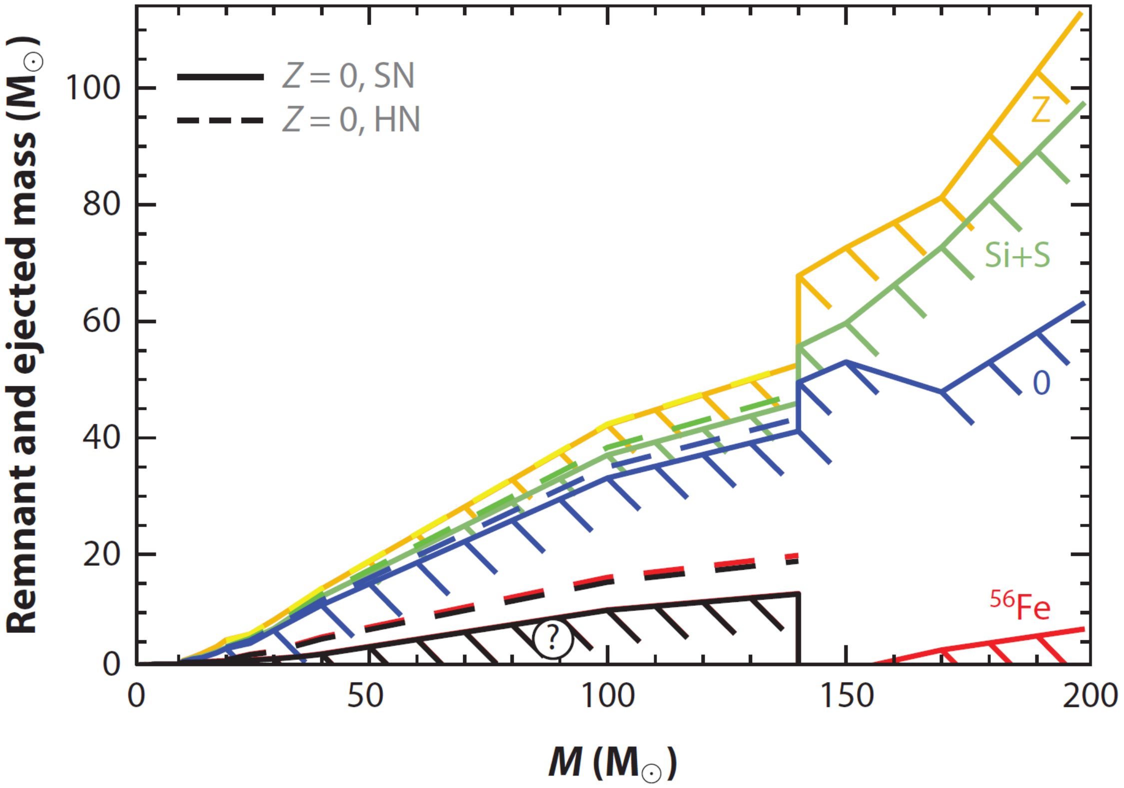

Figure 1.2: Remnant (black) and ejected metal masses as a function of progenitor mass. Above $M > 140 M_\odot$, PISNe leave no remnant. Figure taken from Nomoto et al. (2013).

1.2.1 Stellar Feedback

Supernovae & Hypernovae

Supernovae (SNe) mark a star's explosive end. They may be divided into two broad categories: those caused by the collapse of the core of massive ($M > 8 M_\odot$) stars; and those triggered by the thermonuclear runaway of a degenerate stellar remnant. The most common classes of SNe are type II (SNe II; core collapse), and type Ia (SNe Ia), triggered by accretion of material onto a white dwarf (note: the type designation is based on spectral features, not formation mechanism).

Most stars more massive than $\sim 8 M_\odot$ end their lives as SNe II (Nomoto et al., 2013). In these stars, different fusion pathways occur in shells, and a core of iron is produced since fusion to heavier elements is endothermic. When the core becomes unable to support itself against gravity, it collapses; the outer layers of the star fall onto it and rebound, producing the SN. The pressure and temperature in the outer layers is then sufficient to allow fusion, producing mainly α elements. Depending on the mass of the core, a compact remnant (a neutron star or black hole) may be produced (Janka et al., 2007).

One notable exception is that of low-metallicity stars of mass $140 \lesssim M/M_\odot \lesssim$

300, which are believed to undergo pair-instability supernovae (PISNe; Heger & Woosley, 2002; Umeda & Nomoto, 2002). In such massive stars, the number of gamma rays with sufficient energy to form electron-positron pairs becomes high enough that the loss of these gamma rays to pair production reduces the radiation pressure on the outer layers of the star, and they are no longer supported. This causes the star to contract, heating the core and inducing fusion and gamma ray production, thereby enhancing this effect. The star collapses until the core becomes dense and hot enough for thermonuclear runaway, releasing sufficient energy to unbind the star in a PISN, leaving no remnant; see Fig. 1.2. At higher masses still ($\gtrsim 300 M_\odot$), the endothermic process of photodisintegration occurs as the core collapses, causing the star to collapse directly into a BH.

Such low-metallicity Population III stars may have played a crucial role in the early Universe. From the theory of star formation from primordial gas, the first stars are believed to have been very massive, with masses of the order of $100 M_\odot$, given the limited cooling of molecular hydrogen (e.g., Bromm & Larson, 2004). This depends on fragmentation in a cosmological minihalo, ionization prior to the onset of gravitational collapse, and the accretion rate from the cloud envelope, and it seems possible that lower-mass stars ($\sim 10-40 M_\odot$) may have formed from primordial gas (e.g., Yoshida et al., 2008; Stacy et al., 2010; Greif et al., 2011). On the other hand, if the accretion is not suppressed by feedback from the central star, $\sim 1000 M_\odot$ stars may form (Hirano et al., 2014). This matches with the observed signatures of the first chemical enrichment. The observed elemental abundance patterns of extremely metal-poor stars and metal-poor quasar absorption line systems are consistent not with PISNe but with core-collapse supernovae from $\sim 13-50 M_\odot$ stars that produce $\sim 10 M_\odot$ black holes (Kobayashi et al., 2011). Stars more massive than $\sim 300 M_\odot$ also end up as black holes, and can also be seeds of super-massive black holes.

Given the wide range of progenitor masses and metallicities, there is likely a distribution of SNe II energies. This distribution is unknown; values around $1-1.5 \times 10^{51}$ erg are typical (Woosley, 1988; Blinnikov et al., 2000; Heger et al., 2003), and hypernovae with ~ 10 times as much energy have been estimated from observations (e.g., Nomoto et al., 2001; Tanaka et al., 2009).

To explain the formation of SNe Ia, there are two main theories, the single- and double-degenerate scenarios (e.g., Hillebrandt & Niemeyer, 2000). In the widely-accepted single-degenerate scenario (e.g., Whelan & Iben, 1973; Iben & Tutukov, 1984; Nomoto, 1982), accretion of material onto a CO white dwarf from an evolved, non-degenerate companion overflowing its Roche lobe causes it to approach the Chandrasekhar limit ($\sim 1.4 M_\odot$). As it gains mass, it contracts, heating the core until it becomes hot enough to ignite carbon fusion. This causes a thermonuclear runaway that consumes and unbinds the star (Nomoto et al., 1984), leaving no remnant and ejecting mostly iron-peak elements into the ISM. The double-degenerate scenario (e.g., Iben & Tutukov, 1984; Webbink, 1984) involves the merger of two white dwarfs whose combined mass exceeds the Chandrasekhar limit. Although such systems have a long formation timescale, and must lose angular momentum via gravitational wave emission, some evidence suggests that double-degenerate SNe Ia may be more common (Schaefer & Pagnotta, 2012; Russell & Immler, 2012; Brown et al., 2012;

González Hernández et al., 2012). In either scenario, the timescale for SNe Ia is significantly longer ($\gtrsim 0.1$ Gyr) than for SNe II ($\sim$ Myr).

Stellar Winds

Stellar winds are observed to emanate from the most massive stars (O, B, A, and Wolf-Rayet stars; Conti 1978). These stars are sufficiently luminous that they can drive massive outflows through the scattering of photons off gas at the spectral lines of the gas (e.g., Cassinelli, 1979). Over their lifetime, they can inject $\sim 0.2 \times 10^{51}$ erg for a star of solar metallicity (Abbott, 1982), and more at higher metallicities due to the greater availability of metal lines (Leitherer et al., 1992). Winds are also produced by less massive stars that have evolved onto the asymptotic giant branch (AGB).

1.2.2 Active Galactic Nuclei

Early observations in radio wavelengths revealed extremely bright sources with relatively faint optical counterparts (e.g., Baade & Minkowski, 1954; Jennison & Gupta, 1956; Bennett, 1962). As the resolving power of instruments improved, it became clear that these were extra-galactic sources, some with emission that extended far from their host galaxies, some that were more concentrated and star-like. These 'active galactic nuclei' (AGN) were significantly more powerful in the radio than star formation alone could account for, and it is now believed that these sources are powered by accretion onto super-massive BHs (Salpeter, 1964; Zel'dovich & Novikov, 1965; Lynden-Bell, 1969, 1978). Historically, AGN have been classified based on their spectral and morphological properties: Seyfert galaxies (Seyfert, 1943) show strong emission lines, with narrow forbidden lines, and either broad ($v \sim 1000$ km s^{-1}; Seyfert 1) or narrow ($v \sim 100$ km s^{-1}; Seyfert 2) allowed lines; Fanaroff-Riley (FR) galaxies (Fanaroff & Riley, 1974) display strong, extended, bipolar radio emission, with FR1 galaxies having brighter jets close to the host galaxy, and FR2 galaxies being brighter at the outer edges of the lobes; quasi-stellar radio sources (quasars) are radio sources found to be coincident with 'stars' on photographic plates, but identification of their redshifted emission lines (e.g., Schmidt, 1963) revealed their true nature as AGN. In this thesis I am concerned more with the physics of AGN, and so I do not present a deeper discussion of these classifications (but see e.g., Lawrence 1987). The prevailing theory regarding the nature of AGN posits that all of the above classifications are observations of the same phenomenon at different viewing angles, modulo the local environment (Scheuer & Readhead, 1979; Orr & Browne, 1982; Urry & Padovani, 1995).

The centre of most, if not all, massive galaxies is believed to host a super-massive BH. Direct observational evidence of this is hard to come by since the gravitational sphere of influence of a BH,

$$R_{\rm G} \sim \frac{GM_{\rm BH}}{\sigma^2} = 2.7 \left(\frac{M_{\rm BH}}{10^8 M_\odot}\right) \left(\frac{\sigma}{400\ {\rm km\,s^{-1}}}\right)^{-2}\ {\rm pc}, \tag{1.1}$$

cannot be resolved for any but the nearest galaxies (Eisenhauer et al., 2005; Merritt, 2013). However, the discovery of correlations between the mass of the central black hole and many properties of the host galaxy, including: bulge mass (Magorrian et al., 1998; Marconi & Hunt, 2003; Häring & Rix, 2004; Sani et al., 2011); stellar velocity dispersion (Ferrarese & Merritt, 2000; Gebhardt et al., 2000; Tremaine et al., 2002; Kormendy & Ho, 2013); luminosity (Kormendy & Richstone, 1995; Marconi & Hunt, 2003); and Sérisc index / stellar concentration (Graham et al., 2001; Graham & Driver, 2007; Savorgnan et al., 2013), indicates co-evolution of the two (but see also Jahnke & Macciò, 2011). This had already been indicated from the similar shapes between the observed cosmic star formation history (e.g., Madau et al., 1996) and the quasar space density (e.g., Schmidt et al., 1995). Such observed relations are reproduced by simulations (Croton et al., 2006; Dubois et al., 2012; Taylor & Kobayashi, 2014), as well as a better reproduction of the cosmic SFR (e.g., Booth & Schaye, 2009; Taylor & Kobayashi, 2014; Vogelsberger et al., 2014). Recently, quasar-driven outflows have also been observed (Feruglio et al., 2010; Cicone et al., 2012; McElroy et al., 2015).

Accretion of (dissipative) material onto the BH offers a viable method for powering AGN (Soltan, 1982) due to the relatively high radiative efficiency of ~ 10 per cent for a Schwarzschild BH (e.g., Shakura & Sunyaev, 1973), and as much as 42 per cent for a maximally rotating Kerr BH (compared to ~ 0.4 per cent for hydrogen fusion). In galaxies with AGN, the BH is surrounded by an accretion disk of hot, ionised gas. Material is able to move inwards due to viscous angular momentum transport, likely caused by turbulence (Shakura & Sunyaev, 1973; Lynden-Bell & Pringle, 1974) or magnetorotational instabilities (Balbus & Hawley, 1991; Balbus, 2003), and falls quickly into the BH once it passes the last stable orbit:

$$R_{\mathrm{LSO}} = 3\frac{2GM_{\mathrm{BH}}}{c^2} = 3R_{\mathrm{S}}, \tag{1.2}$$

for a Schwarzschild BH. $R_{\mathrm{S}} = 2GM_{\mathrm{BH}}/c^2$ is the Schwarzschild radius, which defines the BH's event horizon, within which there is no trajectory that a photon may escape along. Radiation from the hot accretion disk, especially near R_{LSO}, and jets perpendicular to the disk, are then responsible for AGN feedback, which, in broad terms, is the coupling of energy to gas within the galaxy, although the exact mechanism by which this coupling occurs is still uncertain.

1.3 Simulations

Accurately simulating the formation and evolution of galaxies is no mean feat. Important processes take place on vastly different physical scales, from the collapse of large-scale structure and cold gas flows along DM filaments, to star formation and the growth of super-massive BHs. It is currently (and is expected to be for some time) quite impossible to resolve all relevant scales in a single simulation large enough to be cosmologically representative; some form of approximation is therefore necessary. Since DM interacts only via gravity, its evolution from cosmological initial conditions (from the power spectrum of the CMB) may be calculated relatively easily. In semi-analytic models (SAMs), the baryonic physics is calculated using simplified parameterizations separately from the calculation of DM structure. Alternatively, it is also possible to simulate DM, gas, stars, and BHs simultaneously and self-consistently in hydrodynamical simulations; I discuss each in the following sections.

1.3.1 Semi-Analytic Models

The semi-analytic method was introduced by White & Frenk (1991); the evolution of DM halo abundance as a function of circular velocity (V_c) was modelled using the Press-Schechter formalism (Press & Schechter, 1974; Narayan & White, 1988), and analytic expressions describing the evolution of the baryonic components of the galaxies they hosted were derived as a function of V_c and z under some simple assumptions. Observable properties of the galaxy population, such as cosmic SFR history and luminosity function, could then be determined. This technique could only predict average properties of the population since it did not model individual haloes, only their number density. Subsequent work by groups in Durham (e.g., Bower, 1991; Cole et al., 1994; Heyl et al., 1995; Baugh et al., 1998) and Munich (e.g., Kauffmann et al., 1993, 1994, 1997), expanded this method to follow the evolution of individual haloes by producing Monte Carlo realisations of the DM halo mass distribution from the linear power spectrum.

As computing power became ever more available, a new method emerged in which the DM was simulated directly from cosmological initial conditions, and haloes were identified and merger trees constructed from the output. This was possible owing to the fact that DM interacts only via gravity, and so is relatively inexpensive to calculate. Perhaps the best known of these N-body simulations is the Millennium Simulation (Springel et al., 2005), which was followed up by the higher resolution Millennium-II Simulation (Boylan-Kolchin et al., 2009) and the larger volume Millennium-XXL Simulation (Angulo et al., 2012). In parallel, more accurate and sophisticated sub-grid models of the baryonic physics have also been developed (e.g., Fanidakis et al., 2011; Lagos et al., 2013; Fu et al., 2013).

Given the scale and dynamic range of these simulations, as well as the speed with which they can be run, SAMs are a popular way of investigating galaxy evolution theoretically. Vast regions of parameter space can be explored efficiently, at relatively high mass resolution (the lowest mass resolved DM haloes in Boylan-Kolchin et al. (2009) are $\sim 10^8 M_\odot$), and can provide valuable insight into the physical processes that give rise to observed features (e.g., Bower et al., 2006; Croton et al., 2006; De Lucia et al., 2010). However, there are limitations to these methods, the most important of which is the fact that DM and baryonic physics are not solved self-consistently. This has two major consequences: SAMs necessarily contain more free parameters than do hydrodynamical models; and SAMs are unable to predict the distribution of baryonic matter within galaxies, only total or average quantities.

1.3.2 Hydrodynamical Simulations

The other main approach from SAMs is to directly implement star formation and feedback into hydrodynamical simulations. Many simulation codes have been developed for studying galaxy formation and evolution, not only of isolated systems (e.g., Burkert & Hensler, 1987; Katz, 1992; Mihos & Hernquist, 1994; Steinmetz & Müller, 1994; Kawata & Gibson, 2003; Kobayashi, 2004) but also for cosmological simulations of individual galaxies (e.g., Navarro & White, 1994) or of the galaxy population as a whole (Cen & Ostriker, 1999; Springel & Hernquist, 2003). With these simulations, it is possible to predict not only averaged properties of galaxies but also internal structures of galaxies, i.e., kinematics and spatial distribution of stars, gas, and metals within galaxies, which have also become available in recent observations with integral field units and multi-object spectrographs.

There are two main formalisms for the codes that run hydrodynamical simulations; particle-based and mesh-based. Each has their advantages and drawbacks (Frenk et al., 1999; O'Shea et al., 2005; Regan et al., 2007; Agertz et al., 2007), and a new breed of hybrid particle-mesh codes are attempting to combine their best aspects. I describe them below.

Mesh-Based Codes

Mesh-based codes (typically) follow the Eulerian formulation of hydrodynamics. The computational domain is divided into a grid of cells, which may be stationary with respect to the domain (e.g., Stone & Norman, 1992), or evolve in time (e.g., Gnedin, 1995; Whitehurst, 1995; Pen, 1998). Additionally, regions of high fluid density may be covered by a greater density of cells (and vice versa) as the fluid evolves in order to increase the spatial resolution in these areas; this is known as adaptive mesh refinement (AMR; Berger & Colella, 1989; Teyssier, 2002). The fluid is then advected across cell boundaries.

Such methods are well-studied and understood, and can offer high spatial precision and accurately evaluate shocks. However, there are fundamental issues surrounding Eulerian methods, one of the most important being their lack of Galilean invariance, meaning that their results are sensitive to bulk motions in the fluid (e.g., Tasker et al., 2008; Wadsley et al., 2008). It is also difficult for AMR to track a highly refined region moving with high velocity. In addition, the mixing of fluid in these models may create excess entropy (e.g., Wadsley et al., 2008), and turbulent motion may not be modelled correctly, depending on the maximum level of refinement (Iapichino et al., 2008; Iapichino & Niemeyer, 2008; Scannapieco & Brüggen, 2008). A further problem encountered in simulations of galaxy formation and evolution is that structures forming under the influence of gravity may not be modelled accurately (O'Shea et al., 2005; Heitmann et al., 2008). This is because it is difficult to follow all of the small density fluctuations at high redshift, and because in refined regions, the resolution increases discontinuously, which is found to suppress the growth of low-mass haloes (e.g., Springel, 2010).

Some of these problems may be overcome, at least in part, by allowing the mesh to move (e.g., Whitehurst, 1995). This method is more Lagrangian in nature, and so avoids the issues fundamental to Eularian methods, but codes are often restricted by computational or algorithmic issues. For example, the work of Gnedin (1995) and Pen (1998) used a continually deformed Cartesian grid, but the need to limit the level of distortions restricted its applicability in clustered environments.

Particle-Based Codes

Particle-based codes are inherently Lagrangian in nature since the particles trace the motion of the fluid. For cosmological simulations, particle codes tend to use smoothed particle hydrodynamics (see Chapter 2 for details; Lucy, 1977; Gingold & Monaghan, 1977; Monaghan, 1992). As well as the benefit over Eularian codes of being automatically Galilean invariant, denser environments are simulated by more particles and so have increased resolution in a continuous manner. There are several drawbacks, however, chief of which is their inability to accurately model steep gradients or discontinuities in density, at shocks for example, which can suppress fluid instabilities (Agertz et al., 2007). Attempts have been made to help overcome these problems though the inclusion of artificial heating, mixing, and viscosity (Dolag et al., 2005; Price, 2008; Wadsley et al., 2008), but their widespread applicability is uncertain.

More recently, the `AREPO` code was described (Springel, 2010), which attempts to combine the features of grid- and particle-based codes. It uses a moving mesh generated by the Voronoi tessellation of particles that trace the fluid flow, as in SPH. In this way, the mesh is Galilean invariant, but retains the advantageous features of Eularian codes. Additionally, improvements to the 'traditional' SHP method have been proposed in recent years, including SPHS (Read & Hayfield, 2012) and SPHGal (Hu et al., 2014).

1.4 Why Simulate AGN?

The Λ Cold Dark Matter (ΛCDM) cosmology is the currently accepted best model for the structure we see in the Universe, and its evolution across cosmic time. On large scales, structure formation is driven by the gravitational influence of dark matter, leading to Mpc-scale filaments, walls, and voids by the present day. Galaxies form within these, and their small-scale evolution is driven primarily by baryonic processes. In the ΛCDM paradigm, all structure forms hierarchically; small haloes collapse first, and merge over time to form ever larger ones. This has been challenged observationally, however, by the downsizing phenomenon: the redshift evolution of the mass of galaxies with active star formation, the mass and redshift dependencies of the specific star formation rates (SFRs; Juneau et al., 2005; Stark et al., 2013), the fundamental plane (Treu et al., 2005), and the [α/Fe] ratios of ETGs (Thomas et al., 2005). The downsizing phenomenon (Cowie et al., 1996; Bundy et al., 2006) is not fully reproduced in any hydrodynamical simulations of galaxies. In hydrodynamical simulations, because most of the stars in massive galaxies have formed in subgalaxies at high-redshift before they merge to the present galaxies, the stellar populations of massive galaxies are older than low-mass galaxies (Kobayashi et al. 2007; see also De Lucia et al. 2006; Fontanot et al. 2009 for semi-analytic models). However, the present star formation rates are still too high in massive galaxies, and thus the specific star formation rates are also too high, and the [α/Fe] ratios are too low for massive early-type galaxies. Some additional feedback that can efficiently work in massive galaxies is required, and AGN feedback is the most plausible.

1.5 Thesis Layout

In this thesis, I describe a model for AGN feedback with a new approach to BH formation, that has been successfully incorporated into the `GADGET-3` code. The details of this model, as well as a description of the stellar feedback model and SPH, are given in Chapter 2. This is followed by an investigation into the effects the model parameters have on the final state of the simulations, and a test that the results are converged. The work presented in this chapter has been published as Taylor & Kobayashi (2014). With a fiducial set of parameters determined, a more in-depth look at the properties of the $z = 0$ galaxy population is shown in Chapter 3, using simulations with over 15 times the volume of those presented in Chapter 2. The work presented in this chapter has been published as Taylor & Kobayashi (2015a). This is followed, in Chapter 4, by an investigation into the evolution of galaxies across cosmic time, comparing simulations with and without AGN to both one another and observational data. The work presented in this chapter has been submitted to MNRAS and is under review. Chapter 5 takes advantage of the hydrodynamical nature of the simulations by showing the evolution of metallicity gradients within galaxies, and how these are influenced by AGN and a galaxy's merger history. In Chapter 6, I focus on the largest galaxy in the simulations and examine the influence of AGN-driven winds on its ISM and its immediate environment. The work in this chapter has been published as Taylor & Kobayashi (2015b). Finally, in Chapter 7, I give an overview of the key results of my work and discuss their implications.

2
Code

2.1 Hydrodynamics

In this Section, I introduce the basic equations governing the evolution of a hydrodynamical system, as well as the SPH method for solving them. While the equations of SPH may be expressed in many different ways, I present them as they are used in the `GADGET`-3 code (Springel et al., 2005).

2.1.1 Basic Equations

The equations governing hydrodynamics comprise: the continuity equation,

$$\frac{\mathrm{D}\rho}{\mathrm{D}t} + \rho \nabla \cdot \mathbf{v} = 0; \tag{2.1}$$

conservation of momentum,

$$\frac{\mathrm{D}\mathbf{v}}{\mathrm{D}t} = -\frac{1}{\rho}\nabla P - \nabla\Phi; \tag{2.2}$$

the evolution of the fluid's thermal energy,

$$\frac{\mathrm{D}u}{\mathrm{D}t} = \frac{P}{\rho^2}\frac{\mathrm{D}\rho}{\mathrm{D}t} + \frac{\nabla \cdot (\kappa \nabla T)}{\rho} + \frac{\mathcal{H} - \Lambda}{\rho}; \tag{2.3}$$

and Poisson's equation,

$$\nabla^2 \Phi = 4\pi G \rho. \tag{2.4}$$

In these equations, $\frac{\mathrm{D}}{\mathrm{D}t}$ denotes the advective derivative with respect to time, ρ is the mass density, and $\mathbf{v}$ the velocity of the fluid. P is the fluid's pressure, Φ its potential, u its specific thermal energy, κ is the coefficient of thermal conductivity, T the temperature of the fluid, and $\mathcal{H}$ and Λ are the heating and cooling functions respectively. The equation of state of an ideal gas is assumed:

$$P = (\gamma - 1)\,\rho u, \tag{2.5}$$

with $\gamma = 5/3$.

2.1.2 SPH

Smoothed particle hydrodynamics (SPH) is a formulation of hydrodynamics in which any function may be interpolated from its values at a set of discrete particles. This method was first set out in Lucy (1977) and Gingold & Monaghan (1977), and reviewed by Monaghan (1992); much of this section follows these works.

The smoothly averaged value of a physical quantity $f(\mathbf{r})$ at location $\mathbf{r}$ is given by

$$f(\mathbf{r}) = \int f(\mathbf{r}')\,W(\mathbf{r}-\mathbf{r}', h)\;\mathbf{dr}', \tag{2.6}$$

where h denotes the length over which the quantity is smoothed, and the smoothing kernel $W(\mathbf{r}-\mathbf{r}', h)$ satisfies

$$\int W(\mathbf{r}-\mathbf{r}', h)\;\mathbf{dr}' = 1, \tag{2.7}$$

and

$$\lim_{h\to 0} W(\mathbf{r}-\mathbf{r}', h) = \delta(\mathbf{r}-\mathbf{r}'). \tag{2.8}$$

The gradient of $f(\mathbf{r})$ is then obtained as

$$\nabla f(\mathbf{r}) = \int f(\mathbf{r}')\,\nabla W(\mathbf{r}-\mathbf{r}', h)\;\mathbf{dr}', \tag{2.9}$$

neglecting the surface term.

SPH is a Lagrangian formulation of hydrodynamics, whereby the continuous fluid is modelled as a collection of discrete particles. Equations (2.6) and (2.9) are therefore modified as so:

$$f(\mathbf{r}_i) = \sum_j \frac{m_j}{\rho_j} f(\mathbf{r}_j)\,W(\mathbf{r}_i-\mathbf{r}_j, h), \tag{2.10}$$

and

$$\nabla f(\mathbf{r}_i) = \sum_j \frac{m_j}{\rho_j} f(\mathbf{r}_j)\,\nabla W(\mathbf{r}_i-\mathbf{r}_j, h), \tag{2.11}$$

where the integral over all space has been replaced by a summation over all particles, and the volume element $\mathbf{dr}'$ by m_j/ρ_j, the ratio of the mass of the particle at $\mathbf{r}_j$ to its density. In practice, the sum runs only over a relatively small number of neighbouring particles for reasons of computational efficiency, and because the assumed form of $W\left(\mathbf{r}_i - \mathbf{r}_j, h\right)$ renders including other particles in the sum unnecessary. In `GADGET-3`, $W\left(r, h\right)$ is given by

$$W\left(r,h\right) = \frac{8}{\pi h^3} \begin{cases} 1 - 6\left(\frac{r}{h}\right)^2 + 6\left(\frac{r}{h}\right)^3, & 0 \leq \frac{r}{h} \leq \frac{1}{2}, \\ 2\left(1 - \frac{r}{h}\right)^3, & \frac{1}{2} < \frac{r}{h} \leq 1, \\ 0, & \frac{r}{h} > 1. \end{cases} \tag{2.12}$$

h has a different value for each particle such that a sphere of volume $\frac{4}{3}\pi h_i^3$ encloses a constant number of neighbouring particles. Particles in regions of high fluid density therefore have lower h. The corresponding expression for the derivative of $W\left(r,h\right)$ is

$$\nabla W\left(r,h\right) = \frac{48}{\pi h^4} \begin{cases} \frac{r}{h}\left(3\frac{r}{h} - 2\right), & 0 \leq \frac{r}{h} \leq \frac{1}{2}, \\ -\left(1 - \frac{r}{h}\right)^2, & \frac{1}{2} < \frac{r}{h} \leq 1, \\ 0, & \frac{r}{h} > 1. \end{cases} \tag{2.13}$$

We are required to solve the equations of Section 2.1.1, recast in the SPH formalism. Instead of using the continuity equation (2.1), the density is calculated as

$$\rho_i = \sum_j m_j W\left(\mathbf{r}_i - \mathbf{r}_j, h\right). \tag{2.14}$$

The momentum equation (2.2) becomes

$$\frac{\mathrm{D}\mathbf{v}_i}{\mathrm{D}t} = -\sum_j m_j \left(\frac{P_i}{\rho_i^2} + \frac{P_j}{\rho_j^2} + \Pi_{ij}\right) \nabla_i W\left(\mathbf{r}_i - \mathbf{r}_j, h\right) - \left(\nabla\Phi\right)_i, \tag{2.15}$$

and the energy equation (2.3) is represented as

$$\frac{\mathrm{D}u_i}{\mathrm{D}t} = -\sum_j m_j \left(\frac{P_i}{\rho_i^2} + \frac{1}{2}\Pi_{ij}\right) \left(\mathbf{v}_i - \mathbf{v}_j\right) \cdot \nabla_i W\left(\mathbf{r}_i - \mathbf{r}_j, h\right) + \frac{\mathcal{H} - \Lambda}{\rho_i}, \tag{2.16}$$

where then thermal conduction is neglected.

The form of equations (2.15) and (2.16) are modified in the `GADGET-3` code. In equation (2.15), the P_i/ρ_i^2 terms are multiplied by an additional factor, f_i, defined as (Springel & Hernquist, 2002; Springel et al., 2005):

$$f_i = \left(1 + \frac{h_i}{3\rho_i}\frac{\partial \rho_i}{\partial h_i}\right)^{-1}. \tag{2.17}$$

Additionally, `GADGET-3` does not integrate the energy equation (2.16), instead choosing to integrate an entropy formulation that conserves both energy and entropy, and gives more accurate results for some problems (Springel & Hernquist, 2002). An entropic function, A, of the specific entropy s is defined as:

$$P = A(s)\rho^{\gamma}, \tag{2.18}$$

and its time evolution is given by

$$\frac{\mathrm{d}A_i}{\mathrm{d}t} = \frac{\gamma - 1}{\rho_i^{\gamma-1}} \left(\frac{1}{2} \sum_j m_j \Pi_{ij} (\mathbf{v}_i - \mathbf{v}_j) \cdot \nabla_i W(\mathbf{r}_i - \mathbf{r}_j, h) - \frac{\mathcal{H} - \Lambda}{\rho_i} \right). \tag{2.19}$$

The specific internal energy is then related to the entropy via

$$u = \frac{A(s)}{\gamma - 1} \rho^{\gamma - 1}. \tag{2.20}$$

The term Π_{ij} in equations (2.15), (2.16), and (2.19) is an artificial viscosity, included to permit the dissipation of kinetic energy into heat via shocks. The `GADGET-3` code does not employ the Monaghan-Balsara form of Π_{ij} (Monaghan & Gingold, 1983; Balsara, 1995) used in many other SPH codes, instead using the slightly modified form of Monaghan (1997):

$$\Pi_{ij}^{\mathrm{M97}} = \begin{cases} -\frac{\alpha}{2} \frac{(c_i + c_j - 3\mu_{ij})\mu_{ij}}{0.5(\rho_i + \rho_j)}, & \mu_{ij} < 0, \\ 0, & \text{otherwise}, \end{cases} \tag{2.21}$$

$$\mu_{ij} = \frac{(\mathbf{v}_i - \mathbf{v}_j) \cdot (\mathbf{r}_i - \mathbf{r}_j)}{|\mathbf{r}_i - \mathbf{r}_j|}, \tag{2.22}$$

where c_i denotes the sound speed at particle i, and $\alpha = 0.5$ is a constant. To limit viscous angular momentum transport in the presence of shear flows, caused by smoothing across the boundary of the shear, Π_{ij}^{M97} is modified thus:

$$\Pi_{ij} = \Pi_{ij}^{\mathrm{M97}} \frac{f_i + f_j}{2}, \tag{2.23}$$

$$f_i = \frac{|\nabla \cdot \mathbf{v}|_i}{|\nabla \cdot \mathbf{v}|_i + |\nabla \times \mathbf{v}|_i + 0.0001 c_i / h_i}, \tag{2.24}$$

where the term $0.0001 c_i/h_i$ is used to prevent f diverging. In pure shear flows ($\nabla \cdot \mathbf{v} = 0$ and $\nabla \times \mathbf{v} \neq \mathbf{0}$), f goes to 0, while in shear-free flows ($\nabla \times \mathbf{v} = \mathbf{0}$) $f = 1$ and the viscosity is unchanged.

Despite the inclusion of an artificial viscosity, shocks may still be poorly modelled by SPH since discontinuities in the density are smoothed out across a scale of $\sim h$, and properties of the gas ‘downstream’ of the shock are influenced by gas particles upstream before the shock reaches them. Simulating at higher resolution with more particles, or choosing a different form for the SPH kernel, may mitigate against these issues, but this is a fundamental limitation of SPH. Recently, the hybrid code AREPO has shown promise in accurately simulating shear flows and shocks, both in idealized test cases (Springel, 2010) and cosmological simulations (Vogelsberger et al., 2012).

2.2 Baryonic Physics

In addition to the hydrodynamics described in the previous section, our simulation code contains other baryonic physics relevant to the formation and evolution of galaxies. In this section, we present our description of: radiative gas cooling; star formation; and stellar feedback, of both energy and metals. Our treatment of BH physics is introduced separately, in Section 2.3.

2.2.1 Radiative Cooling

Radiative cooling is implemented via the cooling function. We assume that the gas is in radiative equilibrium, and note that the non-equilibrium cooling function for $T \gtrsim 10^4$ K (the approximate resolution limit in our simulations) is similar (Nakasato et al., 2000). For primordial or very low-metallicity gas ([Fe/H] < -5), the cooling rate is computed assuming the two-body processes of H and He, as well as free-free emission (Katz et al., 1996). For enriched gas ([Fe/H] ≥ -5), we use the metallicity-dependent cooling function computed by the MAPPINGS III software (Sutherland & Dopita, 1993; Allen et al., 2008). We also include photoionization from a uniform, evolving UV background.

The cooling function, Λ, for the radiative cooling of primordial gas uses the two-body processes given in Katz et al. (1996):

$$\begin{aligned}\Lambda = {} & \Lambda_{\mathrm{e,H_0}} + \Lambda_{\mathrm{e,He_+}} + \Lambda_{\mathrm{i,H_0}} + \Lambda_{\mathrm{i,He_0}} + \Lambda_{\mathrm{i,He_+}} \\ & + \Lambda_{\mathrm{r,H_+}} + \Lambda_{\mathrm{r,He_+}} + \Lambda_{\mathrm{r,He_{++}}} + \Lambda_{\mathrm{d,He_+}} + \Lambda_{\mathrm{ff}} + \Lambda_{\mathrm{C}}.\end{aligned} \tag{2.25}$$

In equation (2.25), subscripts denote the following: e - collisional excitation; i - collisional ionization; r - recombination; d - dielectronic recombination; ff - free-free emission; C - inverse compton; and 0, +, and ++ correspond to neutral, singly, and doubly ionized species, respectively. Expressions for these cooling rates are taken from Black (1981) and Cen (1992):

$$\Lambda_{\mathrm{e,H_0}} = 7.50 \times 10^{-19} e^{-118348.0/T} (1 + T_5^{1/2})^{-1} n_{\mathrm{e}} n_{\mathrm{H_0}}, \tag{2.26}$$

$$\Lambda_{\mathrm{e,He_+}} = 5.54 \times 10^{-17} T^{-0.397} e^{-473638.0/T} (1 + T_5^{1/2})^{-1} n_{\mathrm{e}} n_{\mathrm{He_+}}, \tag{2.27}$$

$$\Lambda_{\mathrm{i,H_0}} = 1.27 \times 10^{-21} T^{1/2} e^{-157809.1/T} (1 + T_5^{1/2})^{-1} n_{\mathrm{e}} n_{\mathrm{H_0}}, \tag{2.28}$$

$$\Lambda_{\mathrm{i,He_0}} = 9.38 \times 10^{-22} T^{1/2} e^{-285335.4/T} (1 + T_5^{1/2})^{-1} n_{\mathrm{e}} n_{\mathrm{He_0}}, \tag{2.29}$$

$$\Lambda_{\mathrm{i,He_+}} = 4.95 \times 10^{-22} T^{1/2} e^{-631515.0/T} (1 + T_5^{1/2})^{-1} n_{\mathrm{e}} n_{\mathrm{He_+}}, \tag{2.30}$$

$$\Lambda_{\mathrm{r,H_+}} = 8.70 \times 10^{-27} T^{1/2} T_3^{-0.2} (1 + T_6^{0.7})^{-1} n_{\mathrm{e}} n_{\mathrm{H_+}}, \tag{2.31}$$

$$\Lambda_{\mathrm{r,He_+}} = 1.55 \times 10^{-26} T^{0.3647} n_{\mathrm{e}} n_{\mathrm{He_+}}, \tag{2.32}$$

$$\Lambda_{\mathrm{r,He_{++}}} = 3.48 \times 10^{-26} T^{1/2} T_3^{-0.2} (1 + T_6^{0.7})^{-1} n_{\mathrm{e}} n_{\mathrm{H_{++}}}, \tag{2.33}$$

$$\Lambda_{\mathrm{d,He_+}} = 1.24 \times 10^{-13} T^{-1.5} e^{-470000.0/T} (1 + 0.3 e^{-94000.0/T}) n_{\mathrm{e}} n_{\mathrm{He_+}}, \tag{2.34}$$

$$\Lambda_{\mathrm{ff}} = 1.42 \times 10^{-27} g_{\mathrm{ff}} T^{1/2} (n_{\mathrm{H_+}} + n_{\mathrm{He_+}} + 4 n_{\mathrm{He_{++}}}) n_{\mathrm{e}}, \tag{2.35}$$

where $T_n = T/10^n$ K, $n_{\rm x}$ is the number density of species x, and the units are $\mathrm{erg\,s^{-1}\,cm^{-3}}$. For free-free emission (equation (2.35)), we use the Gaunt factor (Katz et al., 1996):

$$g_{\rm ff} = 1.1 + 0.34 \exp\left(-\frac{(5.5 - \log T)^2}{3.0}\right). \tag{2.36}$$

Inverse Compton scattering off the CMB is included as:

$$\Lambda_{\rm C} = 5.41 \times 10^{-36} n_{\rm e} \left(T - 2.73(1+z)\right)(1+z)^4 \qquad [\mathrm{erg\,s^{-1}\,cm^{-3}}], \tag{2.37}$$

which depends on redshift, z.

The gas is assumed to be optically thin to, and in ionization (but not thermal) equilibrium with, the UV background. Thus, there is a balance between the rates of creation and destruction of the ionized species:

$$\Gamma_{e-{\rm H_0}} n_{\rm H_0} n_{\rm e} + \Gamma_{\gamma{\rm H_0}} n_{\rm H_0} = \alpha_{\rm H_+} n_{\rm H_+} n_{\rm e}, \tag{2.38}$$

$$\Gamma_{e-{\rm He_0}} n_{\rm He_0} n_{\rm e} + \Gamma_{\gamma{\rm He_0}} n_{\rm He_0} + c_t n_{\rm e}^2 n_{\rm He_+} = (\alpha_{\rm He_+} + \alpha_{\rm d}) n_{\rm He_+} n_{\rm e}, \tag{2.39}$$

$$\begin{aligned} \Gamma_{e-{\rm He_+}} n_{\rm He_+} n_{\rm e} &+ \Gamma_{\gamma{\rm He_+}} n_{\rm He_+} + (\alpha_{\rm He_+} + \alpha_{\rm d}) n_{\rm He_+} n_{\rm e} \\ &= \alpha_{\rm He_{++}} n_{\rm He_{++}} n_{\rm e} + \Gamma_{e-{\rm He_0}} n_{\rm He_0} n_{\rm e} + \Gamma_{\gamma{\rm He_0}} n_{\rm He_0}, \end{aligned} \tag{2.40}$$

$$\alpha_{\rm He_{++}} n_{\rm He_{++}} n_{\rm e} = \Gamma_{e-{\rm He_+}} n_{\rm He_+} n_{\rm e} + \Gamma_{\gamma{\rm He_+}} n_{\rm He_+}, \tag{2.41}$$

where Γ_{e-i} denote collisional ionization rates, $\Gamma_{\gamma i}$ are the photoionization rates, and $\alpha_{\rm i}$ are recombination rates. The left-hand sides of equations (2.38)-(2.41) give the rates at which H I, He I, He II, and He III are destroyed, with the right-hand sides expressing the rates at which they are created from other species. Recombination rates and collisional ionization rates are taken from Black (1981) and Cen (1992):

$$\alpha_{\rm H_+} = 8.4 \times 10^{-11} T^{-1/2} T_3^{-0.2} (1 + T_6^{0.7})^{-1}, \tag{2.42}$$

$$\alpha_{\rm He_+} = 1.5 \times 10^{-10} T^{-0.6353}, \tag{2.43}$$

$$\alpha_{\rm d} = 1.9 \times 10^{-3} T^{-1.5} e^{-470000.0/T} (1 + 0.3 e^{-94000.0/T}), \tag{2.44}$$

$$\alpha_{\rm He_{++}} = 3.36 \times 10^{-10} T^{-1/2} T_3^{-0.2} (1 + T_6^{0.7})^{-1}, \tag{2.45}$$

$$\Gamma_{e-{\rm H_0}} = 5.85 \times 10^{-11} T^{1/2} e^{-157809.1/T} (1 + T_5^{1/2})^{-1}, \tag{2.46}$$

$$\Gamma_{e-{\rm He_0}} = 2.38 \times 10^{-11} T^{1/2} e^{-285335.4/T} (1 + T_5^{1/2})^{-1}, \tag{2.47}$$

$$\Gamma_{e-{\rm He_+}} = 5.68 \times 10^{-11} T^{1/2} e^{-631515.0/T} (1 + T_5^{1/2})^{-1}, \tag{2.48}$$

with units of $\mathrm{cm^3\,s^{-1}}$. The He triplet state is metastable, and so can be collisionally ionized too, contributing to equation (2.39). The ionization rate of He by this process is expressed as $c_t(T) n_{\rm e}^2 n_{\rm He_+}$ (Black, 1981), with $c_t(T)$ given by

$$c_t = 6.56 \times 10^{-16} T^{-0.1687} e^{-55338/T} \qquad [\mathrm{cm^6\,s^{-1}}], \tag{2.49}$$

although this is not included in the `GADGET-3` code.

Photoionization rates are defined as

$$\Gamma_{\gamma i} = \int_{\nu_i}^{\infty} \frac{4\pi J(\nu)}{h\nu} \sigma_i(\nu) \mathrm{d}\nu \qquad [\mathrm{s}^{-1}], \tag{2.50}$$

where $J(\nu)$ is the intensity of the UV field, $\sigma(\nu)$ denotes the cross section for photoionization, and h is Plank's constant. The intensity of the UV background is a function of frequency and redshift:

$$J(\nu, z) = 10^{-22} \left(\frac{\nu}{\nu_{\mathrm{H}_0}}\right)^{-\alpha} \begin{cases} 0, & z \geq 6, \\ 4/(1+z), & 6 > z \geq 3, \\ 1, & 3 > z \geq 2, \\ (3/(1+z))^{-3}, & z < 2, \end{cases} \qquad [\mathrm{erg\,s^{-1}\,cm^{-2}\,sr^{-1}\,Hz^{-1}}], \tag{2.51}$$

with ν_{H_0} the Lyman limit. The spectral index is taken to be $\alpha = 1$. Expressions for the cross sections, σ, are taken from Osterbrock (1989). For H I, with nuclear charge $Z = 1$, and He II ($Z = 2$), we use $h\nu_i = 13.6Z^2$ eV, and

$$\sigma_i = 6.30 \times 10^{-18} Z^{-2} \left(\frac{\nu_i}{\nu}\right)^4 \frac{\exp\left(4 - (4 \arctan \epsilon)/\epsilon\right)}{1 - \exp(-2\pi/\epsilon)}, \tag{2.52}$$

where $\epsilon = \sqrt{\nu/\nu_i - 1}$. For He I ($h\nu_i = 24.6$ eV),

$$\sigma_i(\nu) = 7.83 \times 10^{-18} \left(1.66 \left(\frac{\nu}{\nu_i}\right)^{-2.05} - 0.66 \left(\frac{\nu}{\nu_i}\right)^{-3.05}\right). \tag{2.53}$$

As well as the rate equations (2.38)-(2.41), we also have equations describing the conservation of particle number:

$$n_{\mathrm{H}_0} + n_{\mathrm{H}_+} = n_{\mathrm{H}} = \frac{\rho X}{m_p}, \tag{2.54}$$

$$n_{\mathrm{e}} = n_{\mathrm{H}_+} + n_{\mathrm{He}_+} + 2n_{\mathrm{He}_{++}}, \tag{2.55}$$

$$(n_{\mathrm{He}_0} + n_{\mathrm{He}_+} + n_{\mathrm{He}_{++}})/n_{\mathrm{H}} = y = \frac{Y}{4 - 4Y}, \tag{2.56}$$

where n_{H} is the total number density of all hydrogen species (i.e. H I and H II), and $X = 0.76$ and $Y = 0.24$ are respectively the hydrogen and helium abundances by mass.

For a given temperature, density, and UV background spectrum, equations (2.38)-(2.41) and (2.54)-(2.56) may be written as six independent equations for the six unknown quantities n_{H_0}, n_{H_+}, n_{He_0}, n_{He_+}, $n_{\mathrm{He}_{++}}$, and n_{e}:

$$n_{\mathrm{H}_0} = n_{\mathrm{H}} \alpha_{\mathrm{H}_+} / (\alpha_{\mathrm{H}_+} + \Gamma_{e-\mathrm{H}_0} + \Gamma_{\gamma \mathrm{H}_0}/n_{\mathrm{e}}), \tag{2.57}$$

$$n_{\mathrm{H}_+} = n_{\mathrm{H}} - n_{\mathrm{H}_0}, \tag{2.58}$$

$$n_{\mathrm{He}_+} = y n_{\mathrm{H}} / \left(1 + (\alpha_{\mathrm{He}_+} + \alpha_{\mathrm{d}})/(\Gamma_{e-\mathrm{He}_0} + \Gamma_{\gamma\mathrm{He}_0}/n_{\mathrm{e}}) + (\Gamma_{e-\mathrm{He}_+} + \Gamma_{\gamma\mathrm{He}_+}/n_{\mathrm{e}})/\alpha_{\mathrm{He}_{++}}\right), \tag{2.59}$$

$$n_{\mathrm{He}_0} = n_{\mathrm{He}_+}(\alpha_{\mathrm{He}_+} + \alpha_{\mathrm{d}})/(\Gamma_{e-\mathrm{He}_0} + \Gamma_{\gamma\mathrm{He}_0}/n_{\mathrm{e}}), \tag{2.60}$$

$$n_{\mathrm{He}_{++}} = n_{\mathrm{He}_+}(\Gamma_{e-\mathrm{He}_+} + \Gamma_{\gamma\mathrm{He}_+}/n_{\mathrm{e}})/\alpha_{\mathrm{He}_{++}}, \tag{2.61}$$

$$n_{\mathrm{e}} = n_{\mathrm{H}_+} + n_{\mathrm{He}_+} + 2n_{\mathrm{He}_{++}}. \tag{2.62}$$

The collisional ionization and recombination rates (α_i and Γ_{e-i}) depend only on temperature (equations (2.42)-(2.48)), and so, in the absence of photoionization ($\Gamma_{\gamma i} = 0$), we have that $n_i \propto n_{\mathrm{H}}$, and $\Lambda \propto n_{\mathrm{H}}^2$. Fig. 2.1(a) shows the cooling function (divided by n_{H}^2) as a function of temperature, for primordial gas and without photoionization. The processes described by equations (2.26)-(2.35) are shown, as well as the total cooling function (solid black line). At $T \gtrsim 10^6$ K, gas is fully ionized, and the cooling function is dominated by free-free emission. At $T \sim 2 \times 10^4$ K and $T \sim 10^5$ K, cooling is mostly due to collisional excitation of H I and He II, respectively. Below $T \sim 10^4$ K, the gas is neutral, and collisions do not have sufficient energy to promote electrons from their ground state.

Photoionization also causes heating of the gas, since the liberated electrons carry off extra energy. The heating rate from this process is

$$\mathcal{H} = n_{\mathrm{H}_0}\epsilon_{\mathrm{H}_0} + n_{\mathrm{He}_0}\epsilon_{\mathrm{He}_0} + n_{\mathrm{He}_+}\epsilon_{\mathrm{He}_+} \qquad [\mathrm{erg\ s^{-1}\ cm^{-3}}], \tag{2.63}$$

where

$$\epsilon_i = \int_{\nu_i}^{\infty} \frac{4\pi J(\nu)}{h\nu} \sigma_i(\nu)(h\nu - h\nu_i)\mathrm{d}\nu \qquad [\mathrm{erg\,s^{-1}}]. \tag{2.64}$$

Chemically enriched gas ([Fe/H] > -5) is treated differently, and the cooling function computed by the MAPPINGS III software (Sutherland & Dopita, 1993) at different metallicities is used. The processes included are: collisional line radiation; free-free and two-photon continuum; recombination; photoionization heating; collisional ionization; and Compton heating. The cooling function of gas in ionization equilibrium is given for [Fe/H] $= 0, -1, -2, -3, -4$, and -5; the cooling function is obtained at intermediate values with cubic spline interpolation. Abundance ratios are interpolated between solar and primordial values. In all calculations, oxygen is the most important coolant.

Fig. 2.1(b) shows the cooling function of gas at various metallicities (those provided by MAPPINGS III). It is clear that the cooling rate is greatly enhanced by the presence of metals. At high temperatures, Fe-group line emission processes largely determine the cooling function, while lighter atoms like C, O, and Ne are dominant at lower temperatures. The peaks at $T \sim 2 \times 10^5$ K and $T \sim 8 \times 10^4$ K are

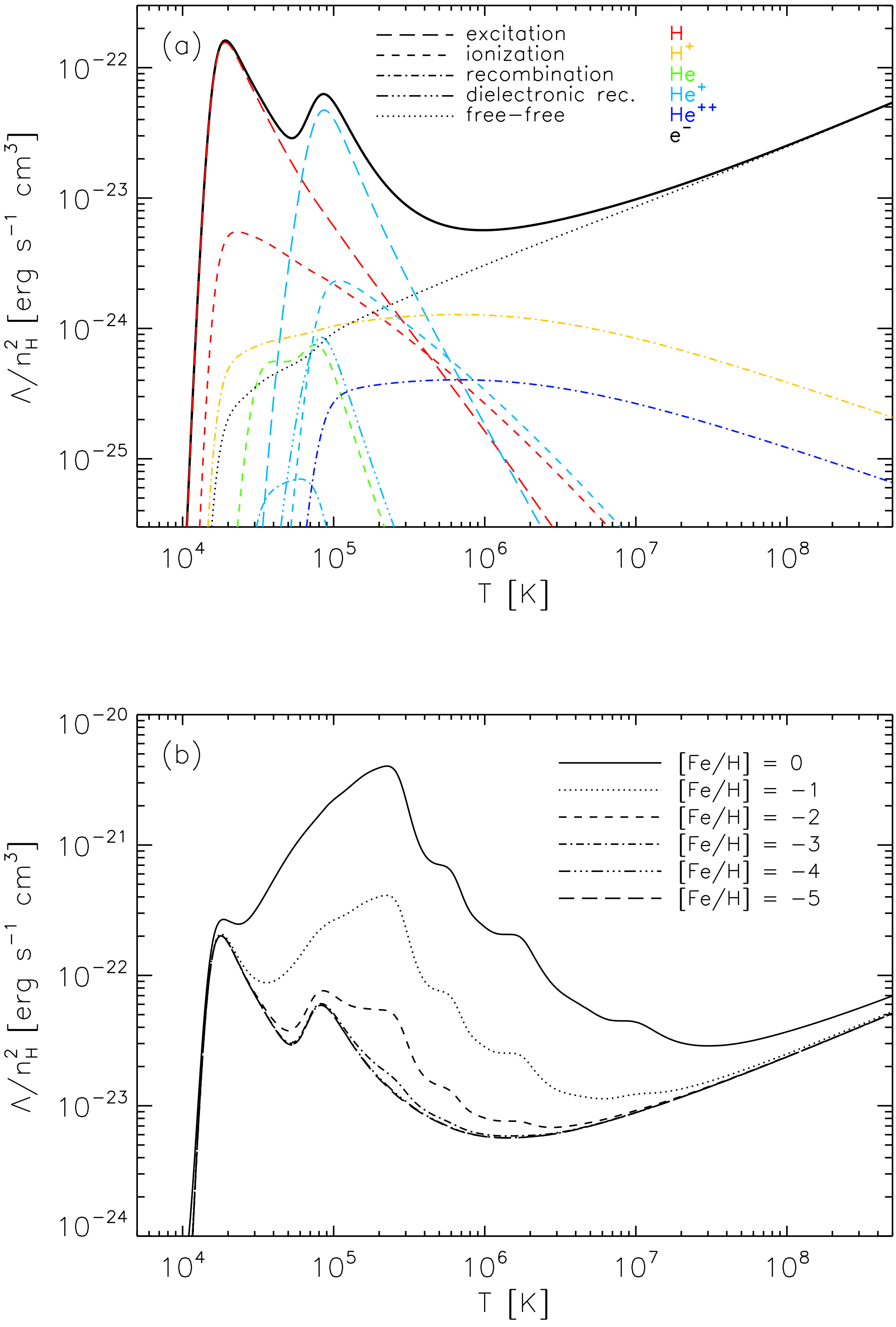

FIGURE 2.1: The top panel (a) shows the cooling function for primordial gas ([Fe/H] < −5, solid black line) in the absence of photoionization, as well as the individual contributions from different processes (collisional excitation and ionization, standard and dielectronic recombination, and free-free emission) and species (H I, H II, He I, He II, He III, and e$^-$). The lower panel (b) shows the metallicity dependence of the cooling function at [Fe/H] = 0, −1, −2, −3, −4, and − 5, as calculated by MAPPINGS III.

due to oxygen and carbon, respectively. For [Fe/H] = 0, the cooling rate at $T \sim 10^5$ K is about 100 times larger than for primordial gas, and so radiative cooling, and hence the rate of star formation, depends strongly on metallicity.

2.2.2 Star Formation

The star formation (SF) criteria we use are the same as in Katz (1992). If a gas particle satisfies the SF criteria, it has a chance to produce a star particle. In our simulations, star particles have masses $\sim 10^6 M_\odot$, and therefore represent collections of many stars.

The SF criteria are that a gas particle should be: (1) converging; (2) cooling; and (3) Jeans unstable,

$$(1) \qquad (\nabla \cdot \boldsymbol{v})_i < 0, \tag{2.65}$$

$$(2) \qquad t_{\rm cool} < t_{\rm dyn}, \tag{2.66}$$

$$(3) \qquad t_{\rm dyn} < t_{\rm sound}, \tag{2.67}$$

where $t_{\rm cool}$, $t_{\rm dyn}$, and $t_{\rm sound}$ represent the cooling, dynamical, and sound crossing times, respectively. They are:

$$t_{\rm cool} = \frac{\rho u}{\Lambda}, \tag{2.68}$$

$$t_{\rm dyn} = \frac{1}{\sqrt{4\pi G\rho}}, \tag{2.69}$$

$$t_{\rm sound} = \frac{h_i}{c_{\rm s}}, \tag{2.70}$$

where u is the specific thermal energy, and $c_{\rm s}$ is the local sound speed. The star formation timescale is taken to be proportional to the dynamical timescale ($t_{\rm sf} \equiv \frac{1}{c_*} t_{\rm dyn}$), where c_* is a star formation timescale parameter, which we set to 0.02 (Murante et al., 2010; Scannapieco et al., 2012), giving better agreement with observations of the cosmic SFR than 0.1 with our adopted Kroupa IMF.

We spawn new star particles as in Kobayashi et al. (2007), namely through a probability criterion, rather than an explicit gas density threshold (e.g., Navarro & White, 1993). Any gas particle that satisfies equations (2.65)-(2.67) has a random number, p, drawn for it from a uniform distribution between 0 and 1. If p then satisfies

$$p \leq \frac{m_{\rm g}}{m_{\rm g}^0/N_*} \left(1 - e^{-\Delta t/t_{\rm sf}}\right), \tag{2.71}$$

where $m_{\rm g}$ is the mass of the gas particle, $m_{\rm g}^0$ is the original gas particle mass, and Δt is the current timestep, then a star particle of mass $m_*^0 = m_{\rm g}^0/N_*$ is formed. We use $N_* = 2$.

We note that these star formation criteria are different to those used by some other groups. For example, the EAGLE simulations (Schaye et al., 2014) use temperature and metallicity-dependent density thresholds to form stars such that the Kennicutt–Schmidt law is preserved (Schaye & Dalla Vecchia, 2008). Gas particles satisfying these criteria then stochastically form star particles. In the Illustris simulations (Vogelsberger et al., 2014), only a density criterion is used, with gas particles having $\rho > 0.13$ cm^{-3} stochastically turned into star particles.

2.2.3 Stellar Feedback

Evolved stars eject gas and heavy elements in the form of winds and supernovae, which heat and enrich their immediate surroundings. The low-density regions created can not be modelled by the SPH method as accurately as high-density regions. Typical supernova remnants are around a few ×10 pc in size, which is much smaller than the resolution obtainable in cosmological SPH simulations ($\gtrsim$ 700 pc). For these reasons, it is necessary to use a simplified model for the release of energy and mass from stars.

The ejected mass and energy is distributed to the nearest $N_{\rm FB} = 72$ neighbouring gas particles, weighted by the SPH smoothing kernel. An alternative method, which we do not use here (but see e.g., Kobayashi, 2004), is to distribute within a sphere of constant radius to a variable number of neighbouring gas particles. Furthermore, energy is distributed in purely thermal form, although a fraction, $f_{\rm kin}$, of it could, in principle, be distributed in kinetic form as a velocity perturbation to the gas particles (Navarro & White, 1993). With $f_{\rm kin} > 0$, feedback is much stronger, and the SFR smaller than $f_{\rm kin} = 0$. However, with our scheme of star formation and supernova feedback, we do not need the kinetic feedback or momentum driven winds that are included in some other codes (e.g., Davé et al., 2006). We also do not apply an artificial multi-phase to gas particles that is included in some other codes (Scannapieco et al., 2006).

The amount of energy per timestep that a star particle distributes to its surroudings as a function of age t is given by

$$E_e(t) = m_*^0(e_{e,\rm SW}\mathcal{R}_{\rm SW}(t) + e_{e,\rm II}\mathcal{R}_{\rm II}(t) + e_{e,\rm Ia}\mathcal{R}_{\rm Ia}(t)), \tag{2.72}$$

where $\mathcal{R}_{\rm SW}$, $\mathcal{R}_{\rm II}$, and $\mathcal{R}_{\rm Ia}$ are the number of SWs, SNe II, and SNe Ia, respectively, per unit mass in the current simulation timestep; these are described in more detail in Section 2.2.4.

The $e_{e,i}$ of equation (2.72) denote the energy per SN/SW. The energy of SWs is estimated to be 0.2×10^{51} erg in stars of solar metallicity, from observations of OB associations (Abbott, 1982). The metallicity of massive stars affects the mass outflow rate, with $\dot{M} \propto Z^{0.8}$ (Leitherer et al., 1992), and so we assume

$$e_{e,\rm SW} = \begin{cases} 0.2 \times 10^{51} \left(\frac{Z}{Z_\odot}\right)^{0.8} & m_{2,u} < m \le m_u \\ 0.2 \times 10^{51} & m_{2,l} < m \le m_{2,u} \end{cases} \quad [\text{erg}], \tag{2.73}$$

where Z is the metallicity of the star particle, and the mass limits are defined in Section 2.2.4.

The typical energies for SNe II and SNe Ia are adopted (Kobayashi, 2004):

$$e_{e,\rm II} = 1.3 \times 10^{51} \qquad (m_{2,l} < m \le m_{2,u}) \qquad [\text{erg}]; \tag{2.74}$$

$$e_{e,\mathrm{Ia}} = 1.3 \times 10^{51} \qquad (m_{1\mathrm{s},l} < m \leq m_{1\mathrm{s},u}) \qquad [\mathrm{erg}]. \tag{2.75}$$

We also include a metallicity-dependent contribution from hypernovae, which have mass-dependent $e_{e,\mathrm{HN}}$ (Kobayashi et al., 2006):

$$e_{e,\mathrm{HN}} = e_{e,\mathrm{II}} \times \begin{cases} 10, & M = 20M_\odot, \\ 10, & M = 25M_\odot, \\ 20, & M = 30M_\odot, \\ 30, & M = 40M_\odot. \end{cases} \tag{2.76}$$

The hypernova fraction is $\epsilon_{\mathrm{HN}} = 0.5$, 0.5, 0.4, 0.01, and 0.01 for $Z = 0$, 0.001, 0.004, 0.02, and 0.05 (Kobayashi & Nakasato, 2011).

In general, other works use very similar prescriptions for stellar feedback, but do not include contributions from HNe. This is true of both EAGLE (Schaye et al., 2014) and Illustris (Vogelsberger et al., 2014), which model SNe II and SNe Ia, AGB stars, and track around a dozen elemental abundances important for gas cooling.

2.2.4 Chemical Enrichment

In our simulations, star particles represent many individual stars. To follow their evolution, we model them as a simple stellar population (SSP), which means that they are the same age and metallicity, but follow a distribution of masses. The mass of the star particle decreases with time as high-mass stars die.

The mass of a star particle, m_*, which has age t is given by

$$m_*(t) = m_*^0 - \int_0^t E_m(t')\mathrm{d}t', \tag{2.77}$$

where E_m is the rate of mass-loss from the star particle. The mass of metal i of the star particle also evolves:

$$m_{z_i,*}(t) = m_*^0 Z_i^0 - \int_0^t E_{z_i}(t')\mathrm{d}t', \tag{2.78}$$

where Z_i^0 is the initial mass fraction of element i in the star particle, and E_{z_i} is its rate of mass loss.

The mass losses per timestep, E_m and E_{z_i}, are written as

$$E_m(t) = m_*^0(e_{m,\mathrm{II}}(t) + e_{m,\mathrm{Ia}}(t)), \tag{2.79}$$

$$E_{z_i}(t) = m_*^0(e_{z_i,\mathrm{II}}(t) + e_{z_i,\mathrm{Ia}}(t)), \tag{2.80}$$

where the $e_{m,i}$ are the specific mass-loss rates for SWs/SNe.

The masses of the stars that make up a star particle are distributed according to the initial mass function (IMF). This is assumed to obey a power law in mass, and be invariant to both metallicity and time:

$$\phi(m) \propto m^{-x}, \tag{2.81}$$

and satisfies

$$\int_{m_l}^{m_u} \phi(m)\mathrm{d}m = 1, \tag{2.82}$$

with $m_l = 0.01M_\odot$ and $m_u = 120M_\odot$. It is a matter of great debate as to the universality and form of the IMF. Even assuming the relatively simple form of equation (2.81), a range of different values for x have been suggested (e.g., Salpeter, 1955; Chabrier, 2003; Kroupa, 2008); we adopt the Kroupa (2008) IMF, for which

$$x = \begin{cases} 1.3, & m \geq 0.5M_\odot, \\ 0.3, & 0.5M_\odot > m \geq 0.08M_\odot, \\ -0.7, & m < 0.08M_\odot. \end{cases} \tag{2.83}$$

The mass lost per unit mass of stars in each timestep for each of SNe II and SNe Ia is given by

$$e_{m,\mathrm{II}} = \int_{\max(m_{2,l},m_t)}^{m_{2,u}} (1 - w_m)\phi(m)\mathrm{d}m, \tag{2.84}$$

$$e_{m,\mathrm{Ia}} = m_{\mathrm{CO}}\mathcal{R}_{\mathrm{Ia}}, \tag{2.85}$$

where m_t is the main-sequence turnoff mass for a population of stars of age t, and the uppper and lower limits of SNe II are $m_{2,u} = 50M_\odot$ and $m_{2,l} = 8_\odot$, respectively. w_m denotes the remnant mass fraction, i.e. the mass fraction of a neutron star or white dwarf left following SWs or a SN II. In SNe Ia, the entire WD progenitor is disrupted, leaving no remnant and ejecting a mass $m_{\mathrm{CO}} = 1.38M_\odot$.

The metal mass losses per unit mass of stars in each timestep are given by

$$e_{z_i,\mathrm{II}} = \int_{m_t}^{m_{2,u}} p_{z_im,\mathrm{II}}\phi(m)\mathrm{d}m + \int_{m_t}^{m_{2,u}} (1 - w_m - p_{z_im,\mathrm{II}})Z_i(t - \tau_m)\phi(m)\mathrm{d}m, \tag{2.86}$$

$$e_{z_i,\mathrm{Ia}} = m_{\mathrm{CO}}p_{z_im,\mathrm{Ia}}\mathcal{R}_{\mathrm{Ia}}. \tag{2.87}$$

Equation (2.86) includes contributions from both SNe II and AGB stars, through the parameter $p_{z_im,\mathrm{II}}$, which is the mass fraction of newly produced and ejected element i. These stellar yields, p_{z_im}, are calculated in nucleosynthesis models (Karakas, 2010; Kobayashi et al., 2011a), with $p_{z_im,\mathrm{II}} = 0$ for $8M_\odot < m < 10M_\odot$ since neither SNe II nor AGB stars contribute in this range; see Figs. 1-5 of Kobayashi et al. (2011b) for more details.

The number of SNe and SWs per unit mass in each timestep, $\mathcal{R}_i$, are calculated as follows: for SNe Ia, we have

$$\mathcal{R}_{\mathrm{Ia}} = b\int_{\max(m_{1\mathrm{p},l},m_t)}^{m_{1\mathrm{p},u}} \frac{1}{m}\phi(m)\mathrm{d}m \int_{\max(m_{1\mathrm{s},l},m_t)}^{m_{1\mathrm{s},u}} \frac{1}{m}\phi_{\mathrm{s}}(m)\mathrm{d}m, \tag{2.88}$$

where the subscripts p and s denote primary (CO WD) and secondary, respectively. The initial mass of the WD progenitor ranges from $m_{1\mathrm{p},l} = 3M_\odot$ to $m_{1\mathrm{p},u} = 8M_\odot = m_{2,l}$. We assume that the secondary is either a main-sequence (MS) or red-giant

TABLE 2.1: Upper and lower mass limits of secondary star for SNe Ia (see equation (2.88)) for different [Fe/H] and red-giant (RG) or main-sequence (MS) stars. This table is reproduced from Kobayashi & Nomoto (2009, their Table 4).

[Fe/H]	-1.1	-1.0	-0.7	0.0	0.4
$m_{\mathrm{RG},l}/M_\odot$	0.9	0.9	0.9	0.9	0.8
$m_{\mathrm{RG},u}/M_\odot$	0.9	1.5	2.0	3.0	3.5
$m_{\mathrm{MS},l}/M_\odot$	1.8	1.8	1.8	1.8	1.8
$m_{\mathrm{MS},u}/M_\odot$	1.8	2.6	4.0	5.5	6.0

(RG) star, and calculate $\mathcal{R}_{\mathrm{Ia}}$ separately for each system with their own (metallicity-dependent) $m_{1\mathrm{s},l}$, $m_{1\mathrm{s},u}$, and binary fraction $b = 0.023$ in both cases (Kobayashi & Nomoto, 2009). Table 2.1 lists the secondary mass limits for various [Fe/H] (reproduced from Kobayashi & Nomoto (2009)). For SNe II and SWs, we have (David et al., 1990)

$$\mathcal{R}_{\mathrm{SW}} = \int_{\max(m_{2,u},m_t)}^{m_u} \frac{1}{m}\phi(m)\mathrm{d}m, \tag{2.89}$$

$$\mathcal{R}_{\mathrm{II}} = \int_{\max(m_{2,l},m_t)}^{m_{2,u}} \frac{1}{m}\phi(m)\mathrm{d}m. \tag{2.90}$$

The main-sequence turnoff mass, m_t at age t, is the mass of the star whose main-sequence lifetime $\tau_m = t$; we use the metallicity-dependent lifetimes of Kodama & Arimoto (1997).

2.3 Black Hole Physics

In this section, we introduce the BH and AGN feedback model used in our code. The results of a test of the efficiency of this code are given in Appendix A.

2.3.1 Seeding BHs

In previous implementations of AGN feedback, a single super-massive BH is spawned in every dark matter halo of sufficient mass (typically $\sim 10^{10} M_\odot$), identified by regular running of a Friend of Friends routine (Springel et al., 2005; Sijacki et al., 2007; Di Matteo et al., 2008; Booth & Schaye, 2009; Schaye et al., 2014; Vogelsberger et al., 2014). A gas particle within such a group, which satisfies some criterion (the most gravitationally bound, or the most dense for example), is converted to a BH, with mass $\sim 10^5 M_\odot$. This ensures that galaxies that later form in these haloes contain a BH.

We adopt a different approach for the formation of seed BHs, motivated by the theory of primordial star formation and the observed signatures of the first chemical enrichment. Much theoretical work has been undertaken in understanding how the first BHs formed, with the most likely candidates being as the remnants of Population III stars or formed by the direct collapse of primordial gas. For the latter scenario, BHs formed via direct collapse of a massive, low angular momentum gas cloud are likely rare due to the conditions necessary for the collapse to occur. In order to maintain a high Jeans mass, the gas must not cool efficiently, since $M_{\rm J} \propto T^{3/2}$. This may be accomplished by suppressing the formation of H_2 with a strong Lyman Werner flux, so that cooling is dominated by atomic hydrogen and the gas is not able to fragment. Modelling of such situations can produce seed BHs as large as $10^5 M_\odot$ (Bromm & Loeb, 2003; Koushiappas et al., 2004; Agarwal et al., 2012). For the former scenario, the deaths of Population III stars, either as core collapse supernovae ($M_{\rm star} \lesssim 140 M_\odot$) or by collapsing directly ($M_{\rm star} \gtrsim 300 M_\odot$), could conceivably produce BH seeds with mass in the range $10 \lesssim M_{\rm seed}/M_\odot \lesssim 10^3$ (Madau & Rees, 2001; Schneider et al., 2002; Bromm et al., 2002).

Our criteria for forming BHs are therefore as follows: any gas particle satisfying

$$\rho_{\rm g} > \rho_{\rm c}, \tag{2.91}$$

and

$$Z = 0, \tag{2.92}$$

where $\rho_{\rm g}$ and Z are the density and metallicity of the gas particle respectively, and $\rho_{\rm c}$ a specified critical density, is converted into a BH with a constant seed mass $M_{\rm seed}$. Similar criteria were adopted in Bellovary et al. (2011) to study the occupation fraction of BHs in simulated haloes. From the above discussion, we consider the range $10^1 \leq M_{\rm seed}/M_\odot \leq 10^5$. We treat $\rho_{\rm c}$ as a free parameter and determine its value by comparing the final state of simulations with observations (see Section 2.5.4). We therefore restrict neither the number of BHs that form, nor the locations where they form.

Note that, due to the limited mass resolution, $M_{\rm seed}$ is much smaller than $M_{\rm gas}$. As in previous works (e.g. Springel et al., 2005; Booth & Schaye, 2009), we store the mass of the BH separately and use $M_{\rm gas}$ as the dynamical mass until $M_{\rm BH}$ reaches $M_{\rm gas}$. We also note that due to the limited spatial resolution of the simulations presented in this thesis (typically a few comoving kpc), it is possible for BHs to 'wander' out of galaxies in a few timesteps solely because of numerical effects. To avoid this artificial effect, at every timestep we calculate the centre of mass of all particles within the smoothing radius of each BH and reposition the BH to that location.

2.3.2 Black hole growth

The seed BHs grow by both gas accretion and mergers with multiple other BHs. In cosmological hydro-simulations, the spatial resolution is usually $\gtrsim 1h^{-1}$kpc, and thus it is not possible to resolve the detailed physics of accretion near BHs. It is therefore necessary to use a sub-resolution model for the processes governing the growth of BHs and the feedback from them. We adopt roughly the same model as in many previous works (Springel et al., 2005; Sijacki et al., 2007; Di Matteo et al., 2008; Booth & Schaye, 2009). The growth rate due to accretion is taken to be proportional to the Bondi-Hoyle accretion rate (Bondi & Hoyle, 1944),

$$\dot{M}_{\rm acc} = \alpha \frac{4\pi G^2 M_{\rm BH}^2 \rho}{(c_{\rm s}^2 + v^2)^{3/2}}, \tag{2.93}$$

where ρ is the gas density local to the BH, $c_{\rm s}$ is the sound speed of the gas local to the BH, v is the relative velocity between the BH and local gas, and the constant factor α accounts for the finite resolution of the simulations. In contrast to other works (e.g., Springel et al., 2005; Booth & Schaye, 2009; Barai et al., 2014), mass is accreted from gas particles in a continuous fashion, rather than stochastically accreting entire gas particles. In each timestep Δt, gas particles neighbouring a BH have their mass decreased by an amount $\dot{M}_{\rm acc}\Delta t$ times their SPH kernel weight. In principle, this procedure could lead to gas particles with masses much less than the simulation resolution, however the accretion rates are sufficiently low compared to the gas particle mass that this problem does not arise; at $z = 0$ in our fiducial simulation, the lowest mass gas particle has 25 per cent of its original mass, and only 3 per cent of gas particles are less massive than initially.

In previous works, values for α as low as 1 (Booth & Schaye, 2009; Khandai et al., 2014), or as high as a few hundred (Springel et al., 2005; Di Matteo et al., 2008; Khalatyan et al., 2008) have been used. In the EAGLE simulations, a variable accretion rate modifier is used,

$$\alpha_{\rm EAGLE} = \min\left(\frac{1}{C_{\rm visc}}\left(\frac{c_{\rm s}}{v_\phi}\right)^3, 1\right), \tag{2.94}$$

with $C_{\rm visc}$ a resolution-dependent, tuneable parameter, and v_ϕ an estimate of the circular velocity of the gas around the BH (Rosas-Guevara et al., 2013). $\alpha_{\rm EAGLE}$ is then an attempt to take account of the timescale for viscous transport within the (unresolved) accretion disc around the BH. We treat α as a free parameter and determine its value by comparing the final state of simulations with observations (see Section 2.5.1). Throughout, we assume that growth is Eddington limited, so that $\dot{M}_{\rm acc} \leq \dot{M}_{\rm Edd}$ at all times. The Eddington accretion rate is given by

$$\dot{M}_{\rm Edd} = \frac{4\pi G M_{\rm BH} m_{\rm p}}{\epsilon_{\rm r}\sigma_{\rm T} c}, \tag{2.95}$$

where $m_{\rm p}$ is the proton mass, and $\sigma_{\rm T}$ the Thompson cross section. Black holes then grow due to accretion at a rate given by

$$\dot{M}_{\rm BH} = (1 - \epsilon_{\rm r}) \times \min(\dot{M}_{\rm acc}, \dot{M}_{\rm Edd}). \tag{2.96}$$

$\epsilon_{\rm r}$ denotes the radiative efficiency of the BH; we set $\epsilon_{\rm r} = 0.1$ throughout this thesis (Shakura & Sunyaev, 1973).

A merger between BHs may occur if the following conditions are met:

$$v_{\rm rel} < c_{\rm s}; \tag{2.97}$$

$$r < \epsilon, \tag{2.98}$$

where $v_{\rm rel}$ is the relative velocity of the BHs, r their separation, and ϵ the gravitational softening length of the BHs. For the condition of equation (2.97), we use the local sound speed $c_{\rm s}$ as a measure of the local velocity scale (Springel et al., 2005; Di Matteo et al., 2008), which precludes BHs undergoing a quick flyby from merging. We note that Booth & Schaye (2009) used $v_{\rm rel} < \sqrt{GM/\epsilon}$ and Schaye et al. (2014) used $v_{\rm rel} < \sqrt{GM/h}$, where M and h are the mass and smoothing length of the most massive BH of the pair. We do not employ such a criterion in the current work since the mass of a BH as calculated by equation (2.93) can be several orders of magnitude lower than the dynamical mass of the BH, used to determine its velocity. Following the merging of BHs, the properties of the primary BH are updated such that mass and linear momentum are conserved, and it is relocated to the centre of mass of the merging particles. Although the processes of BH binary hardening is still not well understood (Makino & Funato, 2004), and would not be resolved in these simulations of galaxies in any case, the conditions of equations (2.97) and (2.98) cause BHs that would be expected to merge eventually to do so.

2.3.3 Energy feedback

In each timestep Δt, a BH produces an amount of energy $E_{\rm FB}$, which is calculated as

$$E_{\rm FB} = \epsilon_{\rm r}\epsilon_{\rm f}\dot{M}_{\rm acc}c^2\Delta t, \tag{2.99}$$

where $\epsilon_{\rm f}$ denotes the fraction of radiated energy that couples to the gas. Previous works have used $\epsilon_{\rm f}$ in the range 0.05 (Springel et al., 2005; Di Matteo et al., 2008) to 0.15 (Booth & Schaye, 2009; Schaye et al., 2014); we treat $\epsilon_{\rm f}$ as a free parameter and determine its value by comparing the final state of simulations with observations (see Section 2.5.2).

$E_{\rm FB}$ is distributed with the same scheme as for supernova feedback; kernel-weighted, to a constant number of neighbouring gas particles. We adopt $N_{\rm FB} = 72$; this value is chosen in order that, at the resolution of our fiducial simulation, gas particles are sufficiently heated that they do not cool too rapidly, but not so much that an excessive mass of gas is expelled from galaxies (Kobayashi et al., 2007). The energy contributes only to the internal energy of the gas particles; there is no kinetic component. We note that the energy coupled to the gas is distributed roughly isotropically at our resolutions, whereas on smaller scales, energy could be injected along jets, as shown in small-scale simulations of AGN (e.g. Wagner & Bicknell, 2011). With such small scale kinetic feedback, star formation may be enhanced (e.g. Silk, 2013). A more realistic such model is left to future works.

TABLE 2.2: Input parameters and present quantities of the simulations for the parameter study. (1) Simulation name. (2) Value of α (see equation (2.93)). (3) Value of $\epsilon_{\rm f}$ (see equation (2.99)). (4) Black hole seed mass. (5) Value of critical density for BH formation (see equation (2.91)). (6) Stellar mass fraction $f_* = M_*/(M_* + M_{\rm g} + M_{\rm BH})$. (7) Total number of BHs. (8) Black hole mass fraction $f_{\rm BH} = M_{\rm BH}/(M_{\rm BH} + M_{\rm g} + M_*)$. (9) Average ratio of BH mass to stellar mass within $R_{\rm e}$. (10) Mass of most massive BH.

Name (1)	α (2)	$\epsilon_{\rm f}$ (3)	$M_{\rm seed}$ $(h^{-1}M_\odot)$ (4)	$\rho_{\rm c}$ $(h^2 m_{\rm H}\,{\rm cm}^{-3})$ (5)	f_* (6)	$N_{\rm BH}$ (7)	$f_{\rm BH}$ $(\times 10^{-5})$ (8)	$\langle M_{\rm BH}/M_{*,R_{\rm e}}\rangle$ $(\times 10^{-3})$ (9)	$\max(M_{\rm BH})$ $(\times 10^7 h^{-1}M_\odot)$ (10)
F	1	0.25	10^3	0.1	0.053	206	1.36	0.7	7.4
A1	10	0.25	10^3	0.1	0.039	195	1.98	3.2	9.4
A2	50	0.25	10^3	0.1	0.030	212	2.26	7.1	9.1
A3	100	0.25	10^3	0.1	0.026	207	2.23	5.0	10.9
E1	1	0.01	10^3	0.1	0.049	201	22.53	12.5	126
E2	1	0.05	10^3	0.1	0.050	198	5.58	2.4	34.1
E3	1	0.15	10^3	0.1	0.054	205	2.12	0.9	11.8
E4	1	0.50	10^3	0.1	0.054	205	0.82	0.4	4.1
M1	1	0.25	10^1	0.1	0.071	210	3e-3	3e-3	9e-3
M2	1	0.25	10^2	0.1	0.069	200	0.15	5e-2	1.1
M3	1	0.25	10^4	0.1	0.039	196	4.56	8.7	18.0
M4	1	0.25	10^5	0.1	0.018	207	24.77	94.3	89.7
R1	1	0.25	10^3	0.5	0.072	126	0.60	3.2	2.0
R2	1	0.25	10^3	1.0	0.075	108	0.40	0.3	1.4

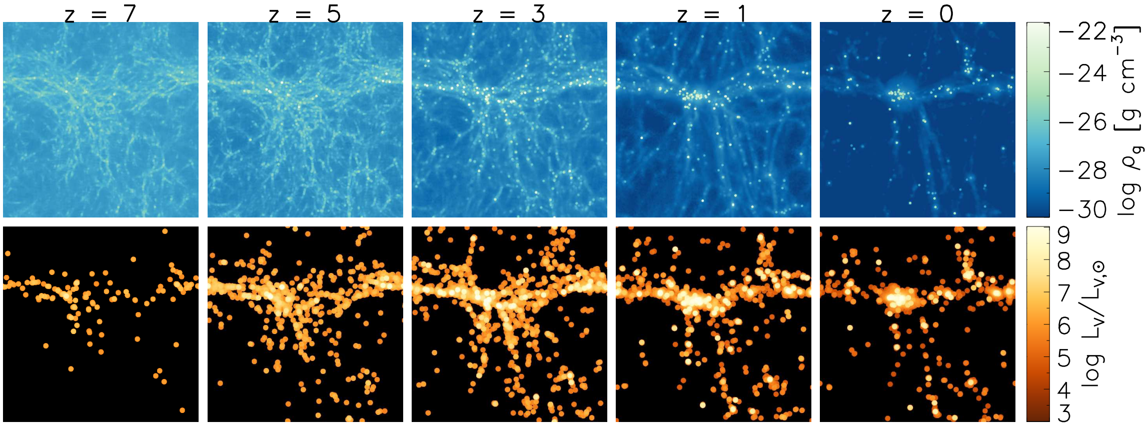

FIGURE 2.2: The time evolution of our fiducial simulation, F, in a periodic box $10h^{-1}$ Mpc on a side. We show projected gas density on the upper row, and V-band luminosity on the lower row.

2.4 The Simulations

We employ a WMAP-9 ΛCDM cosmology (Hinshaw et al., 2013) with $h = 0.70$, $\Omega_{\rm m} = 0.28$, $\Omega_\Lambda = 0.72$, $\Omega_{\rm b} = 0.046$, and $\sigma_8 = 0.82$. The simulations presented in Section 2.5 are run at the same resolution with identical initial conditions, in a periodic, comoving, cubic volume $10h^{-1}$ Mpc on a side. This initial condition is chosen to have a central concentration at $z = 0$, and is different from Kobayashi et al. (2007), which corresponds to typical field of the Universe. The parameters used in each simulation are listed in Table 2.2, as well as $z = 0$ properties of the simulated volumes. The initial conditions contain 96^3 particles of each of dark matter and gas, with masses $M_{\rm DM} = 7.3 \times 10^7 h^{-1} M_\odot$ and $M_{\rm gas} = 1.4 \times 10^7 h^{-1} M_\odot$; by $z = 0$ there are approximately 5 per cent more particles in total due to the formation of star particles. We use a gravitational softening length of $\epsilon_{\rm gas} = 1.125\, h^{-1}$ kpc.

The redshift evolution of our fiducial simulation (see Section 2.5) is shown in Fig. 2.2. At high redshift, a rich filamentary structure exists, to which star and BH formation is mostly confined. The first BH forms at $z \sim 16$ (at the resolution of these simulations) in the region that will subsequently collapse to form the largest cluster in the simulation box. This first BH grows and provides thermal feedback to neighbouring gas particles, as described in Section 2.3.3. Heating by AGN feedback results in the delay of the formation of the first star until $z \sim 11$. Following the hierarchical clustering of dark haloes, cold gas falls along the filaments, which boosts the formation of BHs and stars. Chemical enrichment from the previous generation of stars suppresses the formation of BHs but enhances star formation. As a result, the SFR peaks at $z \sim 2$ (see Figs 2.5-2.8(a) in Section 2.5), coincident with a broader peak in the cosmic BH accretion rate. The BH number density peaks earlier, at $z \sim 5.5$, after which mergers reduce their total number. Fig. 2.3 shows the cosmic BH accretion rate (solid line) and growth rate including BH formation (dashed line),

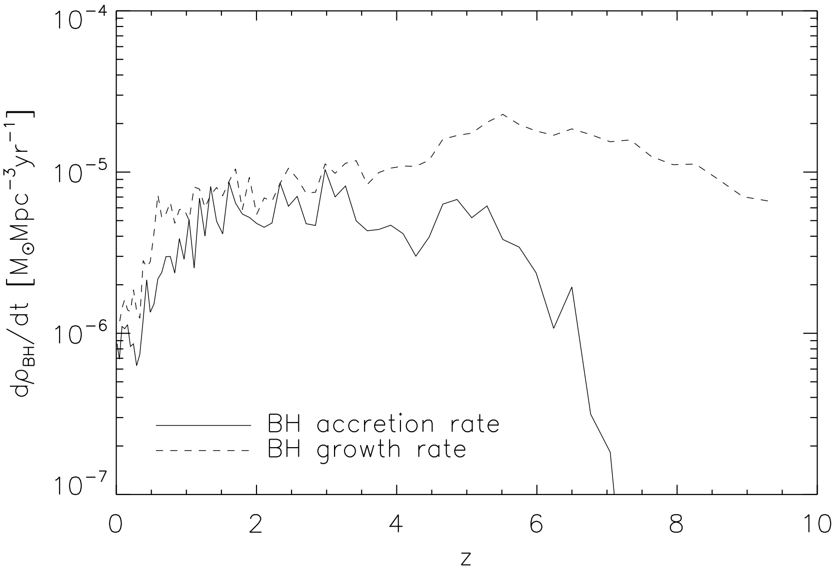

FIGURE 2.3: Cosmic accretion rate density (solid line) and growth rate density (including BH formation, dashed line) of our fiducial simulation, F, with redshift.

for our fiducial simulation. Gas accretion only becomes important in the growth of BHs from $z \sim 4$. By $z = 0$, the accretion rate has fallen to $\sim 10^{-6} M_\odot$ Mpc^{-3} yr^{-1}, consistent with the observational estimate of $1.3 \times 10^{-6} M_\odot$ Mpc^{-3} yr^{-1} from radio luminosities (Smolčić et al., 2009).

Due to the supernova and AGN feedback, galactic winds are generated, which eject interstellar gas into the intergalactic medium. The largest concentration of stars and BHs is seen in a central cluster of galaxies, with a present total mass of $\sim 10^{13} h^{-1} M_\odot$, and which hosts the most massive BH in the simulation volume with a mass $\sim 10^8 h^{-1} M_\odot$. In Fig. 2.4 we show the $z = 0$ spatial distribution of stars and BHs in a $6 \times 6 \times 10$ (h^{-1} Mpc)^3 volume around the largest cluster, as well as the projected gas density. Star and BH particles are found along filaments, coinciding with local peaks in gas density. Although our description of seeding of BHs does not ensure the co-evolution between BHs and galaxies, larger BHs tend to be located in larger galaxies (see Figs. 2.5-2.8(b)).

Galaxies are identified using a Friend of Friends algorithm, in common with previous works (e.g. Springel et al., 2001; Kobayashi et al., 2007; Booth & Schaye, 2009). The algorithm identifies groups of dark matter particles, using a comoving linking length of 0.02 times the mean dark matter particle separation. Gas, star, and BH particles are then associated with their nearest dark matter particle, and join that particle's group. A catalogue is then made of all groups whose total mass is at least $32 M_{\rm DM}$. For the analysis of properties of a galaxy, only those groups containing at least 50 star particles are kept. In the fiducial simulation at $z = 0$, 99 groups are found by the friend of friends algorithm, 76 are classified as galaxies, corresponding to $10^9 \lesssim M_*/M_\odot \lesssim 5 \times 10^{11}$, and 60 of these contain one or more

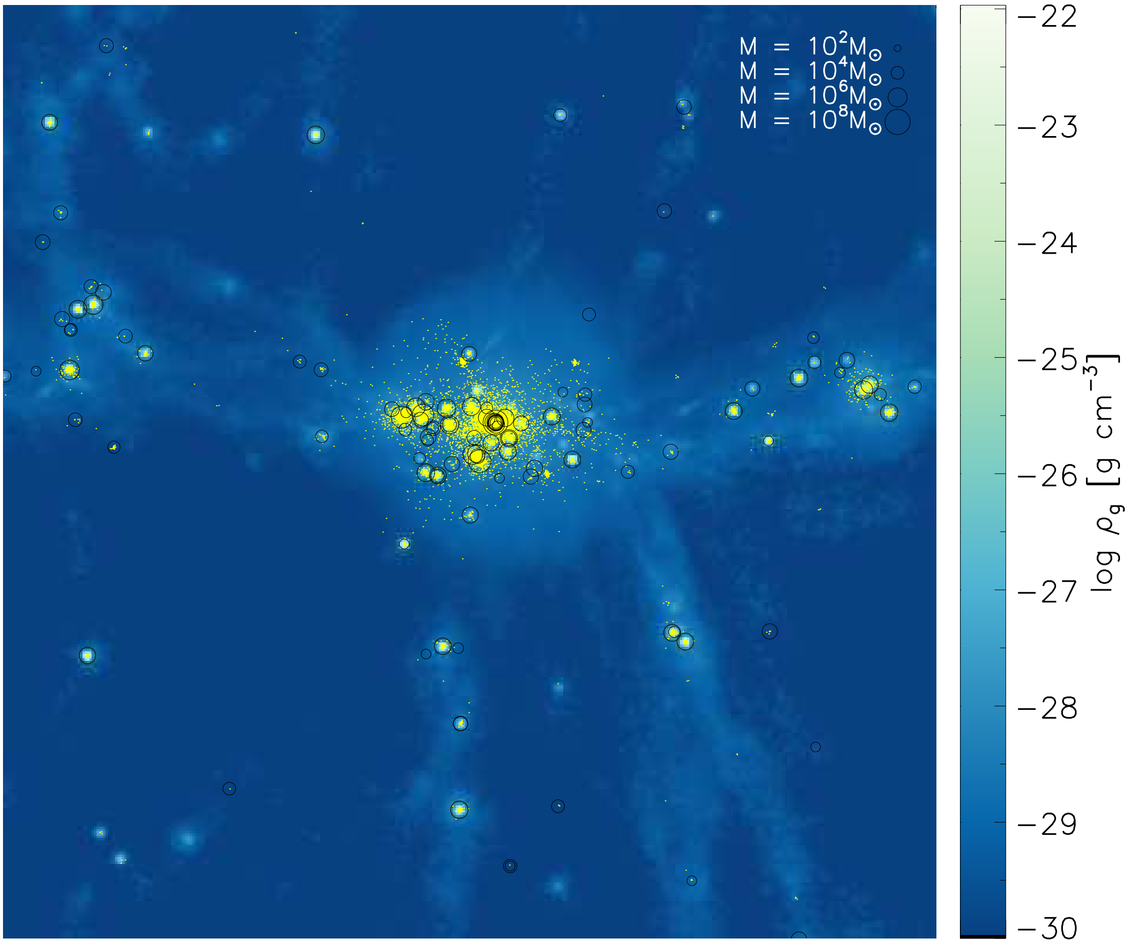

Figure 2.4: The distribution of BHs (black circles, whose radii are proportional to $\log M_{\rm BH}$) and star particles (yellow dots) in a $6 \times 6 \times 10$ (h^{-1} Mpc)^3 volume at $z = 0$ in our fiducial simulation. We also show the projected gas density (blue).

BHs. 4 galaxies host multiple BHs: the most massive galaxy contains 6, while 3 others have 2 BHs each. In all cases, one of the BHs is much more massive than the others; in the most extreme case, that of the most massive galaxy, the most massive BH contains 99.5 per cent of the combined mass of the 6.

The $z = 0$ stellar and BH mass fractions, number of BHs, and the mass of the largest BH in the simulations of Section 2.5 are given in Table 2.2. Larger α and $M_{\rm seed}$, and smaller $\rho_{\rm c}$, results in stronger feedback, which leads to a greater reduction in star formation, and more massive BHs. Larger $\epsilon_{\rm f}$ results in more massive BHs, but does not affect star formation history. Without AGN feedback, the $z = 0$ stellar mass fraction, $f_* = M_*/(M_* + M_{\rm g} + M_{\rm BH})$, is 0.075, which is consistent with the result in Kobayashi et al. (2007). With AGN feedback included, f_* is reduced to 0.053 in our fiducial simulation, which is more comparable with the observational estimate of ~ 0.046 (e.g. Fukugita & Peebles, 2004). Observationally, the BH to bulge mass ratio in galaxies is found to be $M_{\rm BH}/M_{\rm bulge} \sim 2 \times 10^{-3}$ (e.g. Marconi &

Hunt, 2003). We find $\langle M_{\rm BH}/M_*(< R_{\rm e})\rangle = 0.7 \times 10^{-3}$, with $R_{\rm e}$ the effective radius of a galaxy (see Section 2.5 for more details). The small discrepancy comes from the difference between $M_{\rm bulge}$ and M_*; the bulge mass of late type galaxies tends to be smaller than $M_*(< R_{\rm e})$.

2.5 Parameter Study

In this Section, we present the results of a suite of simulations, each with different values of the free parameters of the model described in Section 2.3. We then determine a 'best' set of parameters, such that the simulation using these parameters produce results that most closely match observations. For the observational constraints, we use cosmic SFR history, size–velocity dispersion relations of galaxies (Trujillo et al., 2011), and the $M_{\rm BH} - \sigma$ relation (Kormendy & Ho, 2013). For the cosmic SFR history, observational data are taken from Bouwens et al. (2011), Karim et al. (2011), Cucciati et al. (2012), Oesch et al. (2012), Burgarella et al. (2013), Gunawardhana et al. (2013), and Sobral et al. (2013), adjusted to the Kroupa (2008) IMF (Bernardi et al., 2010). These values are systematically lower than Hopkins & Beacom (2006). Values derived from Hα measurements may be underestimated due to the bivariate selection process (Gunawardhana et al., 2013), and those from UV measurements are sensitive to dust extinction.

For the size–velocity dispersion relation, we fit a core-Sérsic profile to the surface density of the galaxies, and define the effective radius, $R_{\rm e}$, as that which encloses half the stellar mass. The velocity dispersion is measured within the central $R_{\rm e}$ of galaxies. We compare the $M_{\rm BH} - \sigma$ relations obtained from our simulations to the one presented in Kormendy & Ho (2013), who find $\log(M_{\rm BH}/10^9 M_\odot) = -(0.510 \pm 0.049) + (4.377 \pm 0.290)\log(\sigma/200\,{\rm km\ s^{-1}})$. This is in keeping with the findings of other studies (Tremaine et al., 2002; Hu, 2008; Gültekin et al., 2009; Greene et al., 2010), although some have found steeper slopes (e.g. Graham & Scott, 2013). At least some of this disparity is likely due to the different relation observed for bulges that have formed by mergers and those that have not (Hu, 2008; Beifiori et al., 2012; Kormendy & Ho, 2013). We do not make such a distinction in this work, and compare the galaxy population as a whole to observations.

The values of the best set of parameters are $\alpha = 1$, $\epsilon_{\rm f} = 0.25$, $M_{\rm seed} = 10^3\,h^{-1}M_\odot$, $\rho_{\rm c} = 0.1\,h^2 m_{\rm H}\,{\rm cm}^{-3}$. We use this as our fiducial set of parameters (simulation F) in the following subsections. In each subsection, we fix the values of all parameters, except that which is being examined, to their fiducial values.

We first performed this parameter study for a wide range of parameter space at moderate resolution, before homing in on the values that comprise our best set. We then investigated a smaller region of parameter space around these values at higher resolution (see Table 2.2 for details). The results of these higher resolution tests, and the effects of each of the parameters on the evolution of BHs and galaxies, are presented below, but similar trends are seen for all the tests we have performed.

Note that, in the preparation of this thesis, figures in the following sections have been recreated since the publication of Taylor & Kobayashi (2014). None of the results or conclusions is affected, and the primary effect has been to reduce the scatter in measurements that rely on the effective radius; in Taylor & Kobayashi (2014), a Sérsic profile was assumed, whereas we now fit a core-Sérsic profile (see Chapter 3 and Appendix B for more details).

2.5.1 Accretion Rate Modifier

α controls the rate of gas accretion onto BHs via equation (2.93), and therefore influences the amount of feedback energy they produce via equation (2.99). As discussed in Section 2.3, α can be larger than 1, and we apply $\alpha = 1, 10, 50, 100$ for the simulations F and A1-3 (see Table 2.2).

One of the clearest effects of changing the value of α is apparent in Fig. 2.5(a), which shows cosmic SFR as a function of redshift. All curves show a peak in SFR at $z \sim 2$, in agreement with both the simulation without AGN feedback, and observations (Hopkins & Beacom, 2006; Karim et al., 2011; Cucciati et al., 2012; Burgarella et al., 2013; Gunawardhana et al., 2013; Sobral et al., 2013). Of the simulations with AGN feedback, all but the $\alpha = 1$ case show suppressed star formation with respect to the simulation without AGN across all of cosmic time. For the fiducial simulation, with $\alpha = 1$, the peak is almost the same as in the simulation without AGN, and is suppressed at both earlier and later times, which is in better agreement with the observed low SFRs at $z > 6$ (Bunker et al., 2010; Bouwens et al., 2011) than the simulation without AGN. There is a clear trend for simulations with higher α to have more heavily suppressed star formation. Naïvely, one might assume that this is due to α enhancing the accretion rate leading to a greater amount of feedback energy so that some gas particles no longer satisfy the star formation criterion of rapid cooling. However, this is not the case; the effects of the value of α on the growth of BHs are shown in Fig. 2.5(c). The solid lines show the growth of the most massive present day BH, while the dotted lines show the mean BH mass of the entire volume. It is surprising to note that the growth history of both the most massive BH, and the mean BH mass, seem to be insensitive to the value of α, given that its purpose was to modify the accretion rate. If BH growth is self-regulated, then the amount of feedback energy released by a BH over its lifetime should be independent of α. This then implies, from equation (2.99), that the mass a BH accretes should also be independent of α. This self-regulation will be discussed further in Section 2.7.

The independence of BH mass on α is also apparent from Fig. 2.5(b), which shows the $z = 0$ $M_{\rm BH} - \sigma$ relation for the simulated galaxies, with the observational relation and scatter represented by the solid and dashed lines respectively. The fiducial simulation is in good agreement with the observed relation, at the high mass end in particular.

In contrast to the lack of strong dependence of the evolution of BHs, the value of α has a large impact on the properties of their host galaxies. For example, Fig. 2.5(d), which shows the $z = 0$ relation between galaxy effective radius and velocity dispersion, indicates that there is a trend for galaxies in simulations with large α to have larger effective radius. This is due to the fact that larger α suppresses star formation from cooling gas near the centre of galaxies to a greater extent, which results in a more extended distribution of stars at a given galaxy mass. This is the same effect as shown for the dependence of the star formation parameter on the galaxy size in Kobayashi (2005). The fiducial simulation compares well with observations, while those with larger α lie above the observed trend.

As well as the stellar component, the gas component of the simulated galaxies is also affected. We see a trend in Fig. 2.5(e) for galaxies formed in simulations with larger values of α to have both lower baryon fractions and lower total stellar mass, within two effective radii. This is because gas is removed from the central region of galaxies more efficiently when larger α is used. This is further evidenced by Fig. 2.5(f), which shows the gas density local to the most massive BH (solid lines), and the average gas density around BHs (dotted lines). There is a clear trend for larger α to lead to a reduction in gas density near BHs. It is therefore the effect of α on gas density, rather than the amount of feedback energy, that causes the reduction in star formation seen above, by increasing the dynamical time of the gas.

2.5.2 Feedback Efficiency

ϵ_{f} determines the fraction of energy produced by a BH that couples to neighbouring gas particles (see equation (2.99)). ϵ_{f} must be less than 1, and we apply $\epsilon_{\mathrm{f}} = 0.01, 0.05, 0.15, 0.25, 0.50$ for the simulations F and E1-4 (see Table 2.2). It is perhaps surprising then that Fig. 2.6(a) shows that the value of ϵ_{f} seems to have no bearing on the cosmic SRF history, other than to suppress star formation with respect to the simulation without AGN feedback. However, Fig. 2.6(c) shows that the value of ϵ_{f} has an effect on the mass of BHs for $z < 6$, with lower values allowing for more massive BHs. For self-regulated BH growth, the total amount of feedback energy produced by a BH over its lifetime should be independent of the value of ϵ_{f}, explaining why no variation is seen in star formation histories. However, from equation (2.99), this means that the total mass a BH accretes over its lifetime is smaller for larger ϵ_{f}, as seen. This self-regulation will be discussed further in Section 2.7.

This trend is also seen in the $M_{\mathrm{BH}} - \sigma$ relation in Fig. 2.6(b). Lower values of ϵ_{f} make BHs more massive at a given galaxy mass; with low ϵ_{f}, BHs grow above the observed relation, but with higher values BHs lie on the observed relation.We choose $\epsilon_{\mathrm{f}} = 0.25$ as our fiducial value because the high mass end of the relation best matches the observed relation in this case.

Unlike α, the value of ϵ_{f} has no discernible effect on the internal structure of galaxies. There is no trend with ϵ_{f} in the relation between effective radius and velocity dispersion at $z = 0$ (Fig. 2.6(d)). The value of ϵ_{f} has no global effect on the baryonic processes occurring within galaxies. No significant trend is seen in either Fig. 2.6(e), which shows the baryon fraction of galaxies as a function of stellar mass, or Fig. 2.6(f), which shows the gas density local to BHs as a function of redshift. This is another consequence of BH growth being self-regulated - a BH removes the

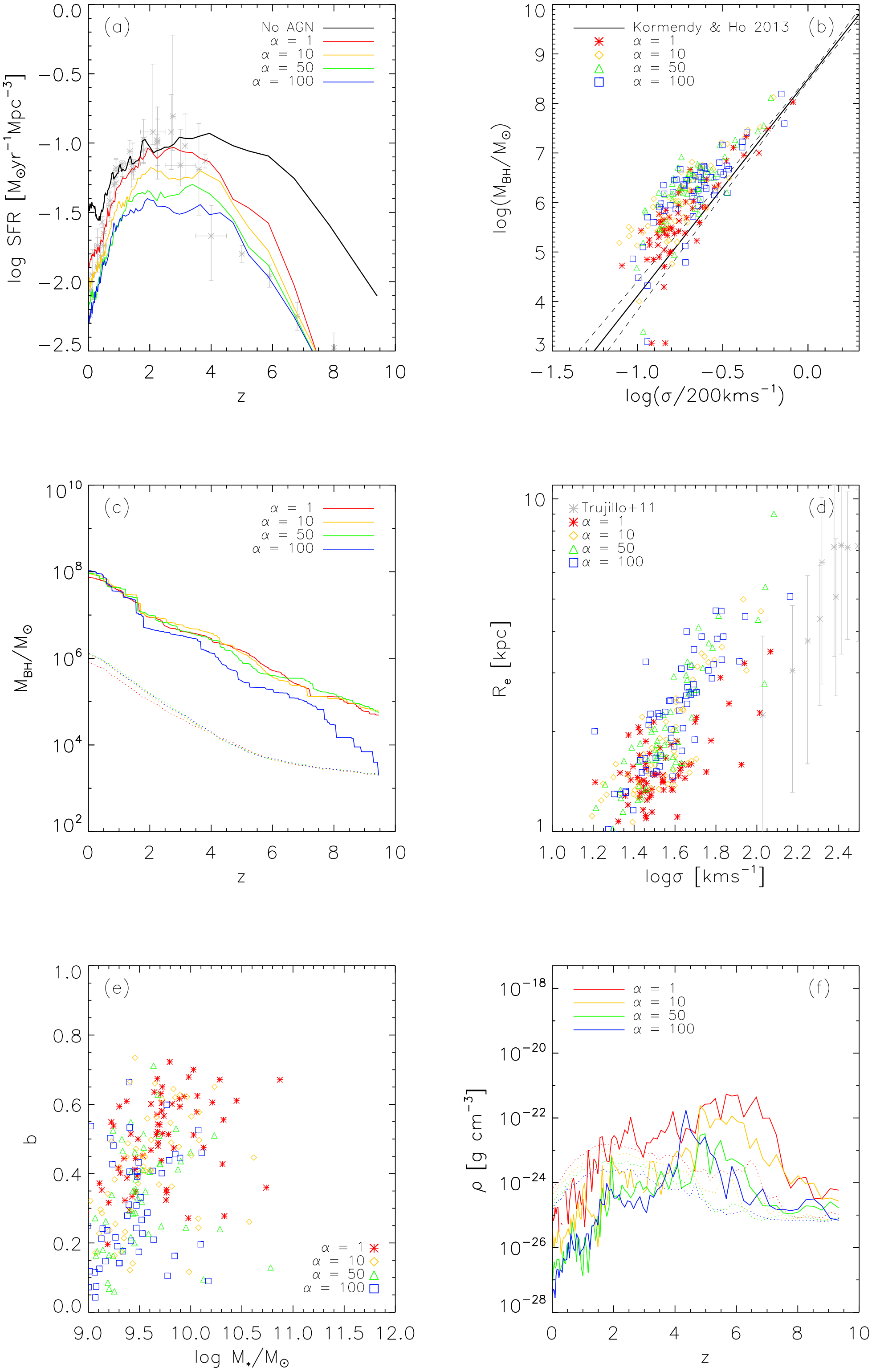

FIGURE 2.5: The influence of α on local and global quantities. (a) Cosmic star formation rate history. See text for sources of observational data (grey). (b) Present day $M_{\rm BH} - \sigma$ relation. The solid and dashed lines are for the observed relation and 1σ width (Kormendy & Ho, 2013), respectively. (c) Black hole mass as a function of redshift. Solid lines are for the most massive BH at $z = 0$, and the dotted lines for the average BH mass in the simulation box. (d) Present relationship between galaxy effective radius, and galaxy velocity dispersion; observational data (grey) are taken from Trujillo et al. (2011). (e) Present relationship between baryon fraction, $b = (M_{\rm gas} + M_*)/M_{\rm tot}$, and central stellar mass for all simulated galaxies. Both quantities are measured in a spherical region at the centre of galaxies of radius $2R_{\rm e}$. (f) Gas density local to BHs as a function of redshift (i.e. ρ in equation (2.93)). Solid lines are for the most massive BH at $z = 0$, and the dotted lines for the average gas density around all BHs in the simulation box.

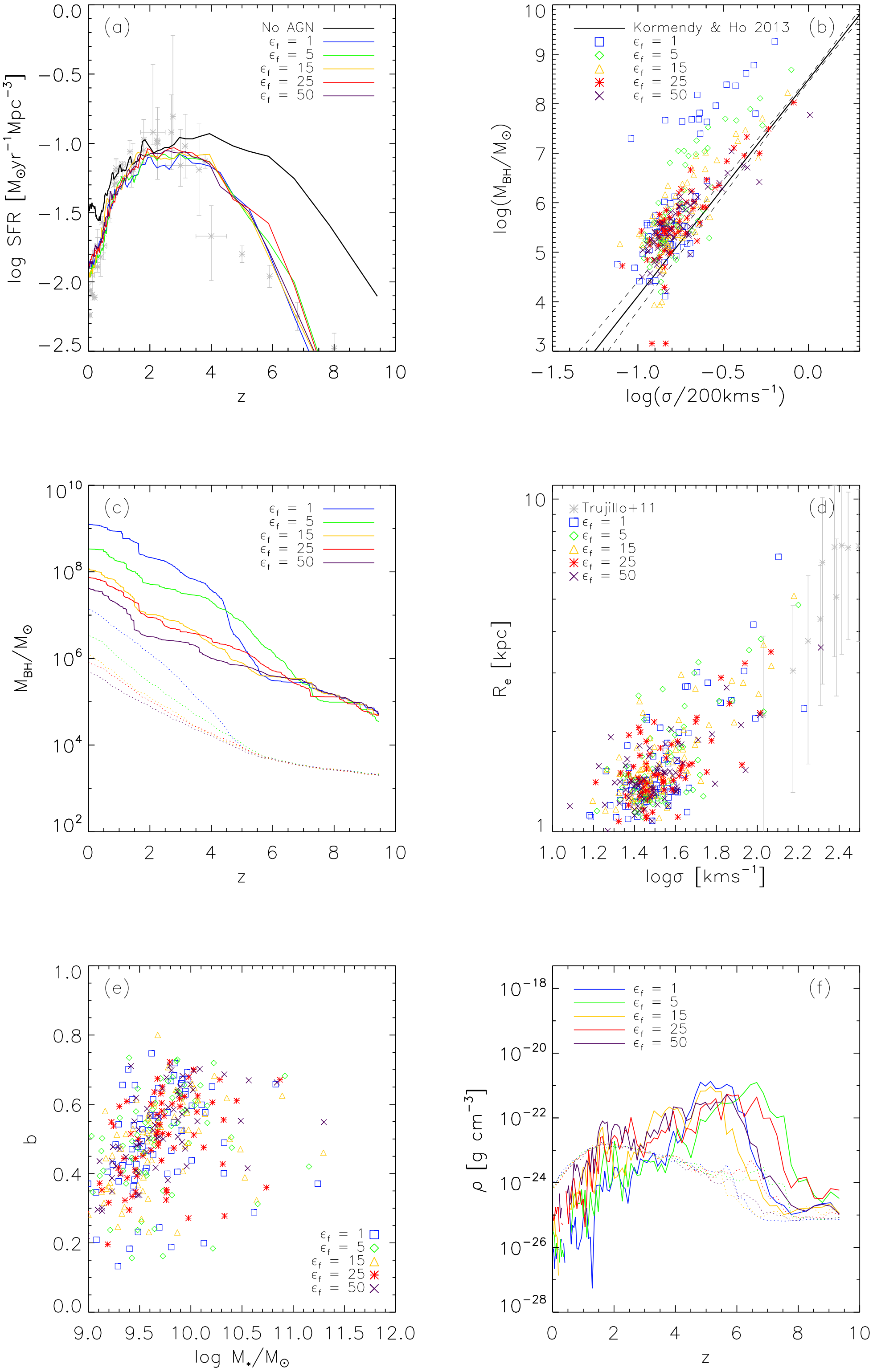

FIGURE 2.6: Same as Fig. 2.5, but for varying $\epsilon_{\rm f}$, and $\alpha = 1$, $M_{\rm seed} = 10^3\,h^{-1}M_\odot$, $\rho_{\rm c} = 0.1\,h^2 m_{\rm H}\,{\rm cm}^{-3}$.

same mass of gas from its galaxy, and does not affect star formation, regardless of the value of $\epsilon_{\rm f}$, and so we see no change in the properties of the galaxy population.

2.5.3 Seed Black Hole Mass

The mass with which a BH is seeded, $M_{\rm seed}$, has a large impact on the subsequent evolution of the BH itself and its host galaxy. This is to be expected since, from equation (2.93), the accretion rate (and hence also the feedback energy) is proportional to the square of the mass. We apply $M_{\rm seed}/M_\odot = 10^1, 10^2, 10^3, 10^4, 10^5\,h^{-1}$ for simulations F and M1-4 (see Table 2.2).

This is exemplified by Fig. 2.7(a), which shows the SFR as a function of redshift for different values of seed mass. There is a general trend that a larger seed mass suppresses star formation more efficiently across all time. This is easily explained by noting that a larger seed mass allows for the growth of more massive BHs, as indicated by Fig. 2.7(c).

We can see again, in Fig. 2.7(b), how the final mass of the BHs is affected by their seed mass. With the seed mass as high as $M_{\rm seed} = 10^5\,h^{-1}M_\odot$, BHs grow several orders of magnitude above the observed $M_{\rm BH}{-}\sigma$ relation. Only in the fiducial simulation, using a seed mass of $10^3 M_\odot$, do the BHs grow onto the observed relation. We discuss this result more in Section 2.7, connecting it to the astrophysical origin of BH seeds.

In common with α, the adopted value of $M_{\rm seed}$ affects the internal structure of galaxies. The $z = 0$ relationship between galaxy effective radius and velocity dispersion is shown in Fig. 2.7(d), in which a trend can be seen for larger seed masses to produce galaxies with larger effective radii. This is due to the fact that more massive BHs quench star formation to a greater extent at the center of galaxies, producing shallower intensity profiles. Galaxies formed in simulations with higher seed masses are seen to have a lower baryon fraction, as well as a less massive stellar component, as seen in Fig. 2.7(e), which shows the baryon fraction as function of stellar mass within two effective radii of galaxies. This is because more massive BHs are able to remove gas more easily from the centres of galaxies. This can be clearly seen in Fig. 2.7(f), which shows the gas density local to the most massive BH of each simulation (solid lines), and the average gas density around all BHs in the simulation box (dotted lines).

2.5.4 Critical Density

$\rho_{\rm c}$ is the critical density for BH formation, which directly determines when BHs form, and how common they are. It is from these two factors that the subsequent effects of the value of $\rho_{\rm c}$ stem. We apply $\rho_{\rm c} = 0.1, 0.5, 1.0\,h^2 m_{\rm H}\,{\rm cm}^{-3}$. Lower $\rho_{\rm c}$ allows BHs to form earlier, and at more locations throughout the simulation volume. This then gives the BH seeds more time to grow and affect their surroundings, although, by definition, starting from a region with lower gas density. With $\rho_{\rm c} = 0.1 h^2\ m_{\rm H}\,{\rm cm}^{-3}$,

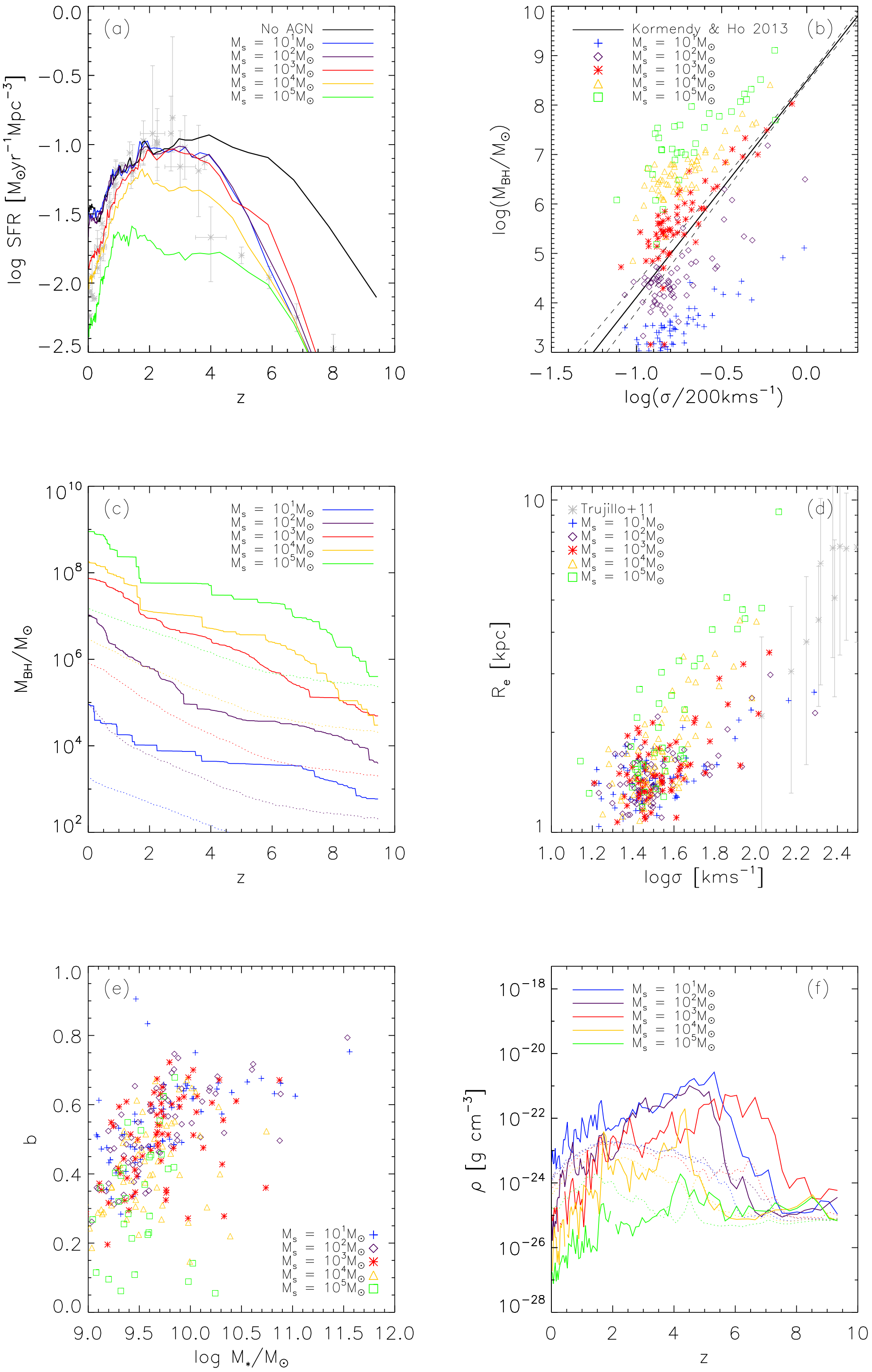

FIGURE 2.7: Same as Fig. 2.5, but for varying $M_{\rm seed}$, and $\alpha = 1$, $\epsilon_{\rm f} = 0.25$, $\rho_{\rm c} = 0.1\,h^2 m_{\rm H}\,{\rm cm}^{-3}$.

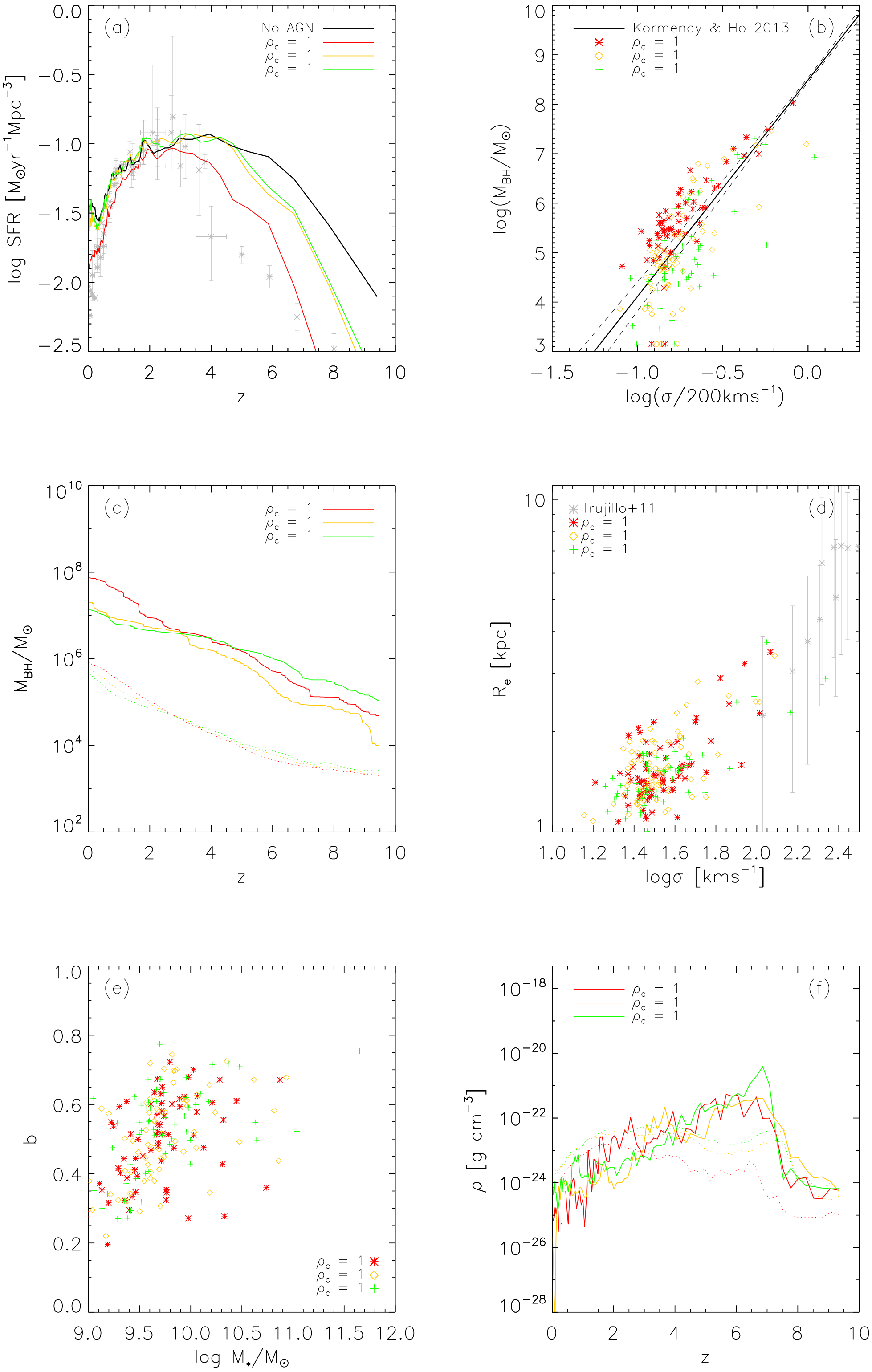

FIGURE 2.8: Same as Fig. 2.5, but for varying ρ_c, and $\alpha = 1$, $\epsilon_f = 0.25$, $M_{seed} = 10^3\,h^{-1}M_\odot$.

BHs can form as early as $z \sim 16$, whereas with $\rho_{\rm c} = 1h^2\ m_{\rm H}{\rm cm}^{-3}$, BHs start forming from $z \sim 13.6$, a difference of about 65 Myr.

The effect of this delay on SFR is apparent in Fig. 2.8(a), in which we see that star formation at high redshift is reduced to a greater extent when $\rho_{\rm c}$ is set to a lower value. For $\rho_{\rm c} \geq 0.5h^2\ m_{\rm H}\,{\rm cm}^{-3}$, the cosmic star formation history at $z \gtrsim 4$ is almost the same, regardless of the value of $\rho_{\rm c}$ used; the BHs form late enough, and in small enough numbers, that by low redshift they have not grown sufficiently to alter the SFR from its value without AGN feedback. In the fiducial simulation with $\rho_{\rm c} = 0.1h^2\ m_{\rm H}\,{\rm cm}^{-3}$, however, the BHs form early enough, and in large enough numbers, that star formation is noticeably quenched also at low redshift, and brought in line with observations.

The influence of delaying the birth time of BHs is also clear in Fig. 2.8(c), where, on average, more massive BHs are produced with lower $\rho_{\rm c}$. This is because they have both more time to accrete gas, and more BHs with which to merge. The trend is also seen in Fig. 2.8(b), which shows the $z = 0$ $M_{\rm BH} - \sigma$ relationship for these simulations. We see that, in simulation F, more BHs have grown onto the observed relation by the present day, and display a smaller scatter than in simulations R1 or R2.

While $\rho_{\rm c}$ influences the evolution of BHs and thus affects the cosmic SFR at high and low redshifts, its impact on the evolution of galaxies is minimal. Figs. 2.8(d) and 2.8(e) show, respectively, effective radius as a function of velocity dispersion and baryon fraction as a function of stellar mass for the simulated galaxies. Neither indicates a strong trend with $\rho_{\rm c}$, implying that the stellar and gas components of present-day galaxies are not influenced by when BHs form. This would seem to be in contradiction to Fig. 2.8(f), which shows that the average gas density local to BHs depends on $\rho_{\rm c}$, with higher values having higher gas densities (dotted lines). However, this is simply due to the fact that BHs are only spawned in high density regions if $\rho_{\rm c}$ is itself large; the trend is not indicative of the BHs' influence in those regions.

2.6 Resolution Effects

In this Section, we present the results of a group of simulations run at different resolutions in order to investigate the influence of resolution on our model. In all cases, the parameters of the fiducial simulation of Section 2.5 are used, specifically $\alpha = 1$, $\epsilon_{\rm f} = 0.25$, $M_{\rm seed} = 10^3\,h^{-1}M_{\odot}$, and $\rho_{\rm c} = 0.1h^2\ m_{\rm H}\,{\rm cm}^{-3}$. Simulations are given names of the form xxxmpcnnn, with xxx the comoving length of each side of the simulation box, and nnn the cube root of the initial number of both gas and dark matter particles (note that 010mpc096 is identical to simulation F of Section 2.5). The highest resolution simulation was run to $z = 2$. Therefore, we show in Table 2.3 properties of all simulations at $z = 2$, as well as the $z = 0$ properties of

Table 2.3: Input parameters and $z = 0$ and $z = 2$ quantities of the simulations for the study of resolution effects. Measured quantities are given at $z = 2$ for all simulations, and $z = 0$ for those that were run to completion. In all cases, values for the model parameters as in simulation F are assumed. (1) Simulation name. (2) Mass of dark matter particles. (3) Initial mass of gas particles. (4) Gravitational softening length. (5) Stellar mass fraction $f_* = M_*/(M_* + M_{\rm g} + M_{\rm BH})$. (6) Total number of BHs. (7) Black hole mass fraction $f_{\rm BH} = M_{\rm BH}/(M_* + M_{\rm g} + M_{\rm BH})$. (8) Average ratio of BH mass to stellar mass within $R_{\rm e}$. (9) Mass of most massive BH. (10) Redshift at which first BH forms.

Name (1)	$M_{\rm DM}$ $(\times 10^6 h^{-1} M_\odot)$ (2)	$M_{\rm gas}$ $(\times 10^6 h^{-1} M_\odot)$ (3)	$\epsilon_{\rm gas}$ $(h^{-1}$ kpc$)$ (4)	f_* (5)	$N_{\rm BH}$ (6)	$f_{\rm BH}$ $(\times 10^{-5})$ (7)	$\langle M_{\rm BH}/M_{*,R_{\rm e}} \rangle$ $(\times 10^{-3})$ (8)	$\max(M_{\rm BH})$ $(\times 10^7 h^{-1} M_\odot)$ (9)	z_i (10)
				$z = 0$					
010mpc054	412	81.1	2.0	0.046	72	1.19	0.7	9.8	11.7
010mpc096	73.4	14.4	1.125	0.053	206	1.36	0.6	7.4	16.0
010mpc128	31.0	6.09	0.844	0.051	370	1.75	1.7	8.4	48.8
				$z = 2$					
010mpc054	412	81.1	2.0	0.012	214	0.09	0.4	0.71	11.7
010mpc096	73.4	14.4	1.125	0.020	643	0.53	1.1	0.89	16.0
010mpc128	31.0	6.09	0.844	0.017	1,132	0.94	3.1	0.74	48.8
010mpc256	3.87	0.76	0.422	0.017	7,517	6.43	30.0	2.83	48.8

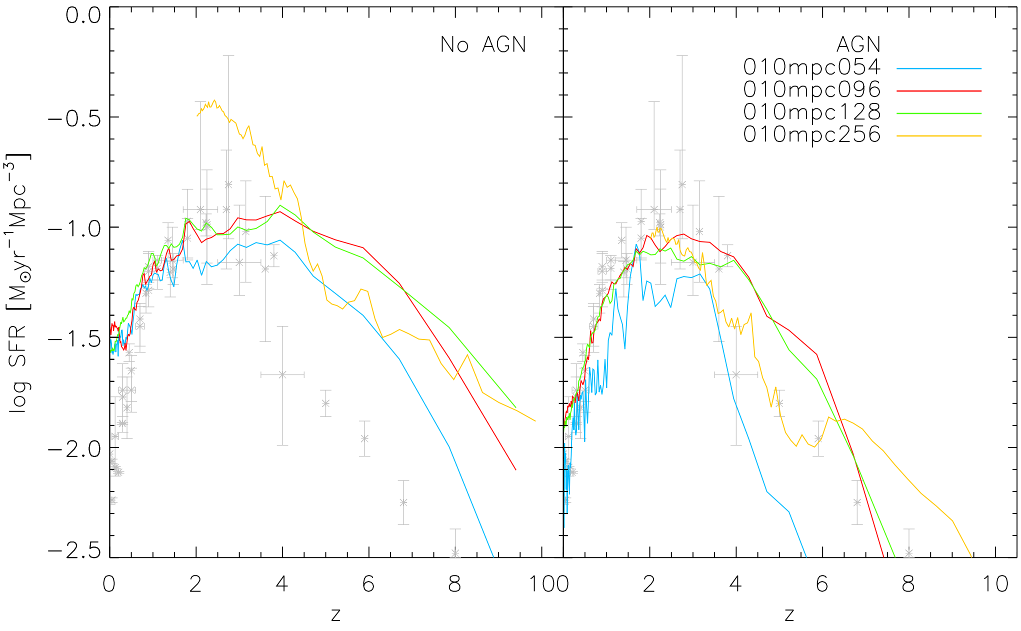

FIGURE 2.9: Cosmic star formation rate history for simulations of various resolutions without (left panel) and with (right panel) AGN feedback. See Fig. 4 for the observational data sources.

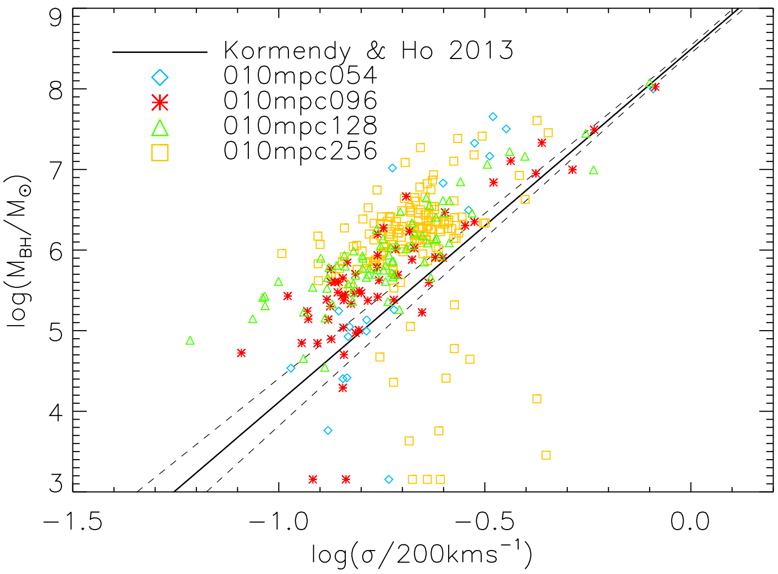

FIGURE 2.10: $M_{\rm BH} - \sigma$ relation at $z = 0$ for simulations of various resolutions, and at $z = 2$ for 010mpc256. The solid and dashed lines show the observed relation and 1σ scatter (Kormendy & Ho, 2013), respectively.

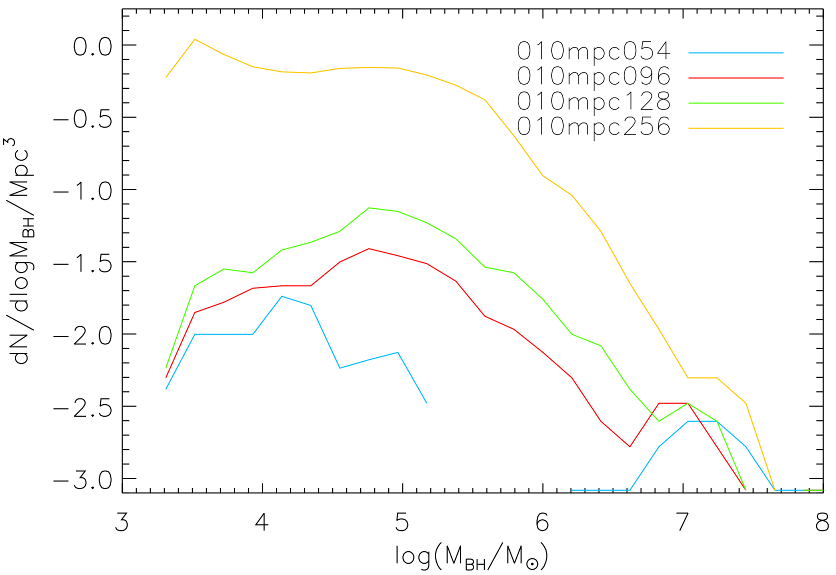

Figure 2.11: Black hole mass function at $z = 2$ for simulations of various resolutions.

those simulations that were run to completion.

As shown in Table 2.3, the stellar mass fractions are almost constant, and the cosmic SFRs at $z \lesssim 2$ do not depend very much on the resolution (Fig. 2.9). However, at high redshifts, some resolution dependencies are seen for both star and BH formation. With higher resolution, it is possible to resolve more high density regions at a given redshift, and therefore cosmic SFRs become higher at high redshift (e.g., Springel & Hernquist, 2003; Booth & Schaye, 2009). Fig. 2.9 shows the cosmic SFRs in our simulations with various resolutions. Without AGN feedback (left panel), higher resolution simulations show higher SFRs at $z \gtrsim 2$. For 010mpc256, supernova feedback also occurs at high redshift, which results in a fluctuating SFR history. The SFR at high redshift could be reduced by adopting a high critical density for star formation (e.g., Guedes et al., 2011), although we do not use density as a star formation criterion in this model (Section 2.3). In our model, increasing $N_{\rm FB}$ with resolution would mitigate against the fluctuations seen. With our AGN model included (right panel), higher resolution simulations have more BHs at a given redshift, which provide more AGN feedback at high redshifts. This is because more high-density regions that satisfy equation (2.91) are resolved, and, with a given $N_{\rm FB}$, more primordial gas particles remain, which satisfy equation (2.92). These resolution effects on star formation act in opposition, and in fact 010mpc96 and 010mpc128 show very similar cosmic SFRs (Fig. 2.9) with the same values of $\rho_{\rm c}$ and $N_{\rm FB}$. However, some resolution dependence is still seen for our highest resolution simulation; 010mpc256 shows higher SFRs at $z > 7$ and lower SFRs at $z = 3 - 5$ than the lower resolution simulations. In this case, convergence in the cosmic SFRs may be obtained with higher $\rho_{\rm c}$ and/or $N_{\rm FB}$. Such a test is left to future works.

Fig. 2.10 shows the $z = 0$ relation between $M_{\rm BH}$ and σ (as well as the $z = 2$

relation for 010mpc256 since little evolution is expected; see Chapter 4 for more details), in which we see that there is good agreement across the simulations above $M_{\rm BH} \sim 10^6 M_\odot$. Below this mass, there is a slight offset, with 010mpc128 and 010mpc256 lying above the observed relation. In higher resolution simulations, gas densities of a given value are resolved earlier, and are more abundant at a given redshift, so BHs are able to form earlier. This then allows BHs more time to grow by gas accretion, as well as providing a larger population of BHs with which to merge. Therefore, both the number and mass fraction of BHs are greater at $z = 0$ in simulations with higher resolution, a trend mirrored at $z = 2$. We see in Fig. 2.11, which shows the BH mass function at $z = 2$, that there is a trend for higher resolution simulations to contain a greater number of BHs. This resolution dependence could be reduced by changing $\rho_{\rm c}$. A lower seed mass will also lower the $z = 0$ mass of BHs so that they lie more closely on the observed $M_{\rm BH} - \sigma$ relation (Fig. 2.10). α would not need changing, since the peak in SFR (Fig. 2.9) is already consistent with observations. Therefore, for higher resolution, high $\rho_{\rm c}$ or lower seed mass may be favoured for the $M_{\rm BH} - \sigma$ relation. We have not studied the effects of $N_{\rm FB}$ on the $M_{\rm BH} - \sigma$ relation.

2.7 Discussion

We have introduced a new AGN model, in which BHs are seeded at local peaks in gas density. Because of this, the growth of BHs is correlated with hierarchical clustering of galaxies. We have demonstrated that our model of the formation and evolution of BHs in cosmological simulations is able to reproduce a number of observations, including the $M_{\rm BH} - \sigma$ relation and the cosmic star formation rate history. The properties of galaxies, such as luminosity functions and colour magnitude relations, will be discussed in future papers. Our model contains four parameters – α, $\epsilon_{\rm f}$, $M_{\rm seed}$, and $\rho_{\rm c}$ – whose effects on the formation and evolution of BHs, stars, and gas have been investigated in Section 2.5. This has allowed us to determine a best set of parameters, in the sense of reproducing observations, with values $\alpha = 1$, $\epsilon_{\rm f} = 0.25$, $M_{\rm seed} = 10^3\,h^{-1} M_\odot$, and $\rho_{\rm c} = 0.1\,h^2 m_{\rm H}\,{\rm cm}^{-3}$.

A seed mass of $10^3 M_\odot$ is several orders of magnitude lower than the value typically used in other cosmological simulations involving the classical scheme of AGN feedback. In principle, it might be possible to obtain a reasonably good fit to observations by simultaneously altering more than one of the model parameters from their fiducial values. Based on the parameter dependencies found in Section 2.5, we ran ~ 50 parameter sets and did not find any better than the fiducial set. We found that with a larger α (25–100) and smaller seed mass ($10^2 M_\odot$), the cosmic SFR history and $M_{\rm BH} - \sigma$ relation are still fairly well reproduced, but the sizes of galaxies tend to be even larger than observed. The required seed mass of $M_{\rm seed} = 10^{2-3} h^{-1} M_\odot$ suggests that the origin of the seed BHs is the deaths of Populations III stars (Section 2.3). Because no signatures of the chemical enrichment from PISNe have yet been observed, we propose the following scenario: the masses of the first stars are

$\lesssim 140 M_{\odot}$ due to fragmentation and suppressed accretion, which explode as core-collapse supernovae. If the accretion is not suppressed, the mass of stellar cores grows beyond $\sim 300 M_{\odot}$, which become our seed BHs.

The value of $\epsilon_{\rm f} = 0.25$ is somewhat higher than has been necessary in earlier studies, which have used $\epsilon_{\rm f}$ in the range 0.05 (Springel et al., 2005; Sijacki et al., 2007; Di Matteo et al., 2008) to 0.15 (Booth & Schaye, 2009) in order to reproduce the observed $M_{\rm BH} - \sigma$ relation, but see also Ragone-Figueroa et al. (2013) who adopt $\epsilon_{\rm f} = 0.2$ or 0.8, depending on the accretion rate. Additionally, observations of massive molecular outflows from the quasar Mrk 231 suggest $0.02 \lesssim \epsilon_{\rm f} \lesssim 0.06$ (Feruglio et al., 2010; Cicone et al., 2012). In our simulations, a constant $\epsilon_{\rm f}$ is applied for all gas at all times. Ultimately, the value of 0.25 found here should be viewed as a rough average used in lieu of a more accurate expression for $\epsilon_{\rm f}$ based on the properties of the gas around BHs. In reality, the extent to which radiation couples to gas will depend on various factors, including the density and metallicity of gas. In addition, we only allow the radiation to affect the thermal energy of the gas; there is no kinetic component, nor do we employ the radiative electromagnetic feedback of Vogelsberger et al. (2013). If the gas is more easily removed from galaxy centres by kinetic coupling, this can reduce the value of $\epsilon_{\rm f}$. However, Di Matteo et al. (2008) argued that the mode of coupling is largely irrelevant as long as the feedback energy is distributed in a volume small compared to that of the galaxy, and in a time shorter than the dynamical time of the galaxy. Indeed, even without kinetic feedback, outflows are seen from massive galaxies in our simulations. In the most massive galaxies, we find that the wind speed is $\gtrsim 100$ km s^{-1} at the edge of galaxies, and can be higher near the centre as observed (e.g., Sturm et al., 2011; Cicone et al., 2012; Maiolino et al., 2012; Veilleux et al., 2013, see also Chapter 6 for a much more detailed study).

That the value of $\epsilon_{\rm f}$ has no bearing on the cosmic star formation history is surprising, as star formation is directly related to the internal energy of gas particles through the rapid cooling condition (equation (2.66)). However, this can be explained by the self-regulation of the BH growth as follows: the simulations F and E1-4 are identical, apart from their value of $\epsilon_{\rm f}$, which means that, to a good approximation, BHs form at the same locations, at the same times, and with the same masses in each. Assuming a power law dependence of $\dot{M}_{\rm BH}$ on $\epsilon_{\rm f}$, we may write

$$\dot{M}_{\rm BH} = k \epsilon_{\rm f}^{\gamma_\epsilon}, \tag{2.100}$$

and calculate γ_ϵ as

$$\gamma_\epsilon = \frac{\log(\overline{\dot{M}}_{\rm BH,1}/\overline{\dot{M}}_{\rm BH,2})}{\log(\epsilon_{\rm f,1}/\epsilon_{\rm f,2})}, \tag{2.101}$$

where $\overline{\dot{M}}_{\rm BH,i}$ denotes the mean BH accretion rate of the simulation with $\epsilon_{\rm f} = \epsilon_{\rm f,i}$. We show γ_ϵ as a function of redshift for pairs of $\epsilon_{\rm f}$ in the left-hand panel of Fig. 2.12. Although there is some scatter, we see that $\gamma_\epsilon \sim -1$ for $z < 4$ (when gas accretion is the dominant growth mode) in all cases. From equation (2.99), we see

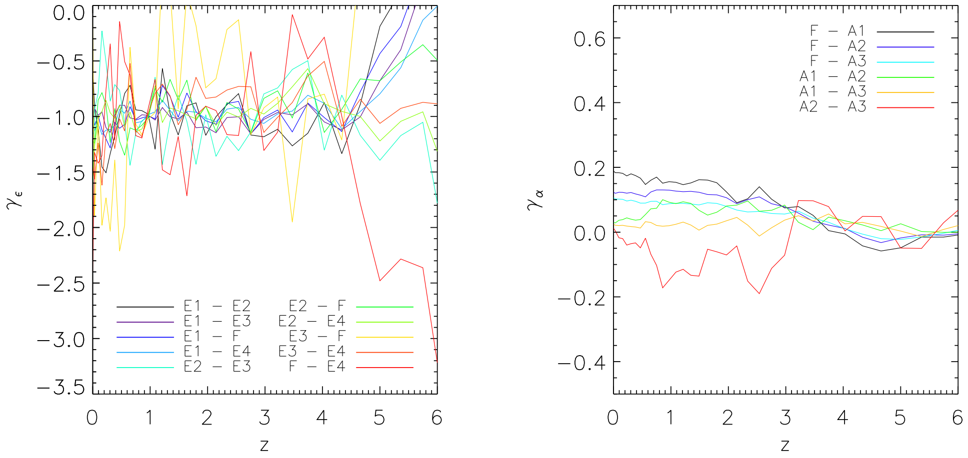

FIGURE 2.12: *Left-hand panel*: Evolution of γ_ϵ (see equations (2.100) and (2.101)) with redshift for all pairings of the simulations F and E1-3. *Right-hand panel*: Evolution of γ_α (see equations (2.102) and (2.103)) with redshift for all pairings of the simulations F and A1-3.

that $\dot{M}_{\rm acc} \propto \epsilon_{\rm f}^{-1}$ implies that $E_{\rm FB}$ is independent of $\epsilon_{\rm f}$, and so that BH growth is self-regulated.

The self-regulated growth also explains the independence of BH mass on the value of α. Again, when and where BHs form is unaffected by the value of α. As before, we assume a power law dependence of $M_{\rm BH}$ on α:

$$M_{\rm BH} = k\alpha^{\gamma_\alpha}, \tag{2.102}$$

and calculate γ_α as

$$\gamma_\alpha = \frac{\log(\overline{M}_{\rm BH,1}/\overline{M}_{\rm BH,2})}{\log(\alpha_1/\alpha_2)}, \tag{2.103}$$

where $\overline{M}_{\rm BH,i}$ denotes the mean BH mass of the simulation with $\alpha = \alpha_{\rm i}$. We show γ_α as a function of redshift for pairs of α in the right-hand panel of Fig. 2.12. It is clear that $\alpha \sim 0$ at all times, and so BH mass is unaffected by α. From equation (2.99), we see that the total energy, E, a BH radiates to gas particles is approximately given by

$$E = \epsilon_{\rm r}\epsilon_{\rm f} M_{\rm acc} c^2, \tag{2.104}$$

$M_{\rm acc}$ being the total accreted gas mass. Since $M_{\rm BH}$ does not depend on the value of α, we can see that E is constant, and hence that the growth is self-regulated.

Our adopted 'best' value for the minimum gas density for BHs to form, $\rho_{\rm c} = 0.1h^2$ $m_{\rm H}\,{\rm cm}^{-3}$, is not intended as a physical density threshold of the gas that would have formed the first BHs in the Universe, because the resolution of our cosmological simulations is insufficient to resolve such small scale physics. Rather, it sets the timescale, for a given resolution, at which BHs start to form as large-scale structure collapses. In higher resolution simulations, a lower value of $\rho_{\rm c}$ causes BHs to form earlier and in greater numbers, as shown in Section 2.6. In the simulations presented in Section 2.6, we apply the same $N_{\rm FB}$ for both supernova and AGN feedback as in Section 2.5, which ensures the same total mass in the feedback region at a given resolution, but results in a smaller region for higher resolution simulations. By adopting a resolution dependent value for $N_{\rm FB}$ such that metals are distributed over the same distance, the number of BHs will be reduced.

A major cause of uncertainty in our model is our prescription for calculating the accretion rate of gas onto BHs. We use the Bondi-Hoyle accretion rate, as in many previous works (e.g. Springel et al., 2005; Di Matteo et al., 2008; Booth & Schaye, 2009). This formulation is for spherical accretion in the Newtonian regime. The angular momentum of infalling gas is ignored, which could, more realistically, cause the gas to settle into a disk around the BH, rather than being accreted by it. Jets may form with a strong magnetic field (Tchekhovskoy et al., 2011), which may help remove angular momentum. Additionally, the gravitational potential felt by the gas is assumed to be dominated by the BH, whereas that of the galaxy will be more important in these simulations. Attempts to address some of these issues have been made; for example, in Power et al. (2011) a two-component 'accretion disk particle' is used that models both a BH and its accretion disk. Gas is accreted onto the disk if it comes within some radius $R_{\rm acc}$ that is of order the gravitational softening length. Anglés-Alcázar et al. (2013), on the other hand, calculate an accretion rate based on angular momentum transport via gravitational torques within the central ~ 1 kpc of galaxies. Such methods require a somewhat higher spatial resolution than in this thesis, and we will leave these to a future study.

2.8 Conclusions

We have presented a new model for the formation of BHs in cosmological simulations, motivated by the first star formation. Black holes are formed from metal free gas of high enough density. They may then grow via both mergers and through gas accretion. In this model, BHs are formed anywhere in the simulation volume with gas satisfying the above criteria. We therefore do not restrict BHs to form only within dark matter haloes, as some previous models have, but still find that most galaxies contain at least one BH by the present. Massive BHs heat the surrounding material, suppressing star formation at the centres of galaxies, and driving galactic winds.

We constrain the parameters of the model by comparing the simulations to observations, and successfully reproduce the BH mass – galaxy mass relation, the cosmic star formation rate history, and the mass – size relation of galaxies. The best model has $\alpha = 1$, $\epsilon_{\rm f} = 0.25$, $M_{\rm seed} = 10^3 h^{-1} M_\odot$, and $\rho_{\rm c} = 0.1 h^2\ m_{\rm H}\,{\rm cm}^{-3}$ (Section 2.5). For high resolution, however, a higher value of critical density for BH formation, $\rho_{\rm c}$, a larger number of feedback neighbours, $N_{\rm FB}$, and/or slightly smaller seed BHs may be favoured (Section 2.6).

The mass with which BHs are seeded is $\sim 10^3\,h^{-1} M_\odot$ in order to match observations fully, though there are sets of parameters with $M_{\rm seed} = 10^2\,h^{-1} M_\odot$ that can reproduce observations fairly well. The required seed mass of $M_{\rm seed} = 10^{2-3}\,h^{-1}M_{\odot}$ suggests that the origin of the seed BHs is the deaths of Population III stars; the masses of the first stars are $\gtrsim 140 M_{\odot}$ due to fragmentation and suppressed accretion, which explode as core-collapse supernovae. If the accretion is not suppressed, the mass of stellar cores grows beyond $300 M_{\odot}$, which become our seed BHs.

We found that BH mass did not depend on the accretion rate modifier, α, and that SFR did not depend on the fraction of radiation that coupled to gas, $\epsilon_{\rm f}$. This suggests that BH growth is self-regulated; the same amount of energy is radiated, or equivalently, the same mass of gas is accreted by BHs regardless of the values of these parameters (Section 2.7).

3

The Properties of Simulated Galaxies at $z = 0$

3.1 Introduction

In Chapter 2, we proposed a new model for AGN feedback in cosmological simulations. With our AGN model, BHs form earlier in our simulations ($z \sim 16$) and with a lower mass ($\sim 10^3 M_\odot$) than previous works ($\sim 10^5 M_\odot$). This means that the effects of AGN feedback are different, especially at high redshift. However, the peak in cosmic SFR density still occurs at $z = 2$, consistent with observations and other theoretical works. Indeed, the majority of stars in galaxies form before feedback from AGN becomes dominant, and so the scaling relations of galaxies are only weakly affected by AGN feedback. We will illustrate this with the mass-metallicity relations (MZR), which is the most stringent constraint on galaxy evolution. The galaxy size–mass relation is more affected, with AGN feedback increasing galaxy effective radius, but is still consistent with observations (see also Dubois et al. (2013) who find that AGN feedback is necessary to match observations).

In this paper, we examine the effects of our AGN feedback model on the chemodynamical evolution of galaxies in a cosmological context. We compare the $z = 0$ properties of galaxies in two cosmological simulations, one with, and one without, AGN with observations, and look in particular at downsizing and galaxy scaling relations. We outline the simulations performed in Section 3.2, as well as describing in more detail three example galaxies that will be used to highlight the differences in the simulations. Our results are presented and discussed in Section 3.3, and we draw our conclusions in Section 3.4.

3.2 The Simulations

In this section, we describe the set-up and large-scale evolution of our simulations, before then describing the properties of three galaxies that will be used for illustrative purposes in Section 3.3 and beyond.

3.2.1 Cosmic Evolution

We present simulations run both with and without the AGN model described in Section 2.3. With AGN feedback included, the fiducial model parameters of Chapter 2 are used, namely $\alpha = 1$, $\epsilon_{\mathrm{f}} = 0.25$, $M_{\mathrm{seed}} = 10^3 h^{-1} M_\odot$, and $\rho_{\mathrm{c}} = 0.1 h^2\, m_{\mathrm{H}}\,\mathrm{cm}^{-3}$. The simulations in this paper are run at the same resolution with identical cosmological initial conditions. We employ a WMAP-9 ΛCDM cosmology (Hinshaw et al., 2013) with $h = 0.70$, $\Omega_{\mathrm{m}} = 0.28$, $\Omega_\Lambda = 0.72$, $\Omega_{\mathrm{b}} = 0.046$, and $\sigma_8 = 0.82$. The initial conditions are in a periodic, comoving, cubic volume 25 h^{-1} Mpc on a side, are chosen to have a central cluster at $z = 0$, and are different from Kobayashi et al. (2007), which corresponds to a typical field of the universe. They contain 240^3 particles of each of dark matter and gas, with masses $M_{\mathrm{DM}} = 7.3 \times 10^7 M_\odot$ and $M_{\mathrm{gas}} = 1.4 \times 10^7 M_\odot$. By $z = 0$ there are approximately 3 per cent more particles in total when AGN feedback is not included due to the formation of star particles. We use gravitational softening lengths of $\epsilon_{\mathrm{DM}} = 2.25 h^{-1}$ kpc and $\epsilon_{\mathrm{gas}} = 1.125 h^{-1}$ kpc for dark matter and gas respectively. The finite volume of the simulation means that we do not necessarily obtain a representative sample of the most massive galaxies, while the low-mass end may be affected by the limited resolution of the simulations. When comparing to observations in the subsequent sections, our simulated galaxies are complete for $9 \lesssim \log M/M_\odot \lesssim 11.4$, $-25.6 \lesssim M_{\mathrm{K}} \lesssim -21$, and $-22.1 \lesssim M_{\mathrm{B}} \lesssim 4(B-V)_0 - 19$, although we compare our simulations to each other across a wider range since their initial conditions are the same.

The redshift evolution of the simulation with AGN is shown in Fig. 3.1, as well as the gas metallicity in the simulation without AGN. In both cases, a rich filamentary structure exists (top row) at high redshift, to which star (second row) and black hole formation is mostly confined. Without AGN, the first star forms at $z \sim 14$ in the region that will subsequently collapse to form the largest cluster in the simulation box. As early as $z = 7$, supernova feedback heats (fourth row) and chemically enriches the gas. This enrichment enhances star formation by allowing the gas to cool more rapidly. The cosmic SFR then peaks at $z \sim 2 - 3$. Supernova feedback causes galactic winds to be produced, which cause the intergalactic medium (IGM) to become enriched by interstellar medium (ISM; sixth row).

With AGN feedback included, BHs start forming from $z > 20$, and prevent stars from forming until $z \sim 11.5$. When these first stars do form, however, they enrich the surrounding gas and inhibit further BH formation. As in the case without AGN, the cosmic SFR peaks at $z \sim 2$, coincident with a broader peak in the BH accretion rate (Fig. 2.3). The BH number density peaks earlier, at $z \sim 5.5$, after which mergers reduce their number. AGN and supernova feedback together produce

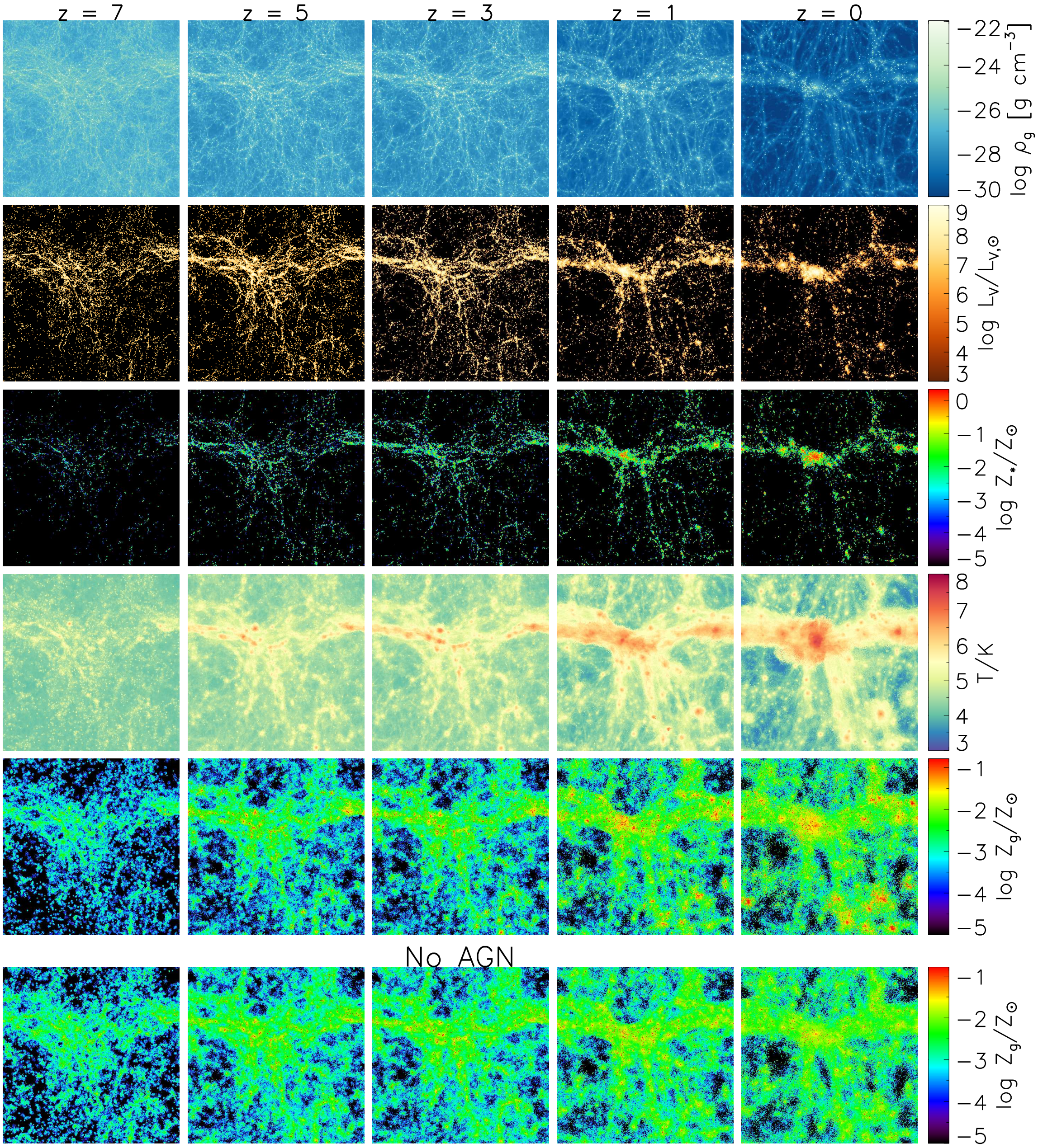

FIGURE 3.1: Evolution of cosmological simulation in $25h^{-1}$ Mpc box with (top 5 rows) and without (final row) AGN feedback included. We show projected gas density on the upper row, rest frame V-band luminosity and stellar metallicity on the second and third, gas temperature on the fourth, and gas metallicity on the final two rows.

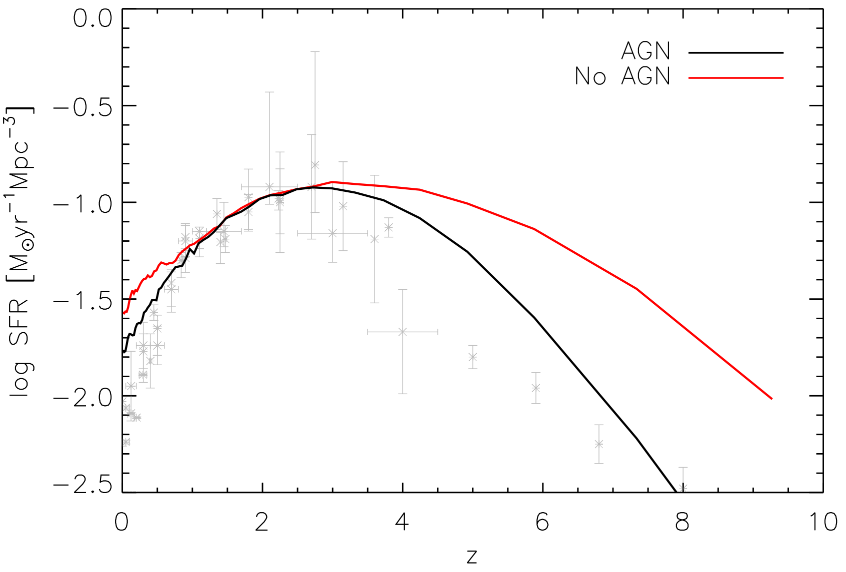

FIGURE 3.2: Cosmic star formation rate density as a function of redshift for the simulations with (black line) and without (red line) AGN feedback. Sources of observational data (grey points) are listed in Section 3.2.1.

stronger galactic winds than supernova feedback alone, and a larger region of the IGM is influenced (fifth row). The largest concentration of stars and BHs is seen in the central cluster of galaxies, with a present total mass of $\sim 10^{14} h^{-1} M_\odot$, and which hosts the most massive black hole in the simulation with a mass of $\sim 2 \times 10^8 h^{-1} M_\odot$.

We show in Fig. 3.2 the cosmic SFR density for the simulations with (black line) and without (red line) AGN feedback. Observational data are plotted in grey, and are taken from Bouwens et al. (2011), Karim et al. (2011), Cucciati et al. (2012), Oesch et al. (2012), Burgarella et al. (2013), Gunawardhana et al. (2013), and Sobral et al. (2013), adjusted to the Kroupa IMF (Bernardi et al., 2010). Both simulations show a peak in SFR of similar magnitude at $z \sim 2 - 3$, in agreement with observations. At higher and lower redshifts, however, the inclusion of AGN significantly reduces the SFR, and the simulated data lie much closer to the observations. At high redshift, although the BHs have not yet grown to be super-massive, gas has not been very much enriched, and so it is unable to cool efficiently. By low redshift, the super-massive BHs are able to accrete a large amount of gas, and provide enough energy to surrounding gas to drive powerful galactic winds.

Table 3.1: $z = 0$ properties of galaxies A, B, and C both with and without AGN feedback. (1) Estimated from core-Sérsic fit. (2) Gas fraction within $R_{\rm e}$, calculated as $f_{\rm g} = M_{\rm g}/(M_{\rm g} + M_* + M_{\rm BH})$. (3) V-band luminosity weighted within $R_{\rm e}$. (4) SFR-weighted within $R_{\rm e}$. Note that there is no star-forming gas in A when AGN is included. (5) Galaxy colour in central $1h^{-1}$ kpc.

Galaxy	M_* $M_\odot$ (1)	M_{200} $h^{-1}M_\odot$	R_{200} h^{-1} kpc	$f_{\rm g}$ (2)	<Age> Gyr (3)	[M/H]$_*$ (3)	[O/H]$_{\rm g}$ (4)	[O/Fe]$_*$ (3)	$(B-V)_0$ (5)	$\log(M_{\rm BH})$ $h^{-1}M_\odot$
A (AGN)	6.8e11	9.5e13	743.2	0.001	9.71	0.23	-	0.18	0.92	8.4
A (No AGN)	1.7e12	9.9e13	752.6	0.03	2.19	0.35	0.39	-0.10	0.41	-
B (AGN)	1.4e11	5.1e12	279.1	0.01	10.09	0.10	0.03	0.20	0.92	7.9
B (No AGN)	3.7e11	6.0e12	295.8	0.05	2.90	0.33	0.41	-0.10	0.37	-
C (AGN)	5.4e9	1.0e11	76.5	0.17	4.79	0.15	0.49	0.05	0.72	5.3
C (No AGN)	4.8e9	1.0e11	77.4	0.22	3.08	0.28	0.35	0.01	0.54	-

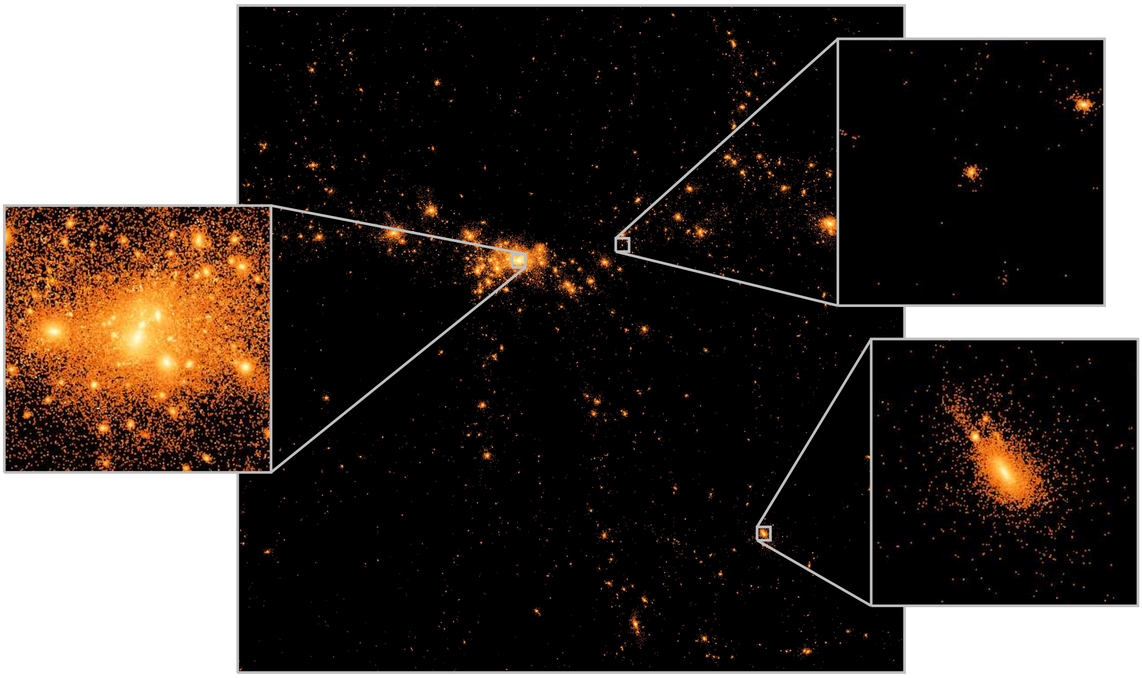

FIGURE 3.3: Integrated V-band luminosity image of the simulation with AGN feedback. The zoom-ins are $400\,h^{-1}$ kpc on a side, and show the locations of galaxies A (left), B (bottom right), and C (top right), as well as their immediate environment in the simulation box ($25\,h^{-1}$ Mpc). See Appendix C for V-band luminosity maps of all present-day simulated galaxies.

3.2.2 Individual Galaxies

Galaxies are identified using a Friend of Friends (FoF) algorithm (Springel et al., 2001), which produces a catalogue of groups of particles whose mass exceeds $32M_{\rm DM}$. For the analysis of properties of a galaxy, only those groups containing at least 50 star particles are used. In the simulation with (without) AGN, 1380 (1009) groups are found by the Friends of Friends algorithm, of which 1125 (742) are classified as galaxies, corresponding to $10^9 \lesssim M_*/M_\odot \lesssim 10^{12}$. These differences are caused by AGN feedback at high redshift; although weak, early feedback from BHs suppresses star formation and low-mass galaxies survive. With AGN feedback included, 957 galaxies contain at least 1 BH.

Galaxy stellar masses and effective radii are estimated by fitting a core-Sérsic profile (Graham et al., 2003; Trujillo et al., 2004) to the surface density. Approximately 80 per cent of galaxies are well fit by such a function, and a further 10 per cent are well fit by a standard Sérsic function. In both cases we restrict the Sérsic index to $n = 4$; this gives a much better fit to our simulated galaxies than with a Sérsic function and varying n as in observations. Galaxies that are not fit by either function tend to be near our resolution limit ($\sim 10^9 M_\odot$) or merging systems, and are excluded from our analysis. Galaxy luminosities are estimated by applying the simple stellar population models of Bruzual & Charlot (2003) to star particles with a Chabrier IMF, which gives very similar results to the Kroupa IMF used in our

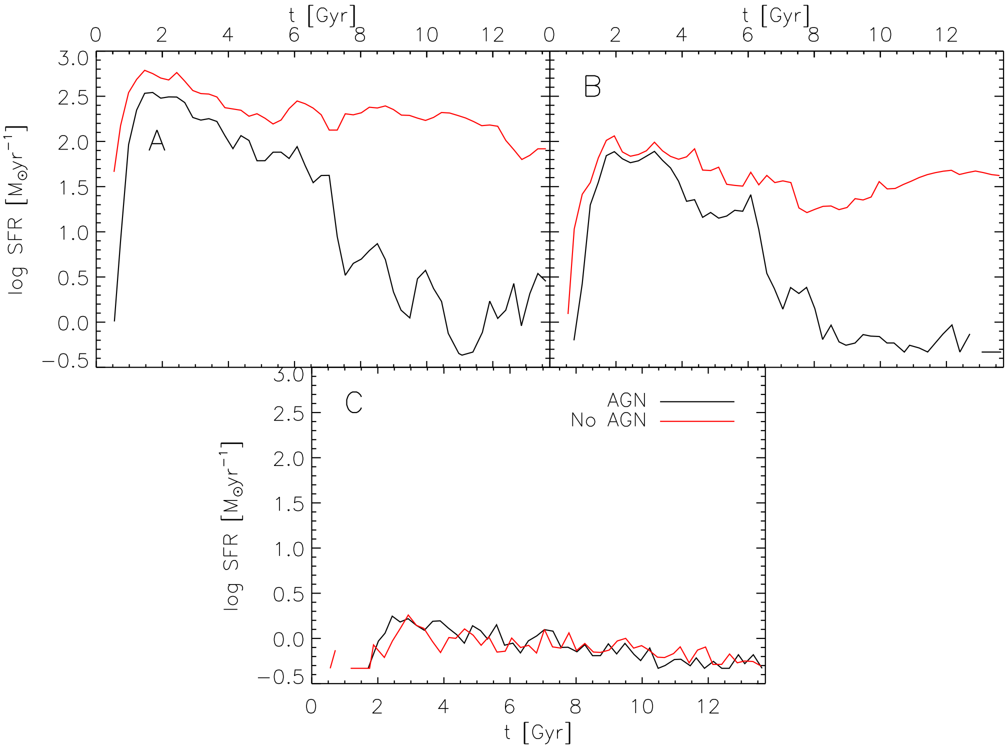

FIGURE 3.4: Star formation rate as a function of time since the Big Bang for the three example galaxies A, B, and C (Section 3.2.2) in the simulations with (black lines), and without (red lines) AGN feedback. See Appendix D for the SFR histories of all present-day simulated galaxies.

simulations.

In Section 3.3 we will highlight the effects of AGN feedback by looking more closely at 3 example galaxies, matched between the runs with and without AGN. These galaxies, which we refer to as A, B, and C, have stellar masses $\sim 10^{12}$, $\sim 10^{11}$, $\sim 10^{9} M_{\odot}$ respectively, evolve in different environments, and are influenced differently by their BHs. We show in Fig. 3.3 images of the three galaxies at $z = 0$ from the simulation with AGN feedback, as well as their locations in the cosmological box of our simulation, colour-coded by integrated V-band luminosity. The global properties of these galaxies are summarized in Table 3.1.

Galaxy A is the most massive galaxy in the simulations, and sits at the centre of the cluster. It experiences a major merger at $z \sim 2$, and numerous minor mergers throughout its life (see Appendix E). With AGN, it hosts the most massive black hole, and AGN-driven outflows are produced intermittently (Chapter 6). AGN feedback heavily suppresses star formation in the centre of A, as shown in the top panel of Fig. 3.4, although a small amount of star formation is ongoing in the outskirts of the galaxy ($\gtrsim 20h^{-1}$ kpc) at $z = 0$ due to minor mergers. As a result, the mass- and luminosity-weighted stellar ages are older, and the stellar mass of A is reduced by a factor of about 2.5. The removal of gas by AGN-driven winds reduces both M_{200} and R_{200}, as well as the present gas fraction of this galaxy. This also changes the distribution of heavy elements in this galaxy; stellar metallicity is slightly lower, though this difference is small enough that the mass-metallicity relations are not affected (Section 3.3.3), and stars show α-enhancement.

Galaxy B is a large field galaxy away from the main cluster (see Fig. 3.3). It undergoes no major mergers, and very few minor ones (see Appendix E). With AGN, an outflow is produced at $z \sim 2$, and by the present, star formation is fully quenched over the whole galaxy by AGN feedback (Fig. 3.4) since, unlike in galaxy A, there is no regular gas supply. There is an enhancement in both gas metallicity and temperature in a wider region of the IGM around B when AGN feedback is included. Its stellar mass is diminished by just over half by $z = 0$, and its gas mass is reduced from $1.5 \times 10^{11} M_\odot$ to $10^{10} M_\odot$, causing its gas fraction to be reduced from 0.13 to 0.03. Both stellar and gas-phase metallicities are lower with AGN feedback, and stars are α-enhanced.

Galaxy C lies on a filament near the main cluster (see Fig. 3.3) and is the smallest of the 3 galaxies. It experiences a single merger at high redshift, but otherwise evolves passively (see Appendix E). AGN feedback has almost no effect on it; from the bottom panel of Fig. 3.4, the star formation rate within this galaxy is similar for the two runs across cosmic time, and the differences are negligible. However, the chemical enrichment of its gas is enhanced with AGN feedback due to external enrichment from the strong, enriched winds generated in more massive galaxies.

3.3 Results

In this section, we present the scaling relations of simulated galaxies in our cosmological simulations, one with the AGN feedback model of Section 2.3 included, and one without. Where applicable, we highlight the effects of AGN feedback by showing how the properties of galaxies A, B, and C (introduced in Section 3.2.2) change.

3.3.1 Luminosity and Stellar Mass Functions

We show in Fig. 3.5 the K-band galaxy luminosity functions for our simulations. In the top panel, our calculated luminosity functions, both with (black line) and without (red line) AGN feedback, are compared to the observational data of Cole et al. (2001, blue triangles) and the Schechter function fit to the data of Huang et al. (2003, green dotted line). For the completeness limit of our simulation $-25.6 < M_\mathrm{K} < -20$, discussed in Section 3.2.1, both simulations show fairly good agreement with observations, though there are more low-luminosity galaxies with AGN feedback (Section 3.2.2), and fewer high-luminosity galaxies, compared to the simulation without AGN. Looking more closely, we see that around the observed value of the Schechter function parameter $M^*_\mathrm{K} \sim -24.3$, both simulations produce very similar results, but are

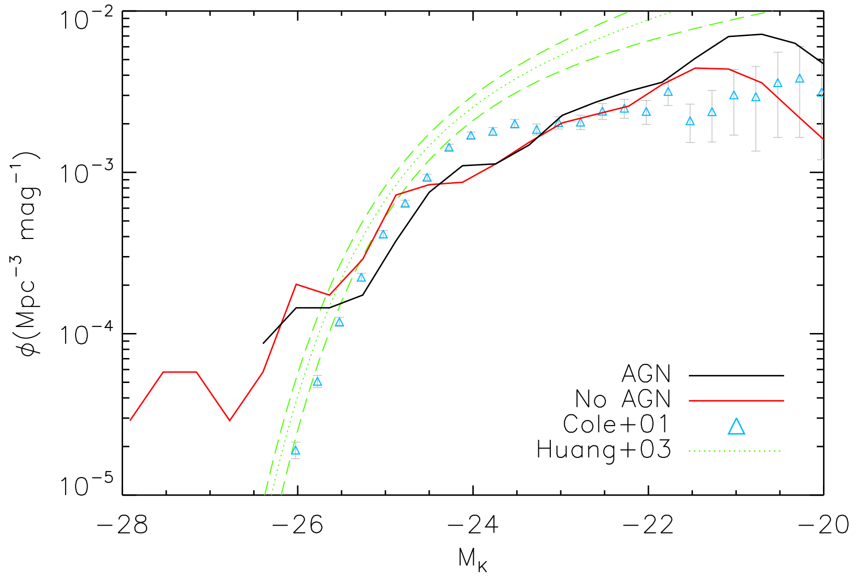

FIGURE 3.5: Luminosity function for the simulations with (black line) and without (red line) AGN feedback included. Our calculated luminosity functions are compared with the observational data of Cole et al. (2001, blue triangles) and the Schechter function fit to the data of Huang et al. (2003, green dotted line).

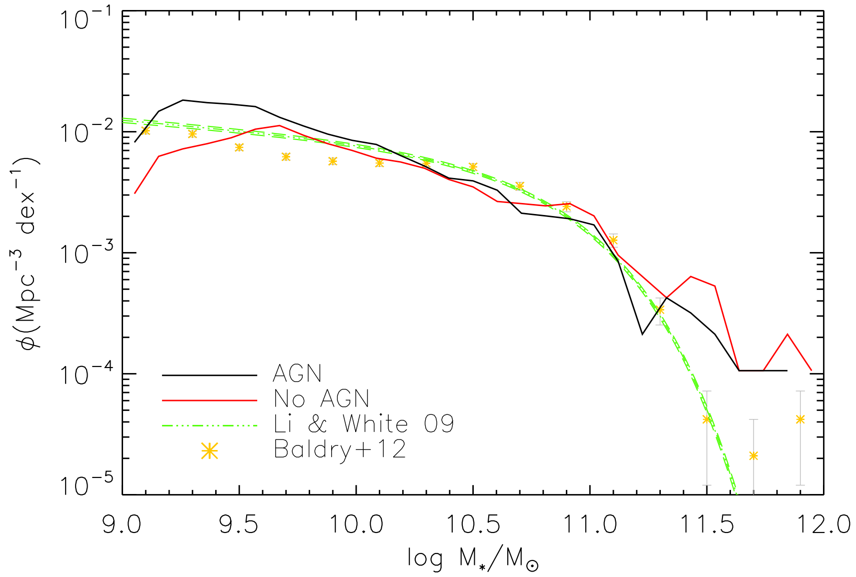

FIGURE 3.6: Stellar mass function for the simulations with (solid black line) and without (dashed red line) AGN feedback. Observational data are from Li & White (2009, green dot-dashed line) who use the SDSS survey, and Baldry et al. (2012, yellow stars) who use GAMA.

slightly lower than observed. This may suggest that supernova, and possibly also AGN, feedback is slightly too strong around this mass in our simulations. The number of the most luminous galaxies ($M_{\rm K} \lesssim -25$) is most affected by AGN feedback, and is decreased by it, but is still slightly higher than in observations. This suggests that a larger simulation box, and possibly stronger AGN feedback at this mass, is required (see Section 3.4 for more discussion). Note that the agreement is not as good as in semi-analytic models (e.g., Bower et al., 2006; Guo et al., 2013; Schaye et al., 2015) where the luminosity function is used to calibrate the parameters of the subgrid physics.

Fig. 3.6 shows the galaxy stellar mass functions for our simulations. Both simulations show good agreement with the data of Li & White (2009) and Baldry et al. (2012) for the completeness limit of our simulations $9 \lesssim \log M/M_\odot \lesssim 11.4$ (Section 3.2.1).The difference between the simulations with and without AGN is not as pronounced at the high-mass end as for the luminosity function, but there are only a small number of galaxies with $\log M/M_\odot > 11.5$. The excess of low-mass galaxies when AGN feedback is included is due to the moderate suppression of SF early in the galaxies' lives (see Section 3.2.2). Despite this, our mass functions show a better fit to the observational data than obtained from other hydrodynamical simulations (e.g., Oppenheimer et al., 2010; Puchwein & Springel, 2013; Khandai et al., 2014, see also Fig. 5 of Schaye et al. (2015)).

3.3.2 Colour – Magnitude Relation

The colours of simulated galaxies are calculated by applying stellar population synthesis spectra (Bruzual & Charlot, 2003) to star particles as a function of age and metallicity. Although the dust content can, in principal, be estimated for simulated galaxies (e.g., De Lucia et al., 2004), the reddening due to dust is not included in this thesis. For this reason, we use optical bands where the bimodality (Kauffmann et al., 2003) is less visible than for UV bands.

Fig. 3.7 shows central $B - V$ colour against B-band magnitude for our simulations; black stars with, and red diamonds without, AGN feedback. Colour is measured within the central $1h^{-1}$ kpc for galaxies, for comparison with the observational data of Bender et al. (1993). Note that integrated colours across the whole galaxy tend to be bluer due to their colour gradient. In both cases, a distinct red sequence ($(B - V)_0 \gtrsim 0.8$), blue cloud ($(B - V)_0 \lesssim 0.8$), and green valley ($(B - V)_0 \sim 0.8$) are seen. The colours of massive galaxies become redder with AGN feedback, and consistent with the observations of Bender et al. (1993, grey triangles). At $M_{\rm B} > -18$, the simulated galaxies are on the extrapolated observed trend, but the number of these galaxies seems to be larger than observed, which may be affected by the resolution of our simulations. This result is very similar to Kobayashi (2005)'s simulations of elliptical galaxies, although AGN feedback is not

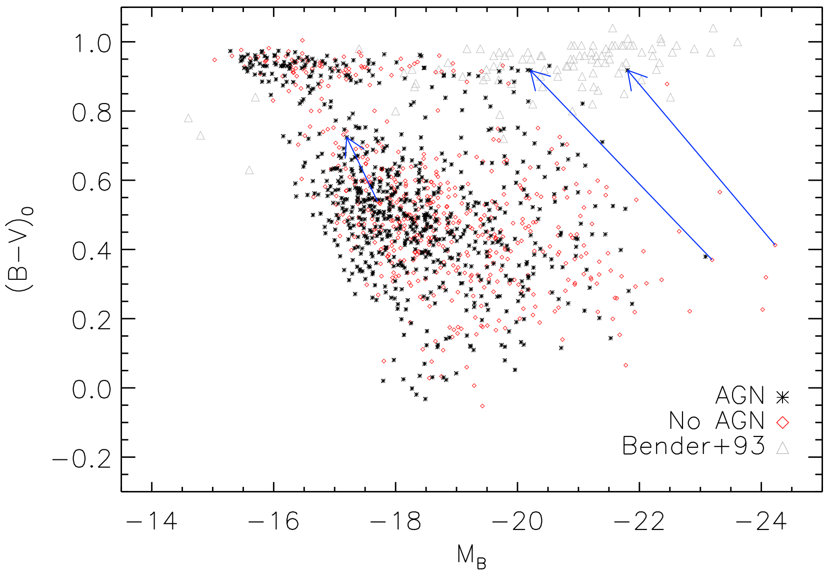

FIGURE 3.7: Colour–magnitude relation for our simulated galaxies with (black stars) and without (red diamonds) AGN feedback. Colours are measured within the central $1h^{-1}$ kpc. Arrows show the motion of galaxies A, B, and C through the colour–magnitude plane when AGN feedback is included. Observational data (grey triangles) are taken from Bender et al. (1993).

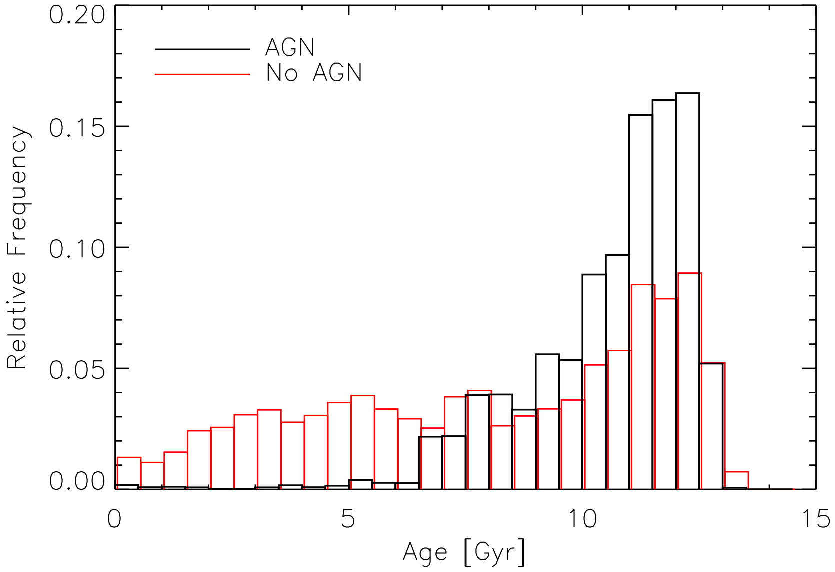

FIGURE 3.8: Histograms of stellar age in the largest galaxy (A) in the simulation with (black) and without (red) AGN feedback.

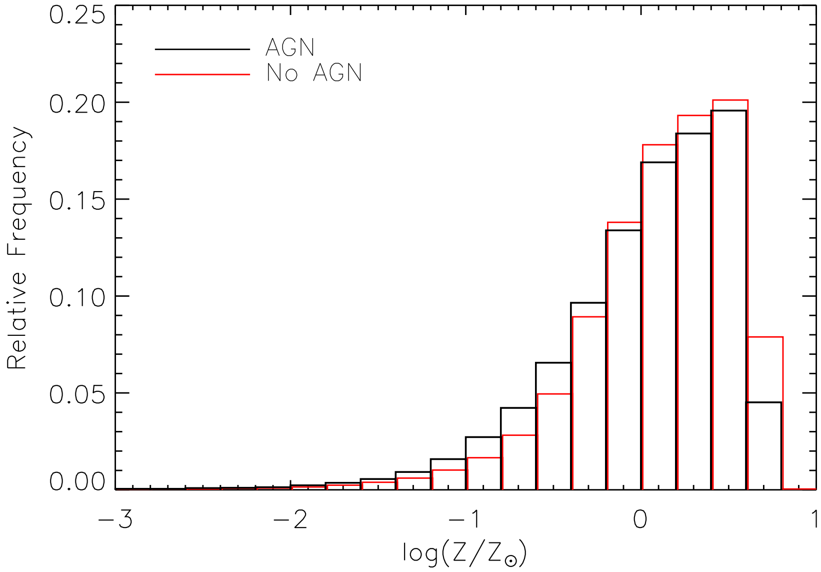

FIGURE 3.9: Histograms of stellar metallicity in the largest galaxy (A) in the simulation with (black) and without (red) AGN feedback.

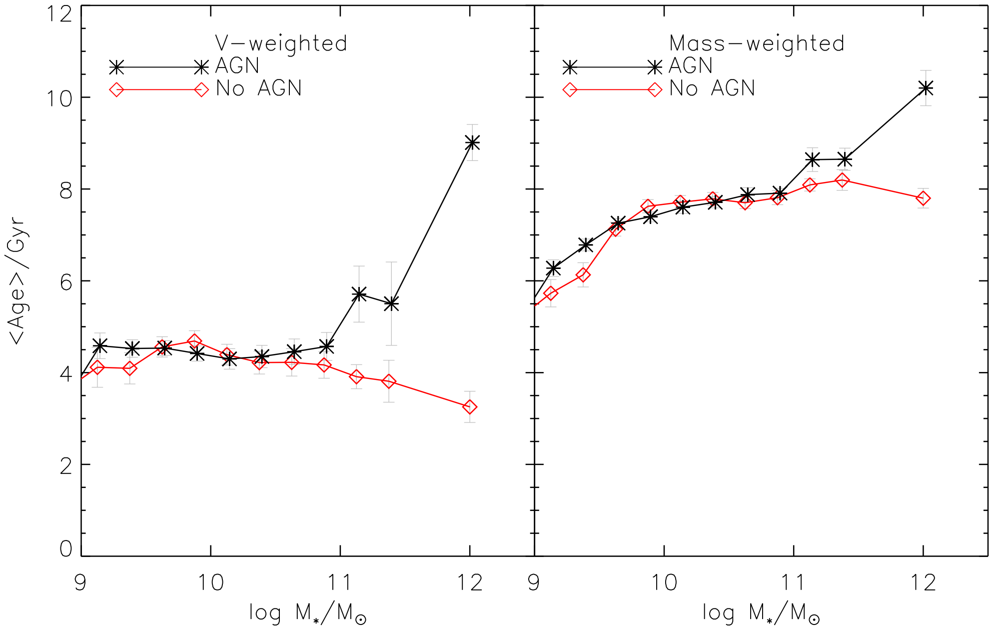

FIGURE 3.10: Mean V-band luminosity-weighted (left panel) and mass-weighted (right panel) ages of galaxies as a function of stellar mass. Error bars show the standard error on the mean. Black stars denote the simulation with AGN feedback, and the red diamonds without.

included there.

The movement of galaxies A, B, and C through the colour-magnitude plane is shown by the arrows. Galaxy A becomes much redder and less luminous, with AGN. Due to the significant reduction in star formation at low redshift (as shown in the top panel of Fig. 3.4), and the dominance of very old stars (>10 Gyr) in the age distribution (Fig. 3.8), this galaxy moves onto the red sequence when AGN is included. Most of the young stars form in the outer regions of the galaxy as a result of mergers with gas-rich satellites. Fig. 3.9 shows the metallicity distribution of this galaxy, which remains mostly unchanged with the inclusion of AGN, except for the most metal-rich bin. The mass-weighted metallicity is not changed, but the luminosity-weighted metallicity is slightly decreased with AGN, and does not help in making colours redder. If star formation is enhanced by AGN (e.g., Silk, 2013), the metallicity, and thus colour, could be larger.

Galaxy B also sees a significant reduction in star formation at late times when AGN feedback is included, to the extent that, by $z = 0$, star formation has been shut off almost entirely (Fig. 3.4). Unlike in A, there are no significant mergers to provide gas, and so star formation almost totally stops once the BH has heated or removed the gas from the galaxy. This allows B to move onto the red sequence. In galaxy C, the BH grows to only $2 \times 10^5 h^{-1} M_{\odot}$, and is not able to significantly affect star formation or colour.

Fig. 3.10 provides another representation of the age difference. More massive galaxies tend to be older, and in particular those with $\log M_*/M_{\odot} \gtrsim 11$ are older when AGN feedback is included. This difference at $\log M_*/M_{\odot} \gtrsim 11$ is more pronounced for luminosity-weighted ages (left panel). This AGN effect is in keeping with the findings of Croton et al. (2006), but their galaxies were systematically older than our mass-weighted ages (right panel), which may be due to their cosmic SFR peaking at $z \sim 4$.

3.3.3 Mass–Metallicity Relation

We show in the previous section that the stellar metallicity distribution in the most massive galaxy was not much affected by the inclusion of AGN (Fig. 3.9). We now show, in the left panel of Fig. 3.11, the stellar mass–metallicity relation (MZR) for galaxies in the simulations with and without AGN. In order to compare with observations of optical absorption lines, we show the V-band luminosity-weighted stellar metallicity measured within the central $15h^{-1}$ kpc of each galaxy. We note that, due to the metallicity gradient within galaxies, slightly higher values of $[\mathrm{M/H}]_*$ are obtained with a smaller radius, but this effect is much smaller than the scatter in the simulated relation. There is no significant change in the MZR between the two simulations. This is because AGN feedback quenches star formation most efficiently at low redshift, after the peak of star formation and chemical enrichment. The simulated galaxies are in excellent agreement with the observations of Thomas et al. (2005), with $[\mathrm{M/H}]_* \sim 0.2$ at $M_* \sim 10^{11} M_{\odot}$. The scatter of the simulations is also comparable to that of observations. Note that Gallazzi et al. (2005)'s MZR of

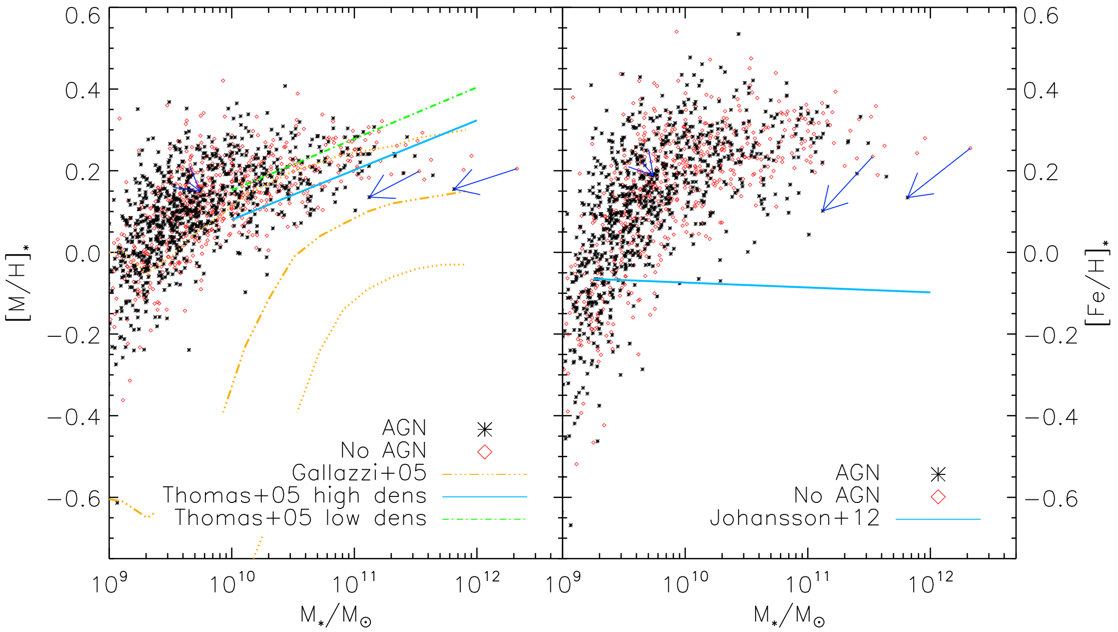

Figure 3.11: Stellar mass metallicity relation for simulations with (black stars) and without (red diamonds) AGN feedback. Left-hand panel: V-band luminosity-weighted total metallicity in $15h^{-1}$ kpc. Observational data are taken from Thomas et al. (2005, solid blue and dashed green lines), and Gallazzi et al. (2005, dot-dashed yellow line; scatter indicated by dotted lines). Right-hand panel: V-band luminosity-weighted iron abundances in $15h^{-1}$ kpc. The observed relation of Johansson et al. (2012) is also shown by the solid line. Arrows show the movement of galaxies A, B, and C through the MZR when AGN feedback is included.

SDSS galaxies gives systematically lower metallicities at all masses, and even lower metallicities below $M_* \sim 10^{10} M_\odot$. Although these observations are subject to large scatter, most of our simulated galaxies lie above this MZR.

In the right panel of Fig. 3.11, we show the stellar mass–iron abundance relation. A stellar mass–iron abundance relation is seen in our simulations because, although there is less SN Ia enrichment in massive galaxies (as we show in the [α/Fe] ratios of the following section), half of iron is produced from core-collapse supernovae, and thus the iron abundance also increases for massive galaxies. We see that this relation mirrors closely the MZR in the left panel, albeit with greater scatter. However, there is no $[\mathrm{Fe/H}]_*$–M_* relation in Johansson et al. (2012)'s analysis of SDSS data, which may be due to the uncertainties in measuring elemental abundances from integrated spectra.

The slope of the MZR of our simulations is almost the same as in Kobayashi et al. (2007), but there is a systematic offset. This is because the Kroupa IMF is used in this paper, rather than the Salpeter IMF in Kobayashi et al. (2007). Although the slope of massive stars is very similar between these IMFs, the difference for low-mass stars changes the normalization, which changes the net yields from $0.6Z_\odot$ to $1Z_\odot$ (Kobayashi et al., 2011a). The slope of the MZR is generated by the mass-dependent

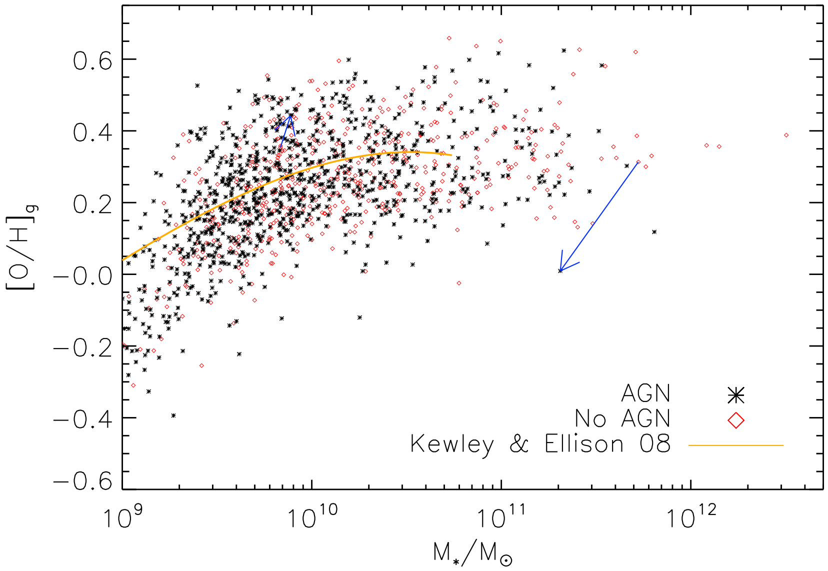

Figure 3.12: Gas phase mass–metallicity relation. SFR-weighted gas metallicity for the simulations with (black stars) and without (red diamonds) AGN feedback. The solid line shows the SDSS observations, taken from Kewley & Ellison (2008) with Kewley & Dopita (2002)'s method, and arrows show how galaxies B and C move through the MZR when AGN feedback is included (there is no star-forming gas in A at $z = 0$ when AGN feedback is included). All metallicities are measured within $15h^{-1}$ kpc of the galactic centre.

galactic winds (Kobayashi et al., 2007), which is also the case in this paper.

Arrows denote the movement of galaxies A, B, and C through the MZR. Galaxies A and B, in which star formation is efficiently quenched, move down the observed relation to lower stellar mass and slightly lower (~ 0.1 dex) metallicity. Galaxy C, on which the effect of AGN feedback is minimal, moves only very slightly in either stellar mass or metallicity.

We show also, in Fig. 3.12, the gas-phase MZR, using SFR-weighted oxygen abundances for comparison with observations that are estimated from emission lines. We again compare the simulations with and without AGN, and include all of the gas in the central $15h^{-1}$ kpc of each galaxy. As with the stellar MZR, there is no significant difference between these simulations. The simulated galaxies are consistent with SDSS observations, taken from Kewley & Ellison (2008) with Kewley & Dopita (2002)'s method (shown as the solid line), but there is much greater scatter than observed. The scatter is also greater than has been found in other simulations (e.g. Davé et al., 2011), though the adopted models differ both in their nucleosynthesis yields and the fact that our model includes feedback from AGN.

The movement of B and C through the gas-phase MZR is within the scatter, and is more complicated. As well as influencing the enrichment history of galaxies, AGN feedback also drives galactic winds from the most massive galaxies. This alters the

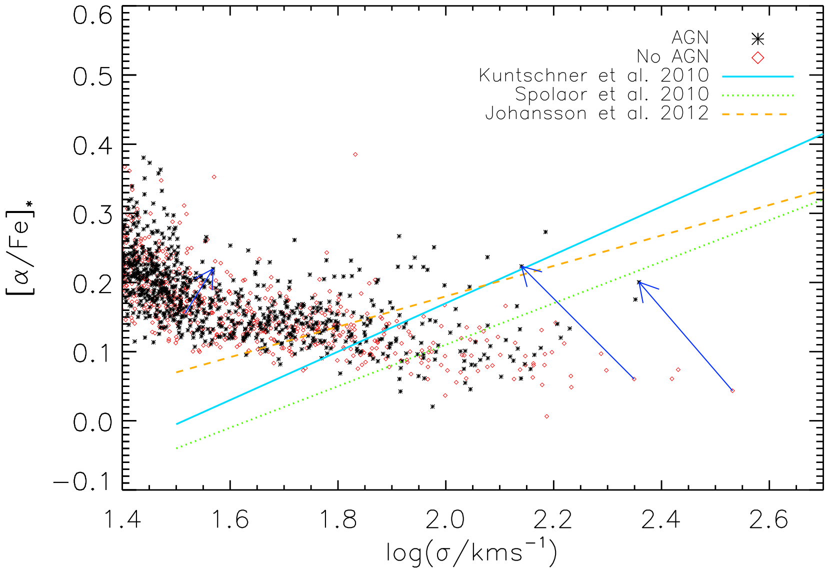

FIGURE 3.13: $[\alpha/\mathrm{Fe}]$–σ relation for our simulations with (black stars) and without (red diamonds) AGN feedback. Arrows denote the movement of galaxies A, B, and C through the $[\alpha/\mathrm{Fe}]$–σ relation when AGN feedback is included. Observational data from Kuntschner et al. (2010, solid blue line), Spolaor et al. (2010, dotted green line), and Johansson et al. (2012, orange dashed line) are also shown. V-band luminosity-weighted [O/Fe] is measured within 1 effective radius for the simulated galaxies.

metallicity of both the ISM and IGM compared to the case without AGN (Fig. 3.1). Consequently, there is no trend on the movement of our example galaxies (note that there is no star-forming gas in galaxy A at $z = 0$, and so it has no arrow in Fig. 3.12).

3.3.4 $[\alpha/\mathrm{Fe}]$ - Velocity Dispersion Relation

The ratio of α-elements to iron abundances gives information about the star formation timescale of a galaxy (e.g., Kobayashi & Nomoto, 2009). α-elements are mostly produced by core-collapse supernovae with a short timescale (~Myr), while iron-peak elements are produced more by SNe Ia on longer timescales (~Gyr). Therefore, at the early stages of galaxy formation, only core-collapse supernovae contribute to the chemical enrichment of the galaxy, leading to a higher α/Fe ratio relative to the solar abundance. At later stages, due to the delayed iron production by SNe Ia, $[\alpha/\mathrm{Fe}]$ decreases as a function of time. The timescale of SNe Ia is an important issue, and depends on the progenitor model of SNe Ia; we take the best theoretical model that reproduces the observed $[\alpha/\mathrm{Fe}]$–[Fe/H] relation in the Milky Way Galaxy (Section 2.2.4).

Fig. 3.13 shows the $[\alpha/\mathrm{Fe}]$–σ relation for galaxies in our simulations with and

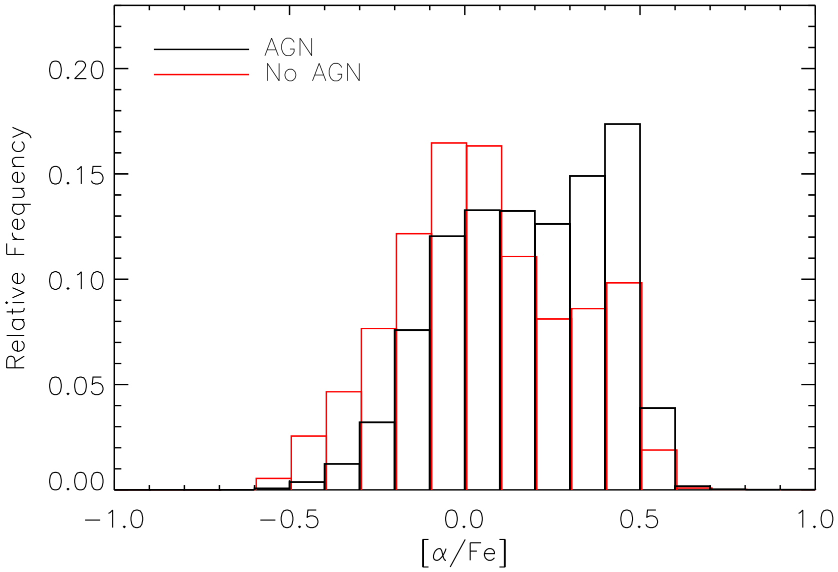

FIGURE 3.14: Histograms of [α/Fe] in the largest galaxy (A) in the simulation with (black line) and without (red line) AGN feedback.

without AGN feedback. [α/Fe] is measured, V-band luminosity-weighted, within the central effective radius of a galaxy. Velocity dispersion, σ, is also measured within $1R_\mathrm{e}$ of the centre. Without AGN, star formation takes place longer in more massive galaxies because of their deep potential well, and thus [α/Fe] is lower for more massive galaxies, which is totally opposite to the observed relations. This was also the case in Kobayashi et al. (2007), where AGN was not included. With AGN, it is possible to quench the recent star formation in massive galaxies. Although the effects of AGN feedback depend on environment, on average AGN feedback is more effective at quenching star formation in more massive galaxies. These galaxies are made up of older stellar populations than their counterparts without AGN, as can be seen in Fig. 3.10 (and is shown explicitly for the most massive galaxy in Fig. 3.8). Since star formation is most suppressed at low redshift, the majority of stars formed from gas that had not been as enriched with iron as in the case without AGN. As a result, more massive galaxies tend to have higher values of [α/Fe] when BHs are included; this is shown explicitly for galaxy A in Fig. 3.14. The movement of galaxies A and B, in which AGN feedback is strong, in the [α/Fe]–σ plane also illustrate this, while C moves very little, since its star formation is not affected much.

Observational data show a tight relation between [α/Fe] and galaxy mass for both central values (Thomas et al., 2003; Johansson et al., 2012) and values within R_e (Kuntschner et al., 2010; Spolaor et al., 2010), although the slope and absolute values depend on the analysis of the observed absorption lines. The aperture effect should be negligible as the observed radial gradient of [α/Fe] is very small.

When AGN feedback is included, a number of galaxies move towards the observed

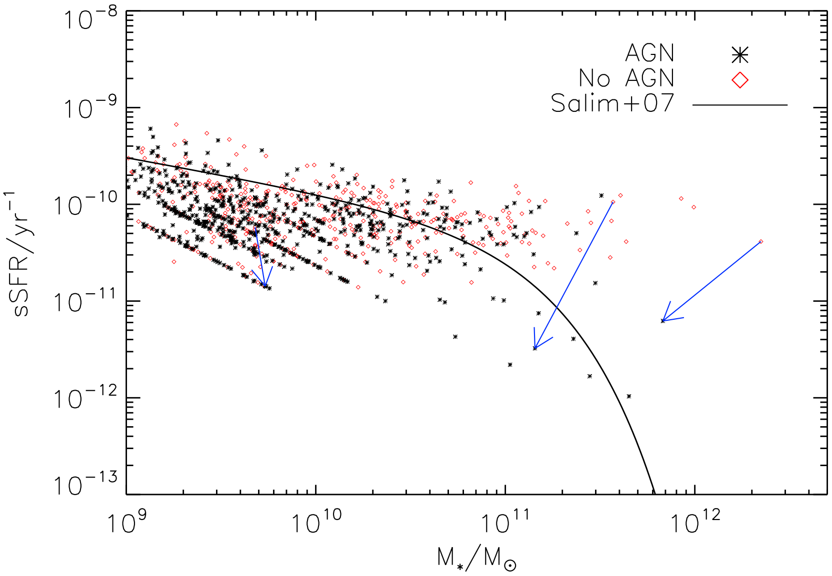

FIGURE 3.15: Specific star formation rate against stellar mass for the simulations with (black stars) and without (red diamonds) AGN feedback. Arrows show the effect of AGN feedback on galaxies A, B, and C. The fit to observational data by Salim et al. (2007) is shown by the solid black line.

relations for early-type galaxies (Kuntschner et al., 2010; Spolaor et al., 2010; Johansson et al., 2012, note that all simulated galaxies are displayed). For $\log\sigma \gtrsim 2.1$, the relation is reversed when AGN is included, more in keeping with observations. However, the scatter of the simulations is still larger than observed. An improved model of AGN feedback may be required, or other possibilities have been discussed in Kobayashi (2005), including (i) IMF, (ii) nucleosynthesis yields, (iii) binary fraction, and (iv) selective mass loss.

The $[\alpha/\mathrm{Fe}]$–σ relation was also shown with semi-analytic models with AGN feedback in Arrigoni et al. (2010) and Gargiulo et al. (2014), both with a top-heavy IMF, and in Calura & Menci (2009) with a variable IMF. Yates et al. (2013) also requires modification of the SN Ia model. However, our results suggest that the $[\alpha/\mathrm{Fe}]$–σ relation can basically be reproduced with our AGN feedback and standard stellar physics (IMF, binary fraction, and SN Ia model).

3.3.5 Specific Star Formation Rate

Finally, in Fig. 3.15 we show the relationship between specific SFR (sSFR) and stellar mass for our simulated galaxies. In both simulations, we see a trend for more massive galaxies to have lower sSFR, which is caused by supernova feedback. This is in qualitative agreement with observations (e.g. Salim et al., 2007; Ciambur et al., 2013). With AGN feedback included, the most massive galaxies, such as A and B, show significant reduction in sSFR. Smaller galaxies are less affected - for example, C moves very little in the sSFR–M_* plane.

Both observations and semi-analytic modelling (Ciambur et al., 2013) find a bimodal distribution of sSFR at $z = 0$, corresponding to low-mass galaxies with ongoing star formation, and quenched massive galaxies. Our results do not show such a distinction, which may be because there is only a small number of galaxies with $\log M_*/M_\odot > 11$ in our simulation box, and because the sSFR of $\lesssim 10^{-10}$ yr^{-1} in less-massive galaxies ($\sim 10^{10} M_\odot$) are affected by the resolution of our simulations (linear features in Fig. 3.15).

3.4 Conclusions

We have shown the effects of feedback from AGN on galaxy evolution using two cosmological hydrodynamical simulations, whose only difference is whether AGN feedback is included. In our AGN model, black holes originate from Population III stars, in contrast to the merging origin of previous works, and grow via mergers and gas accretion. Cosmic SFRs are greatly reduced at both high redshift ($z \gtrsim 3$) and low redshift ($z \lesssim 1$; Fig. 3.2) with AGN feedback. Since the black hole mass–galaxy mass relation is reproduced, massive galaxies host massive BHs. These produce AGN-driven winds and quench the star formation there, causing them to be less massive, less compact, and redder by $z = 0$ than their counterparts without AGN. On the other hand, smaller galaxies do not host a super-massive BH and their star formation history is affected very little, but can get external enrichment from nearby AGN, depending on environment. Nevertheless, galaxy mass–metallicity relations are not affected much since most stars form before AGN feedback becomes dominant. The [α/Fe] ratio of stellar populations is higher for massive galaxies due to their shorter star formation timescale, without modifying stellar physics (i.e., IMF, nucleosynthesis yields, SN Ia progenitors, and binary fraction). Feedback from AGN plays an essential role in galaxy formation, namely in reproducing downsizing phenomena such as the colour-magnitude relation (Fig. 3.7), specific star formation rates (Fig. 3.15), and the α enhancement in early type galaxies (Fig. 3.13).

Although our simulated galaxies are in better agreement with observations, there are still some mismatches seen, including: the luminosity function overpredicts the number of the most luminous galaxies; and the [α/Fe]–σ relation shows a larger scatter than observed. These suggest stronger feedback to suppress star formation at low redshift ($z \lesssim 0.5$; Fig. 3.2). This cannot be achieved simply by changing the parameters of BH physics in our model, as these were chosen in Chapter 2 to provide the best reproduction of observational constraints: the cosmic SFR; M_{BH}–σ relation; and galaxy size–mass relation. There may be room for improvement by simultaneously changing the number of feedback neighbour particles, as discussed in detail in Section 2.7. Alternatively, including smaller scale physics of AGN, kinetic feedback from jets, and induced star formation may be required, which will be investigated in future works.

Furthermore, our results must be viewed in the context that our simulation volumes are not cosmologically representative, and we focus on a cluster of galaxies in which differences caused by AGN are expected to be more prominent. The finite size limits the number of galaxies that exist by $z = 0$, especially at the high mass end, which directly leads to the mass and luminosity functions derived from our simulations being much less smooth than those from observations. The simulation box is, however, large enough for the galaxy mass function to be well sampled around the observed value of $\log M^*/M_\odot \sim 10.6$.

The box size also fundamentally limits the largest scales we can probe; our simulations allow for wavenumbers $k \gtrsim 0.2h$ Mpc^{-1}, while the matter power spectrum obtained from observations peaks at $k \sim 0.02h$ Mpc^{-1}. The influence of structures on these scales, which lie 'outside' our simulation box, through their gravity or gas reservoirs, is therefore not included.

4

Galaxy Properties Across Cosmic Time

4.1 Introduction

In Chapter 3, we introduced a new pair of simulations, one run with the model introduced in Chapter 2, the other identical but for its omission of AGN feedback. We showed how the final states of these simulations changed due to the action of AGN feedback by examining galaxy scaling relations, and found that it is essential in order to better match observed downsizing phenomena. Despite the parameterization of small-scale physics due to the finite numerical resolution, our fiducial simulation gives good agreement with various physical properties of present-day galaxies. In this chapter, using these simulations, we predict the physical properties of galaxies in the past. We show: the galaxy stellar mass function and the K- and B-band luminosity functions (Section 4.2.1); the M_{BH}–σ relation (Section 4.2.2); the stellar and gas-phase mass–metallicity relations (Section 4.2.3); and the star formation main sequence (Section 4.2.5) between $z = 0$ and $z = 4$. We compare the simulations to observations where available; all galaxy masses are converted to a Kroupa IMF, unless a Chabrier IMF was used since they give very similar values. Additionally, as in Chapter 3, we show galaxies A, B, and C, traced back through the simulation. In this chapter, we aim to provide predictions that can be directly compared with ongoing and future observational surveys. Since small-scale physics such as SF, SNe, and AGN may not be fully captured by our models, our predictions may not match with some available observations. However, we do not aim here to tune our simulations to match them at this stage; this can be achieved in future work.

4.2 Results

4.2.1 Mass and Luminosity Functions

We show in Fig. 4.1 the evolution of the galaxy stellar mass function from $z = 0 - 4$. In the upper-rightmost panel, we show the simulated mass functions of the two simulations at a range of redshifts ($z = 0, 0.5, 1, 2, 3$, and 4). At all redshifts, there are fewer high-mass galaxies when AGN feedback is included, which is easily understood due to the suppression of star formation (Section 3.2). There are more low-mass galaxies with AGN feedback at all but the highest redshift. This is due to the suppression of star formation in low-mass galaxies early in their lives by relatively weak feedback from BHs. The AGN feedback is insufficient to disrupt the galaxies, but since there is also less star formation, energy injection from SNe is also less and the galaxies are able to survive. The excess of small galaxies could be due to the limited simulation volume; the initial conditions produce a cluster of galaxies that is not cosmologically representative, producing more sites for galaxy formation than might be expected in a random volume of this size. A similar phenomenon has also been seen in other simulations (e.g., Oppenheimer & Davé, 2006; Davé et al., 2011; Hirschmann et al., 2014), where it was attributed to the inadequacy of the model for the production of stellar winds. It may therefore be the case that our prescription for stellar feedback needs altering, or that BHs are exerting too much influence on the early stages of these galaxies due to our relatively simplistic model. From $z = 4 - 2$, there is some evolution in ϕ^*, and there is strong evolution in M^* at all epochs. These trends are opposite to the observed strong evolution in ϕ^* and relative constancy of M^* (e.g., Pérez-González et al., 2008; Ilbert et al., 2013; Tomczak et al., 2014), but similar to the semi-analytic simulations of Guo et al. (2011) and Guo et al. (2013) who also find that low-mass galaxies form too early compared to observations.

As was discussed in Chapter 3, at the present, the simulated mass function agrees fairly well with observational data of Pérez-González et al. (2008), Li & White (2009), and Baldry et al. (2012) except around the observed value of M^* (see Section 3.3.1; also note that better agreement is obtained by adopting $M_* = M_{\mathrm{FoF}}$ (Appendix B)). This is also true at $z = 0.5$, where we compare with the observational data of Pérez-González et al. (2008), Ilbert et al. (2013), Muzzin et al. (2013), and Tomczak et al. (2014). There is better agreement with the observed high-mass end at this redshift than $z = 0$, but the low-mass slope is still too steep. At $z = 1$, both simulations, particularly the one that includes AGN feedback, underpredict the number of M^* galaxies and overpredict the abundance of low-mass galaxies ($M_* \lesssim 10^{10} M_\odot$). The discrepancy at low masses is even more pronounced at $z = 2$ compared with the observations of Marchesini et al. (2009) and Tomczak et al. (2014); the observed normalization, ϕ^*, decreases by ~ 0.5 dex between $z = 1$ and 2, while the simulated value remains unchanged. The high-mass end, on the other hand, is well-reproduced, especially by the simulation without AGN feedback. This is true also at $z = 3$, although there is greater scatter between different observational

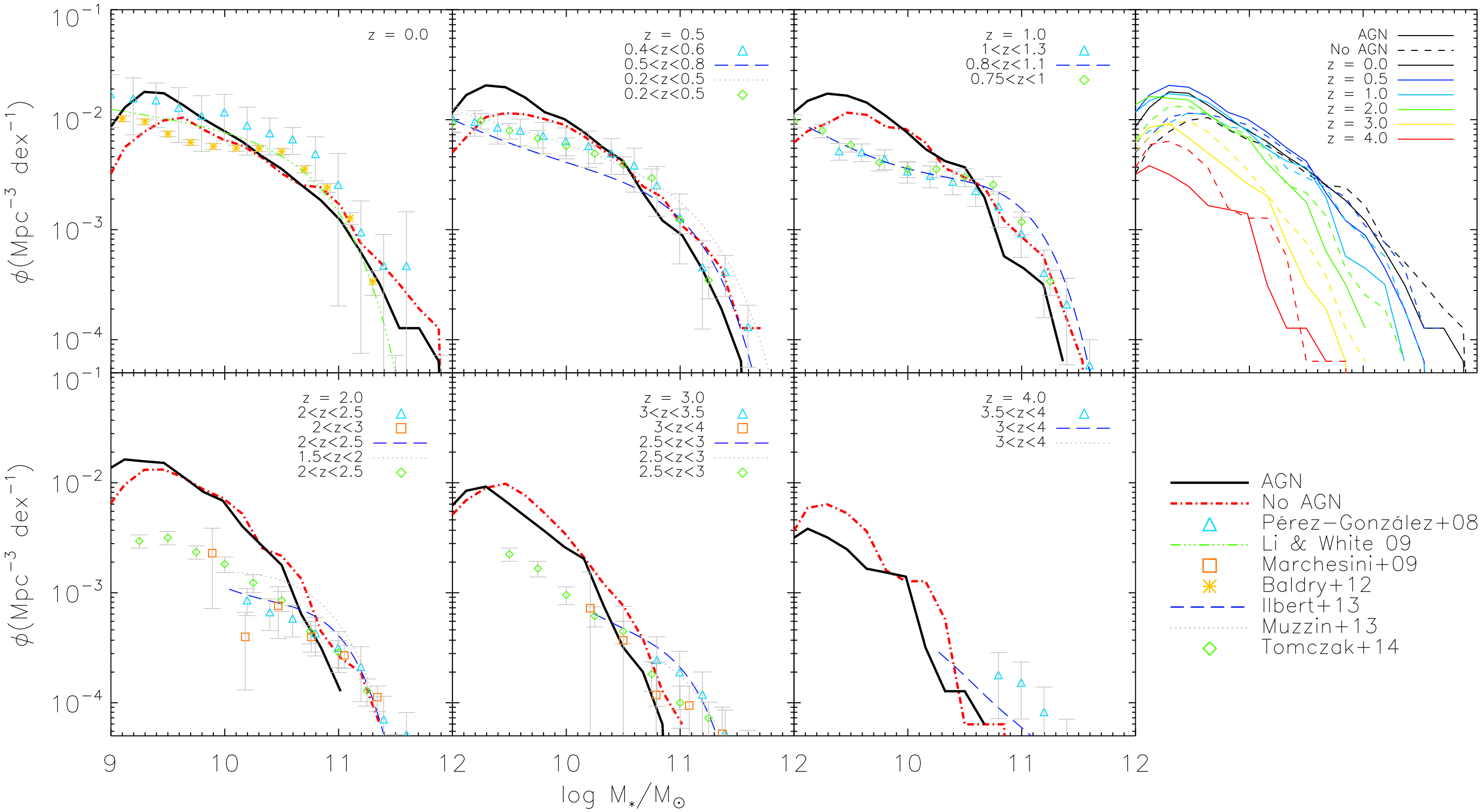

FIGURE 4.1: Evolution of the galaxy stellar mass function. Simulated data are shown as the solid black and red dot-dashed lines (with and without AGN respectively). The observational data from Pérez-González et al. (2008), Marchesini et al. (2009), Baldry et al. (2012), and Tomczak et al. (2014) are shown, as well as the Schechter function fits of Li & White (2009), Ilbert et al. (2013), and Muzzin et al. (2013).

Table 4.1: Fitted parameters to equations (4.1) and (4.2), which describe the redshift evolution of the luminosity function, from Caputi et al. (2006) and Cirasuolo et al. (2010).

	α^*	$M_K^*(0)$	k_ϕ	z_ϕ	k_M	z_M	$\phi^*(0)\,/\mathrm{Mpc}^{-3}$
Caputi et al. (2006)	-1.09	-24.16	1.67	1.78	0.63	1.88	3.9×10^{-3}
Cirasuolo et al. (2010)	-1.07	-24.16	1.47	1.70	0.47	1.78	3.5×10^{-3}

datasets, and even though the simulated ϕ^* has decreased, there are still more low-mass galaxies than observed. At high redshift, $z = 4$, observations can constrain only the high-mass end of the mass function. The simulated data lie below the observations of Pérez-González et al. (2008) and Ilbert et al. (2013), but are limited by the finite simulation volume.

Related to the mass function, we show in Fig. 4.2 the K-band galaxy luminosity function of our simulations at $z = 0, 0.5, 1, 2, 3,$ and 4, as well as observational data and fitted Schechter functions to data. Note that, different from Section 3.3.1, we calculate the luminosity of each galaxy simply by adding the contribution of each star particle in its FoF group, and not by estimating the total luminosity by fitting a Sérsic function. This means that all galaxies identified in the simulation contribute to the luminosity function, and since galaxy light is centrally concentrated the magnitudes obtained are fairly consistent by the two different methods. This has the effect that, at ever lower masses, more galaxies contribute to the luminosity function than in Section 3.3.1, but the differences between simulations found in that section remain, and none of our conclusions is compromised.

At $z = 0$, the high-mass end of the simulated data with AGN shows very good agreement with the observations of Cole et al. (2001) and Jones et al. (2006), and the fits to the data of Bell et al. (2003) and Huang et al. (2003), while the simulation without AGN greatly overpredicts the number of such galaxies. Caputi et al. (2006) and Cirasuolo et al. (2010) fit an evolving Schechter function to their data at various redshifts with

$$M_K^*(z) = M_K^*(0) - \left(\frac{z}{z_M}\right)^{k_M}, \tag{4.1}$$

$$\phi^*(z) = \phi^*(0) \exp\left[-\left(\frac{z}{z_\phi}\right)^{k_\phi}\right], \tag{4.2}$$

and fixed low-mass slope α^*. The fitting parameters of these equations determined by Caputi et al. (2006) and Cirasuolo et al. (2010) are given in Table 4.1; these values are used in each of the panels in Fig. 4.2, and the luminosity function plotted in the approximate range of magnitudes for which data were available. There is also good agreement between the simulation with AGN at the high-mass end and these fits at $z = 0$. Both our simulations overpredict the number of low-mass galaxies compared to observations, except those of Huang et al. (2003), who find a much steeper low-mass slope ($\alpha^* = -1.37$) than contemporaneous and subsequent studies ($\alpha^* \sim -1$). By $z = 0.5$, neither the simulated nor the observed luminosity

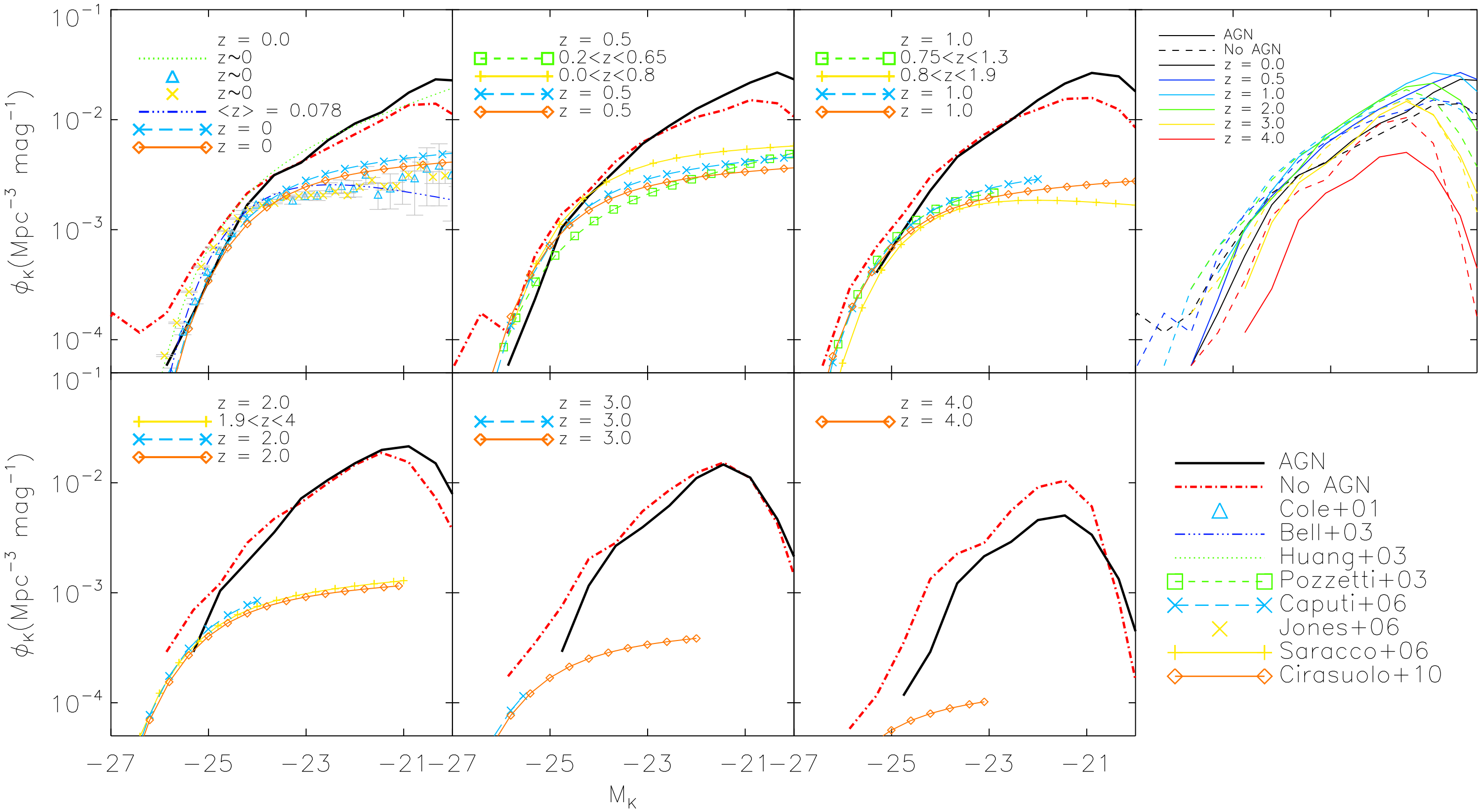

FIGURE 4.2: Evolution of the rest-frame K-band luminosity function. Simulated data are shown as the solid black and red dot-dashed lines (with and without AGN respectively). Observational data from Cole et al. (2001) and Jones et al. (2006) are shown, as well as the Schechter function fits of Bell et al. (2003), Huang et al. (2003), Pozzetti et al. (2003), and Saracco et al. (2006), and the evolving Schechter function fits (see text) of Caputi et al. (2006) and Cirasuolo et al. (2010).

functions have changed much compared to $z = 0$, and the simulation without AGN still vastly overpredicts the numbers of the most luminous galaxies. At $z = 1$, the observed decline of ϕ^* with redshift is apparent, while no such change is seen in the simulations. This trend continues out to $z = 4$, with both simulations overpredicting the number of galaxies at all luminosities compared to observations. The simulation with AGN produces consistently fewer galaxies at a given magnitude than the other simulation, at all but the lowest luminosities (Section 3.2.2).

The panel in the upper right of Fig. 4.2 shows the K-band luminosity function of both simulations at a range of redshifts. The constancy of the normalization, ϕ^*, across a wide range of redshifts is clear, as is the increase of M_K^* to lower masses. These trends lie in opposition to observations (but are the same as the evolution in the K-band luminosity function); the values of k_M and k_ϕ in Table 4.1 imply only weak evolution of M_K^* with redshift, but relatively strong evolution of ϕ^*. Indeed, M_K^* is found to decrease in observations, but appears to increase in our simulations (though this may be due to our limited box size). The fact that there is not much evolution in the luminosity function in our simulations from high redshift implies that galaxies grow hierarchically and do not show downsizing. However, we know from Fig. 3.10 that the stars that form the most massive galaxies at $z = 0$ are very old in the simulation with AGN, while low-mass galaxies are, on average, much younger. The large number of low-mass galaxies at high redshift may therefore be the progeny of today's most massive galaxies, with more low-mass galaxies forming at low redshift, leading to the constant normalization of the luminosity function.

We also show, in Fig. 4.3, the B-band galaxy luminosity function from our simulations, as well as Schechter function fits to observational data (all M_B^* from observations have had 0.09 added to them to convert from the AB to Vega magnitude system (Blanton & Roweis, 2007)). It is worth noting that the B band is more affected by dust extinction in observations than is K, but we do not include a prescription for dust extinction in our simulations.

As with the K-band luminosity function, the simulation with AGN feedback predicts fewer high-luminosity galaxies than the simulation without at all redshifts. At low redshift, $z \lesssim 0.5$, the simulated luminosity function is consistent with observations at low luminosities, while both overpredict the prevalence of high luminosity galaxies. As redshift increases, the agreement between simulation and observation at the low-luminosity end becomes worse as the observed normalization, ϕ_B^*, decreases more rapidly than in the simulations. By $z \sim 3 - 4$, the simulation with AGN becomes consistent with observations at the high-luminosity end.

The upper-rightmost panel shows the evolution of the simulated B-band luminosity function. M_B^* tends to decrease with increasing redshift, in qualitative agreement with observations. The B band traces recent star formation, which is quenched in the most massive galaxies at low redshift, leading to the observed evolution. The decrease of ϕ_B^* is slower than observed, and only apparent from $z \sim 2$.

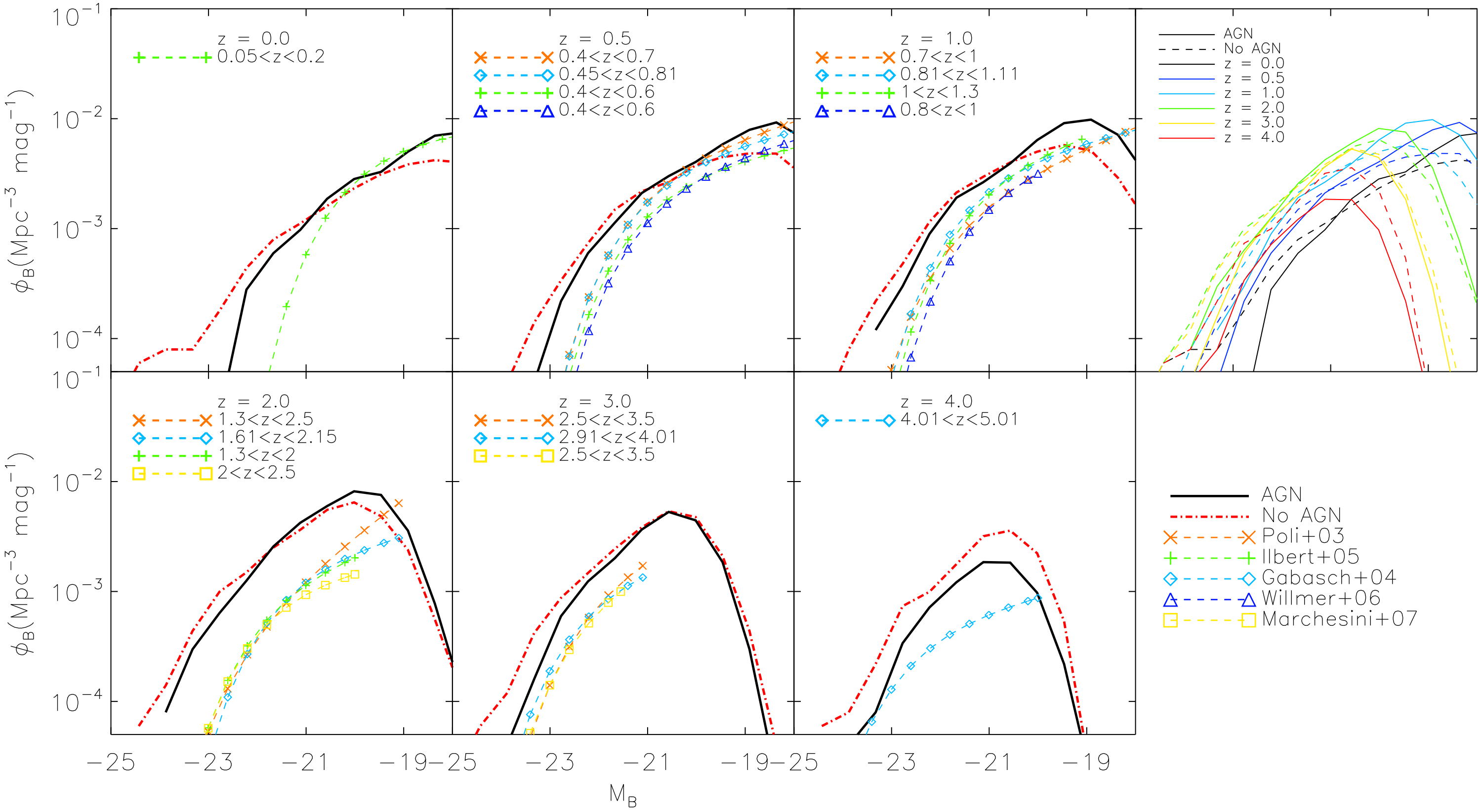

FIGURE 4.3: Evolution of the rest-frame *B*-band luminosity function. Simulated data are shown as the solid black and red dot-dashed lines (with and without AGN respectively). The Schecter function fits to the observational data of Poli et al. (2003), Gabasch et al. (2004), Ilbert et al. (2005), Willmer et al. (2006), and Marchesini et al. (2007) are also shown.

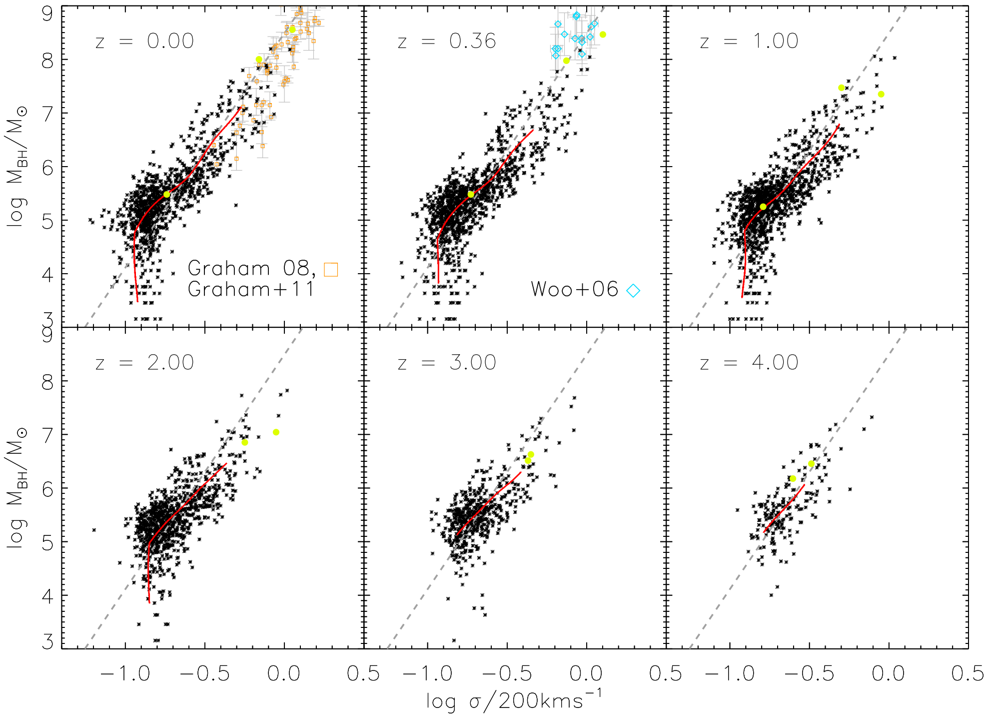

FIGURE 4.4: Evolution of the $M_{\rm BH}$–σ relation from our simulation. In all panels, the red line shows the ridge line of the simulated relation, and the dashed grey line shows the observed local relation from Kormendy & Ho (2013). Also plotted are the observational data at $z = 0$ from Graham et al. (2011), and at $z = 0.36$ from Woo et al. (2006). Lime green dots show the positions of galaxies A, B, and C.

4.2.2 $M_{\rm BH}$–σ

Of the many correlations between super-massive BH mass and galaxy properties, the correlation with the central line-of-sight velocity dispersion of the stellar bulge is one of the tightest and most straightforward to measure. We show in Fig. 4.4 the $M_{\rm BH}$–σ relation at 6 redshifts ($z = 0, 0.36, 1, 2, 3, 4$), with σ measured within the central projected $2h^{-1}$ kpc of a simulated galaxy. In all panels, the grey dashed line corresponds to the local relation given in Kormendy & Ho (2013), extrapolated below the observational limit of $\sim 10^6 M_\odot$, and the solid red line denotes the ridge line of the 2D histogram of the data. We are limited by resolution for $\log\left(\sigma/200{\rm km\,s^{-1}}\right) \lesssim -0.8$, giving rise to the vertical feature present in most panels. BHs therefore join the relation at this velocity dispersion, and $\log M_{\rm BH}/M_\odot = 3 - \log h$ (from Chapter 2), but quickly grow onto the observed relation. While their mass is small, BH growth is dominated by mergers rather than gas accretion; this gives rise to the horizontal features that can be seen at $z \leq 2$.

The evolution of galaxies A, B, and C is shown as well, with their positions on the $M_{\rm BH}$–σ relation shown at each redshift by the lime dots (galaxy A is the most massive of the three at each redshift). To provide additional information for these three

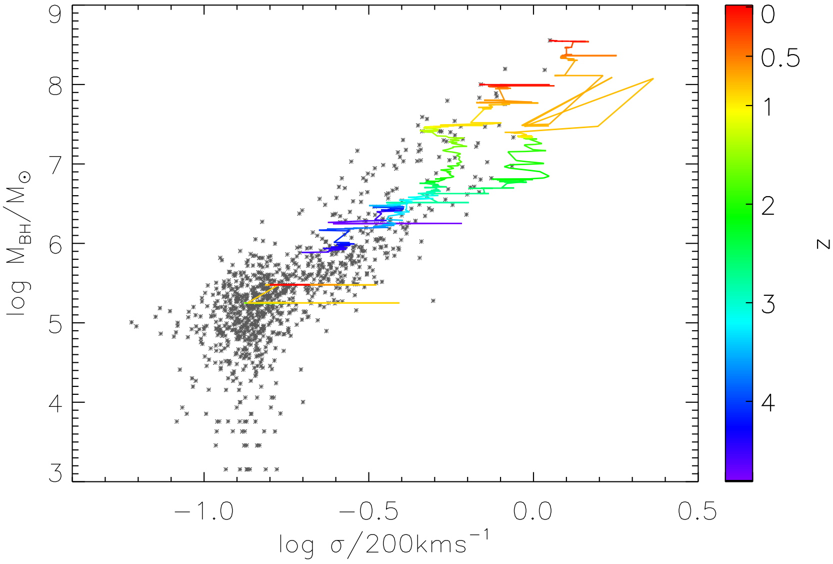

FIGURE 4.5: Evolution of the $M_{\rm BH}$–σ relation of galaxies A, B, and C from our simulation. The position of each galaxy in the $M_{\rm BH}$–σ plane is colour-coded by redshift. Also shown is the $z = 0$ relation for all galaxies in the simulation (grey stars).

galaxies, we also show their $M_{\rm BH}$–σ evolution with much finer time sampling in Fig. 4.5. Galaxies A and B form at $z > 4$, and lie close to the observed local relationship at this time. At $z \sim 2.5$, A evolves away from the observed local relation, with σ increasing more quickly than $M_{\rm BH}$, and grows back onto the relation at $z \sim 0.5$ (the apparently unphysical movement of A at $z \sim 0.75$ is caused by an incorrect BH being identified as belonging to A in two snapshots). Galaxy B, on the other hand, lies relatively close to the observed local relation at all times. This difference is most likely due to the different merger histories of the two galaxies (see Appendix E); A undergoes several major mergers that increase its mass before gas is accreted by the BH, whereas the growth of B is dominated by quiescent gas accretion that fuels both star formation and BH growth. The narrow, horizontal features followed by rapid BH growth are probably caused by galaxy mergers followed by BH mergers. Galaxy C forms between $z = 1$ and 2, and its BH grows quickly onto the observed local relation, but does not evolve at lower redshifts due to the passive nature of the galaxy's growth. The fine details of the coupled evolution of a galaxy and its BH will be investigated in a future work.

Our simulated $M_{\rm BH}$–σ relation does not evolve, and lies on the observed local relation of Kormendy & Ho (2013) at all redshifts. At $z = 0$, the high-mass end of our relation is consistent with the data of Graham (2008, updated in Graham et al. 2011). Data at $z > 0$ are difficult to obtain due to the necessary resolution needed to obtain $M_{\rm BH}$ (Section 1.2.2), but we include the measurements of Woo et al. (2006) at $z = 0.36$, with which our data are also consistent. A lack of or weak evolution in $M_{\rm BH}$–σ (or the related $M_{\rm BH}$–M_*) has been seen in many other theoretical works,

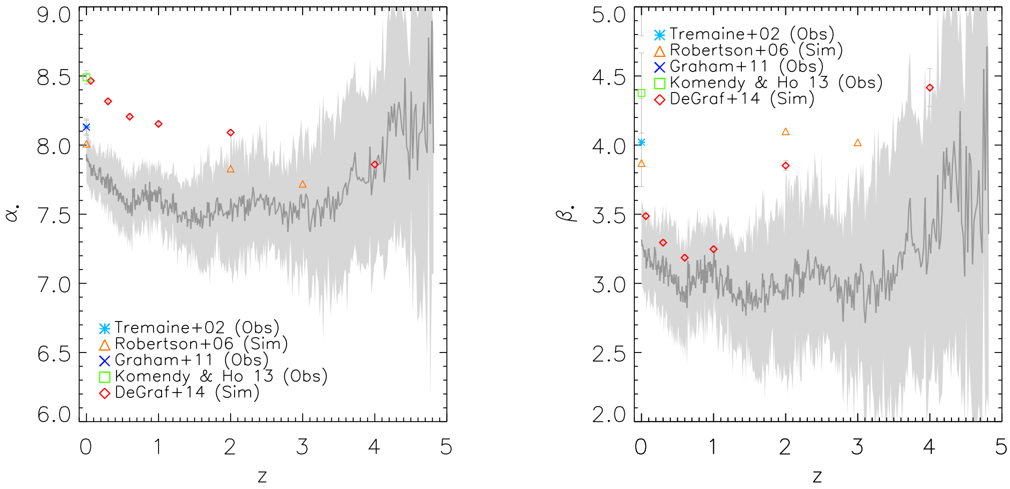

FIGURE 4.6: Evolution of the fitted parameters of the $M_{\rm BH}$–σ relation (see equation (4.3)). The left-hand panel shows how the normalization, $\alpha_\bullet$, changes with redshift in our simulation (dark grey line and light grey shading), while the right-hand panel shows the evolution of the gradient, $\beta_\bullet$. Also shown are the $z = 0$ observations of Tremaine et al. (2002), Graham et al. (2011), and Kormendy & Ho (2013), as well as the simulated evolution from Robertson et al. (2006) and DeGraf et al. (2014).

using different models and simulation techniques (e.g., Robertson et al., 2006; Di Matteo et al., 2008; Hirschmann et al., 2014; Khandai et al., 2014; DeGraf et al., 2014), which is due to the fundamental nature of the co-evolution of galaxies and BHs. To provide a quantitative comparison, we show in Fig. 4.6 the evolution of the intercept, $\alpha_\bullet$, and gradient, $\beta_\bullet$, of $M_{\rm BH}$–σ, defined by the equation

$$\log\left(M_{\rm BH}/M_\odot\right) = \alpha_\bullet + \beta_\bullet \log\left(\sigma/200{\rm km\,s^{-1}}\right). \tag{4.3}$$

Most studies fit this relationship following the work of Tremaine et al. (2002, see also Gültekin et al. 2009; McConnell & Ma 2013; Graham 2015), using a χ^2 minimisation technique. Due to the presence of the artificial features in our data discussed above, we employ a slightly different method, fitting a straight line to the ridge line of the 2D histogram (the red lines in Fig. 4.4) in the range $\log M_{\rm BH}/M_\odot > 5$ and $\log\left(\sigma/200{\rm km\,s^{-1}}\right) > -0.9$.

The left hand panel of Fig. 4.6 shows the evolution of $\alpha_\bullet$ with redshift for our simulations (dark grey line, light grey shaded area shows 1σ uncertainties). At low redshift, our data are lower than the observed values of Tremaine et al. (2002, $\alpha_\bullet = 8.13{\pm}0.06$), Graham et al. (2011, $\alpha_\bullet = 8.13{\pm}0.05$), and Kormendy & Ho (2013, $\alpha_\bullet = 8.490 \pm 0.049$), as well as the theoretical predictions of Robertson et al. (2006) and DeGraf et al. (2014). However, at higher redshift, these model predictions are consistent with our values (although these are subject to quite large uncertainties). Intriguingly, the evolution of $\alpha_\bullet$ in DeGraf et al. (2014) at low redshift ($0 < z < 1$) shows a very similar trend to our data, but offset by ~ 0.5 dex. A similar effect is seen in the right hand panel of Fig. 4.6, where we show the evolution of $\beta_\bullet$ with redshift. Again, the values from DeGraf et al. (2014) follow our data with a small offset, in this case ~ 0.2. The agreement with observations at $z = 0$ is not so good, however; the values of 4.02 ± 0.32 and 4.377 ± 0.290, from Tremaine et al. (2002) and Kormendy & Ho (2013) respectively, are ~ 1 larger than we measure, while the value of 5.13 ± 0.34 from Graham et al. (2011) is larger by almost 2. It may be that the 'bump' above the observed relation at $\log\left(\sigma/200\mathrm{km\,s^{-1}}\right) \sim -0.9$ is artificial, and caused by the very rapid growth of young BHs towards the relationship, but always at that velocity dispersion due to our finite resolution. This feature then causes the gradient to be underestimated. In any case, it is worth reiterating that the fitting procedure we used to obtain $\alpha_\bullet$ and $\beta_\bullet$ is different to that typically used in the literature, and that the overwhelming majority of our BHs do not grow more massive than $10^6 M_\odot$, while the values obtained from observations involve BHs with $M_{\mathrm{BH}} \gg 10^6 M_\odot$.

4.2.3 Mass–Metallicity Relation

We show in Fig. 4.7 the stellar mass–stellar metallicity relation for our simulations, at various redshifts, and with observational data where available. Stellar metallicity is measured within the central projected $15h^{-1}$ kpc, weighted by V-band luminosity to compare with observations of absorption lines. Due to the metallicity gradient present within galaxies (Chapter 5), our results could be sensitive to this radius, but modest changes to it cause metallicities to change by less than the scatter in the MZR. Values for individual galaxies in our simulations are shown by black stars (AGN) and red diamonds (no AGN), while the median and 1σ scatter are shown, respectively, by the solid and dotted lines of the same colours.

At $z > 0$, very few observational data are available; we show the $z \sim 0.7$ MZR of Gallazzi et al. (2014) alongside our $z = 0.5$ results. Our simulated MZR shows enrichment at least $0.2 - 0.3$ dex higher than observed. As at $z = 0$, the two simulations are consistent with one another, and in fact show no evolution in the MZR to at least $z = 1$. At $z = 2$, the simulated MZRs are ~ 0.05 dex lower than at lower redshift, and from $z = 2 - 1$, the MZR experiences its strongest evolution (top rightmost panel). Only at high redshift ($z \geq 4$) do the two simulations differ from one another; the galaxies in the simulation with AGN have metallicities on average ~ 0.1 dex lower than their counterparts in the other simulation, comparable to the 1σ scatter, which is due to the delayed onset of SF due to AGN feedback. The most massive galaxies tend to be in better agreement between the simulations, which would indicate that they have evolved more quickly than low-mass galaxies, and is suggestive of downsizing.

The evolution of the position of galaxies A, B, and C in the MZR is shown by the lime and light orange dots (with and without AGN, respectively; A, B, and C are ordered by mass at all redshifts in both simulations). All three galaxies grow along the relation, which explains the low scatter of this relation in our simulations, and by $z \sim 1 - 2$, A and B have attained their present-day metallicities, while C

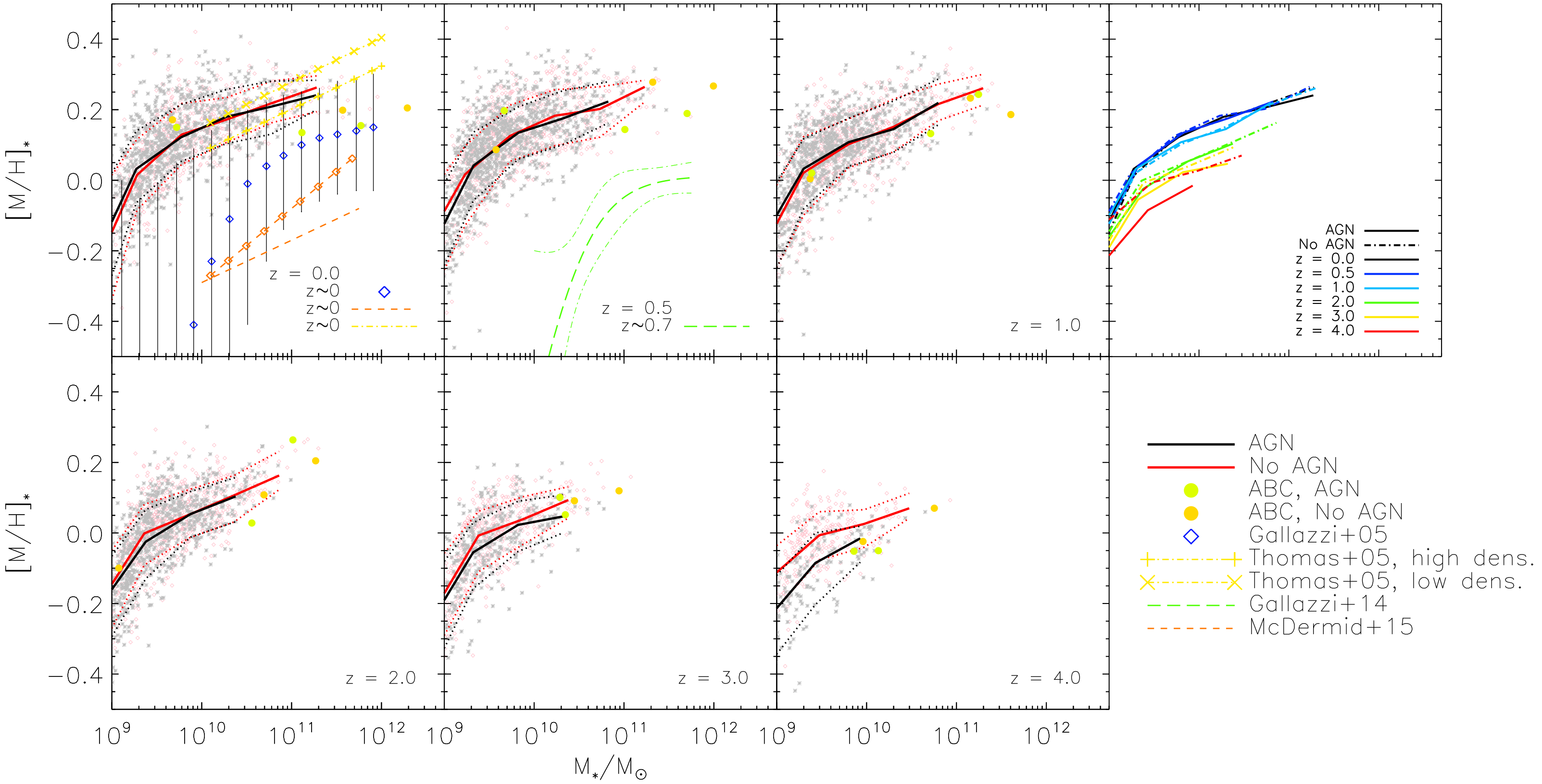

Figure 4.7: Evolution of the galaxy stellar MZR. Simulated data are shown by the black stars (with AGN) and red diamonds (without AGN), with their median (solid lines) and 1σ scatter (dotted lines) overlaid. The median local relation and scatter from Gallazzi et al. (2005) are denoted by the blue diamonds and black error bars, and the fits to observations from Thomas et al. (2005), Gallazzi et al. (2014), and McDermid et al. (2015) are also shown.

continues to be enriched to low redshift.

Estimating stellar metallicity is difficult to do with observations at high redshift due to the spatial resolution and even at $z = 0$ because of the age-metallicity degeneracy, and so there can be a significant offset between different authors, as well as large scatter in individual catalogues. For example, the 1σ scatter in the relation for SDSS galaxies at $z = 0$ from Gallazzi et al. (2005, blue diamonds and error bars in top left panel) is larger than the 1σ scatter from our simulations, shown by the dotted lines. It also lies offset from our median simulated relations, with a greater difference at lower masses. By contrast, our simulations agree well with the fits of Thomas et al. (2005), especially for $10^{10} \leq M_*/M_\odot \leq 2 \times 10^{11}$, although the most massive galaxies are under-enriched by ~ 0.1 dex with respect to these observations. The fit of McDermid et al. (2015) to data from the ATLAS^{3D} survey shares the gradient found by Thomas et al. (2005), but is offset by ~ -0.4 dex, the reason for which is uncertain. AGN feedback has no significant effect on the MZR at this redshift, with both the median and scatter consistent between the simulations at all galaxy masses.

Unlike the stellar MZR, the gas-phase MZR (Fig. 4.8) is consistent between the two simulations to high redshift. The relation becomes flatter from $z = 3 - 4$, with fewer low-metallicity galaxies at a given mass at higher redshift. This implies that galaxies that form earlier evolve most quickly and enrich their ISM, while later galaxies evolve more slowly; this is further evidence for downsizing in our simulations. For example, galaxies A and B reach their present-day metallicities at $z \sim 1 - 2$ (though low-redshift AGN-driven winds subsequently remove much of the gas in these galaxies), while for galaxy C this happens at lower redshift (and more quickly with AGN feedback since enriched winds from the central cluster help to pollute this galaxy).

We measure gas oxygen abundance within the central $15h^{-1}$ kpc of each galaxy (regardless of the gas' temperature), weighted by SFR to compare with observations, which are estimated from emission lines. The simulated results are displayed in the same way as in Fig. 4.7. All data from the literature have been converted to a Kroupa IMF (unless a Chabrier IMF was used, since this gives very similar results), converted to our adopted solar metallicity, $12 + \log(\mathrm{O/H})_\odot = 8.78$, and converted to the method of Kewley & Dopita (2002) using the procedure given in Kewley & Ellison (2008). In cases where the assumed solar value was not given, we adopted $12 + \log(\mathrm{O/H})_\odot = 8.66$ (Asplund et al., 2005) for papers earlier than 2009, and $12 + \log(\mathrm{O/H})_\odot = 8.69$ (Asplund et al., 2009) otherwise.

At $z = 0$, in the top left panel, there is excellent agreement between our simulations (which are fully consistent with one another) and the observations of Tremonti et al. (2004), Kewley & Ellison (2008), Maiolino et al. (2008), and Sánchez et al. (2013) at all galaxy masses, as well as Mannucci et al. (2010) at $M_* > 10^{10} M_\odot$. The fit of Zahid et al. (2014, solid green line) is systematically lower than both our simulations and other observational data by ~ 0.1 dex, the reason for which is unknown. We also find the scatter in the simulated MZRs to be greater than observed. This may be because we do not consider only cold ($T < 1.5 \times 10^4$ K) gas, which

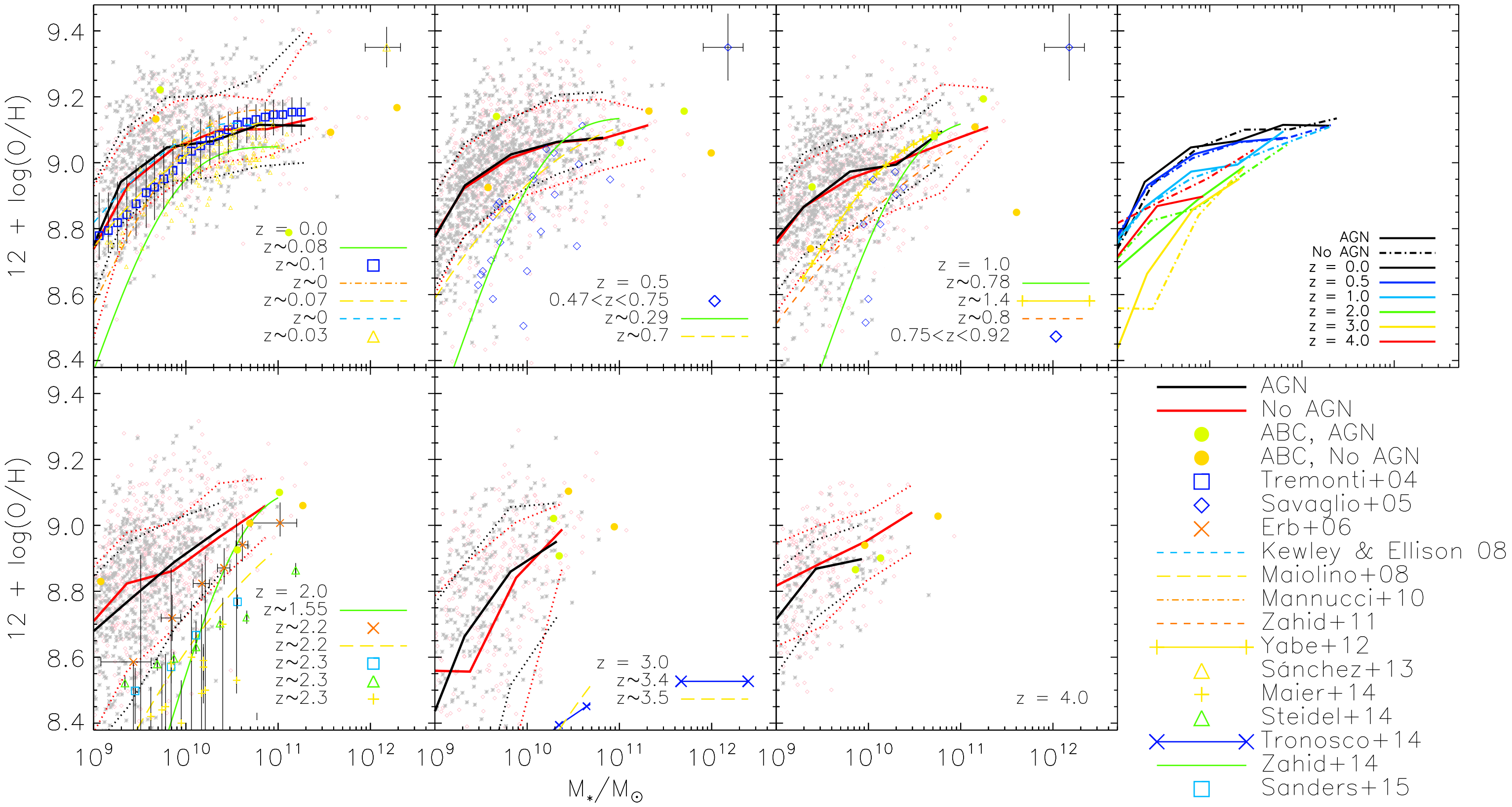

FIGURE 4.8: Evolution of the galaxy gas-phase MZR. Simulated data are shown by the black stars (with AGN) and red diamonds (without AGN), with their median (solid lines) and 1σ scatter (dotted lines) overlaid. Also shown are the observational data of Tremonti et al. (2004), Savaglio et al. (2005), Erb et al. (2006), Sánchez et al. (2013), Maier et al. (2014), Steidel et al. (2014), and Sanders et al. (2015), as well as the fits to data from Kewley & Ellison (2008), Maiolino et al. (2008), Zahid et al. (2011), Yabe et al. (2012), Troncoso et al. (2014), and Zahid et al. (2014). All observational data have been converted to our metallicity scale, a Kroupa IMF, and to the method of Kewley & Dopita (2002) using the procedure given in Kewley & Ellison (2008).

observations are sensitive to, though weighting by SFR should alleviate this effect.

At higher redshifts, out to $z = 2$, our simulations tend to agree well with observational data for high-mass galaxies, but show excess enrichment in low-mass galaxies compared to observations. By $z = 3$, where few data are available, the simulated relations lie ~ 0.5 dex above the observations of Maiolino et al. (2008) and Troncoso et al. (2014) at all masses.

4.2.4 Size–Mass Relation

The size–mass relation of galaxies gives information about where, on average, stars formed in the initial collapsing gas cloud, and therefore can constrain the SF timescale (Kobayashi, 2005). However, cosmological simulations have struggled to produce galaxies as large as observed, and AGN feedback has been found to offer a solution by suppressing star formation at the centres of massive galaxies (e.g., Dubois et al., 2013; Taylor & Kobayashi, 2014, but see also Snyder et al. 2015's analysis of galaxies in the Illustris simulation, which can be larger than observed). In Fig. 4.9, we show the galaxy size–mass relation for our simulated galaxies at various redshifts, as well as several published observed relations (blue lines are for late-type galaxies, red for early-type). Galaxy masses and effective radii ($\equiv$ half mass radii) are calculated using the procedure described in detail in Appendix B, and basically involves fitting a core-Sérsic function (Graham et al., 2003; Trujillo et al., 2004) to the surface density. In all panels, the simulated relationship flattens towards lower masses, and all galaxies have $R_\mathrm{e} \sim 1 - 2$ kpc, which corresponds to the gravitational softening length. The effects of AGN feedback are only apparent in the most massive galaxies, but at $z = 0$ this steepens the relationship, and brings it more in line with observations (Shen et al., 2003; Shankar et al., 2010; Newman et al., 2012; Cappellari et al., 2013), i.e. the time evolution is stronger with AGN feedback. Note that the agreement with the relation of Shen et al. (2003) for local late-type galaxies is by chance, and is caused by our fitting procedure and the finite resolution of the simulations. At higher redshift, the difference between the simulations with and without AGN becomes less pronounced because BHs have had less time to influence star formation since the peak of star formation at $z = 2$, which is almost unaffected by AGN feedback (Fig. 3.2). There is, however, between $z \sim 1$ and 3, an excess of galaxies with AGN that lie above the main relation and close to the observed relation for LTGs of van der Wel et al. (2014) compared to the simulation without AGN. Other than their large radii, these galaxies do not exhibit properties that set them apart; their colours are not systematically bluer, as might be expected for LTGs, and they are most likely due to imperfect fits, but we note that it is not possible to resolve disc structure in these simulations.

The three example galaxies, A, B, and C, are denoted by the lime and light orange dots (AGN and no AGN, respectively). There is little difference in their evolution in the different simulations until $z < 1$, when A and B exhibit much larger effective radii in the simulation with AGN feedback, due to the suppression of central star formation at late times. Galaxy C, on the other hand, evolves consistently in

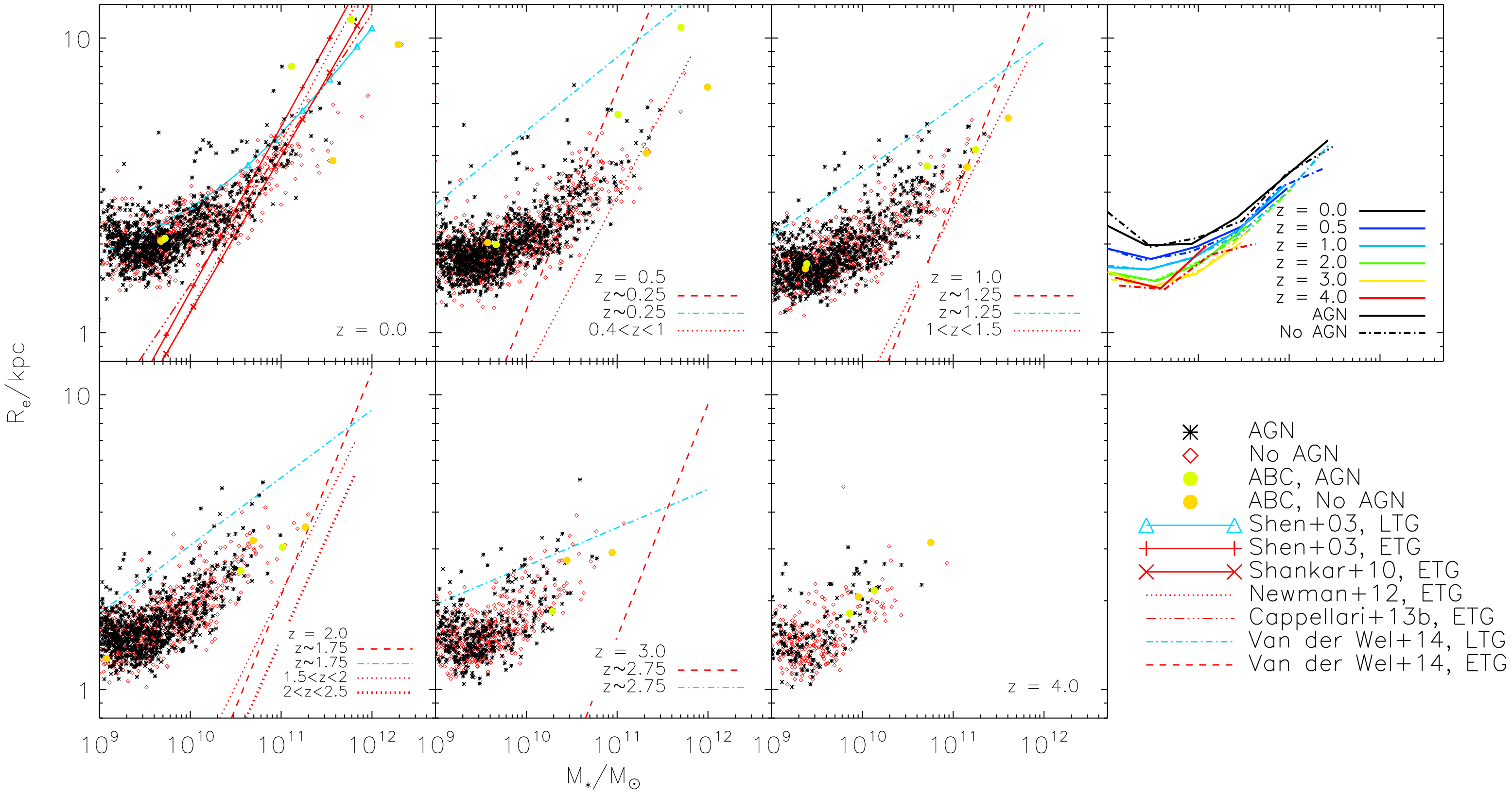

FIGURE 4.9: Evolution of the galaxy size–mass relation. Simulated data are shown by the black stars (with AGN) and red diamonds (without AGN). Fits to observed relations are shown for ETGs by the red lines (Shen et al., 2003; Shankar et al., 2010; Newman et al., 2012; Cappellari et al., 2013; van der Wel et al., 2014), and for LTGs by the blue lines (Shen et al., 2003; van der Wel et al., 2014).

both simulations since it does not experience strong AGN feedback at any time.

The median size–mass relation for both simulations at several redshifts is shown in the rightmost upper panel of Fig. 4.9. The difference between the simulations at $z \lesssim 0.5$ is not discernible due to the low number of galaxies that are strongly affected. It is clear that there is very little evolution of the slope with redshift, but the normalisation increases as galaxies grow.

4.2.5 Star Formation Main Sequence

The star formation main sequence (SFMS) describes the correlation between galaxy mass and star formation rate, with more massive galaxies tending to have larger star formation rates. Fig. 4.10 shows the SFMS for our two simulations at various redshifts, along with fits to observational data (Daddi et al., 2007; Elbaz et al., 2007; Dunne et al., 2009; Magdis et al., 2010; Oliver et al., 2010; Elbaz et al., 2011; Karim et al., 2011; Bouwens et al., 2011; Lee et al., 2012; Zahid et al., 2012; Tacconi et al., 2013; Renzini & Peng, 2015). The influence of AGN feedback is clear at $z = 0$ since some galaxies have SFRs much lower than would be expected given their mass. These are galaxies in which AGN feedback is quenching star formation, and lie in the region of the M_*–SFR plane occupied by ETGs (e.g., Wuyts et al., 2011; Renzini & Peng, 2015). There is a clear dearth of high-mass ($M_* > 10^{11} M_\odot$) galaxies on the SFMS compared to the simulation without AGN, but it is otherwise unchanged by the inclusion of AGN feedback. It is also quite consistent with observations, with a very similar gradient, but slightly lower normalisation (to Daddi et al. (2007) in particular). These trends are also seen out to high redshift, until $z = 4$ when the SFR of galaxies with AGN feedback is, on average, higher than those without.

Galaxies A, B, and C are shown as the lime and light orange dots (with and without AGN, respectively). At all times other than $z \sim 2$, when the cosmic SFR peaks, the galaxies in the simulation with AGN have a lower SFR than their counterparts in the other simulation. This is most clearly seen for galaxies A and B at $z \lesssim 0.5$, when these galaxies move off the SFMS, due to the suppression of star formation, and into a region occupied, observationally, by ETGs (Wuyts et al., 2011).

In the upper rightmost panel of Fig. 4.10, we show the median SFMS for each of the simulations at different redshifts, which indicates that AGN feedback has very little effect on it except at the high-mass end. In addition, while the normalisation shows fairly strong evolution with redshift, the gradient does not change, which is consistent with observations (Whitaker et al., 2014).

4.3 Conclusions

We have presented the evolution of a population of simulated galaxies from $z = 4$ to the present day. Two cosmological hydrodynamical simulations were used, one with a prescription for AGN feedback, the other without. The influence of AGN feedback is most apparent at $z < 2$, after the peak in cosmic SFR, and preferentially in more

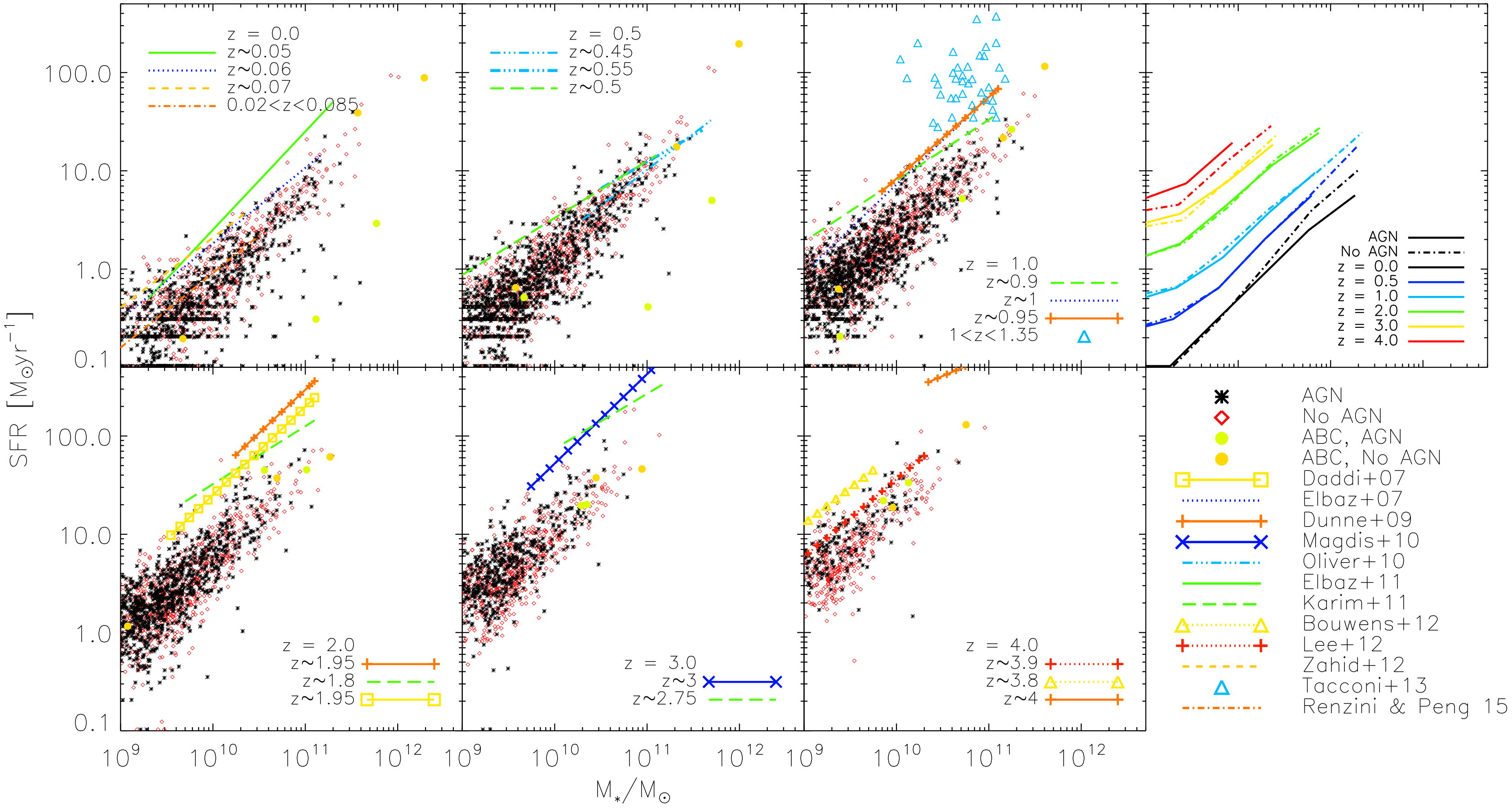

FIGURE 4.10: Evolution of the SFMS. Simulated data are shown by the black stars (with AGN) and red diamonds (without AGN). Observational data from Tacconi et al. (2013) are also plotted, along with the fits to observations of Daddi et al. (2007), Elbaz et al. (2007), Dunne et al. (2009), Magdis et al. (2010), Oliver et al. (2010), Elbaz et al. (2011), Karim et al. (2011), Bouwens et al. (2012), Lee et al. (2012), Zahid et al. (2012), and Renzini & Peng (2015).

massive galaxies. These galaxies host the most massive BHs (Fig. 4.4), and may have high accretion rates at late times when they have grown to be super-massive. The primary effect of this feedback is to quench star formation in the central regions of massive galaxies, thereby reducing the prevalence of high-mass and high-luminosity galaxies (Figs. 4.1 and 4.2), increasing their effective (half-mass) radii, and moving them off the star formation main sequence at low redshift ($z \lesssim 0.5$). We also found that AGN feedback does not affect much the mass–metallicity relations out to high redshift; these are mostly established at a galaxy's first starburst, which is typically before its BH has grown sufficiently to strongly affect SF or stellar feedback.

As well as comparing our simulations to one another, we also compared them with observations, finding excellent agreement in many cases at low redshift, and fairly good agreement out to $z = 2 - 3$, especially for the most massive galaxies, with the agreement usually better for the simulation with AGN feedback (for the size–mass relation in particular, Fig. 4.9). However, several conflicts between our simulated data and observations still remain, which may be partially due to uncertainties in the observations. We find that the simulated mass and K-band luminosity functions significantly overpredict the number of low-mass galaxies at all redshifts, and that their evolution is not in keeping with observations. This may be due, at least in part, to the fact that the size of our simulation box, $(25h^{-1}\ \mathrm{Mpc})^3$, is not cosmologically representative (by a factor of ~ 64, Vogelsberger et al. (2014); Schaye et al. (2015)), but simulates a cluster of galaxies. It may also be the case that our feedback prescriptions are not able to capture accurately enough the physical processes in these lower mass systems (e.g., Oppenheimer & Davé, 2006; Davé et al., 2011; Hirschmann et al., 2014). A potentially related issue is that low-mass galaxies in our simulations are over-enriched compared to observations (Fig. 4.8). While the conversion of measured line ratios into oxygen abundance is fraught with uncertainty, this disparity could also be partially due to our model.

Finally, we found evidence for downsizing in our simulations, whereby the most massive galaxies at the present day formed and evolved most quickly. These galaxies showed substantial chemical enrichment at relatively high redshift, and attained their present day metallicity as early as $z \sim 2$. Subsequent evolution of the MZR was restricted to lower-mass galaxies, causing the MZR to become flatter.

As was found in Chapter 3, AGN feedback is an essential ingredient in cosmological simulations of galaxy formation and evolution, not only to reproduce observations at $z = 0$, but across cosmic time as well.

5

Metallicity Gradients

5.1 Introduction

Understanding the evolution of galaxies, and the physical processes that drive it, is of great importance for our understanding of the Universe around us. But when we look into the sky, we see galaxies at a single snapshot in their lives, and must try to piece together their history given our observations of them, as well as our knowledge of galaxies at other times in the history of the Universe. Much may be learned by simply looking at the distribution of stars and gas; morphological disturbances and tidal features are indicative of recent merger activity, and gas outflows may suggest strong stellar or AGN feedback. Such data are useful for understanding the recent history of a galaxy, but galaxy-scale observational signatures of even the most extreme merging events can be lost in only a few Gyr (e.g., Hopkins et al., 2008). More subtle clues may also be available; spatially resolved kinematics of both gas and stars from IFUs such as SAURON (e.g., Kuntschner et al., 2010), CALIFA (e.g., Sánchez et al., 2012), SAMI (e.g., Fogarty et al., 2014; Ho et al., 2014) and its successor HECTOR (e.g., Bland-Hawthorn, 2015), and MaNGA (e.g., Bundy et al., 2015) reveal decoupled gas and stellar kinematics, as well as kinematically decoupled stellar cores. Such surveys are set to produce a wealth of data, and vast galaxy catalogues will be produced over the coming decades (e.g., Bland-Hawthorn, 2015).

IFUs can also map the distribution of stellar and gas-phase metals across the face of a galaxy. The effects of processes like galaxy mergers and AGN feedback on these quantities are less clear, since metals may be formed from induced star formation, redistributed within a galaxy, or removed completely, depending on the details of the process. Kobayashi (2004) studied how mergers alter the stellar metallicity gradients of elliptical galaxies, and found that major mergers cause flattening of

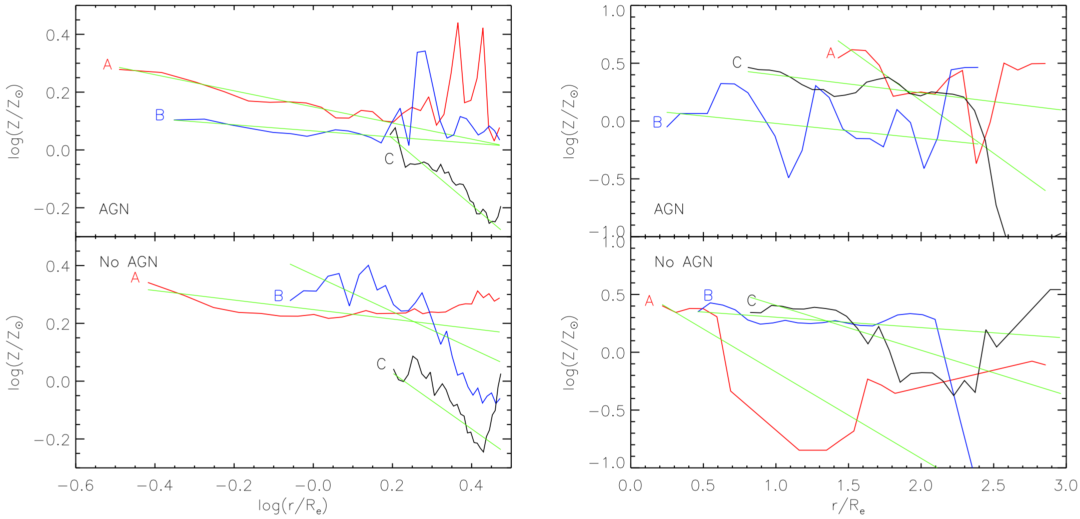

FIGURE 5.1: Stellar and gas-phase metallicity profiles (left and right panels, respectively) of galaxies A, B, and C both with and without AGN (top and bottom panels, respectively). Green lines show the resulting straight-line fit to the ranges given in the main text, but plotted out to $3R_e$. See Appendix F for stellar metallicity profiles of all present-day simulated galaxies.

the gradients, with mergers of larger mass ratios exerting the greatest influence. Conversely, mergers between gas-rich galaxies induced strong central star formation, which caused steepening of the gradients. In this chapter, we present both stellar and gas-phase metallicity gradients of the galaxies of our simulations at $z = 0$, as well as following the evolution of the gradients in three example galaxies. This allows us to determine their utility as probes of a galaxy's history.

This chapter is arranged as follows: in Section 5.2 we describe the procedure used to measure the metallicity gradients of galaxies in our simulations, before showing the present-day distribution of stellar gradients in Section 5.3. In Section 5.4 we describe the evolution of the stellar metallicity gradients of three example galaxies (A, B, and C of Section 3.2.2), matched between simulations, across cosmic time. Sections 5.5 and 5.6 repeat this analysis for gas-phase metallicity gradients. Finally, we give our conclusions in Section 5.7.

5.2 Fitting Procedure

In this section, we describe the method used to obtain metallicity gradients, illustrated with the metallicity profiles of galaxies A, B, and C (Chapter 3). Galaxies are identified by a Friends of Friends code (Section 3.2.2; Springel et al., 2001) and the method described in Appendix H to separate individual galaxies from the same FoF group, and all star or gas particles within a projected radius of $r = \max(2R_e, 10h^{-1}\text{kpc})$ from the galaxy centre are identified. These particles

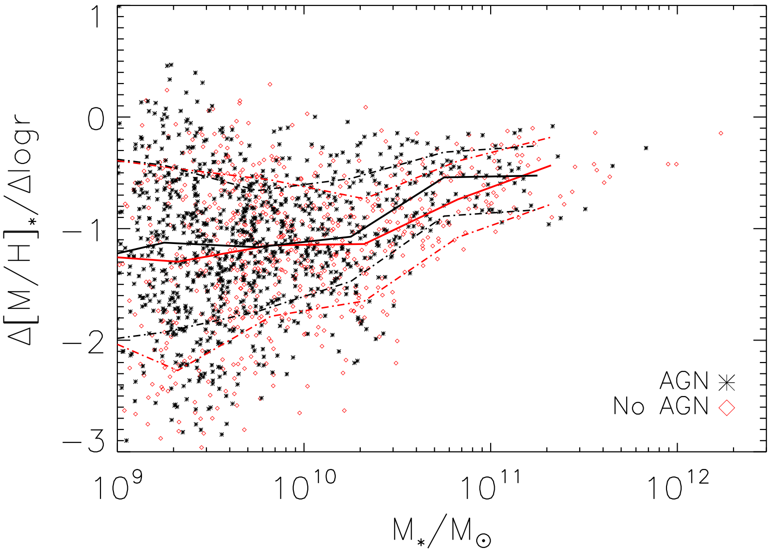

FIGURE 5.2: Stellar metallicity gradient as a function of galaxy mass at $z = 0$ for galaxies in the simulation with (black stars) and without (red diamonds) AGN feedback. Solid and dot-dashed lines show the median and 1σ trends, respectively.

are to be binned by galactrocentric distance, but since there are often only a small number of particles per bin in the limited range being looked at, we split each particle into several new particles with the same intrinsic properties and extrinsic ones scaled by the reciprocal of the number of new particles, and distribute them around their initial location as described in Appendix G. This also accounts for the fact that the particles in the simulation are not point-like, and should contribute to several bins. These particles are then radially binned, and the mean metallicity of each bin calculated, weighted by V-band luminosity or star formation rate for stars and gas respectively. We assume Poissonian errors for the metallicity value of each bin; this is not meant as an accurate estimate of the uncertainty, rather these values are used by the fitting code to weight the contribution of each bin to the fit. We use `mpfit` (Markwardt, 2009), which performs χ^2 minimisation with errors, to find the best fit to the data, of the form

$$\log X/X_\odot = af(r) + b, \tag{5.1}$$

where $X =$ Z, Fe, O, O/Fe, and $f(r) = \log r$ for stars, and r for gas. The desired gradient is then simply the value of a in Equation (5.1) returned by `mpfit`. In Fig. 5.1 we show the radial profiles of stellar and gas-phase metallicity of the galaxies A, B, and C (red, blue, and black lines, respectively), along with their best straight-line fits (green lines) for the simulations with and without AGN.

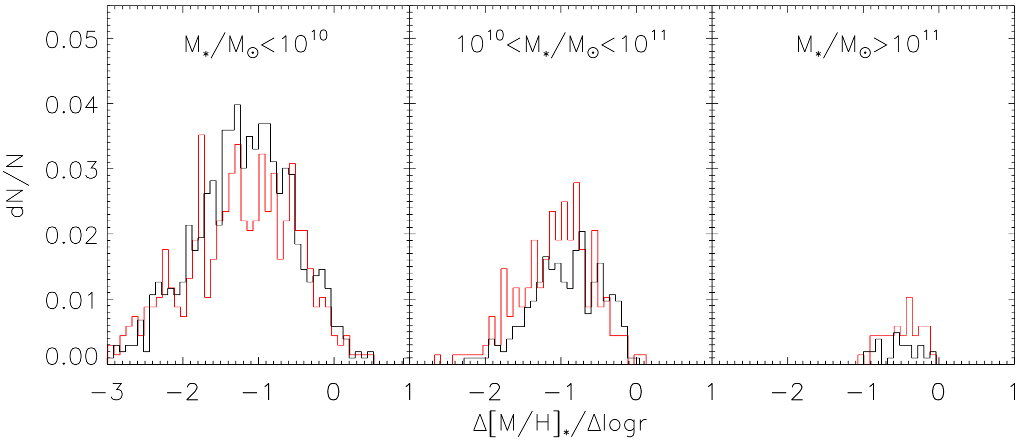

FIGURE 5.3: Present-day, stellar metallicity gradient distributions for galaxies in three different mass bins: $M_*/M_\odot < 10^{10}$; $10^{10} < M_*/M_\odot < 10^{11}$; and $M_*/M_\odot > 10^{11}$. Black histograms denote the simulation with AGN, and red without. The histograms are normalised by the total number of galaxies in each simulation.

TABLE 5.1: KS test p-values comparing the stellar metallicity and [O/Fe] gradients of galaxies in our simulations with and without AGN in three different mass bins.

	$M_*/M_\odot < 10^{10}$	$10^{10} < M_*/M_\odot < 10^{11}$	$M_*/M_\odot > 10^{11}$
$\Delta[\mathrm{M/H}]_*/\Delta\log r$	0.198	0.011	0.718
$\Delta[\mathrm{O/Fe}]_*/\Delta\log r$	0.077	0.034	0.973

5.3 Stellar Metallicity Gradients at $z = 0$

The stellar metallicity gradient of a galaxy may offer clues about its merging history (e.g., Kobayashi, 2004). In our simulations, we know the full history of all galaxies, and so can see how different processes affect the evolution of the metallicity gradient. We show in Fig. 5.2 metallicity gradient as a function of mass at $z = 0$ for both simulations. The median and 16th and 84th percentiles are shown by the solid and dot-dashed lines, respectively. There is a trend for more massive galaxies to have shallower gradients, and there is much greater scatter at lower masses, some of which is intrinsic, and some due to the difficulties fitting the metallicity profile of these small objects.

The median and 1σ trends of the two simulations seem consistent with one another across the range of galaxy masses probed. Spolaor et al. (2010) found that the observed trend showed an upturn at low masses, that is not seen in the median relations shown here; however, the scatter in our data is too large for low-mass galaxies for such a trend to be seen. In order to provide a more quantitative discussion, we bin the galaxies by mass and look at the resulting distributions, which are shown in Fig. 5.3. We perform a Kolmogorov–Smirnov (KS) test on each bin,

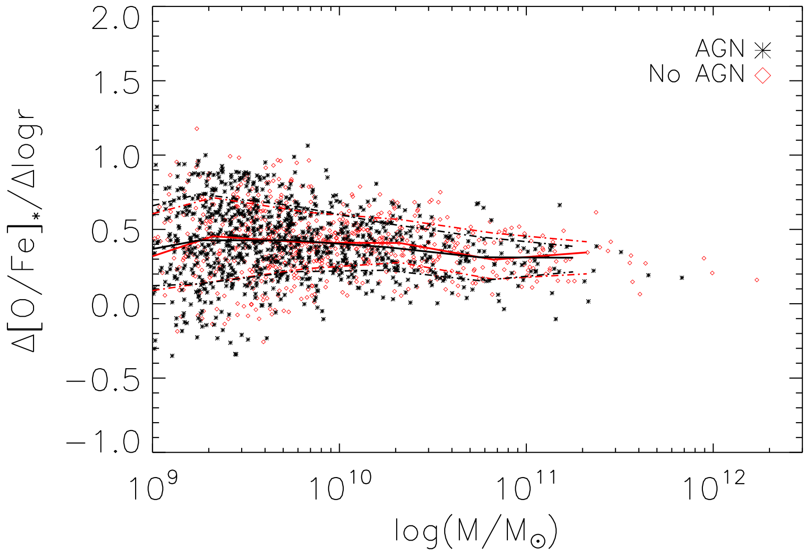

FIGURE 5.4: Same as Fig. 5.2, but for stellar [O/Fe] gradients.

the results of which are given in Table 5.1. In the two lower-mass bins, the p-value returned is small, but the null hypothesis (that these distributions are drawn from the same parent distribution) cannot be rejected at the 1 per cent level. This suggests that AGN feedback does not affect the distribution of stellar metallicity gradients in our simulations. Such a result is not surprising since AGN feedback couples only to gas particles and the majority of stars have formed before AGN feedback becomes effective in massive galaxies, and although this leads to a small reduction in metal mass in stars at the centre of the galaxies, it does not change much the stellar metallicity (see Section 3.3.3).

It is also worth noting that the median gradient in each of the mass bins of Fig. 5.3 increases with increasing mass. In our simulations, the most massive galaxies tend to experience major mergers at some point in their evolution that flatten their metallicity gradient (see Section 5.4). Repeating the procedure on a simulation of a more field-like environment may offer insight into how influential mergers are on the present-day gradients. The distribution obtained in the highest-mass bin is more similar to the result of Kobayashi (2004), who studied elliptical galaxies, than the distribution of the entire simulated galaxy population.

We also show, in Fig 5.4, the gradient in [O/Fe] for the galaxy population of our two simulations at $z = 0$. Again, the solid and dot-dashed lines show the median and 1σ scatter. Most galaxies have a small positive gradient, indicating a longer star formation timescale towards the centre of the galaxy. The gradient is generally slightly shallower in more massive galaxies, which may be indicative of downsizing since this suggests that more massive galaxies form the bulk of their stellar mass on

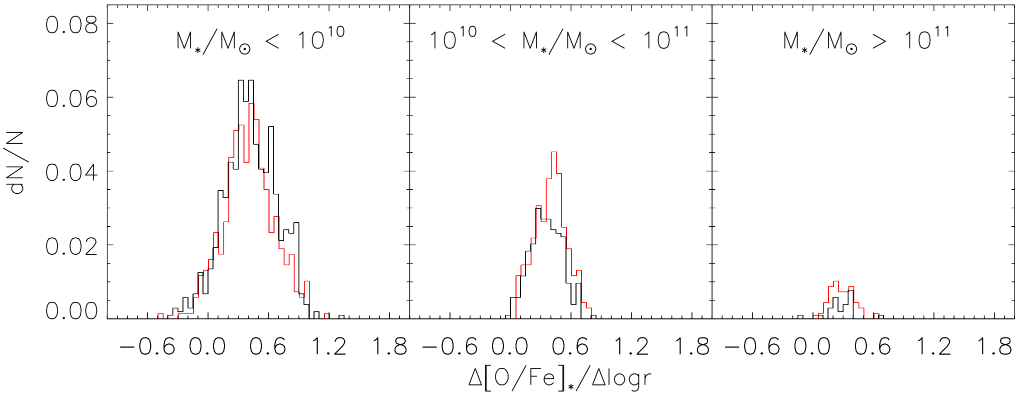

FIGURE 5.5: Same as Fig. 5.3, but for stellar [O/Fe] gradients.

shorter timescales than less massive ones.

We again bin galaxies by mass, and the resulting distributions are shown in Fig. 5.5. By eye, the different simulations seem to give similar results at all masses, and this is reinforced by the results of KS tests on the distributions of each bin, shown in Table 5.1. In all bins, the p-value is greater than 0.03, and we can not reject the null hypothesis, meaning that our results are consistent with AGN not affecting the stellar [O/Fe] gradient of galaxies.

5.4 Stellar Metallicity Gradients Across Cosmic Time

In order to interpret gradients seen at $z = 0$, it is necessary to understand what physical processes affect them over the course of the galaxy's life. We show in Fig. 5.6 the evolution of the metallicity gradient in our three example galaxies (A, B, and C; see Section 3.2.2) as a function of cosmic time. Also shown, by the vertical lines, are the approximate times of all mergers onto these galaxies with a stellar mass ratio of at least 1/20 (blue with AGN, orange without). The height of each line is proportional to the mass ratio of the merger, with a 1:1 merger represented by a line reaching to the first major tick on the ordinate axis.

In galaxy A, at early times before the major mergers at $t \sim 6.75$ Gyr, the evolution of the metallicity gradient is determined by the occurrence of mergers. Major mergers at $t \sim 2.5$ and 4.75 Gyr without AGN, and ~ 3 Gyr with, cause the metallicity gradient to become shallower, as metal-rich stars from the centre of the galaxy are redistributed further out. By contrast, this galaxy is involved in no mergers in the simulation with AGN in the range $3.75 \lesssim t/\mathrm{Gyr} \lesssim 6.75$, during which time the gradient becomes steadily steeper due to ongoing and undisturbed star formation and chemical enrichment in the centre of the galaxy. In both simulations, galaxy A experiences a triple galaxy merger with similar mass components at $t \sim$ 6.75 Gyr (in the simulation with AGN, the merger is erroneously identified twice,

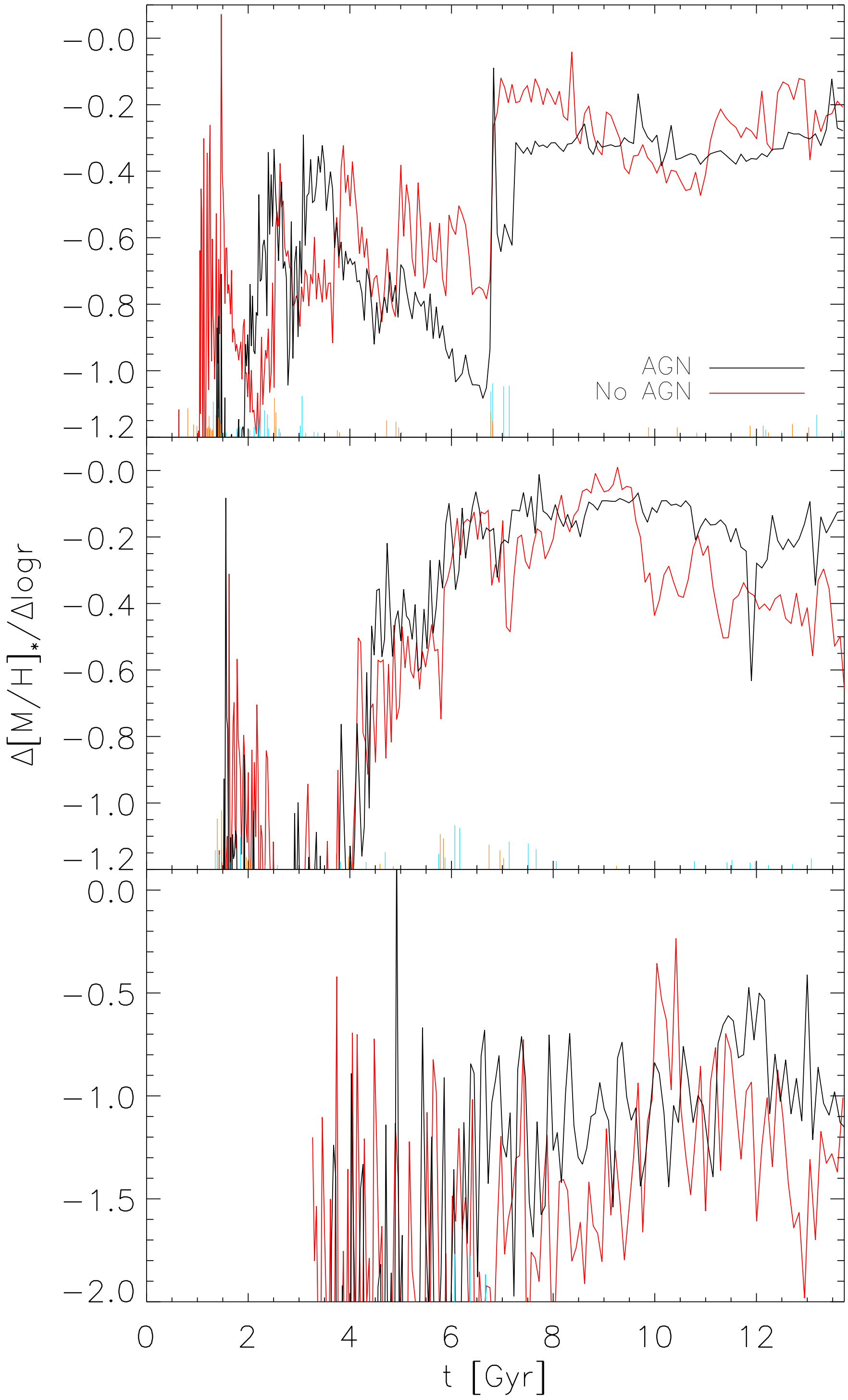

FIGURE 5.6: Stellar metallicity gradients in the galaxies A (top panel), B (middle panel), and C (bottom panel; see Section 3.2.2) across cosmic time both with (black) and without (red) AGN. Vertical lines show the approximate times that these galaxies undergo a merger with mass ratio 1/20 or greater (blue with AGN, orange without). The height of the lines is proportional to the mass ratio, with a 1:1 merger reaching to the first major tick mark on the ordinate axis.

leading to the lines at ~ 7 Gyr). This event is highly disruptive to the structure of all three components, and the gradient becomes significantly shallower as a result. In the simulation with AGN, this merger also triggers the growth of this galaxy's BH, and SF is suppressed by AGN feedback by an order of magnitude or more for the remainder of its life (Fig. 3.4). Therefore, the gradient is not able to steepen again, unlike in the simulation without AGN.

The gradient of galaxy B starts off steeper than that of A, since it does not experience as many mergers early in its life. It too experiences a major merger at $t \sim 6$ Gyr, increasing its gradient to ~ -0.1. As in galaxy A, this merger triggers strong AGN activity that heavily suppresses SF for the remainder of that simulation. For this reason, we again see that the gradient remains relatively flat from 6 Gyr, whereas in the simulation without AGN it steepens, reaching ~ -0.6 by $z = 0$.

Galaxy C evolves significantly more passively than A or B, and only experiences mergers in the simulation with AGN (there are a greater number of low-mass galaxies in this simulation; see Section 4.2.1). In addition, its BH does not grow massive enough to significantly affect SF at any time. There is, however, a tendency for the gradient to be shallower when AGN feedback is included, despite the large scatter. While this may be a purely stochastic effect, it may be due to the external enrichment this galaxy receives from enriched outflows in the main cluster (Section 3.2 and Chapter 6). This would cause all the stars in the galaxy to form from more enriched gas than in the simulation without AGN, and make the gradient shallower.

We also show, in Fig. 5.7, the evolution of the gradient in stellar [O/Fe] for galaxies A, B, and C, with all lines having the same meaning as in Fig. 5.6. Initially, the evolution of the gradient in [O/Fe] proceeds similarly to metallicity, with mergers making the gradients shallower, and quiescent star formation over Gyr time scales causing them to become steeper due to the increased contribution of SNe Ia. In galaxy A, following the major merger at $t \sim 7$ Gyr, star formation is heavily suppressed with AGN (Fig. 3.4), and the [O/Fe] gradient is effectively locked at its value caused by the merger. When AGN feedback is not included, however, the ongoing central star formation is able to steepen the gradient again over a few Gyr. Galaxy B shows similar evolution in its [O/Fe] gradient, and by the present day, the simulation without AGN has a steeper gradient than in the simulation without due to the contribution at late times of SNe Ia in the centre of this galaxy. In galaxy C the evolution is simpler, and there is good agreement between the two simulations with and without AGN. By $z = 0$, the simulation with AGN feedback has a slightly steeper gradient, which may be due to external enrichment from AGN-driven winds in more massive galaxies.

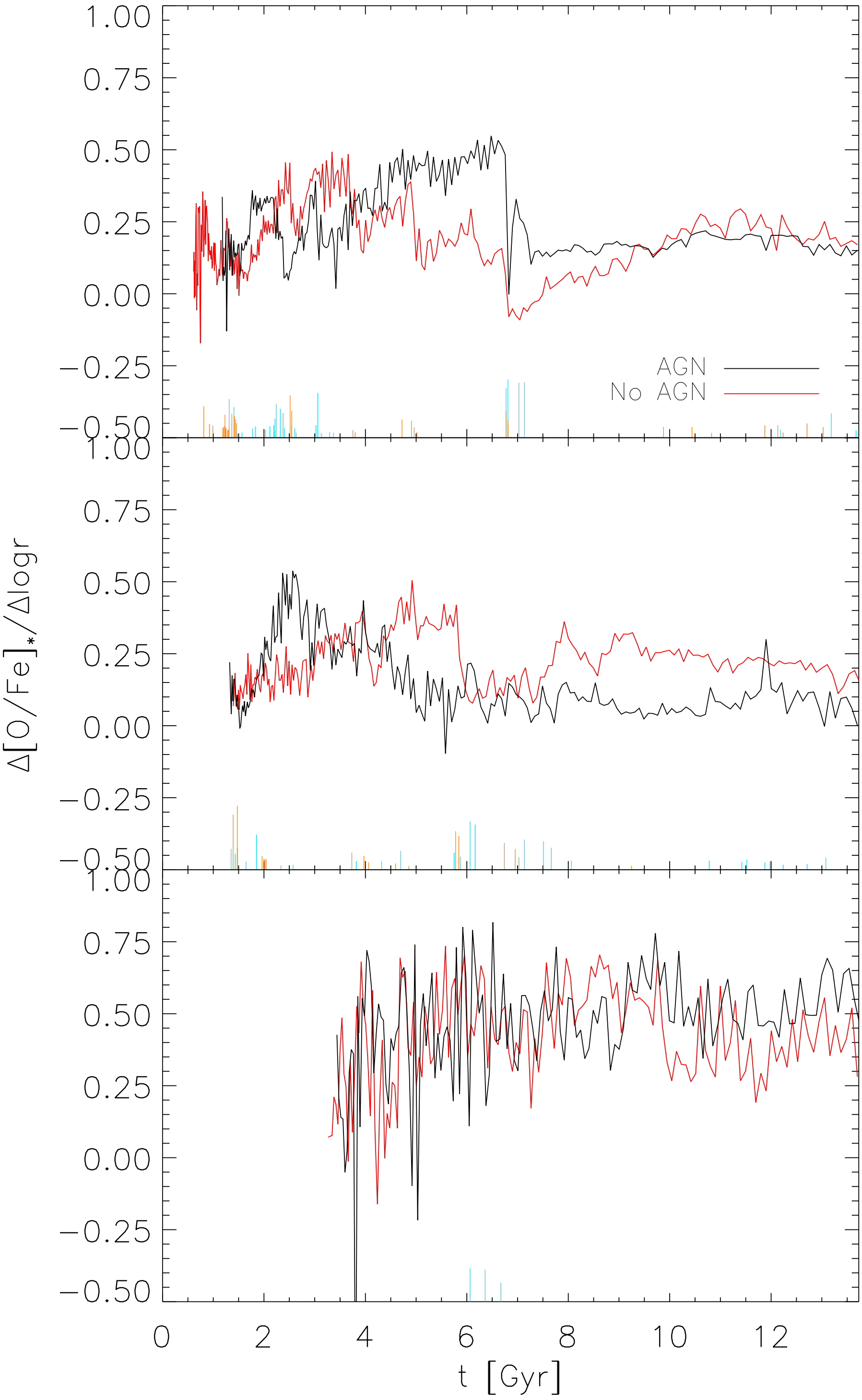

Figure 5.7: Same as Fig. 5.6, but for stellar [O/Fe] gradient.

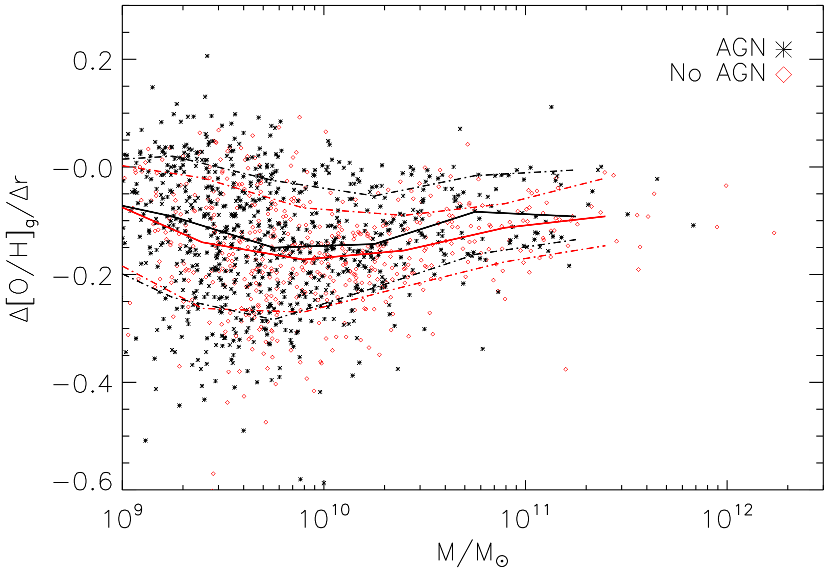

FIGURE 5.8: Same as Fig. 5.2, but for gas-phase oxygen abundance gradients.

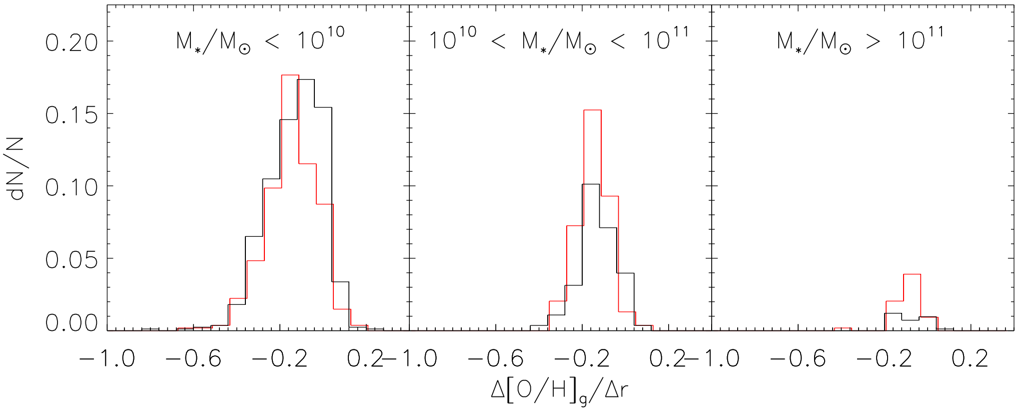

FIGURE 5.9: Same as Fig. 5.3, but for gas-phase oxygen abundance gradients.

TABLE 5.2: KS test p-values comparing the gas-phase oxygen abundance and [O/Fe] gradients of galaxies in our simulations with and without AGN in three different mass bins.

	$M_*/M_\odot < 10^{10}$	$10^{10} < M_*/M_\odot < 10^{11}$	$M_*/M_\odot > 10^{11}$
$\Delta[\mathrm{O/H}]_\mathrm{g}/\Delta r$	8.54e-4	6.71e-4	0.153
$\Delta[\mathrm{O/Fe}]_\mathrm{g}/\Delta r$	1.10e-3	1.43e-4	0.945

5.5 Gas Metallicity Gradients at $z = 0$

Understanding the evolution of gas in galaxies is of great importance since it is the fuel for star formation, and the medium in which metals are transported both within and outside a galaxy. Indeed, the origin of gas in ETGs is the subject of ongoing uncertainty (e.g., Young et al., 2011; Lagos et al., 2014). The gradient in gas metallicity within a galaxy may be useful as a tracer of its AGN history, and can be observed out to higher redshift than can stellar metallicities (Zaritsky et al., 1994; Yuan et al., 2011). We now examine the gas-phase metallicity gradients of galaxies to see how it is affected by different physical processes.

Fig. 5.8 shows the distribution of gas-phase oxygen gradients with galaxy stellar mass at $z = 0$ for our different simulations. The median and 1σ scatter are shown by the solid and dot-dashed lines respectively. In both simulations, gradients are, on average, steepest in intermediate-mass galaxies at around $-0.2\,\mathrm{dex\,kpc^{-1}}$. At higher and lower masses, gradients are shallower by $\sim 0.1\,\mathrm{dex\,kpc^{-1}}$, and high-mass galaxies in the simulation with AGN have near-flat gradients, approximately $0.1\,\mathrm{dex\,kpc^{-1}}$ higher again than the simulation without AGN. These values are consistent with the measurements of Kudritzki et al. (2015), who find $-0.1 \lesssim \Delta[\mathrm{O/H}]_\mathrm{g}/\Delta r \lesssim 0$ for their sample of 20 local spiral galaxies, as well as the measurements with CALIFA of Ho et al. (2015) who find a slightly broader distribution.

The upturns in the simulated relationship at high and low masses are likely due to stellar and AGN feedback. In low mass systems in both simulations, stellar feedback is strong enough to move gas from the centre to the outskirts of the galaxy, causing the gradient to flatten. At high masses without AGN, galaxies maintain a high SFR throughout their lives (Fig. 3.4), so stellar feedback may move gas away from the centre of deep potential wells. With AGN, although SF is heavily suppressed, AGN feedback itself is strong enough to remove enriched gas from the galactic centre (see Chapter 6), and more efficiently than can stellar feedback.

As in Section 5.3, we compute KS statistics in different mass bins to test the consistency of the simulations; these values are given in Table 5.2, and the distributions of gradients within these mass bins are shown in Fig. 5.9. The p-values given indicate that we may reject the null hypothesis at the 1 per cent level for the two lower mass bins, both having $p < 10^{-3}$, suggesting that AGN feedback does significantly change the distribution of gas metallicity gradients seen at the present day. The high-mass bin has $p = 0.153$, which does not allow us to reject the null hypothesis at the 1 per cent level, despite the difference in medians seen in Fig. 5.8. This may be due to the very small number of galaxies in this bin, since several of the most massive galaxies from the simulation with AGN are not included because they have very little or no gas, and a measurement of the gradient could not be obtained.

Fig. 5.10 shows the distribution of gas-phase [O/Fe] gradients as a function of stellar mass at $z = 0$ for the galaxies of our simulations. The relation is consistent with being flat, and shows very little scatter ($\sim 0.04\,\mathrm{dex\,kpc^{-1}}$), at all masses in both

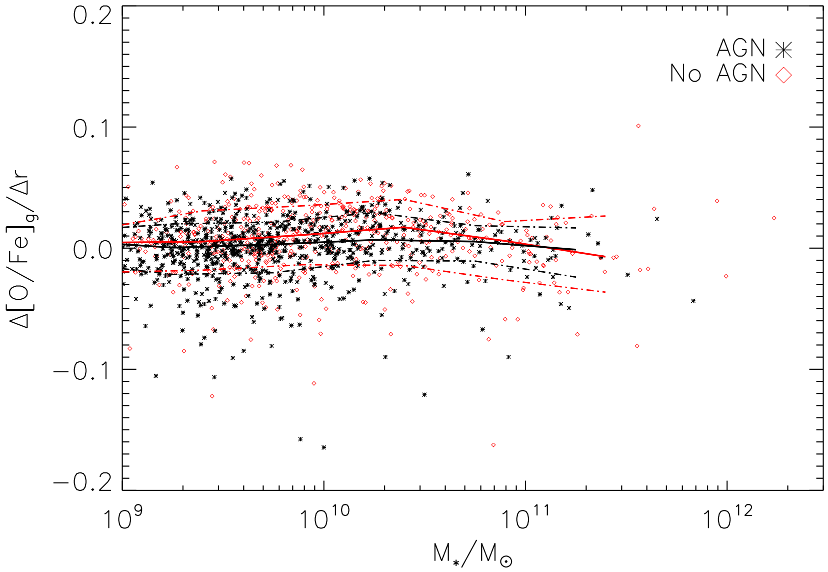

FIGURE 5.10: Same as Fig. 5.2, but for gas-phase [O/Fe] gradients.

simulations, though the galaxies of the simulation without AGN have an average gradient that is slightly positive and larger than those of the simulation with AGN. These trends are made clearer in Fig. 5.11, which shows the distribution of [O/Fe] gradients in three mass bins. In the two lower mass bins, the median gradient is clearly larger when AGN feedback is not included, and the *p*-values given in Table 5.2 for these bins ($\lesssim 10^{-3}$) again suggest that AGN feedback significantly changes the distributions. This is not the case in the high-mass bin, but we again caution that there are very few galaxies in this bin.

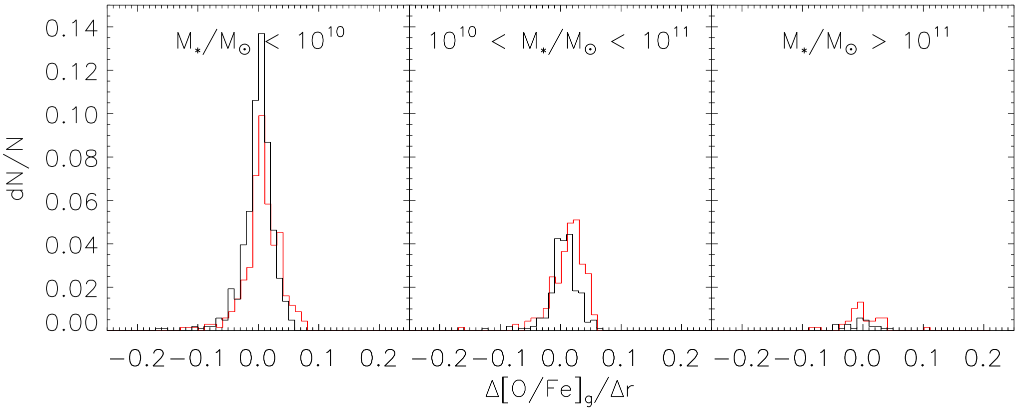

FIGURE 5.11: Same as Fig. 5.3, but for gas-phase [O/Fe] gradients.

5.6 Gas Metallicity Gradients Across Cosmic Time

The influence of AGN feedback on the evolution of gas-phase metallicity gradients in our simulations is relatively simple; Fig. 5.12 shows this evolution for galaxies A, B, and C. In A and B, gas gradients are shallower with AGN feedback, due to its redistribution of enriched gas from the galactic centre to the edges and beyond, and by $z = 0$ both have nearly flat profiles. Mergers play almost no role in determining the gas-phase gradient, other than by triggering AGN feedback. In galaxy C, where AGN feedback is not very strong, there is no difference between the two simulations within the scatter of the measurements.

5.7 Conclusions

We have presented the stellar and gas-phase metallicity gradients of galaxies in our cosmological simulations, both for the full population of galaxies at $z = 0$, and for the lifetime of three example galaxies. By comparing the distribution of metallicity gradients at $z = 0$ obtained with the two different simulations, we found that AGN feedback does not significantly affect stellar metallicity gradients in any mass range. AGN feedback does not affect stars directly, and the galaxy stellar mass–metallicity relation is established at the first star burst, before the onset of strong AGN feedback. Stellar metallicity gradients are, however, significantly affected by galaxy mergers (Section 5.4), with major mergers causing the gradient to become shallower, in keeping with previous findings (Kobayashi, 2004). AGN feedback does affect the number of galaxies that form in the simulation (Section 3.2.2), and can therefore alter the merger history of galaxies (e.g., Fig. 5.6), which may change the evolution of the metallicity gradient of individual galaxies (as seems to be the case for galaxy B). However, given the complicated stellar evolution of galaxies, and the fact that the global distribution of gradients is unchanged, stellar metallicity gradients are more useful as an indicator of the merging histories of galaxies, rather than previous AGN activity.

The gas-phase metallicity gradients, on the other hand, are significantly affected by AGN feedback. We showed in Section 5.5 that the distribution of metallicity gradients at $z = 0$ is altered by AGN feedback, with galaxies having, on average, flatter metallicity profiles. This was true for all but the most massive galaxies ($M_* > 10^{11} M_\odot$), although there are only a small number of such galaxies in our simulations, which may affect the statistics. It may also be the case that stellar feedback in these galaxies when AGN feedback is not included is sufficiently strong, due to the sustained, high star formation rates, that enriched gas is removed from the cores of these galaxies in a similar, if less extreme, manner to AGN feedback. Ideally, a simulation of much larger volume would be needed to resolve this issue by providing a larger sample of high-mass galaxies. Even the lowest-mass galaxies, where local AGN feedback is least effective, had statistically different gradients. This may be due to external enrichment from winds generated in massive galaxies

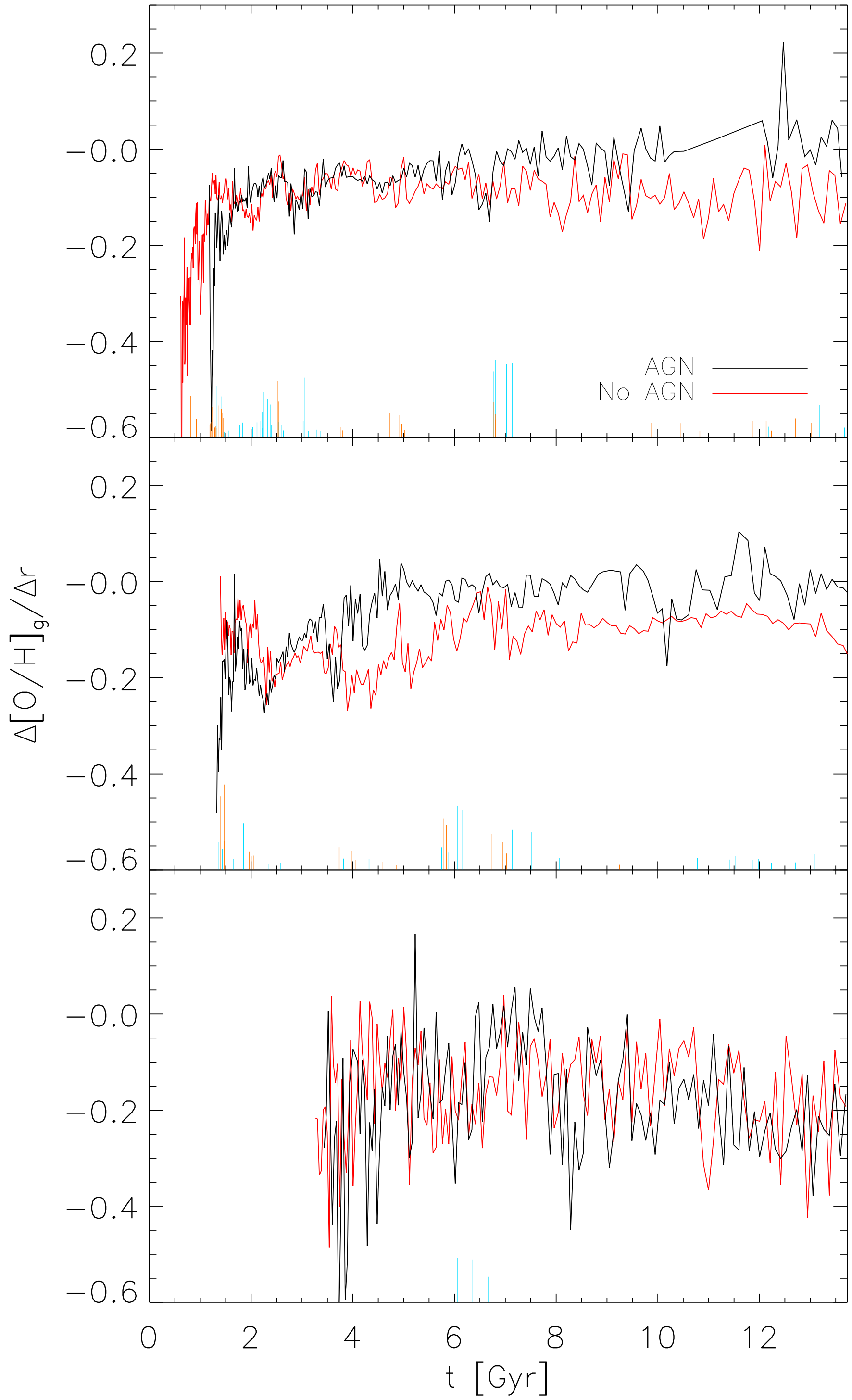

FIGURE 5.12: Same as Fig. 5.6, but for gas-phase oxygen abundance gradient.

(as is the case for galaxy C; see Section 3.2.2), which affect the entire galaxy. In gross terms, AGN feedback tends to homogenize the metallicity structure of the ISM of a galaxy.

The gas-phase gradients were also found to be less dependent on a galaxy's merger history than stellar gradients, and were affected by AGN feedback from moderately high redshift ($z \sim 2$; Section 5.6), although exactly when depends on the galaxy's merger history and triggering of AGN activity. As with stellar metallicity gradients, it is impossible to deduce the evolution of a single galaxy from its gas-phase metallicity gradient at the present day. However, our results imply that it is possible to say statistically whether or not it is likely that a galaxy has been influenced by AGN activity, either directly or through external enrichment, from its present-day gas-phase metallicity gradient. To more accurately determine the evolution of a single galaxy, other data would be useful, if not required, such as: evidence of morphological disturbance; spatially resolved stellar and gas kinematics; and evidence of outflowing gas, as well as information on the galaxy's local environment.

6

Outflows

6.1 Introduction

The importance of feedback from AGN has been underscored by the discovery of the relationship between the mass of the central black hole and the mass of the host galaxy bulge (Magorrian et al., 1998; Kormendy & Ho, 2013), suggesting co-evolution of black holes and their host galaxies. This has already been indicated from the similar shapes between the observed cosmic star formation history (e.g., Madau et al., 1996) and the quasar space density (e.g., Schmidt et al., 1995). AGN feedback has been implemented in cosmological simulations, which provided an excellent agreement with the Magorrian relation (e.g., Springel et al., 2005) and a better reproduction of the cosmic star formation rates (e.g., Booth & Schaye, 2009). The [α/Fe] problem in ETGs also requires AGN feedback, which plays an essential role in quenching star formation in massive galaxies where supernova feedback is inefficient (Chapter 3).

For the quenching mechanism, supernova-driven galactic winds have been proposed (Larson, 1974; Arimoto & Yoshii, 1987), but are not efficient enough for massive galaxies in hydrodynamical simulations with dark matter (e.g., Kobayashi, 2005; Kobayashi et al., 2007). There is observational evidence for galactic winds both locally and at high redshifts, from low-mass star-forming galaxies (e.g., M82, Ohyama et al., 2002) to AGN-hosting massive galaxies (e.g., Centaurus A, Kraft et al., 2009). Supernova-driven winds typically have velocities of a few $10^2 - 10^3$ $\mathrm{km\,s^{-1}}$ and an outflow rate comparable to the star formation rate (e.g., Heckman et al., 2000; Pettini et al., 2000), while AGN-driven winds show much higher velocities and outflow rates. The presence of outflows in luminous quasars and AGN has been evidenced in broad absorption lines (Lynds, 1967). The nearest quasar, Mrk 231, shows a multi-phase outflow containing ionized, neutral (Rupke & Veilleux,

TABLE 6.1: Total and metal (Z, Fe, O) masses of the outflows when they are first identified.

z	$M_{\rm g}$ $10^{10}M_\odot$	$M_{\rm Z}$ $10^{6}M_\odot$	$M_{\rm Fe}$ $10^{6}M_\odot$	$M_{\rm O}$ $10^{6}M_\odot$
0.41	12.3	268.5	27.7	130.0
0.31	8.6	196.6	20.6	93.3

2013; Teng et al., 2014), and molecular gas (Feruglio et al., 2010; Cicone et al., 2012), which may be explained by a bipolar outflow and an accretion disk. Winds are also seen in Seyfert galaxies (e.g., Tombesi et al., 2011, 2013; Pounds & King, 2013; Pounds, 2014), in which velocity probably depends on the distance from the central black holes on ∼pc to ∼kpc scales (Tombesi et al., 2013), and in other ultra-luminous infrared galaxies with velocities depending not on star formation rate but on AGN luminosity (Sturm et al., 2011). At high redshifts, AGN-hosting galaxies also show evidence of outflows (e.g., Nesvadba et al., 2008; Harrison et al., 2012; Maiolino et al., 2012, for $z = 6$). These suggest that AGN feedback should be activate at high redshifts. This is the case in our AGN model where super-massive black holes originate from the first stars.

Galactic winds are the most plausible origin of mass–metallicity relations of galaxies (e.g., Tinsley, 1980); low-mass galaxies have lower metallicities because of larger metal loss by winds (Kobayashi et al. 2007, see also Davé et al. 2011). These metals are distributed to the circumgalactic medium (CGM), intracluster medium (ICM), and intergalactic medium (IGM). The detailed mechanism of this metal transport has not been well-studied yet. Direct observations of outflows from AGN and of chemical abundances near AGN will provide another stringent constraint on the modelling of AGN in galaxy simulations. In Chapter 3, we showed that the mass–metallicity relation is preserved when AGN feedback is included, even though the mass of metals in massive galaxies is reduced; in this chapter we will investigate how the matter and heavy elements are redistributed from galaxies to the CGM and IGM by AGN-driven winds.

In this chapter, we investigate two unambiguously AGN-driven outflows identified emanating from the most massive galaxy (A) in our cosmological simulations. In Section 6.2, we describe how the gas particles that constitute the outflows are identified, before describing their impact on the metallicity of the host galaxy, CGM, and IGM in Section 6.3. Finally, we present our conclusions in Section 6.4.

6.2 Definition of Outflows

We detect inflows and outflows by tracing gas particles for the lifetime of galaxy A (Section 3.2.2). We first look at the net radial galactocentric momentum (measured in the galaxy's rest frame) of gas particles towards the outskirts of the galaxy,

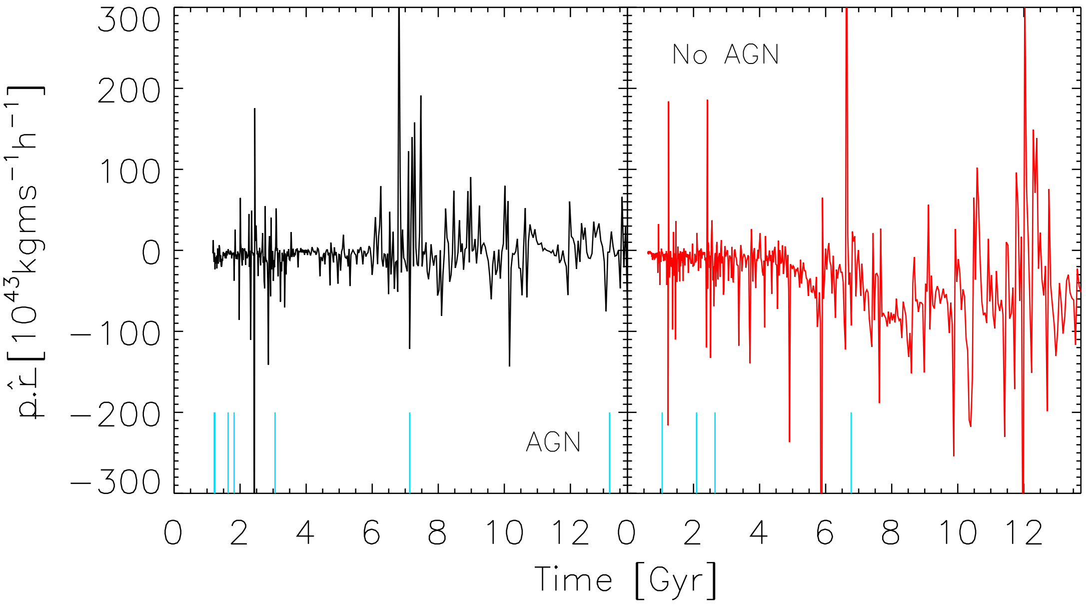

FIGURE 6.1: Net radial momentum of all gas particles in a shell $20 - 25h^{-1}$ kpc from the centre of the largest galaxy (at $z = 0$) in the simulation across cosmic time. Positive and negative values indicate a net outflow and inflow of gas through the shell, respectively. This value is shown for the simulation with (without) AGN feedback in the left (right) panel. In both panels, blue vertical lines indicate the occurrence of major mergers.

specifically at galactocentric radii $20h^{-1}$ kpc $< r < 25h^{-1}$ kpc, for the lifetime of the galaxy. This range was chosen to be close enough to the galaxy that gas particles passing through the shell could be associated with the galaxy, but sufficiently distant that the orbits of gas within the galaxy would not affect it. This quantity is shown as a function of time for both simulations with and without AGN feedback in Fig. 6.1. Negative values indicate a net inflow of gas; at late times, the galaxy without AGN (right panel) shows prolonged accretion of gas, punctuated by short-lived, supernova-driven winds. The same is not true of the galaxy when AGN feedback is included (left panel); at late times, there are a number of long-lived events in which the galaxy loses gas, most clearly between 10.5 and 12 Gyr. In both panels, blue lines indicate the occurrence of major mergers (defined as having a mass ratio of 1:3 or greater).

Although disentangling the contributions from AGN and stellar processes is not trivial, two very massive outflows at $t \sim 9.2$ Gyr ($z = 0.41$) and $t \sim 10.1$ Gyr ($z = 0.31$) are unambiguously AGN-driven, and so we further analyse these. In order to define the outflows, we determine which gas particles form them. Since we are searching for AGN-driven outflows, we expect their constituent particles to be travelling radially from the galaxy centre. Therefore, we select those particles within $500h^{-1}$ kpc of the galaxy whose radial momentum exceeds 95 per cent of its total momentum, p, i.e. $\boldsymbol{p} \cdot \hat{\boldsymbol{r}} > 0.95p$. Choosing a slightly higher or lower threshold does not affect our results in the following sections. Fig. 6.2 gives a visualization

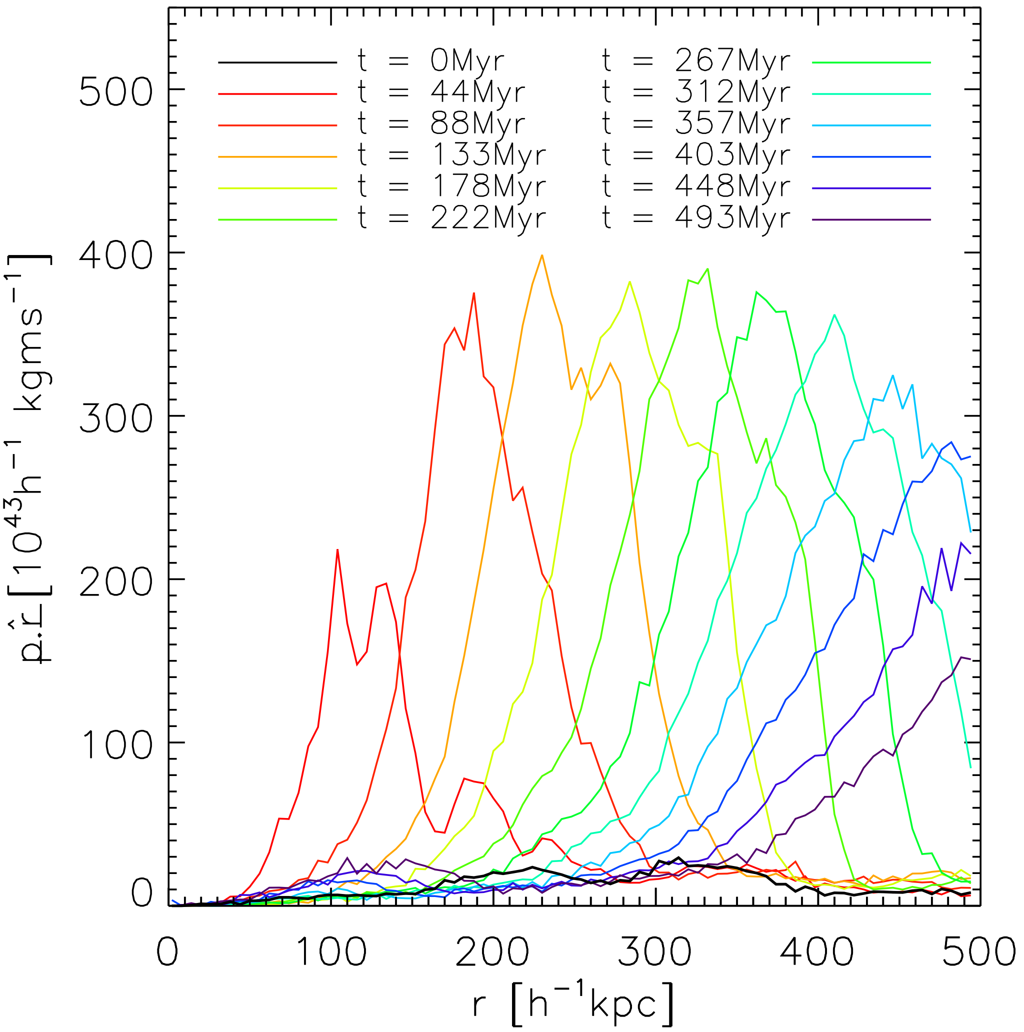

FIGURE 6.2: Radial distribution of the net radial momentum of outflowing gas particles (see text for definition), within $500h^{-1}$ kpc of the most massive galaxy in the simulation with AGN. We show this distribution at several different times (labelled relative to 9.201 Gyr after the Big Bang), allowing the progression of the outflow away from the galaxy to be seen.

of the outflow at $t \sim 9.2$ Gyr from the centre of galaxy A, showing the radial distribution, at several epochs, of the particles obtained by the above method. Times are given relative to the time of the snapshot immediately preceding the outflow's identification, 9.201 Gyr after the Big Bang (black line). The progression of the outflow from the galaxy into the IGM is clear, and it can also be seen to become broader and more massive as it sweeps up other gas particles.

The total masses and metal masses of the AGN-driven outflows when they are first identified (red line of Fig.6.2) are given in Table 6.1. In order to decouple the outflow caused by the AGN and the (AGN-enhanced) supernova wind, we ignore the particles identified from the snapshot immediately preceding it (i.e. the black line in Fig. 6.2). Those particles that remain are defined to be the AGN-driven outflow; they are hot ($T > 10^7$ K) and low-density ($\sim 10^3\ m_{\rm H}\ {\rm m}^{-3}$). Compared with the total gas mass $4.4 \times 10^{12} M_\odot$ in R_{200}, the outflow mass is rather small. However, over the next several 100 Myr they travel further into the IGM, heating and chemically enriching it (Section 6.3).

We also estimate the velocity of these outflows. To each of the radial distributions in Fig. 6.2 we fit a Gaussian function in order to estimate its centre, from which we calculate an average speed at various stages of the outflow. These velocities are ~ 3900 and ~ 3400 km s^{-1} near the galaxy for the outflows at $z = 0.41$ and 0.31, respectively, falling to ~ 1000 km s^{-1} at larger scales and later times. With values for the mass and speed of the outflows, we can also estimate their kinetic energies (albeit with large uncertainties) to be $\sim 10^{60-61}$ erg. Note that the physical scale of our wind is much larger than for the available observations (Section 6.1), and our estimates of velocity and energy are larger than the observational estimates.

With our usual timestep between simulation snapshots ($\sim 25 - 45$ Myr at these redshifts), these outflows are identified when they are already far from galactic centre (> 100 kpc). Therefore, we re-run the same simulation from the snapshot immediately preceding the outflow at 9.201 Gyr (i.e., from the black line to the red line in Fig. 6.2), producing a larger number of snapshots with timesteps of $\sim 175,000$ yr. This allows us to trace the initial phase of the outflow, which is necessary to understand its origin. The super-massive black hole in this galaxy undergoes a period of accretion at 75 per cent its Eddington rate, which heats a small amount of gas close to the black hole. On such a small scale, the gas is not distributed homogeneously and isotropically around the black hole, and so it is not straightforward to estimate the velocity. If we measure the initial velocity with a kernel-weighted average of the radial velocity of the 72 gas particles nearest to the black hole, we obtain ~ 8000 km s^{-1}, which is comparable to observations of AGN-driven outflows on very small scales (Tombesi et al., 2010, 2011; King et al., 2013; Tombesi et al., 2013; Pounds, 2014). The outflowing gas soon slows and entrains more gas, eventually stalling ~ 100 kpc from the black hole. This suggests that there are at least 2 separate accretion events, separated by at most 88 Myr (since the second event must happen between the times corresponding to the red and dark orange lines of Fig. 6.2), which power the outflow seen at $z = 0.41$ on the largest scales. The AGN energy produced by this accretion is able to account for the kinetic energy of the large-scale outflow.

6.3 Metal Content of Outflows

We show in Fig. 6.3 the net flux of metal mass through a shell at $20h^{-1}$ kpc $< r < 25h^{-1}$ kpc from the centre of the galaxy, analogous to the radial momentum flux of Fig. 6.1. As in Section 6.2, there is a trend for net accretion of metals when

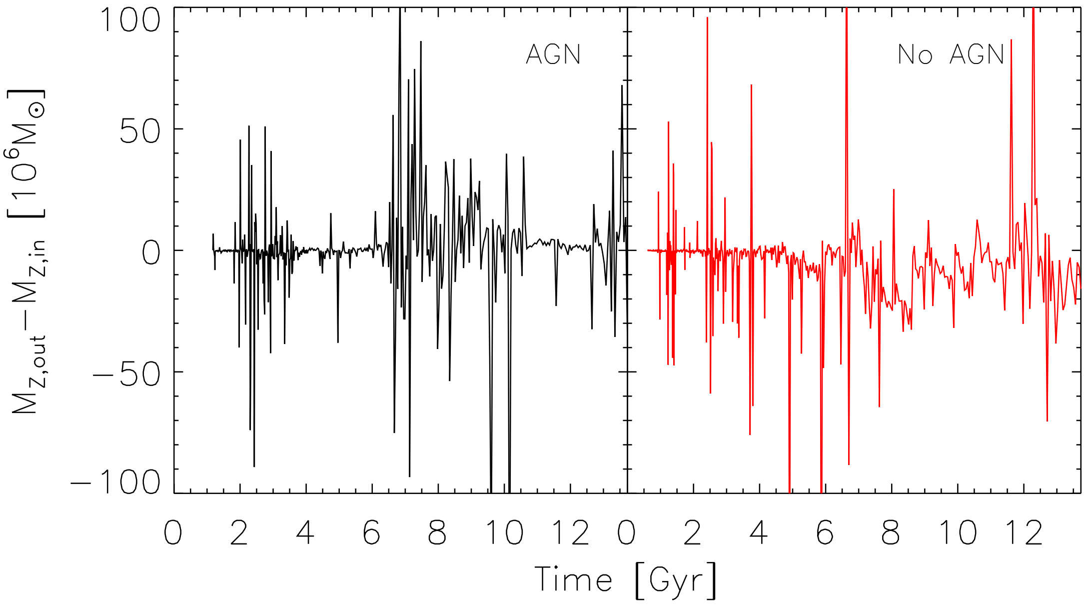

FIGURE 6.3: Net flux of metal mass of all gas particles in a shell $20 - 25h^{-1}$ kpc from the centre of the largest galaxy at $z = 0$ in the simulation, across cosmic time. Positive and negative values indicate a net outflow and inflow of metals through the shell, respectively. This value is show for the simulation with (without) AGN feedback in the left (right) panel.

AGN feedback is not included, but a net loss of metals with AGN.

This can be seen even more clearly in the top panel of Fig. 6.5, in which we show the metal mass in the central comoving $10h^{-1}$ kpc of the galaxy, normalized by the total metal produced by stars (by $z = 0$), as a function of time. With AGN, the galaxy has $3.4 \times 10^{11} M_\odot$ of stars in its central $10h^{-1}$ kpc, while without AGN the stellar mass is $1.2 \times 10^{12} M_\odot$. Although the star formation rate is lower at all times (Fig. 3.2), initially the metal mass is larger with AGN feedback, since star formation and the subsequent supernova feedback are suppressed early in the life of the galaxy, and therefore a lower fraction of metals are ejected compared to the simulation without AGN feedback. At later times, after the black hole has grown to be super-massive, strong AGN feedback removes a much larger fraction than supernovae alone. The blue arrows in Fig. 6.5 denote the times that the large AGN-driven outflows occur, as determined by the method of Section 6.2. It can be seen that they correspond exactly with sudden drops in the metal content of the galaxy. In fact the values of these drops match very closely with the values given in Table 6.1, obtained by identifying the outflowing particles at much greater radii, lending credence to the method in Section 6.2.

Similar drops are seen for the gas mass and the gas fraction, as shown in Fig. 6.4. At ~ 8 Gyr, this galaxy contains a significant amount of gas (a few $\times 10^9 M_\odot$ in $10h^{-1}$ kpc). The gas mass suddenly decreases due to the outflow at 9.2 Gyr, but

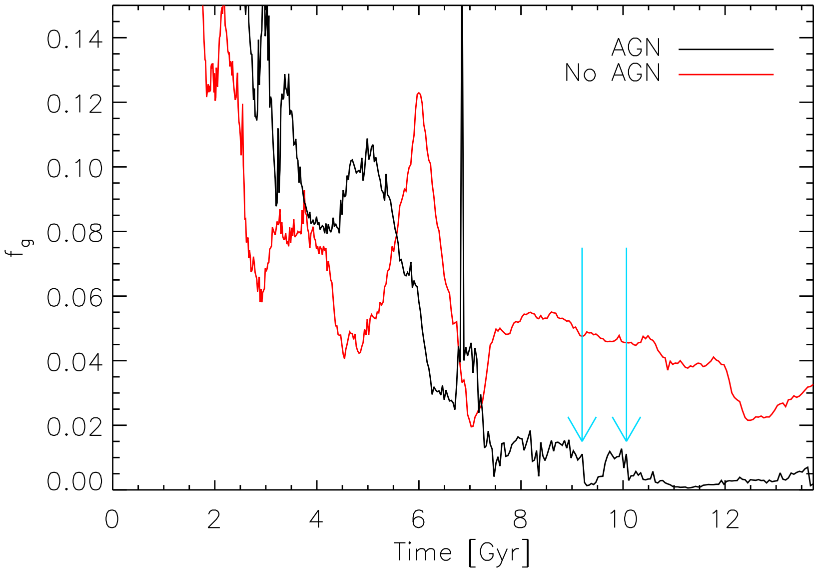

FIGURE 6.4: Evolution of gas fraction, $f_{\rm g} = M_{\rm g}/(M_{\rm g} + M_* + M_{\rm BH})$, in the galaxy over cosmic time, measured in the central comoving $10h^{-1}$kpc of the galaxy. The black (red) line indicates the simulation with (without) AGN feedback. The blue arrows indicate the times that the large outflows are first identified by the method of Section 6.2.

recovers quickly in only a few ×100 Myr, which suggests that cold streams are not disrupted for long, even with this powerful outflow. However, by tracing the ID numbers of gas particles, we find that most of the outflowing gas at 10.1 Gyr does not fall back to the centre later. At $\gtrsim$ 10 Gyr, the gas mass becomes lower than $10^9 M_\odot$, which results in a gas fraction below one per cent, significantly lower than five per cent in the case without AGN feedback.

The metallicities of the outflowing gas are much lower than the average gas-phase metallicity of the galaxy in $10h^{-1}$ kpc (interstellar medium (ISM) in Table 6.2). This is because the gas fuelling the black hole originates outside the galaxy from cold flows that have undergone much less chemical enrichment; by tracing the particles back through the simulation to high redshift, we find that $\sim$ 97 per cent of the gas that constitutes the $z = 0.41$ outflow originates in cold flows. The ISM metallicity increases slightly from 0.33 to 0.37 at the $z = 0.41$ outflow, due to the removal of this low-metallicity gas.

Some of the ejected material accretes back onto the galaxy, and is present in the second large outflow $\sim$ 860 Myr later. At $t \gtrsim 12$ Gyr, the metal mass of the ISM increases (Fig. 6.5). We can identify this origin by tracing the particles, and find that it is due to both in-situ star formation within the galaxy and mergers with gas-rich satellites. As a result, the present gas-phase metal fraction is only a few per cent lower than the case without AGN feedback; this is the reason why AGN

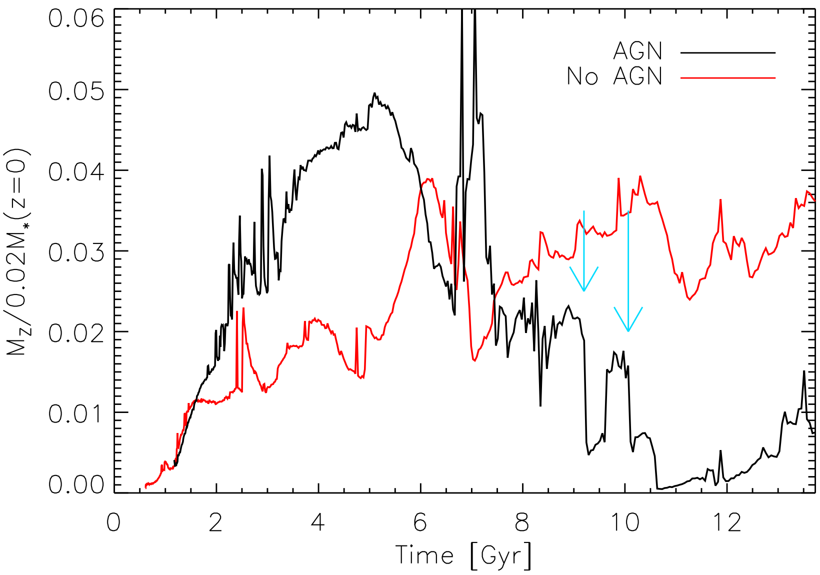

FIGURE 6.5: Evolution of metal mass in the galaxy over cosmic time, normalized with the total metal produced from the stars at $z = 0$, i.e. the net yield $\times M_*(z = 0)$. This quantity is measured in the central comoving $10h^{-1}$kpc of the galaxy. The black (red) line indicates the simulation with (without) AGN feedback. The blue arrows indicate the times that the large outflows are first identified by the method of Section 6.2.

feedback does not affect very much the mass-metallicity relations (Chapter 3).

The AGN-driven outflows remove a significant fraction of the galaxy's metal mass, transporting it to the CGM and the IGM. Table 6.2 gives the present metallicities of the CGM, measured in $r < 150h^{-1}$ kpc, and of the IGM, which is calculated for all gas particles that do not belong to Friend of Friends groups. In this simulated galaxy, the oxygen mass of the CGM is $8.1 \times 10^8 M_\odot$, which is more comparable to the lower limit of $\sim 10^7 M_\odot$ estimated by Tumlinson et al. (2011) than the simulation without AGN ($1.4 \times 10^9 M_\odot$). However, the fraction of CGM metals relative to the total produced in the Galaxy A is higher with AGN feedback (17.6 per cent and 13.2 per cent with and without AGN feedback, respectively), which results in the higher metallicity, [M/H] $= -0.78$. With AGN feedback, 18.4 per cent of the total produced metals in the simulation box are in the IGM at $z = 0$, compared with only 9.6 per cent when it is not included. The IGM metallicity is also higher than the case without AGN, and [M/H] $= -1.78$; this is higher than the estimate by Schaye et al. (2003), but there is a large variation in metallicities within the simulation box. Note that, different from the simulation in Kobayashi et al. (2007), our simulation has a central concentration of galaxies, which may cause the relatively high metallicity of the IGM.

Finally, we find a difference in the elemental abundance ratio in the lower redshift outflow (see Table 6.2); [O/Fe] ratio of the outflowing gas is -0.18, which is lower than for the ISM in the galaxy ([O/Fe] $= 0.14$). The opposite trend is seen in the

TABLE 6.2: Metal abundances and [O/Fe] of the IGN and CGM at $z = 0$, as well as the outflows, and the ISM at the redshifts of the outflows.

	[M/H]	[Fe/H]	[O/H]	[O/Fe]
CGM (AGN)	-0.80	-0.67	-0.78	-0.14
CGM (No AGN)	-0.96	-0.73	-0.96	-0.20
IGM (AGN)	-1.78	-1.77	-1.72	0.00
IGM (No AGN)	-2.00	-2.12	-1.92	0.16
Outflow ($z = 0.41$)	-0.97	-0.78	-0.96	-0.09
ISM ($z = 0.41$)	0.39	0.62	0.39	-0.22
Outflow ($z = 0.31$)	-0.95	-0.75	-0.94	-0.18
ISM ($z = 0.31$)	0.13	0.17	0.17	0.14

higher redshift outflow. This may correspond to the selective mass-loss discussed in Kobayashi (2005). Even after star formation is quenched by the first outflow, Fe is produced by SNe Ia with a long delay. The second outflow may be collecting this SNe Ia contribution. On the other hand, supernova-driven outflows should contain higher [α/Fe] ratios as seen in Martin et al. (2002). Observational estimates of the metallicities and elemental abundance ratios of outflows are very important to put further constraints on the modelling of AGN feedback.

6.4 Conclusions

We have shown that AGN feedback drives massive outflows from the most massive galaxy in our cosmological simulations. These outflows remove gas and metals from the host galaxy, and enhance metal-rich supernova-driven winds, causing the CGM and the IGM to become hotter and display greater chemical enrichment compared to the simulation without AGN. Nonetheless, the mass–metallicity relation of galaxies is not affected very much by AGN feedback.

With AGN feedback, it is clear from Figs. 6.1 and 6.3 that the net rate of inflow of both gas and metals into the galaxy is reduced across cosmic time. Focusing on the two most massive outflows detected by the net flows, we visualize the motion of outflowing gas (Fig. 6.2) and quantify the AGN-driven mass and metal ejection (Tables 6.1 and 6.2). By tracing the particles, we find that most of outflowing gas originates in metal-poor cold flows, and that most of metals in outflowing gas do not fall back to the centre of the galaxy by the present. We also find evidence for 'selective' mass loss of iron relative to oxygen (Section 6.3). AGN feedback is an important process not only to quench star formation at late times in massive galaxies, but also to explain chemical enrichment in circumgalactic and intergalactic medium.

7
Conclusions

In this chapter, I present a summary of the work undertaken for this thesis, and the conclusions we have drawn from it. I will also discuss the limitations of what we have done, as well as avenues for future study.

7.1 Summary and Conclusions

The work presented in this thesis has, in broad terms, been concerned with AGN feedback in cosmological, hydrodynamical simulations. Therefore, we introduced our model for BH physics and AGN feedback in Chapter 2. This consists of BH formation, BH growth via gas accretion and merging, and energy feedback to neighbouring gas particles. The BH growth and energy feedback prescriptions are as standard in the literature, but we seed BHs from primordial gas of high enough density, rather than based on DM halo properties. With the model constructed, we found the set of model parameters that gave a simulation that best reproduced the cosmic SFR and present-day M_{BH}–σ and R_{e}–σ relations for galaxies, and adopted these as our fiducial set in subsequent chapters. This investigation suggested that the initial BH mass needed to be only $M_{\mathrm{seed}} = 10^{2-3} h^{-1} M_{\odot}$, which is significantly smaller than in previous works, and is consistent with Population III stars being the progenitors of the present-day super-massive BHs.

In Chapter 3 we introduced a new pair of simulations, one without AGN and one run with our fiducial model, which have over 15 times the volume of the simulations of Chapter 2. With these, it was possible to see the effects of AGN feedback on the population of galaxies as a whole, as well as looking in more detail at how it influenced three individual galaxies matched between the two simulations. We were able to match fairly well several key observables at $z = 0$, including the galaxy stellar mass function, with a generally better agreement between simulation and observations when AGN feedback was included. Indeed, we found that it was required for AGN feedback to be included in order to reproduce indicators of downsizing, such as the colour–magnitude and $[\alpha/\mathrm{Fe}]$–σ relations.

In Chapter 4, we extended our comparison of simulations and observations out to high redshift ($z = 4$), and examined how our population of galaxies evolved across cosmic time, and what changes were introduced by AGN feedback. The effects of AGN feedback became most noticeable at $z \lesssim 1-2$, once BHs had grown sufficiently massive. This growth occurred in parallel with the growth of galaxies since there was no evolution seen in the M_{BH}–σ relation. Agreement with observations tended to be less good at high redshifts, but observational data were subject to larger uncertainties too. Additionally, our simulation volume is not large enough to be cosmologically representative, and high-redshift brightness-limited observations may be subject to the Malmquist bias. We again found evidence for downsizing, whereby the most massive galaxies attained their present-day metallicities earlier and faster than lower mass galaxies. As in Chapter 3, AGN feedback was an essential ingredient in our simulations to help reproduce observations.

The work of Chapter 5 took advantage of the hydrodynamical nature of our simulations, where we investigated the stellar and gas-phase metallicity gradients of our galaxies at both $z = 0$ and across cosmic time. Galaxy mergers were found to make stellar metallicity gradients shallower, in agreement with the findings of previous studies, but had little effect on gas-phase metallicity gradients. By contrast, AGN feedback was found to make gas-phase metallicity gradients shallower, but had little effect on the stellar metallicity gradients. These results suggest that observing both the stellar and gas-phase metallicity gradients of galaxies could offer information about both their merging and AGN history. We also found yet more evidence for downsizing in the evolution of our galaxies in the (positive) stellar [O/Fe] gradients at $z = 0$, which were found to be shallower in more massive galaxies, indicating a shorter SF timescale in the centre of these systems.

Finally, we focused on a single simulated galaxy in Chapter 6 - the most massive at $z = 0$ - and investigated the effect AGN-driven outflows had on both the galaxy and its surroundings. The gas fraction and metal mass of the galaxy were significantly reduced by two strong outflows identified at $z \sim 0.41$ and $z \sim 0.31$. The ejected material caused heating and chemical enrichment of the IGM compared to the simulation without AGN feedback, and therefore AGN feedback may be necessary to explain the observed metallicity in clusters.

We have shown that our model for AGN feedback in cosmological hydrodynamical simulations is able to produce a population of galaxies with realistic properties that compare well with observations. Although our simulation volume is only fairly small ($(25h^{-1}\ \mathrm{Mpc})^3$), our results compare relatively favourably with recent, large-scale simulations such as Illustris and EAGLE.

7.2 Future Work

The model for AGN feedback introduced in Chapter 2 has produced more realistic simulations, despite its relative simplicity. Of all its underlying assumptions, perhaps the most troubling is that of Bondi-Hoyle gas accretion, which assumes spherical accretion in the Newtonian regime, and in our simulations is active on scales of $\sim$kpc. In reality, accretion most likely takes place from a disc around the BH on significantly smaller scales, and the method by which the gas loses angular momentum is an important consideration. This configuration may also lead to highly collimated jet outflows, which are not included in our model. In order to better understand the importance of this small-scale AGN physics, we are preparing (in collaboration with G. Bicknell and A. Wagner) to run galaxy-scale simulations using regions of our simulations for the initial conditions, so that the galaxy evolves in a cosmological setting.

To further highlight the need for improved subgrid modelling, we mention some of the difficulties even state of the art simulations like Illustris and EAGLE have in comparison to those presented in this thesis. The properties of low mass, but resolved, galaxies ($M_* \lesssim 10^{10} M_\odot$) are often more difficult to reproduce than their more massive counterparts. We showed in Fig. 4.1 the galaxy mass function at different redshifts, finding that too many low mass galaxies were produced at low redshift compared to observations; this was also the case in the Illustris simulations (Genel et al., 2014), while the EAGLE simulations produced an excess of low mass galaxies at $z \sim 2$. Our low mass galaxies were also over-enriched with respect to the SDSS results of Gallazzi et al. (2005, see Fig. 4.7), and this trend was also seen in the EAGLE simulations (Schaye et al., 2014), though both EAGLE and our simulations reproduced the gas phase MZR well. Even global properties like the cosmic SFR cannot be fully reproduced: at low redshift, both Illustris and our simulations over-predict the SFR by ~ 0.3 dex (Genel et al., 2014, Fig. 3.2), while EAGLE has ~ 0.2 dex too little star formation at $z \lesssim 3$ (Furlong et al., 2015). It is also worth noting that Sijacki et al. (2015) suggest that the value of $\epsilon_{\rm f} = 0.05$ used in Illustris may need to be a factor of $2 - 4$ larger since they assumed a radiative efficiency $\epsilon_{\rm r} = 0.2$, which may be too large to match the observed AGN luminosity function. However, the inability of different models to use a consistent value, or for that value to agree with what observational estimates exist ($0.02 \lesssim \epsilon_{\rm f} \lesssim 0.06$; e.g., Feruglio et al., 2010; Cicone et al., 2012), perhaps hints at the limitations of the models themselves to faithfully capture the relevant physics occurring on scales much smaller than can be resolved.

There are, of course, small updates to the model that can be made:

- $M_{\rm seed}$ is not expected to be constant, but will depend on local properties like the Jeans mass and cooling rate, and therefore should follow some distribution (analogous to the IMF for stars). At present, this distribution is unknown, but work such as Hirano et al. (2014) will help inform this problem.

- The assumption that $\epsilon_{\rm f}$, too, is constant is a simplistic one. In reality, its values should depend on the local gas density and metallicity, as well, possibly, as the BH accretion rate in order to mimic the quasar and maintenance modes of AGN feedback. Indeed, a metallicity dependence may work to reduce the excessive number of low-mass galaxies seen in the simulation with AGN feedback (Chapter 4): a parameterization of the form

$$\epsilon_{\mathrm{f}}(Z) = \epsilon_{\mathrm{f},0}\left(1+\frac{Z}{Z_{\odot}}\right)^{\zeta}, \tag{7.1}$$

with $\zeta > 0$, would achieve this, but would introduce an additional free parameter into the model.

- It may also be the case that the relatively large value of $\epsilon_{\mathrm{f}} = 0.25$ that is necessary in our model is due to losses from radiative cooling. In some other works (e.g., Schaye et al., 2015), feedback energy from BHs is 'stored' until it is able to heat the surrounding gas to some minimum temperature so that these losses are negligible. In our model, which does not do this, we may need to couple more energy to the gas to compensate for these losses.
- Since we link the formation of super-massive BH seeds with star formation in the early universe, adopting different BH formation criteria that mirror more closely star formation criteria (e.g., Federrath et al., 2010) may remove the strong resolution dependence on the value of ρ_{c} (Section 2.6).

Our investigation into AGN-driven outflows (Chapter 6) has, so far, focused almost exclusively on their effects on the IGM, however many important questions remain:

- What is the origin of the fuel for these outflows (mergers or cold flows)?
- What is the fate of the ejected gas?
- On what galaxy mass scales do these outflows occur?
- Is there an environmental/morphological dependence?

These questions lie at the heart of understanding the evolution of BHs and their host galaxies.

Finally, it is encouraging to note that the simulation 025mpc240 produces a much more massive BH ($10^{8.6} M_{\odot}$ at $z = 0$) in its biggest galaxy than does 010mpc096 ($10^{8.0} M_{\odot}$). It would therefore be interesting to run a simulation of much higher volume ($\gtrsim$ 100 Mpc) until $z \sim 4$ to investigate the high redshift population of BHs, and compare to the observations of extremely massive BHs in the early universe (e.g., Wu et al., 2015). The ability or otherwise of this model to reproduce such observations could then inform theories regarding their formation.

A

Code Efficiency Test

In this appendix we present the results of a simple test of the speed of the simulation code on different numbers and types of compute node, for different box sizes and resolutions, and when AGN is switched on or off. In all cases, the 500^{th} snapshot of the relevant simulation (corresponding to $z = 6.07$) is used for the initial conditions, and the simulation is run until snapshot 600 ($z = 3.78$). This redshift range was chosen to cover the epoch when BHs have their greatest number density, at $z \sim 5$. Timing each run was performed within the code, and the time taken printed at completion.

The different types of node used are designated 'CAR' and 'Main'. CAR consists of two chassis of 16 nodes, each of which hosts 12 cores, giving 192 cores per chassis. One chassis is formed of Xeon X5650 processors, the other of Xeon X5675s; both have quad data rate (QDR) infiniband. Main is made up of 3 chassis of 16 nodes, each of which hosts 8 cores, and is formed of the older Xeon E5520 processors, using double data rate (DDR) infiniband. Communication between nodes on a common chassis is via switches internal to that chassis, while inter-chassis communication is via external switches and tends to be slower.

Fig. A.1 shows how the time taken for each of these runs depends on the number of cores used, as well as whether AGN was turned on or off (star and diamond symbols, respectively), and whether it was run on the CAR or Main nodes (dashed and solid lines, respectively). Simulations 010mpc096 and 010mpc128 from Chapter 2, and the larger volume simulations introduced in Chapter 3 (025mpc240 by the naming convention of Chapter 2), are used for this study (black, red, and blue lines, respectively). In general, simulations involving a greater number of particles tend to take a greater time to run on a given number of cores. Additionally, simulations run on Main nodes tend to take slightly longer than their counterparts on CAR, presumably due to the cores on CAR being newer and faster. It can also be seen

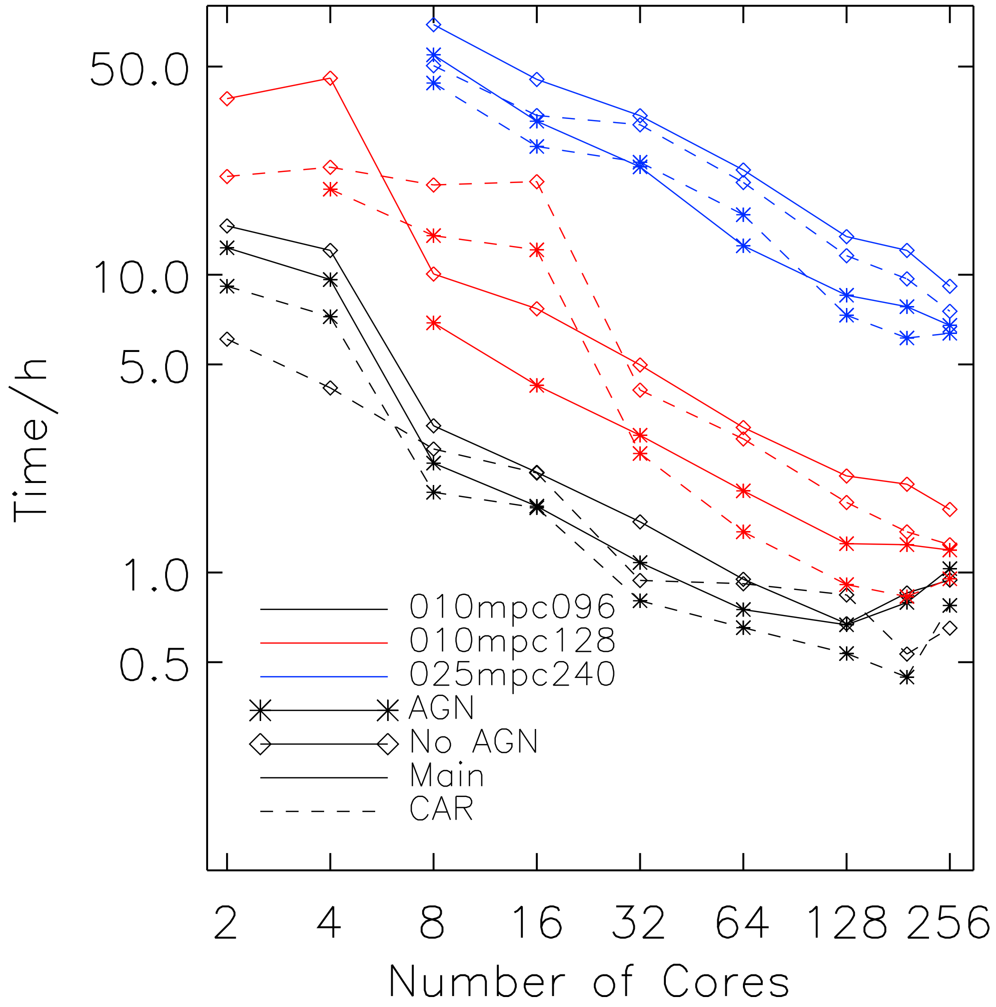

FIGURE A.1: Time taken for simulation runs for different numbers and types of compute node, box sizes and resolutions, and when AGN is switched on or off.

that simulations with AGN tend to run more quickly than without, despite the extra burden of the AGN code. This is because the numbers of BH particles remains relatively small compared to stars, and so does not introduce much extra computational overhead, but AGN feedback does lower the number of star particles so that stellar feedback, and, of particular importance, chemical enrichment calculations are reduced. This more than makes up for the additional computation needed for the BHs.

Interestingly, 010mpc096 seems to run most efficiently with ∼ 128 Main cores, or ∼ 192 CAR cores; with more, time spent on inter-core data exchange exceeds the gains made by the code's parallel nature. The fact that this happens at a larger number of cores on CAR may be due to its use of QDR infiniband compared to DDR on Main. It may also be affected by the fact that communication between chassis is necessary with more cores. The simulations with more particles do not show such an effect up to 256 cores.

B
The Effective Radius

In this appendix, we describe the fitting procedure used to obtain galaxy effective radii, R_e. As well as providing R_e, it also gives the galaxy stellar masses used throughout this thesis (referred to below as M_∞ to distinguish them from the FoF stellar mass, M_FoF), and, as such, underpins many of the results presented. Instead of the Sérsic or de Vaucouleurs profiles often used, we opt to fit the surface density (or brightness) with a core-Sérsic profile (Graham et al., 2003; Trujillo et al., 2004):

$$\Sigma\left(r\right) = \Sigma_b 2^{-\gamma/\alpha} \exp\left(b\left(2^{1/\alpha}\frac{r_b}{R_e}\right)^{1/n}\right)\left(1+\left(\frac{r_b}{r}\right)^{\alpha}\right)^{\gamma/\alpha} \exp\left(-b\left(\frac{r^\alpha + r_b^\alpha}{R_\mathrm{e}^\alpha}\right)^{1/\alpha n}\right). \tag{B.1}$$

This allows us to fit the entire surface density profile to $r = 0$ since the region within the gravitational softening length is fitted by the core part of the profile. This is advantageous since it does not introduce artificial effects caused by choosing an inner fitting radius.

At $r \gg r_b$, equation (B.1) reduces to the standard Sérsic formula,

$$\Sigma\left(r\right) = \Sigma_0 \exp\left(-b\left(\frac{r}{R_\mathrm{e}}\right)^{1/n}\right), \tag{B.2}$$

with some suitable relation between Σ_b and Σ_0, while at $r \ll r_b$ it is a power law with slope γ. The parameter r_b itself is where the transition between these two regimes takes place, and α controls how sharply, with larger α producing a sharper transition. n is the Sérsic index, and b a function of n, often parameterized in a simple way (e.g., Caon et al., 1993; Graham et al., 2001):

$$b \approx 1.9992n - 0.3271, \tag{B.3}$$

for $1 \lesssim n \lesssim 10$. We do not assume this form of b, and instead treat the combination $b/R_\mathrm{e}^{1/n}$ as a single parameter, k, to be fitted. In practice, it is often difficult to find converged fits with physically meaningful parameters, and so we fix the value of $n = 4$. This is different to what is done in observations, where n is allowed to vary (and is found to correlate well with morphology).

The star particles of each FoF group undergo the procedure described in Appendix G, and then binned radially from the group's centre of mass. $\Sigma(r)$ is then obtained by calculating the average surface density in each annulus. To this is fitted, using `mpfit` (Markwardt, 2009), equation (B.1). From this we obtain the total stellar mass of the galaxy,

$$M_\infty = \int_0^\infty 2\pi r \Sigma(r) \mathrm{d}r \tag{B.4}$$

which must be integrated numerically. We define a 'good' fit as one for which M_∞ satisfies

$$0.9 < \frac{M_\infty}{M_{\mathrm{FoF}}} < 1.1. \tag{B.5}$$

Empirically, the majority of galaxies satisfy this criterion. For those that do not, we attempt to fit a Sérsic function (equation (B.2)), and apply the same criterion. Some galaxies are not well-fit by either function, as defined by equation (B.5); these tend to be near our resolution limit, or are merging systems.

For those galaxies that do satisfy equation (B.5), the effective radius, R_{e}, is the solution of

$$\frac{1}{2} M_\infty = \int_0^{R_{\mathrm{e}}} 2\pi r \Sigma(r) \mathrm{d}r. \tag{B.6}$$

B.1 Future Improvements

While the method described above works reasonably well for most galaxies, it does have some drawbacks: it assumes all galaxies have no ellipticity; and the smoothing of particles can still be quite noisy, depending on the number of new particles created and the widths of the annular bins. We have recently developed a new method for calculating smoothed quantities as a function of particle position for our analysis: we assume a Gaussian smoothing kernel as in Appendix G

$$\mathcal{G}(\mathbf{r}) = \frac{1}{\sqrt{2\pi (0.3\epsilon)^2}^3} \exp\left(-\frac{\mathbf{r}\cdot\mathbf{r}}{2\,(0.3\epsilon)^2} \right), \tag{B.7}$$

so the contribution of a particle at $\mathbf{p} = \begin{pmatrix} p_0 \\ p_1 \\ p_2 \end{pmatrix}$ to the cell defined by $\mathbf{x}_l$ and $\mathbf{x}_u$ is

$$f_{\mathrm{cell}} = \frac{f}{8} \prod_{i=0}^{2} \left(\mathrm{erf}\left(\frac{x_{u,i} - p_i}{0.3\sqrt{2}\epsilon} \right) - \mathrm{erf}\left(\frac{x_{l,i} - p_i}{0.3\sqrt{2}\epsilon} \right) \right), \tag{B.8}$$

where f denotes the value of an extrinsic property of the particle at $\mathbf{p}$, and $\mathrm{erf}(x)$ is the error function, defined as

$$\mathrm{erf}(x) = \frac{2}{\sqrt{\pi}} \int_0^x e^{-t^2} \mathrm{d}t. \tag{B.9}$$

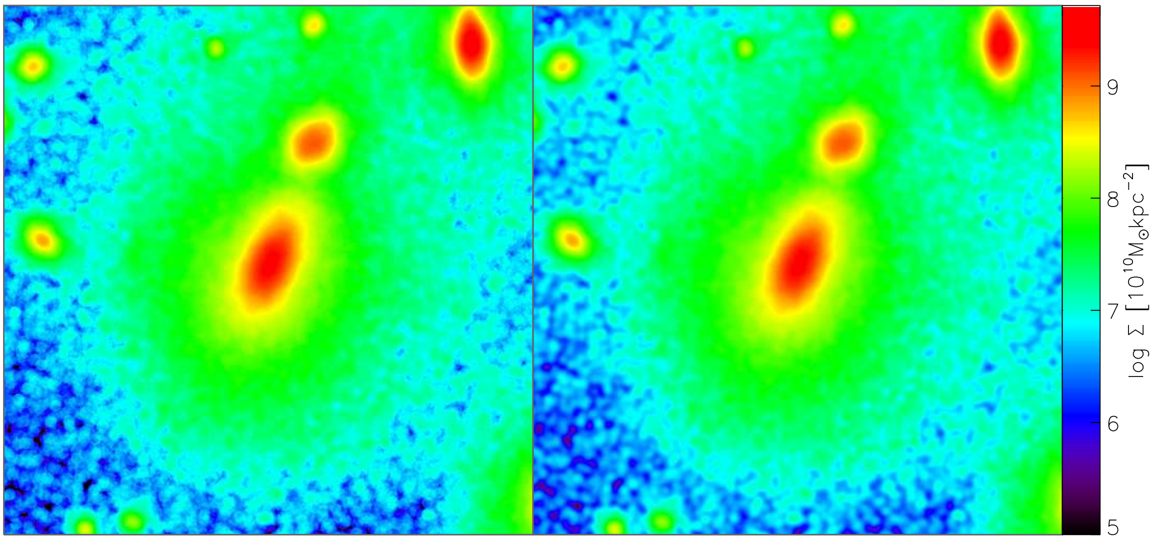

FIGURE B.1: Comparison of our old (left) and new (right) smoothing code, showing the stellar surface density in a region 100 × 100 kpc centred on galaxy A. In poorly sampled regions, the circular smoothing kernel is clear in the old code, while regions of high stellar density are highly consistent between the two codes.

Summing over all particles then gives the smoothed quantity as a function of position. For the surface density, we have

$$\Sigma_{cell} = \sum_j \frac{m_j}{4} \prod_{i=0}^{1} \frac{\mathrm{erf}\left(\frac{x_{u,i}-p_{j,i}}{0.3\sqrt{2}\epsilon}\right) - \mathrm{erf}\left(\frac{x_{l,i}-p_{j,i}}{0.3\sqrt{2}\epsilon}\right)}{x_{u,i}-x_{l,i}}. \tag{B.10}$$

In principle, there is no requirement for $x_{u,i} - x_{l,i}$ to be constant, but is in the current implementation.

This method lies in contrast to our previous smoothing code (used to produce Figs. 2.2, 2.4, 3.1, and 3.3, amongst others), in which the kernel used took the form $W(r) \propto 1 - H(r - r_\mathrm{s})$, where H represents the Heaviside function, and r_s is a smoothing radius. In that implementation, r_s was proportional to the size of the cells (rather than e.g., the smoothing length of the simulation), and the cells were restricted to be the same size. We show for comparison surface density maps of galaxy A with the two different methods in Fig. B.1. The constant smoothing kernel used in the old code (left) is apparent in low-density regions, while high-density regions are consistent with both codes. Our new code will therefore be most useful for the fitting of low-mass galaxies. It should also be noted that it is $\sim 8\times$ faster than the old code. With these readily-available 2-dimensional maps of surface density and brightness, more sophisticated models may be employed (e.g., Cappellari, 2008), rather than using a Sérsic or core-Sérsic profile.

C

V-Band Luminosity Maps

In this appendix, we show the V-Band luminosity maps of the present-day galaxies from the simulations introduced in Chapter 3. Fig. C.1 shows the 1131 galaxies from the simulation with AGN, and Fig. C.2 the 754 galaxies from the simulation without AGN. Galaxies are ordered from top left to bottom right by their total FoF group mass. In both figures, galaxies A, B, and C are outlined in blue.

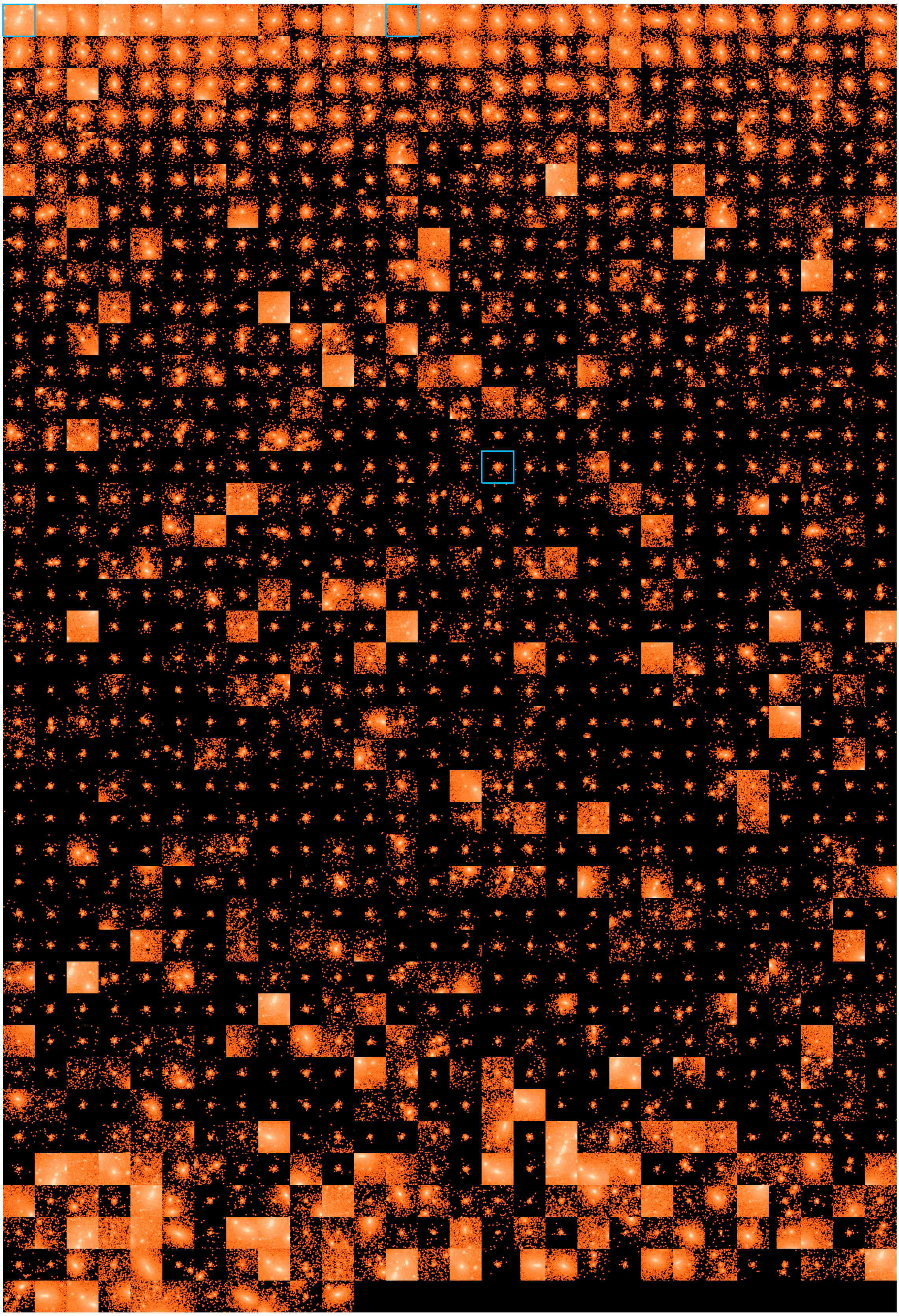

FIGURE C.1: *V*-Band luminosity maps of the present-day galaxies in our simulation with AGN feedback. Galaxies A, B, and C are outlined in blue.

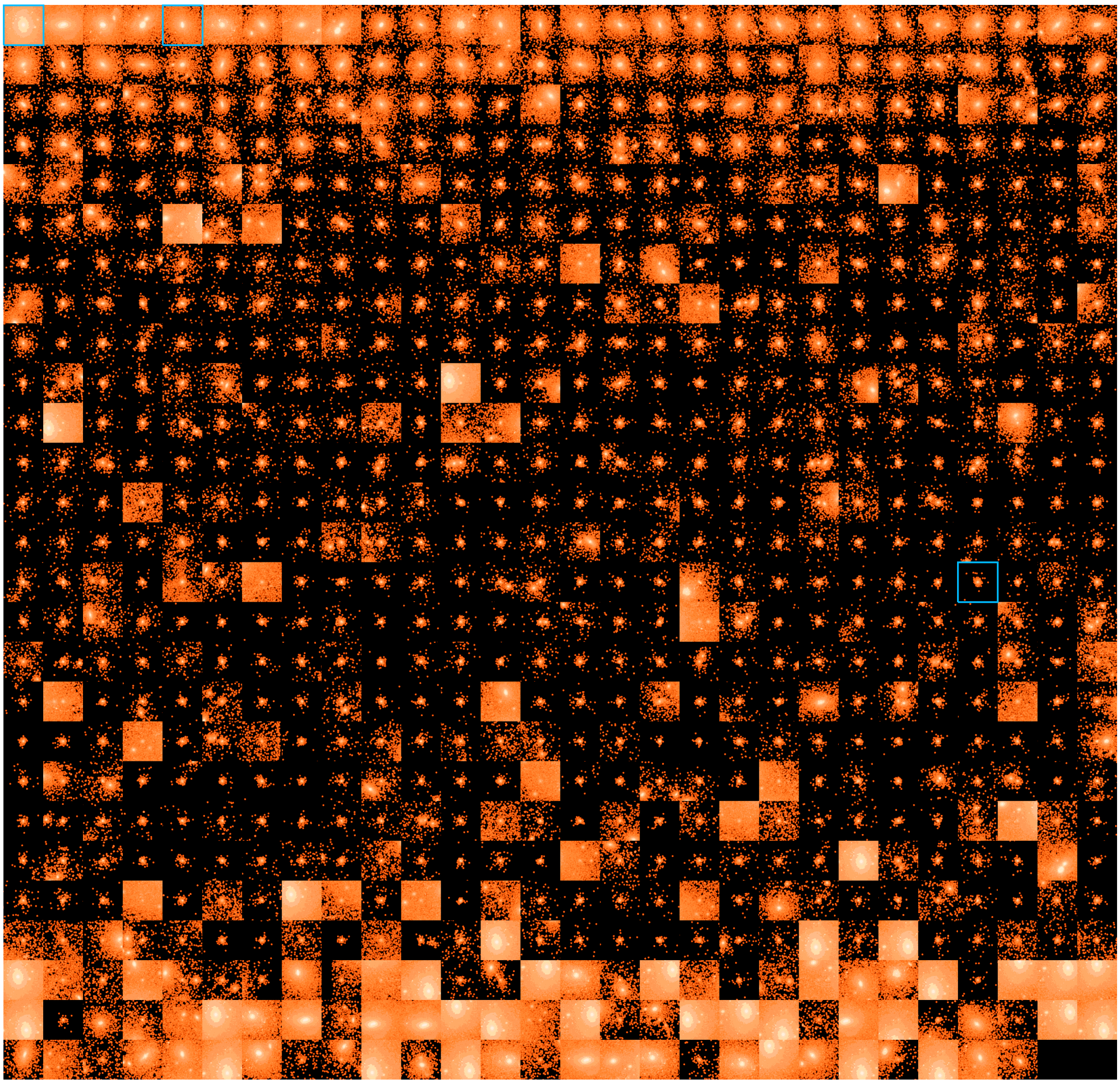

Figure C.2: Same as Fig. C.1, but for the simulation without AGN feedback.

D

Star Formation Histories

In this appendix, we show the star formation histories of the present-day galaxies from the simulations introduced in Chapter 3. Fig. D.1 shows the 1131 galaxies from the simulation with AGN, and Fig. D.2 the 754 galaxies from the simulation without AGN. Galaxies are ordered from top left to bottom right by their total FoF group mass. In both figures, galaxies A, B, and C are highlighted in red.

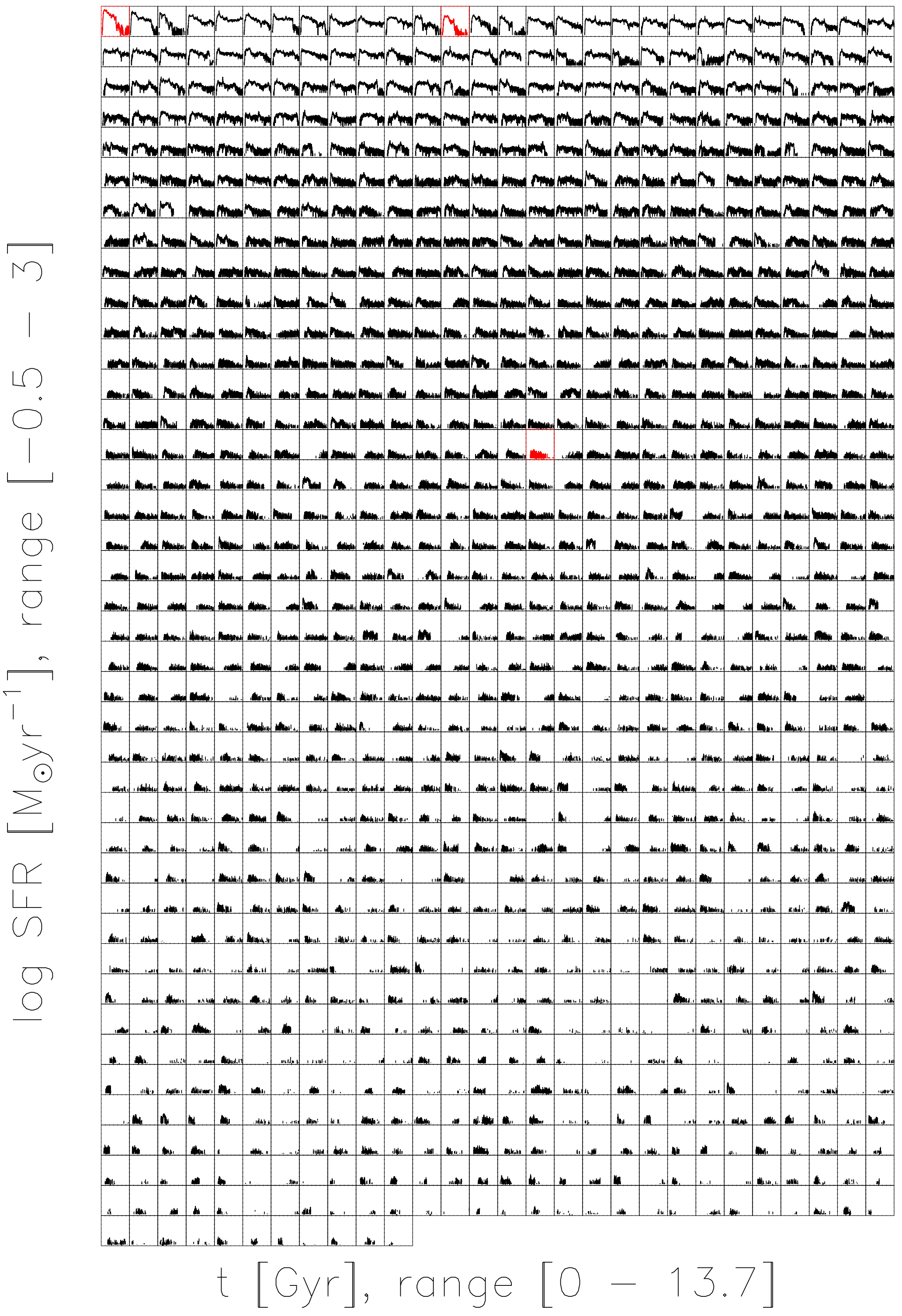

FIGURE D.1: Star formation histories of the present-day galaxies in our simulation with AGN feedback. Galaxies A, B, and C are highlighted in red.

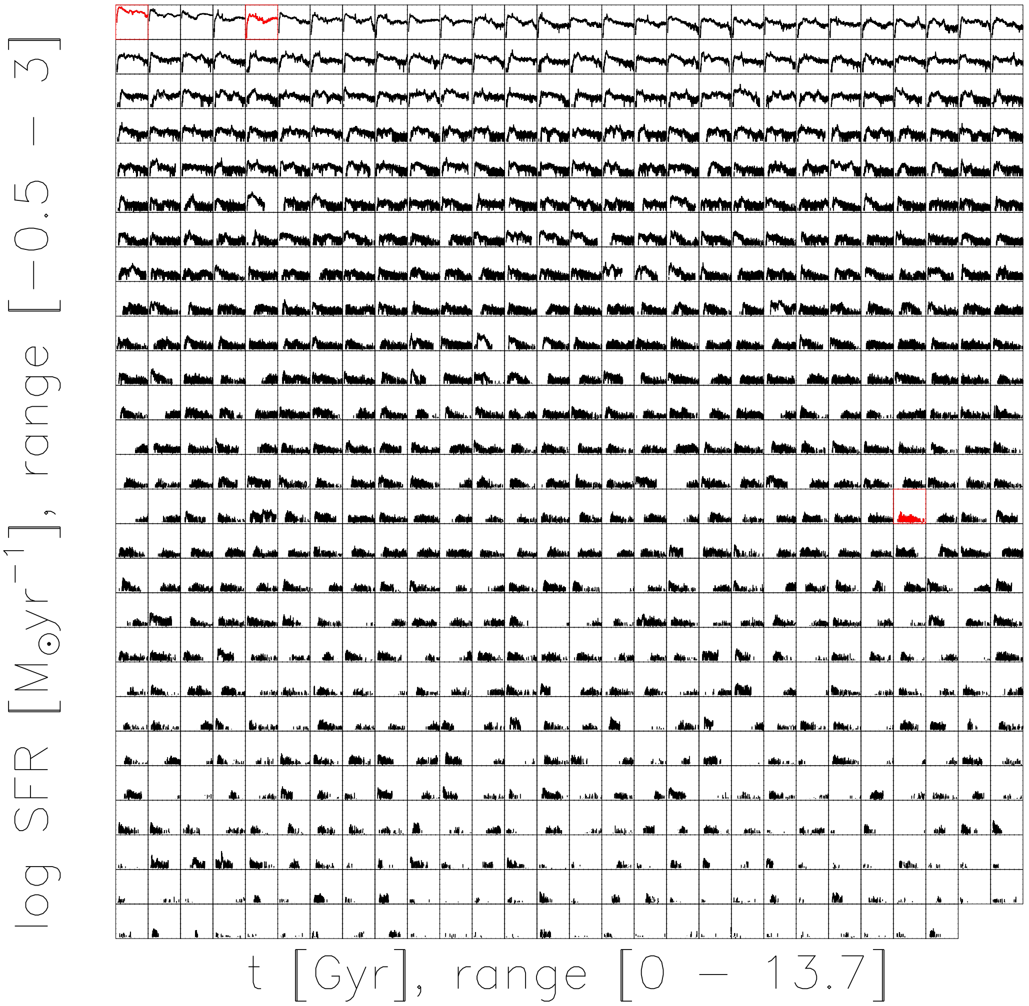

FIGURE D.2: Same as Fig. D.1, but for the simulation without AGN feedback.

E

Merger Trees

In this appendix we show merger trees for the galaxies A, B, and C, with galaxy positions plotted as as function of both time and redshift for the simulations both with and without AGN feedback. The ordinate axis shows one component of position relative to the position of either A, B, or C. In all figures, A (and the galaxies that will merge with it) is in black, B in blue, and C in red. The plotted circles have radii proportional to the logarithm of the galaxy's stellar mass at that time.

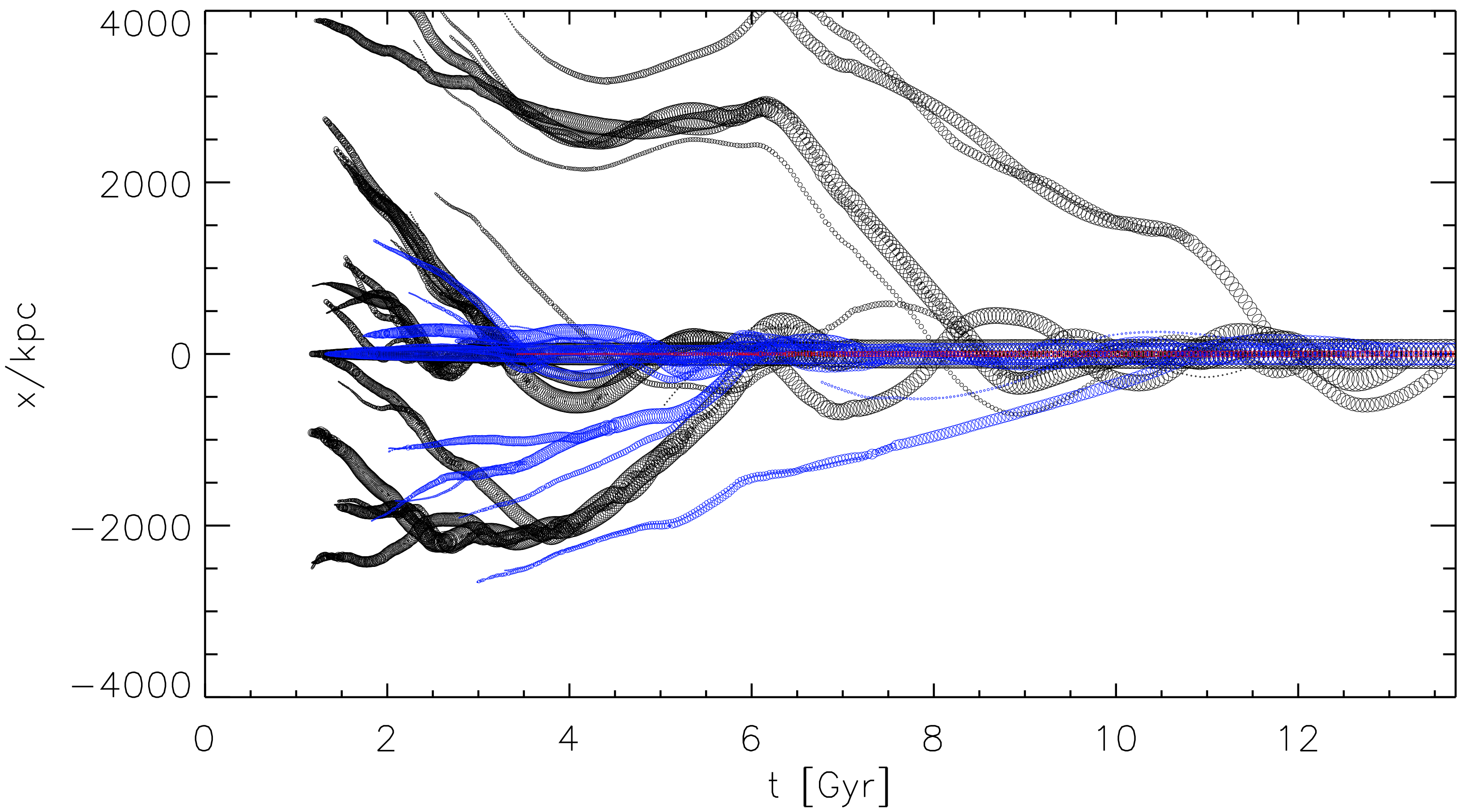

FIGURE E.1: Merger trees for galaxies A (black), B (blue), and C (red) in the simulation with AGN feedback as a function of time since the Big Bang. A single component of the separation vector from A, B, or C is shown. The plotted circles have radii proportional to the logarithm of the galaxy's stellar mass.

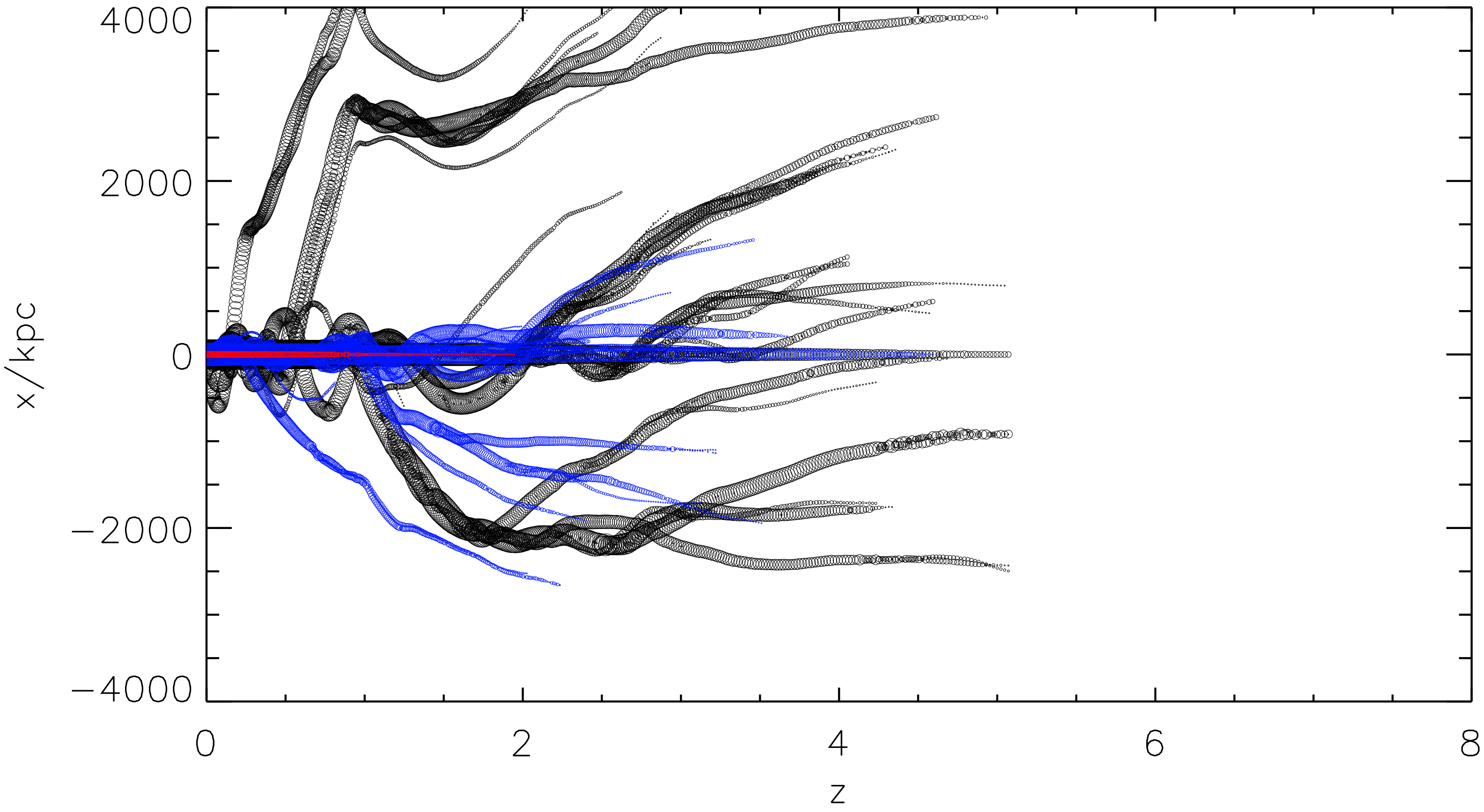

FIGURE E.2: Same as Fig. E.1, but shown as a function of redshift.

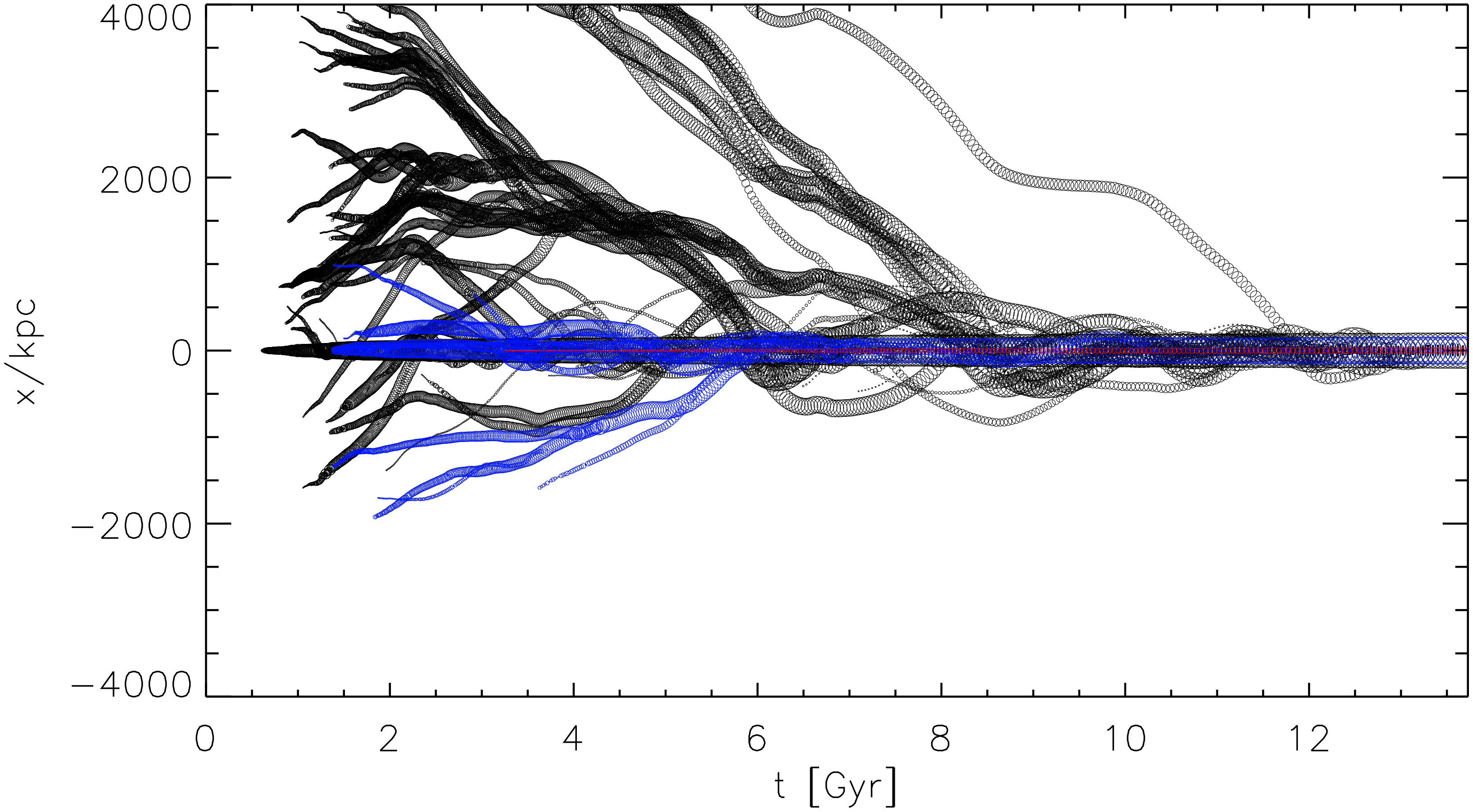

Figure E.3: Same as Fig. E.1, but for the simulation without AGN feedback.

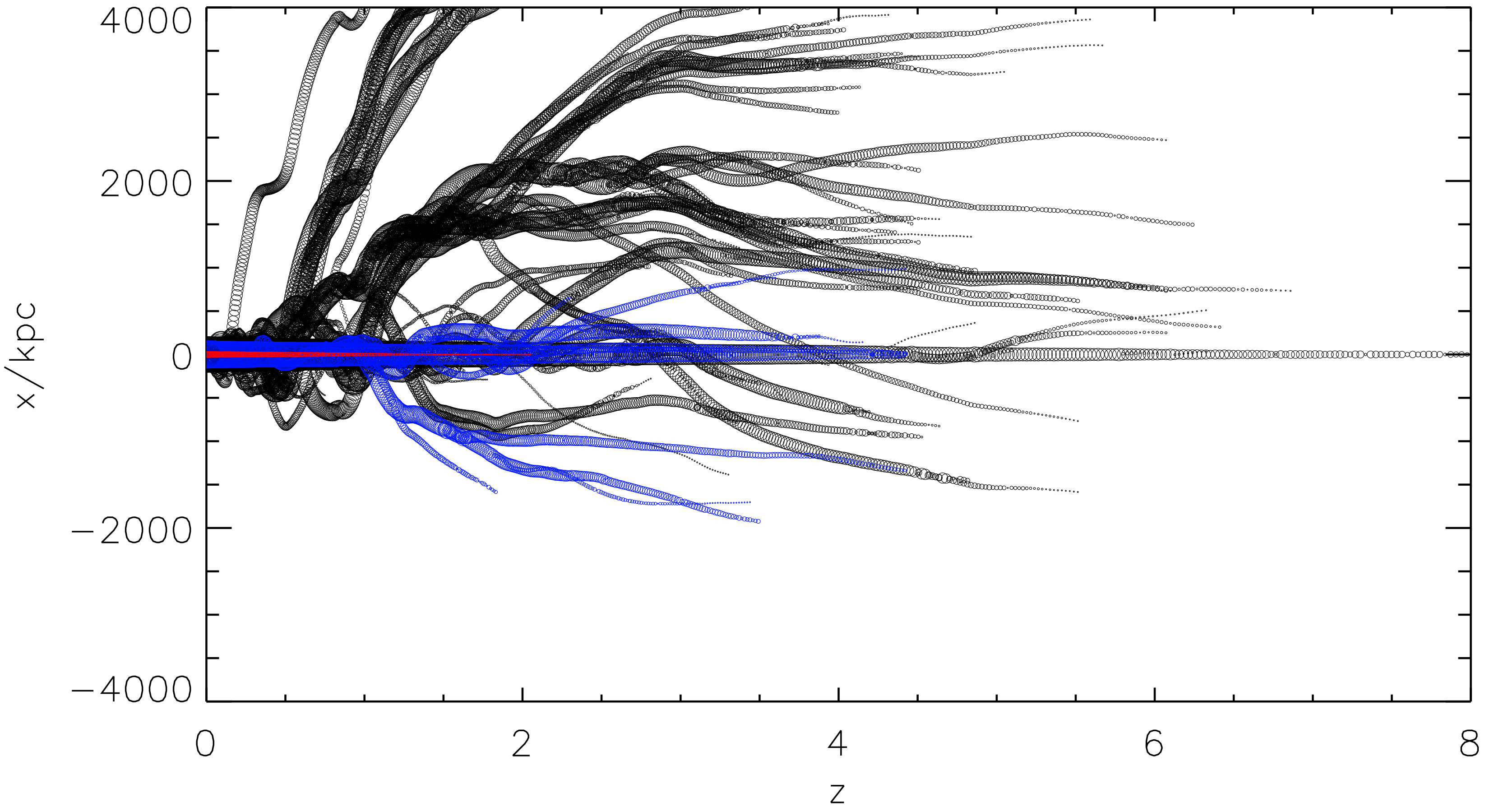

FIGURE E.4: Same as Fig. E.1, but shown as a function of redshift for the simulation without AGN feedback.

F

Stellar Metallicity Gradients

In this appendix, we show the stellar metallicity gradients of the present-day galaxies from the simulations introduced in Chapter 3. Fig. F.1 shows the 1131 galaxies from the simulation with AGN, and Fig. F.2 the 754 galaxies from the simulation without AGN. Galaxies are ordered from top left to bottom right by their total FoF group mass. In both figures, galaxies A, B, and C are outlined in blue.

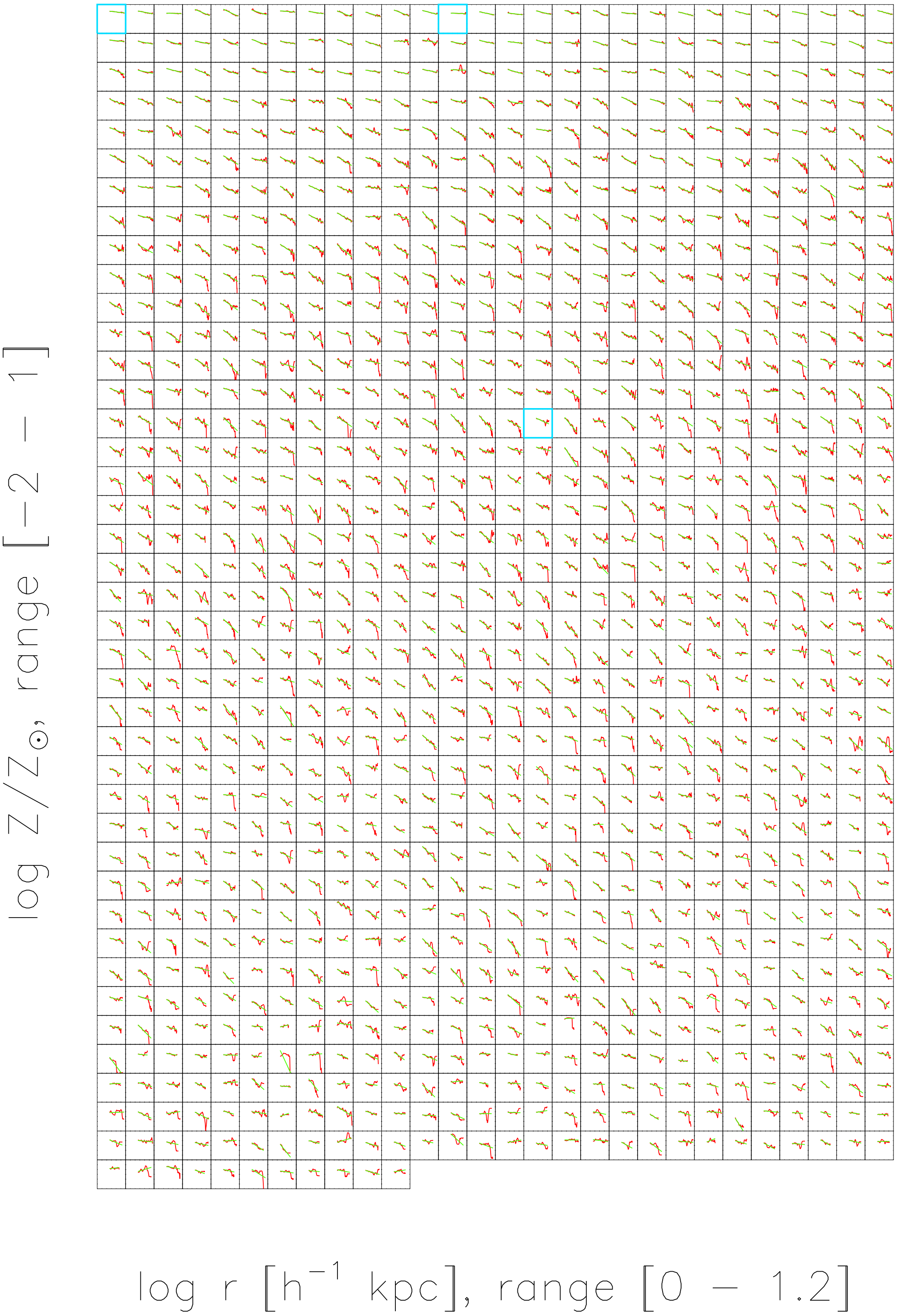

FIGURE F.1: Stellar metallicity gradient profiles of the present-day galaxies in our simulation with AGN feedback. Galaxies A, B, and C are outlined in blue.

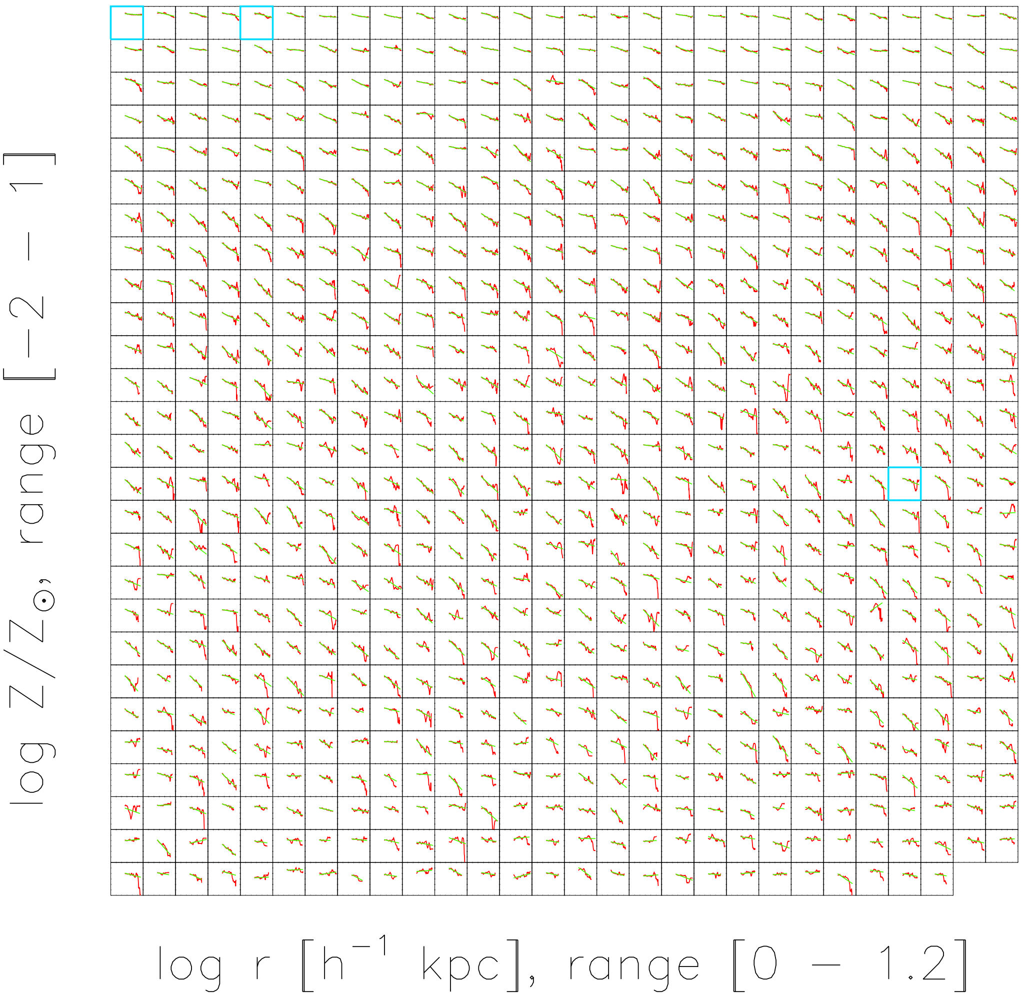

Figure F.2: Same as Fig. F.1, but for the simulation without AGN feedback.

G

Particle Refinement

In this appendix, we describe the process by which we increase the number of simulated particles for the purpose of function fitting. First, the positions of the particles as read from the snapshot file are replicated the desired number of times. We then generate the following quantities for each of the new particles:

$$r = |n| \times 0.3\epsilon; \tag{G.1}$$

$$\cos\theta = 2u_\theta - 1; \tag{G.2}$$

$$\phi = 2\pi u_\phi, \tag{G.3}$$

and update each position as:

$$\mathbf{p}_{\text{new}} = \mathbf{p}_{\text{old}} + \begin{pmatrix} r\sin\theta\cos\phi \\ r\sin\theta\sin\phi \\ r\cos\theta \end{pmatrix}. \tag{G.4}$$

In these equations, n denotes a normally distributed random variable, u a uniformly distributed random variable on the interval [0,1], and ϵ is the gravitational softening. The factor 0.3 enters equation (G.1) to match fairly closely the smoothing kernel used in the simulation, as shown in Fig. G.1.

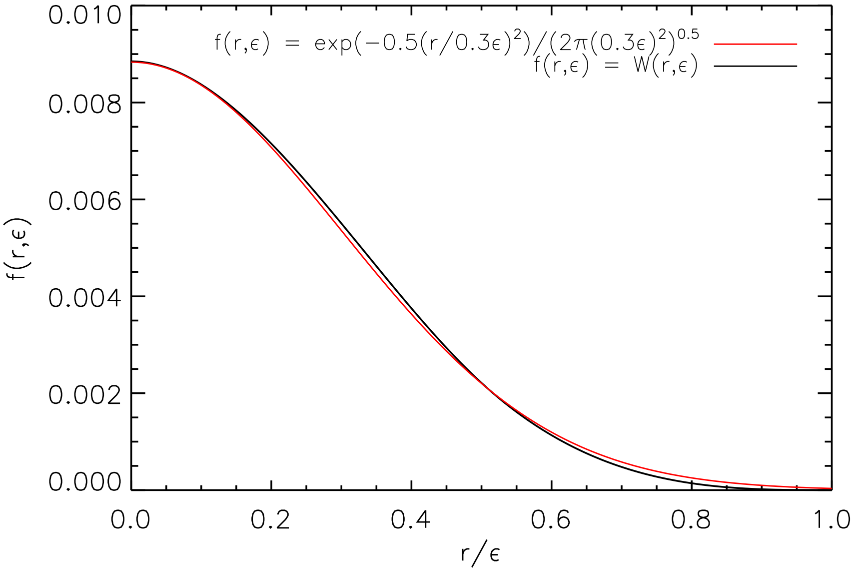

FIGURE G.1: Comparison between the smoothing kernel used in our simulations, $W(r, \epsilon)$, and a Gaussian with dispersion 0.3ϵ.

H

Galaxy Separation

In this appendix, we describe the process by which merging galaxies, identified as members of the same FoF group, are separated. First, the FoF groups are read, and the process described in Appendix G is applied to the star particles of each. The 3-dimensional histogram of these particles is obtained and all local maxima (defined as having a value, η, greater than any of the 6 immediately adjacent bins) are identified. For any pair of maxima separated by at least $10h^{-1}$ kpc, a plane is defined by their separation vector, $\mathbf{r}_{12} = \mathbf{r}_1 - \mathbf{r}_2$, and their average location weighted by η^{-1}:

$$\mathbf{r}_{12} \cdot \left(\mathbf{r} - \frac{\mathbf{r}_1 \eta_1^{-1} + \mathbf{r}_2 \eta_2^{-1}}{\eta_1^{-1} + \eta_2^{-1}} \right) = 0. \tag{H.1}$$

This plane then describes two new groups. An example of the result of this procedure is shown in Fig. H.1; the top panel shows the most massive FoF group found in the $25h^{-1}$ Mpc simulation with AGN (black points), while the bottom panel shows this group split into three separate galaxies (in red, green, and yellow).

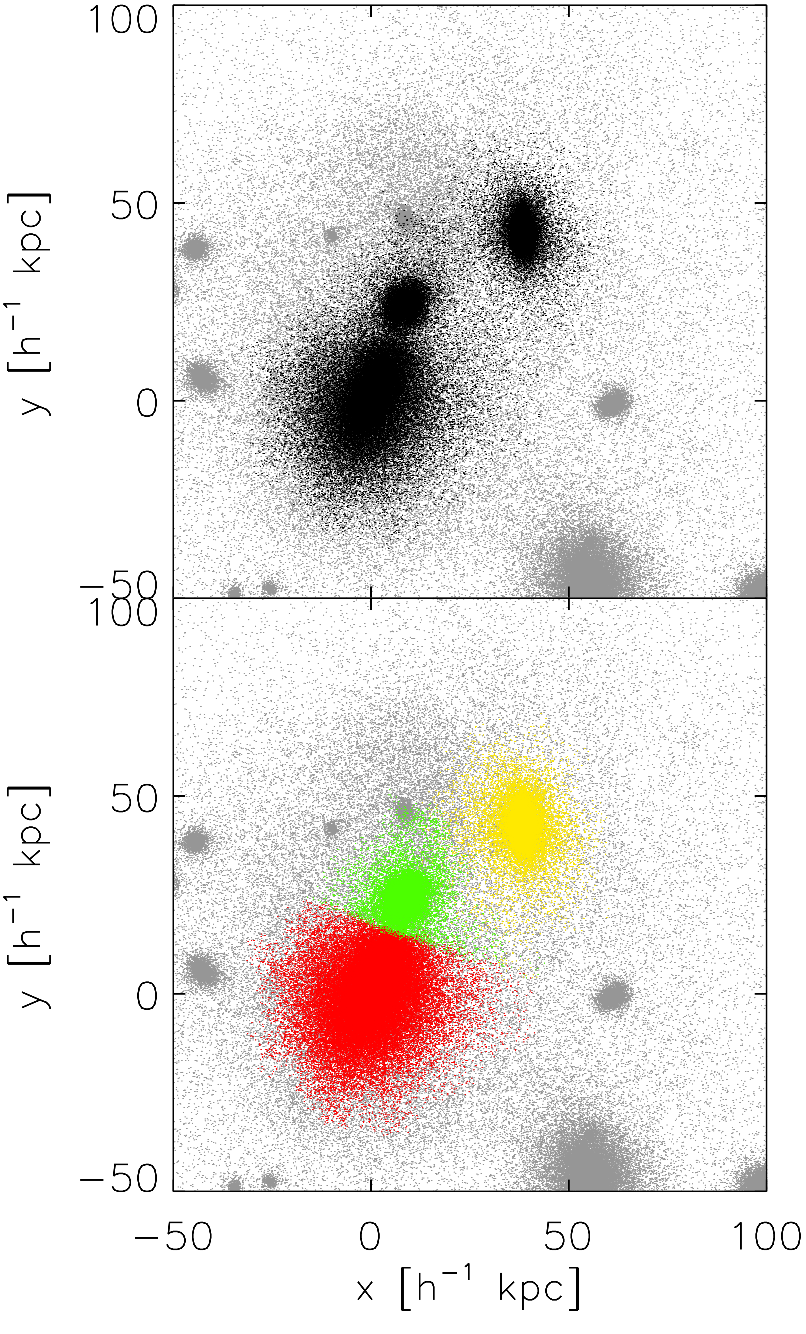

FIGURE H.1: Top panel: the black points show the most massive FoF group in the $25h^{-1}$ Mpc simulation with AGN, and the grey show all star particles in the plotted region. Bottom panel: the three galaxies this group is split into are shown by the red, green, and yellow points; the galaxy shown in red is galaxy A.

References

Abbott D. C., 1982, ApJ, 259, 282 7, 23

Agarwal B., Khochfar S., Johnson J. L., Neistein E., Dalla Vecchia C., Livio M., 2012, MNRAS, 425, 2854 27

Agertz O. et al., 2007, MNRAS, 380, 963 10, 11

Allen M. G., Groves B. A., Dopita M. A., Sutherland R. S., Kewley L. J., 2008, ApJS, 178, 20 17

Anglés-Alcázar D., Özel F., Davé R., 2013, ApJ, 770, 5 49

Angulo R. E., Springel V., White S. D. M., Jenkins A., Baugh C. M., Frenk C. S., 2012, MNRAS, 426, 2046 9

Arimoto N., Yoshii Y., 1987, A&A, 173, 23 107

Arrigoni M., Trager S. C., Somerville R. S., Gibson B. K., 2010, MNRAS, 402, 173 68

Asplund M., Grevesse N., Sauval A. J., 2005, in Barnes III T. G., Bash F. N., eds, Astronomical Society of the Pacific Conference Series Vol. 336, Cosmic Abundances as Records of Stellar Evolution and Nucleosynthesis. p. 25 83

Asplund M., Grevesse N., Sauval A. J., Scott P., 2009, ARA&A, 47, 481 83

Baade W., Minkowski R., 1954, ApJ, 119, 206 7

Balbus S. A., 2003, ARA&A, 41, 555 8

Balbus S. A., Hawley J. F., 1991, ApJ, 376, 214 8

Baldry I. K. et al., 2012, MNRAS, 421, 621 xi, xii, 59, 60, 72, 73

Balsara D. S., 1995, Journal of Computational Physics, 121, 357 16

Barai P., Viel M., Murante G., Gaspari M., Borgani S., 2014, MNRAS, 437, 1456 28

Baugh C. M., Cole S., Frenk C. S., Lacey C. G., 1998, ApJ, 498, 504 9

Beifiori A., Courteau S., Corsini E. M., Zhu Y., 2012, MNRAS, 419, 2497 34

Bell E. F., McIntosh D. H., Katz N., Weinberg M. D., 2003, ApJS, 149, 289 xii, 74, 75

Bellovary J., Volonteri M., Governato F., Shen S., Quinn T., Wadsley J., 2011, ApJ, 742, 13 27

Bender R., Burstein D., Faber S. M., 1993, ApJ, 411, 153 xi, 60, 61

Bennett A. S., 1962, MmRAS, 68, 163 7

Bennett C. L. et al., 2003, ApJ, 583, 1 1

Berger M. J., Colella P., 1989, Journal of Computational Physics, 82, 64 10

Bernardi M., Shankar F., Hyde J. B., Mei S., Marulli F., Sheth R. K., 2010, MNRAS, 404, 2087 34, 54

Black J. H., 1981, MNRAS, 197, 553 17, 18

Bland-Hawthorn J., 2015, in Ziegler B. L., Combes F., Dannerbauer H., Verdugo M., eds, IAU Symposium Vol. 309, IAU Symposium. pp 21–28 91

Blanton M. R., Roweis S., 2007, AJ, 133, 734 76

Blinnikov S., Lundqvist P., Bartunov O., Nomoto K., Iwamoto K., 2000, ApJ, 532, 1132 6

Bondi H., Hoyle F., 1944, MNRAS, 104, 273 28

Booth C. M., Schaye J., 2009, MNRAS, 398, 53 8, 26, 27, 28, 29, 32, 45, 47, 49, 107

Bouwens R. J. et al., 2012, ApJ, 754, 83 xiv, 88

Bouwens R. J. et al., 2011, ApJ, 737, 90 34, 35, 54, 87

Bower R. G., 1991, MNRAS, 248, 332 9

Bower R. G., Benson A. J., Malbon R., Helly J. C., Frenk C. S., Baugh C. M., Cole S., Lacey C. G., 2006, MNRAS, 370, 645 9, 60

Boylan-Kolchin M., Springel V., White S. D. M., Jenkins A., Lemson G., 2009, MNRAS, 398, 1150 9

Bromm V., Coppi P. S., Larson R. B., 2002, ApJ, 564, 23 27

Bromm V., Larson R. B., 2004, ARA&A, 42, 79 6

Bromm V., Loeb A., 2003, ApJ, 596, 34 27

Brown P. J. et al., 2012, ApJ, 753, 22 6

Bruzual G., Charlot S., 2003, MNRAS, 344, 1000 56, 60

Bundy K. et al., 2015, ApJ, 798, 7 91

Bundy K. et al., 2006, ApJ, 651, 120 3, 11

Bunker A. J. et al., 2010, MNRAS, 409, 855 35

Burgarella D. et al., 2013, A&A, 554, A70 34, 35, 54

Burkert A., Hensler G., 1987, in Hillebrandt W., Kuhfuss R., Mueller E., Truran J. W., eds, Lecture Notes in Physics, Berlin Springer Verlag Vol. 287, Nuclear Astrophysics. pp 159–173 10

Burles S., Nollett K. M., Turner M. S., 2001, ApJ, 552, L1 1

Calura F., Menci N., 2009, MNRAS, 400, 1347 68

Caon N., Capaccioli M., D'Onofrio M., 1993, MNRAS, 265, 1013 125

Cappellari M., 2008, MNRAS, 390, 71 127

Cappellari M. et al., 2011, MNRAS, 416, 1680 4

Cappellari M. et al., 2013, MNRAS, 432, 1862 xiii, 85, 86

Caputi K. I., McLure R. J., Dunlop J. S., Cirasuolo M., Schael A. M., 2006, MNRAS, 366, 609 xii, xvii, 74, 75

Cassinelli J. P., 1979, ARA&A, 17, 275 7

Cen R., 1992, ApJS, 78, 341 17, 18

Cen R., Ostriker J. P., 1999, ApJ, 519, L109 10

Chabrier G., 2003, PASP, 115, 763 25

Ciambur B. C., Kauffmann G., Wuyts S., 2013, MNRAS, 432, 2488 68, 69

Cicone C., Feruglio C., Maiolino R., Fiore F., Piconcelli E., Menci N., Aussel H., Sturm E., 2012, A&A, 543, A99 8, 47, 108, 119

Cirasuolo M., McLure R. J., Dunlop J. S., Almaini O., Foucaud S., Simpson C., 2010, MNRAS, 401, 1166 xii, xvii, 74, 75

Cole S., Aragon-Salamanca A., Frenk C. S., Navarro J. F., Zepf S. E., 1994, MNRAS, 271, 781 9

Cole S. et al., 2001, MNRAS, 326, 255 xi, xii, 58, 59, 74, 75

Conti P. S., 1978, ARA&A, 16, 371 7

Cowie L. L., Songaila A., Hu E. M., Cohen J. G., 1996, AJ, 112, 839 3, 11

Croton D. J. et al., 2006, MNRAS, 365, 11 8, 9, 63

Cucciati O. et al., 2012, A&A, 539, A31 34, 35, 54

Daddi E. et al., 2007, ApJ, 670, 156 xiv, 87, 88

Davé R., Finlator K., Oppenheimer B. D., 2006, MNRAS, 370, 273 23

Davé R., Finlator K., Oppenheimer B. D., 2011, MNRAS, 416, 1354 65, 72, 89, 108

David L. P., Forman W., Jones C., 1990, ApJ, 359, 29 26

De Lucia G., Boylan-Kolchin M., Benson A. J., Fontanot F., Monaco P., 2010, MNRAS, 406, 1533 9

De Lucia G., Kauffmann G., White S. D. M., 2004, MNRAS, 349, 1101 60

De Lucia G., Springel V., White S. D. M., Croton D., Kauffmann G., 2006, MNRAS, 366, 499 12

DeGraf C., Di Matteo T., Treu T., Feng Y., Woo J.-H., Park D., 2014, ArXiv e-prints xiii, 80, 81

Di Matteo T., Colberg J., Springel V., Hernquist L., Sijacki D., 2008, ApJ, 676, 33 26, 27, 28, 29, 47, 49, 80

Dolag K., Vazza F., Brunetti G., Tormen G., 2005, MNRAS, 364, 753 11

Dressler A., 1980, ApJ, 236, 351 4

Dubois Y., Devriendt J., Slyz A., Teyssier R., 2012, MNRAS, 420, 2662 8

Dubois Y., Gavazzi R., Peirani S., Silk J., 2013, MNRAS, 433, 3297 51, 85

Dunne L. et al., 2009, MNRAS, 394, 3 xiv, 87, 88

Eggen O. J., Lynden-Bell D., Sandage A. R., 1962, ApJ, 136, 748 2

Eisenhauer F. et al., 2005, ApJ, 628, 246 8

Elbaz D. et al., 2007, A&A, 468, 33 xiv, 87, 88

Elbaz D. et al., 2011, A&A, 533, A119 xiv, 87, 88

Erb D. K., Shapley A. E., Pettini M., Steidel C. C., Reddy N. A., Adelberger K. L., 2006, ApJ, 644, 813 xiii, 84

Fabian A. C., ed. 1992, Clusters and superclusters of galaxies NATO Advanced Science Institutes (ASI) Series C Vol. 366 2

Fanaroff B. L., Riley J. M., 1974, MNRAS, 167, 31P 7

Fanidakis N., Baugh C. M., Benson A. J., Bower R. G., Cole S., Done C., Frenk C. S., 2011, MNRAS, 410, 53 9

Federrath C., Banerjee R., Clark P. C., Klessen R. S., 2010, ApJ, 713, 269 120

Ferrarese L., Merritt D., 2000, ApJ, 539, L9 8

Feruglio C., Maiolino R., Piconcelli E., Menci N., Aussel H., Lamastra A., Fiore F., 2010, A&A, 518, L155 8, 47, 108, 119

Fixsen D. J., 2009, ApJ, 707, 916 2

Fogarty L. M. R. et al., 2014, MNRAS, 443, 485 91

Fontanot F., De Lucia G., Monaco P., Somerville R. S., Santini P., 2009, MNRAS, 397, 1776 12

Frenk C. S. et al., 1999, ApJ, 525, 554 10

Fu J. et al., 2013, MNRAS, 434, 1531 9

Fukugita M., Peebles P. J. E., 2004, ApJ, 616, 643 33

Furlong M. et al., 2015, MNRAS, 450, 4486 119

Gabasch A. et al., 2004, A&A, 421, 41 xii, 77

Gallazzi A., Bell E. F., Zibetti S., Brinchmann J., Kelson D. D., 2014, ApJ, 788, 72 xiii, 81, 82

Gallazzi A., Charlot S., Brinchmann J., White S. D. M., Tremonti C. A., 2005, MNRAS, 362, 41 xi, xiii, 63, 64, 82, 83, 119

Gargiulo I. D. et al., 2014, ArXiv:1402.3296 e-prints 68

Gebhardt K. et al., 2000, ApJ, 539, L13 8

Genel S. et al., 2014, MNRAS, 445, 175 119

Gingold R. A., Monaghan J. J., 1977, MNRAS, 181, 375 11, 14

Gnedin N. Y., 1995, ApJS, 97, 231 10, 11

González Hernández J. I., Ruiz-Lapuente P., Tabernero H. M., Montes D., Canal R., Méndez J., Bedin L. R., 2012, Nat, 489, 533 7

Graham A. W., 2008, PASA, 25, 167 79

Graham A. W., 2015, ArXiv e-prints 80

Graham A. W., Driver S. P., 2007, ApJ, 655, 77 8

Graham A. W., Erwin P., Caon N., Trujillo I., 2001, ApJ, 563, L11 8, 125

Graham A. W., Erwin P., Trujillo I., Asensio Ramos A., 2003, AJ, 125, 2951 56, 85, 125

Graham A. W., Onken C. A., Athanassoula E., Combes F., 2011, MNRAS, 412, 2211 xiii, 78, 79, 80, 81

Graham A. W., Scott N., 2013, ApJ, 764, 151 34

Greene J. E. et al., 2010, ApJ, 721, 26 34

Greif T. H., Springel V., White S. D. M., Glover S. C. O., Clark P. C., Smith R. J., Klessen R. S., Bromm V., 2011, ApJ, 737, 75 6

Guedes J., Callegari S., Madau P., Mayer L., 2011, ApJ, 742, 76 45

Gültekin K. et al., 2009, ApJ, 698, 198 34, 80

Gunawardhana M. L. P. et al., 2013, MNRAS, 433, 2764 34, 35, 54

Guo Q., Cole S., Eke V., Frenk C., Helly J., 2013, MNRAS, 434, 1838 60

Guo Q., White S., Angulo R. E., Henriques B., Lemson G., Boylan-Kolchin M., Thomas P., Short C., 2013, MNRAS, 428, 1351 72

Guo Q. et al., 2011, MNRAS, 413, 101 72

Häring N., Rix H.-W., 2004, ApJ, 604, L89 8

Harrison C. M. et al., 2012, MNRAS, 426, 1073 108

Heckman T. M., Lehnert M. D., Strickland D. K., Armus L., 2000, ApJS, 129, 493 107

Heger A., Fryer C. L., Woosley S. E., Langer N., Hartmann D. H., 2003, ApJ, 591, 288 6

Heger A., Woosley S. E., 2002, ApJ, 567, 532 6

Heitmann K. et al., 2008, Computational Science and Discovery, 1, 015003 10

Heyl J. S., Cole S., Frenk C. S., Navarro J. F., 1995, MNRAS, 274, 755 9

Hillebrandt W., Niemeyer J. C., 2000, ARA&A, 38, 191 6

Hinshaw G. et al., 2013, ApJS, 208, 19 31, 52

Hirano S., Hosokawa T., Yoshida N., Umeda H., Omukai K., Chiaki G., Yorke H. W., 2014, ApJ, 781, 60 6, 119

Hirschmann M., Dolag K., Saro A., Bachmann L., Borgani S., Burkert A., 2014, MNRAS, 442, 2304 72, 80, 89

Ho I.-T. et al., 2014, MNRAS, 444, 3894 91

Ho I.-T., Kudritzki R.-P., Kewley L. J., Zahid H. J., Dopita M. A., Bresolin F., Rupke D. S. N., 2015, MNRAS, 448, 2030 101

Hopkins A. M., Beacom J. F., 2006, ApJ, 651, 142 34, 35

Hopkins P. F., Hernquist L., Cox T. J., Kereš D., 2008, ApJS, 175, 356 4, 91

Hu C.-Y., Naab T., Walch S., Moster B. P., Oser L., 2014, MNRAS, 443, 1173 11

Hu J., 2008, MNRAS, 386, 2242 34

Huang J.-S., Glazebrook K., Cowie L. L., Tinney C., 2003, ApJ, 584, 203 xi, xii, 58, 59, 74, 75

Hubble E. P., 1926, ApJ, 64, 321 2

Iapichino L., Adamek J., Schmidt W., Niemeyer J. C., 2008, MNRAS, 388, 1079 10

Iapichino L., Niemeyer J. C., 2008, MNRAS, 388, 1089 10

Iben Jr. I., Tutukov A. V., 1984, ApJS, 54, 335 6

Ilbert O. et al., 2013, A&A, 556, A55 xii, 72, 73, 74

Ilbert O. et al., 2005, A&A, 439, 863 xii, 77

Jahnke K., Macciò A. V., 2011, ApJ, 734, 92 8

Janka H.-T., Langanke K., Marek A., Martínez-Pinedo G., Müller B., 2007, Phys. Rep., 442, 38 5

Jennison R. C., Gupta M. K. D., 1956, Philosophical Magazine, 1, 65 7

Johansson J., Thomas D., Maraston C., 2012, MNRAS, 421, 1908 xi, xii, 64, 66, 67, 68

Jones D. H., Peterson B. A., Colless M., Saunders W., 2006, MNRAS, 369, 25 xii, 74, 75

Juneau S. et al., 2005, ApJ, 619, L135 3, 11

Karakas A. I., 2010, MNRAS, 403, 1413 25

Karim A. et al., 2011, ApJ, 730, 61 xiv, 34, 35, 54, 87, 88

Katz N., 1992, ApJ, 391, 502 10, 22

Katz N., Weinberg D. H., Hernquist L., 1996, ApJS, 105, 19 17, 18

Kauffmann G., Guiderdoni B., White S. D. M., 1994, MNRAS, 267, 981 9

Kauffmann G. et al., 2003, MNRAS, 341, 33 60

Kauffmann G., Nusser A., Steinmetz M., 1997, MNRAS, 286, 795 9

Kauffmann G., White S. D. M., Guiderdoni B., 1993, MNRAS, 264, 201 9

Kaviraj S., Peirani S., Khochfar S., Silk J., Kay S., 2009, MNRAS, 394, 1713 4

Kawata D., Gibson B. K., 2003, MNRAS, 340, 908 10

Kewley L. J., Dopita M. A., 2002, ApJS, 142, 35 xii, xiii, 65, 83, 84

Kewley L. J., Ellison S. L., 2008, ApJ, 681, 1183 xii, xiii, 65, 83, 84

Khalatyan A., Cattaneo A., Schramm M., Gottlöber S., Steinmetz M., Wisotzki L., 2008, MNRAS, 387, 13 28

Khandai N., Di Matteo T., Croft R., Wilkins S. M., Feng Y., Tucker E., DeGraf C., Liu M.-S., 2014, ArXiv:1402.0888 e-prints 28, 60, 80

King A. L. et al., 2013, ApJ, 762, 103 111

Kobayashi C., 2004, MNRAS, 347, 740 4, 10, 23, 91, 94, 95, 103

Kobayashi C., 2005, MNRAS, 361, 1216 36, 60, 68, 85, 107, 115

Kobayashi C., Karakas A. I., Umeda H., 2011a, MNRAS, 414, 3231 25, 64

Kobayashi C., Karakas A. I., Umeda H., 2011b, MNRAS, 414, 3231 25

Kobayashi C., Nakasato N., 2011, ApJ, 729, 16 24

Kobayashi C., Nomoto K., 2009, ApJ, 707, 1466 xvii, 26, 66

Kobayashi C., Springel V., White S. D. M., 2007, MNRAS, 376, 1465 12, 22, 29, 31, 32, 33, 52, 64, 65, 67, 107, 108, 114

Kobayashi C., Tominaga N., Nomoto K., 2011, ApJ, 730, L14 6

Kobayashi C., Umeda H., Nomoto K., Tominaga N., Ohkubo T., 2006, ApJ, 653, 1145 24

Kodama T., Arimoto N., 1997, A&A, 320, 41 26

Kormendy J., Ho L. C., 2013, ARA&A, 51, 511 x, xiii, 8, 34, 37, 44, 78, 79, 80, 81, 107

Kormendy J., Richstone D., 1995, ARA&A, 33, 581 8

Koushiappas S. M., Bullock J. S., Dekel A., 2004, MNRAS, 354, 292 27

Kraft R. P. et al., 2009, ApJ, 698, 2036 107

Krajnović D. et al., 2008, MNRAS, 390, 93 3

Kroupa P., 2008, in Knapen J. H., Mahoney T. J., Vazdekis A., eds, Astronomical Society of the Pacific Conference Series Vol. 390, Pathways Through an Eclectic Universe. p. 3 25, 34

Kudritzki R.-P., Ho I., Schruba A., Burkert A., Zahid H. J., Bresolin F., Dima G. I., 2015, ArXiv e-prints 101

Kuntschner H. et al., 2010, MNRAS, 408, 97 xii, 66, 67, 68, 91

Lagos C. d. P., Davis T. A., Lacey C. G., Zwaan M. A., Baugh C. M., Gonzalez-Perez V., Padilla N. D., 2014, MNRAS, 443, 1002 101

Lagos C. d. P., Lacey C. G., Baugh C. M., 2013, MNRAS, 436, 1787 9

Larson R. B., 1974, MNRAS, 169, 229 107

Lawrence A., 1987, PASP, 99, 309 7

Lee K.-S. et al., 2012, ApJ, 752, 66 xiv, 87, 88

Leitherer C., Robert C., Drissen L., 1992, ApJ, 401, 596 7, 23

Li C., White S. D. M., 2009, MNRAS, 398, 2177 xi, xii, 59, 60, 72, 73

Lucy L. B., 1977, AJ, 82, 1013 11, 14

Lynden-Bell D., 1969, Nat, 223, 690 7

Lynden-Bell D., 1978, Phys. Scr., 17, 185 7

Lynden-Bell D., Pringle J. E., 1974, MNRAS, 168, 603 8

Lynds C. R., 1967, ApJ, 147, 396 107

Madau P., Ferguson H. C., Dickinson M. E., Giavalisco M., Steidel C. C., Fruchter A., 1996, MNRAS, 283, 1388 8, 107

Madau P., Rees M. J., 2001, ApJ, 551, L27 27

Magdis G. E., Rigopoulou D., Huang J.-S., Fazio G. G., 2010, MNRAS, 401, 1521 xiv, 87, 88

Magorrian J. et al., 1998, AJ, 115, 2285 8, 107

Maier C., Lilly S. J., Ziegler B. L., Contini T., Pérez Montero E., Peng Y., Balestra I., 2014, ApJ, 792, 3 xiii, 84

Maiolino R. et al., 2012, MNRAS, 425, L66 47, 108

Maiolino R. et al., 2008, A&A, 488, 463 xiii, 83, 84, 85

Makino J., Funato Y., 2004, ApJ, 602, 93 29

Mannucci F., Cresci G., Maiolino R., Marconi A., Gnerucci A., 2010, MNRAS, 408, 2115 83

Marchesini D. et al., 2007, ApJ, 656, 42 xii, 77

Marchesini D., van Dokkum P. G., Förster Schreiber N. M., Franx M., Labbé I., Wuyts S., 2009, ApJ, 701, 1765 xii, 72, 73

Marconi A., Hunt L. K., 2003, ApJ, 589, L21 8, 33

Markwardt C. B., 2009, in Bohlender D. A., Durand D., Dowler P., eds, Astronomical Society of the Pacific Conference Series Vol. 411, Astronomical Data Analysis Software and Systems XVIII. p. 251 93, 126

Martin C. L., Kobulnicky H. A., Heckman T. M., 2002, ApJ, 574, 663 115

Mather J. C., 1982, Optical Engineering, 21, 769 1

McConnell N. J., Ma C.-P., 2013, ApJ, 764, 184 80

McDermid R. M. et al., 2015, MNRAS, 448, 3484 xiii, 82, 83

McElroy R., Croom S. M., Pracy M., Sharp R., Ho I.-T., Medling A. M., 2015, MNRAS, 446, 2186 8

McIntosh D. H., Guo Y., Hertzberg J., Katz N., Mo H. J., van den Bosch F. C., Yang X., 2008, MNRAS, 388, 1537 4

Merritt D., 2013, Dynamics and Evolution of Galactic Nuclei 8

Mihos J. C., Hernquist L., 1994, ApJ, 437, 611 10

Monaghan J. J., 1992, ARA&A, 30, 543 11, 14

Monaghan J. J., 1997, Journal of Computational Physics, 136, 298 16

Monaghan J. J., Gingold R. A., 1983, Journal of Computational Physics, 52, 374 16

Murante G., Monaco P., Giovalli M., Borgani S., Diaferio A., 2010, MNRAS, 405, 1491 22

Muzzin A. et al., 2013, ApJ, 777, 18 xii, 72, 73

Nakasato N., Mori M., Nomoto K., 2000, ApJ, 535, 776 17

Narayan R., White S. D. M., 1988, MNRAS, 231, 97P 9

Navarro J. F., White S. D. M., 1993, MNRAS, 265, 271 22, 23

Navarro J. F., White S. D. M., 1994, MNRAS, 267, 401 10

Nesvadba N. P. H., Lehnert M. D., De Breuck C., Gilbert A. M., van Breugel W., 2008, A&A, 491, 407 108

Newman A. B., Ellis R. S., Bundy K., Treu T., 2012, ApJ, 746, 162 xiii, 85, 86

Nomoto K., 1982, ApJ, 253, 798 6

Nomoto K., Kobayashi C., Tominaga N., 2013, ARA&A, 51, 457 ix, 5

Nomoto K., Mazzali P. A., Nakamura T., Iwamoto K., Danziger I. J., Patat F., 2001, in Livio M., Panagia N., Sahu K., eds, Supernovae and Gamma-Ray Bursts: the Greatest Explosions since the Big Bang. pp 144–170 6

Nomoto K., Thielemann F.-K., Yokoi K., 1984, ApJ, 286, 644 6

Oesch P. A. et al., 2012, ApJ, 759, 135 34, 54

Ohyama Y. et al., 2002, PASJ, 54, 891 107

Oliver S. et al., 2010, MNRAS, 405, 2279 xiv, 87, 88

Oppenheimer B. D., Davé R., 2006, MNRAS, 373, 1265 72, 89

Oppenheimer B. D., Davé R., Kereš D., Fardal M., Katz N., Kollmeier J. A., Weinberg D. H., 2010, MNRAS, 406, 2325 60

Orr M. J. L., Browne I. W. A., 1982, MNRAS, 200, 1067 7

O'Shea B. W., Nagamine K., Springel V., Hernquist L., Norman M. L., 2005, ApJS, 160, 1 10

Osterbrock D. E., 1989, Astrophysics of gaseous nebulae and active galactic nuclei 19

Pen U.-L., 1998, ApJS, 115, 19 10, 11

Penzias A. A., Wilson R. W., 1965, ApJ, 142, 419 1

Pérez-González P. G. et al., 2008, ApJ, 675, 234 xii, 72, 73, 74

Pettini M., Steidel C. C., Adelberger K. L., Dickinson M., Giavalisco M., 2000, ApJ, 528, 96 107

Planck Collaboration et al., 2014, A&A, 571, A1 1

Planck Collaboration et al., 2015, ArXiv e-prints 2

Poli F. et al., 2003, ApJ, 593, L1 xii, 77

Pounds K. A., 2014, MNRAS, 437, 3221 108, 111

Pounds K. A., King A. R., 2013, MNRAS, 433, 1369 108

Power C., Nayakshin S., King A., 2011, MNRAS, 412, 269 49

Pozzetti L. et al., 2003, A&A, 402, 837 xii, 75

Press W. H., Schechter P., 1974, ApJ, 187, 425 9

Price D. J., 2008, Journal of Computational Physics, 227, 10040 11

Puchwein E., Springel V., 2013, MNRAS, 428, 2966 60

Ragone-Figueroa C., Granato G. L., Murante G., Borgani S., Cui W., 2013, MNRAS, 436, 1750 47

Read J. I., Hayfield T., 2012, MNRAS, 422, 3037 11

Regan J. A., Haehnelt M. G., Viel M., 2007, MNRAS, 374, 196 10

Renzini A., Peng Y.-j., 2015, ApJ, 801, L29 xiv, 87, 88

Robertson B., Hernquist L., Cox T. J., Di Matteo T., Hopkins P. F., Martini P., Springel V., 2006, ApJ, 641, 90 xiii, 80

Rosas-Guevara Y. M. et al., 2013, ArXiv e-prints 28

Rupke D. S. N., Veilleux S., 2013, ApJ, 768, 75 107

Russell B. R., Immler S., 2012, ApJ, 748, L29 6

Salim S. et al., 2007, ApJS, 173, 267 xii, 68

Salpeter E. E., 1955, ApJ, 121, 161 25

Salpeter E. E., 1964, ApJ, 140, 796 7

Sánchez S. F. et al., 2012, A&A, 538, A8 91

Sánchez S. F. et al., 2013, A&A, 554, A58 xiii, 83, 84

Sanders R. L. et al., 2015, ApJ, 799, 138 xiii, 84

Sani E., Marconi A., Hunt L. K., Risaliti G., 2011, MNRAS, 413, 1479 8

Saracco P. et al., 2006, MNRAS, 367, 349 xii, 75

Savaglio S. et al., 2005, ApJ, 635, 260 xiii, 84

Savorgnan G., Graham A. W., Marconi A., Sani E., Hunt L. K., Vika M., Driver S. P., 2013, MNRAS, 434, 387 8

Scannapieco C., Tissera P. B., White S. D. M., Springel V., 2006, MNRAS, 371, 1125 23

Scannapieco C. et al., 2012, MNRAS, 423, 1726 22

Scannapieco E., Brüggen M., 2008, ApJ, 686, 927 10

Schaefer B. E., Pagnotta A., 2012, Nat, 481, 164 6

Schaye J., Aguirre A., Kim T.-S., Theuns T., Rauch M., Sargent W. L. W., 2003, ApJ, 596, 768 114

Schaye J. et al., 2014, ArXiv:1407.7040 e-prints 22, 24, 26, 29, 119

Schaye J. et al., 2015, MNRAS, 446, 521 60, 89, 120

Schaye J., Dalla Vecchia C., 2008, MNRAS, 383, 1210 22

Scheuer P. A. G., Readhead A. C. S., 1979, Nat, 277, 182 7

Schmidt M., 1963, Nat, 197, 1040 7

Schmidt M., Schneider D. P., Gunn J. E., 1995, AJ, 110, 68 8, 107

Schneider R., Ferrara A., Natarajan P., Omukai K., 2002, ApJ, 571, 30 27

Schramm D. N., Turner M. S., 1998, Reviews of Modern Physics, 70, 303 1

Searle L., Zinn R., 1978, ApJ, 225, 357 2

Seyfert C. K., 1943, ApJ, 97, 28 7

Shakura N. I., Sunyaev R. A., 1973, A&A, 24, 337 8, 28

Shankar F., Marulli F., Bernardi M., Dai X., Hyde J. B., Sheth R. K., 2010, MNRAS, 403, 117 xiii, 85, 86

Shen S., Mo H. J., White S. D. M., Blanton M. R., Kauffmann G., Voges W., Brinkmann J., Csabai I., 2003, MNRAS, 343, 978 xiii, 85, 86

Sijacki D., Springel V., Di Matteo T., Hernquist L., 2007, MNRAS, 380, 877 26, 27, 47

Sijacki D., Vogelsberger M., Genel S., Springel V., Torrey P., Snyder G. F., Nelson D., Hernquist L., 2015, MNRAS, 452, 575 119

Silk J., 2013, ApJ, 772, 112 29, 63

Smolčić V. et al., 2009, ApJ, 696, 24 32

Snyder G. F. et al., 2015, ArXiv e-prints 85

Sobral D., Smail I., Best P. N., Geach J. E., Matsuda Y., Stott J. P., Cirasuolo M., Kurk J., 2013, MNRAS, 428, 1128 34, 35, 54

Soltan A., 1982, MNRAS, 200, 115 8

Spolaor M., Kobayashi C., Forbes D. A., Couch W. J., Hau G. K. T., 2010, MNRAS, 408, 272 xii, 66, 67, 68, 94

Springel V., 2010, MNRAS, 401, 791 10, 11, 16

Springel V., Di Matteo T., Hernquist L., 2005, MNRAS, 361, 776 13, 15, 26, 27, 28, 29, 47, 49, 107

Springel V., Hernquist L., 2002, MNRAS, 333, 649 15

Springel V., Hernquist L., 2003, MNRAS, 339, 289 10, 45

Springel V. et al., 2005, Nat, 435, 629 9

Springel V., White S. D. M., Tormen G., Kauffmann G., 2001, MNRAS, 328, 726 32, 56, 92

Stacy A., Greif T. H., Bromm V., 2010, MNRAS, 403, 45 6

Stark D. P., Schenker M. A., Ellis R., Robertson B., McLure R., Dunlop J., 2013, ApJ, 763, 129 11

Steidel C. C. et al., 2014, ApJ, 795, 165 xiii, 84

Steigman G., 2004, Measuring and Modeling the Universe, p. 169 1

Steinmetz M., Müller E., 1994, A&A, 281, L97 10

Stone J. M., Norman M. L., 1992, ApJS, 80, 753 10

Stringer M. J., Benson A. J., Bundy K., Ellis R. S., Quetin E. L., 2009, MNRAS, 393, 1127 3

Sturm E. et al., 2011, ApJ, 733, L16 47, 108

Sutherland R. S., Dopita M. A., 1993, ApJS, 88, 253 17, 20

Tacconi L. J. et al., 2013, ApJ, 768, 74 xiv, 87, 88

Tanaka M. et al., 2009, ApJ, 692, 1131 6

Tasker E. J., Brunino R., Mitchell N. L., Michielsen D., Hopton S., Pearce F. R., Bryan G. L., Theuns T., 2008, MNRAS, 390, 1267 10

Taylor P., Kobayashi C., 2014, MNRAS, 442, 2751 8, 12, 34, 35, 85

Taylor P., Kobayashi C., 2015a, MNRAS, 448, 1835 12

Taylor P., Kobayashi C., 2015b, MNRAS, 452, L59 12

Tchekhovskoy A., Narayan R., McKinney J. C., 2011, MNRAS, 418, L79 49

Teng S. H. et al., 2014, ApJ, 785, 19 108

Teyssier R., 2002, A&A, 385, 337 10

Thomas D., Maraston C., Bender R., 2003, MNRAS, 339, 897 3, 67

Thomas D., Maraston C., Bender R., Mendes de Oliveira C., 2005, ApJ, 621, 673 xi, xiii, 11, 63, 64, 82, 83

Tinsley B. M., 1980, Fundam. Cosm. Phys., 5, 287 108

Tombesi F., Cappi M., Reeves J. N., Nemmen R. S., Braito V., Gaspari M., Reynolds C. S., 2013, MNRAS, 430, 1102 108, 111

Tombesi F., Cappi M., Reeves J. N., Palumbo G. G. C., Braito V., Dadina M., 2011, ApJ, 742, 44 108, 111

Tombesi F., Cappi M., Reeves J. N., Palumbo G. G. C., Yaqoob T., Braito V., Dadina M., 2010, A&A, 521, A57 111

Tomczak A. R. et al., 2014, ApJ, 783, 85 xii, 72, 73

Toomre A., Toomre J., 1972, ApJ, 178, 623 4

Tremaine S. et al., 2002, ApJ, 574, 740 xiii, 8, 34, 80, 81

Tremonti C. A. et al., 2004, ApJ, 613, 898 xiii, 83, 84

Treu T., Ellis R. S., Liao T. X., van Dokkum P. G., 2005, ApJ, 622, L5 3, 11

Troncoso P. et al., 2014, A&A, 563, A58 xiii, 84, 85

Trujillo I., Erwin P., Asensio Ramos A., Graham A. W., 2004, AJ, 127, 1917 56, 85, 125

Trujillo I., Ferreras I., de La Rosa I. G., 2011, MNRAS, 415, 3903 x, 34, 37

Tumlinson J. et al., 2011, Science, 334, 948 114

Umeda H., Nomoto K., 2002, ApJ, 565, 385 6

Urry C. M., Padovani P., 1995, PASP, 107, 803 7

van der Wel A. et al., 2014, ApJ, 788, 28 xiii, 85, 86

Veilleux S. et al., 2013, ApJ, 776, 27 47

Vogelsberger M., Genel S., Sijacki D., Torrey P., Springel V., Hernquist L., 2013, MNRAS, 436, 3031 47

Vogelsberger M. et al., 2014, MNRAS, 444, 1518 8, 23, 24, 26, 89

Vogelsberger M., Sijacki D., Kereš D., Springel V., Hernquist L., 2012, MNRAS, 425, 3024 16

Wadsley J. W., Veeravalli G., Couchman H. M. P., 2008, MNRAS, 387, 427 10, 11

Wagner A. Y., Bicknell G. V., 2011, ApJ, 728, 29 29

Webbink R. F., 1984, ApJ, 277, 355 6

Whelan J., Iben Jr. I., 1973, ApJ, 186, 1007 6

Whitaker K. E. et al., 2014, ApJ, 795, 104 87

White S. D. M., Frenk C. S., 1991, ApJ, 379, 52 9

Whitehurst R., 1995, MNRAS, 277, 655 10, 11

Willmer C. N. A. et al., 2006, ApJ, 647, 853 xii, 77

Woo J.-H., Treu T., Malkan M. A., Blandford R. D., 2006, ApJ, 645, 900 xiii, 78, 79

Woosley S. E., 1988, ApJ, 330, 218 6

Wu X.-B. et al., 2015, Nat, 518, 512 120

Wuyts S. et al., 2011, ApJ, 742, 96 87

Yabe K. et al., 2012, PASJ, 64, 60 xiii, 84

Yates R. M., Henriques B., Thomas P. A., Kauffmann G., Johansson J., White S. D. M., 2013, MNRAS, 435, 3500 68

Yoshida N., Omukai K., Hernquist L., 2008, Science, 321, 669 6

Young L. M. et al., 2011, MNRAS, 414, 940 101

Yuan T.-T., Kewley L. J., Swinbank A. M., Richard J., Livermore R. C., 2011, ApJ, 732, L14 101

Zahid H. J., Dima G. I., Kewley L. J., Erb D. K., Davé R., 2012, ApJ, 757, 54 xiv, 87, 88

Zahid H. J., Dima G. I., Kudritzki R.-P., Kewley L. J., Geller M. J., Hwang H. S., Silverman J. D., Kashino D., 2014, ApJ, 791, 130 xiii, 83, 84

Zahid H. J., Kewley L. J., Bresolin F., 2011, ApJ, 730, 137 xiii, 84

Zaritsky D., Kennicutt Jr. R. C., Huchra J. P., 1994, ApJ, 420, 87 101

Zel'dovich Y. B., Novikov I. D., 1965, Soviet Physics Doklady, 9, 834 7